STRUCTURE-PROPERTY RELATIONSHIPS OF NONLINEAR

OPTICAL CHROMOPHORES AND THEIR APPLICATION

TOWARDS SENSING IN BIOLOGICAL SYSTEMS

A Dissertation
Presented to
The Academic Faculty

by

John P. Tillotson

In Partial Fulfillment
of the Requirements for the Degree
Doctor of Philosophy in the
School of Chemistry and Biochemistry

Georgia Institute of Technology
December 2018

STRUCTURE-PROPERTY RELATIONSHIPS OF NONLINEAR

OPTICAL CHROMOPHORES AND THEIR APPLICATION

TOWARDS SENSING IN BIOLOGICAL SYSTEMS

Approved by:

Dr. Joseph W. Perry, Advisor
School of Chemistry and Biochemistry
Georgia Institute of Technology

Dr. Bridgette Barry
School of Chemistry and Biochemistry
Georgia Institute of Technology

Dr. John Reynolds
School of Chemistry and Biochemistry
School of Materials Science and Engineering
Georgia Institute of Technology

Dr. Carlos Silva, Co-Advisor
School of Chemistry and Biochemistry
School of Physics
Georgia Institute of Technology

Dr. Christoph Fahrni
School of Chemistry and Biochemistry
Georgia Institute of Technology

Dr. Younan Xia
School of Biomedical Engineering
School of Chemistry and Biochemistry
Georgia Institute of Technology

Date Approved: October 19, 2018

To my loving family

ACKNOWLEDGEMENTS

I would like to express my profound gratitude to everyone who has helped me in my journey to receiving my doctorate. First and foremost, I want to thank my research advisor, Prof. Joseph W. Perry, for all he has done for me over the years. Dr. Perry accepted me as an undergraduate research assistant during the summer after my freshman year back in May of 2008. During my undergrad, Dr. Perry always encouraged me to make everything my own and delve into anything I found interesting. Because of his support and mentorship, I remained with his group until I graduated from undergrad in 2011 and then decided to continue on for my graduate work. I am eternally grateful for all of his inspiration, patience, enthusiasm, and trust he has shown me in our long tenure working together.

I also want to thank Prof. Carlos Silva, my co-advisor, for everything that he has done to help me over the final year of my doctoral journey. This last year has been a challenging experience, but without all of your help and support, it would have been truly insurmountable.

I would like to thank my thesis committee members, Prof. Bridgette Barry, Prof. Christoph Fahrni, Prof. John Reynolds, and Prof. Younan Xia for their guidance and commitment to my success.

Throughout my research experience in the Perry group, I have had the privilege of working on a very large number of different projects. As a result, I have had several mentors and friends who have made this journey possible. I want to thank my first research mentor, Dr. Philseok Kim, for helping me to navigate through my initial

iv

TABLE OF CONTENTS

CHAPTER 4: STRUCTURE-PROPERTY RELATIONSHIPS AND
SOLVATOCHROMIC BEHAVIOR OF DONOR-ACCEPTOR POLYENES

CHAPTER 6: CHROMOPHORES WITH LARGE HYPERPOLARIZABILITIES FOR THE SENSING AND IMAGING OF TRANSMEMBRANE POTENTIALS IN MEMBRANE ANALOGUES

LIST OF TABLES

LIST OF FIGURES

LIST OF SCHEMES

LIST OF SYMBOLS AND ABBREVIATIONS

μ	Dipole moment (in Debye)
α	Linear polarizability
β	First hyperpolarizability
γ	Second Hyperpolarizability
E	Electric field
P	Macroscopic polarization
$\chi^{(n)}$	n^{th} order succeptibility
ε_0	Permittivity of free space
c	speed of light in a vacuum
λ	wavelength (in nm)
N	Number density
N_A	Avogadro's number
n_0 (or n)	linear refractive index
n_2	Nonlinear refractive index
ω	Frequency (in cm^{-1})
υ	Frequency (in Hz)
1PA	One-photon absorption
2PA	Two-photon Absorption
TPEM	Two-photon excitation microscopy
σ	linear absorbance cross section
δ	Two-photon absorbance cross section

GM	Göppert-Mayer (unit of δ)
TPIF	Two-photon induced fluorescence
ND2PA	Non-degenerate two-photon absorption
VB-CT	Valence bond – charge transfer
BLA	Bond length alternation (in Å)
BOA	Bond order alternation
$<\Delta J>$	Average difference in coupling constants (BLA by NMR)
HRS	Hyper-Rayleigh scattering
SHG	Second harmonic generation
D-A	Donor-acceptor
DCV[n]	dicyanovinyl – terminated series
TB[n]	1,3-diethyl-2-thiobarbituric acid – terminated series
TCF[n]	Tricyanofuran – terminated series
ID[n]	1,3-indanedione – terminated series
R	Reaction field (in V/cm)
a	Onsager cavity radius
s, d, t, q, m	Singlet, doublet, triplet, quartet, and multiplet (NMR)
ABq	Apparent quartet of an AB spin system

SUMMARY

This dissertation investigates the use of nonlinear optical chromophores, typically with strong second-order nonlinearities, for sensing applications in biological systems. The two main areas of focus, in terms of biological sensing, are the two-photon excited fluorescent sensing of metal ions in biological environments and the sensing of transmembrane potentials, such as an action potential in a neuron.

The metal ion sensing work can be broken down into two major approaches. First, a calcium ion sensitive dye with a donor-π-donor-binding domain architecture was synthesized in excellent yield by sequential Horner-Wadsworth-Emmons reactions. This chromophore, BAPTA-bisstyrylbenzene (BAPTA-BSB), shows a strong two-photon absorbance (2PA) cross-section of about 400 GM. The second major phase of the metal ion sensing work is the investigation of the effects of surface charge on the sensing efficacy of chromophore with a donor-π-acceptor-binding domain architecture, which is sensitive to zinc ions. This chromophore, called SL-35, was synthesized by Dr. Sumalekshmy in Professor Christoph Fahrni's research group. The architecture of SL-35 was purposefully designed, such that the binding of the zinc ion increase the acceptor strength of the acceptor, resulting in an increase in the charge transfer and the 2PA cross-section. This increase in acceptor strength also results in redshifted absorbance and fluorescence spectra, allowing for ratiometric sensing. The sensitivity of SL-35 was assessed in micelles of varying surface charge: cetyltrimethylammonium bromide (CTAB) – positive, Triton-X – neutral, and sodium dodecylsulfate (SDS) – negative. Zn(II) titrations of SL-35 encapsulated in micelles of the three surfactants listed above,

demonstrate the surface charge affects the sensing efficacy of the chromophore. In SDS micelles, the negative charge of the micelle acts to increase the sensitivity of SL-35 toward Zn(II) ions, while CTAB micelles diminish its sensitivity. The observed results can be explained by the electrostatic interactions between the micelles and the zinc cations. The CTAB micelles repel the similarly charged metal ions, while the SDS micelles attract the oppositely charged ions.

The investigation of neural circuitry has become a very important to the medical field over the last few decades. The action potential was first described as a rapid reorganization of ions across a neuronal membrane in 1945. Though the phenomenon has been measured and described, the understanding of the communications between neurons in a network is lacking. Our approach to this problem is based on second harmonic generation (SHG) imaging. SHG is well suited to sensing transmembrane potentials because it offers the distinct advantage of being sensitive to an external electric field. The maximization of SHG sensitivity is investigated by two main approaches. First, the use of cyanine dyes seems counterintuitive for SHG applications as they have minimal second order nonlinearities. That said, the maximal change in SHG signal in response to an electric field occurs where the signal is at its smallest. Second, the scaling behavior of the ratio of the third-order (γ) to the second-order (β) nonlinearities increases with the length of a strongly dipolar chromophore. The SHG sensitivity is directly proportional to the ratio of γ/β. A series of strong merocyanines of varying length and acceptor strength were used to investigate this scaling behavior. The SHG sensitivity of both sets of chromophores was estimated by three methods. First the static nonlinearities were used to investigate the completely electrooptic components of SHG based on the ratio of γ/β.

Second, the field-dependent second-order nonlinearities were used to estimate the SHG sensitivity. The field was changed by varying the solvent, evoking the Onsager reaction field. These fields changes are significantly larger that of an action potential. Finally, the SHG sensitivity was estimated by measuring the change in response of target chromophores encapsulated in phosphatidyl choline vesicles. The potential was created by varying the potassium ion concentration inside and outside of the vesicles. The introduction of a potassium ions – specific ionophore allowed for the generation of a transmembrane potential. Through these methods, we see significant SHG sensitivities of more than a 25% change per 100 mV of field change in several of the merocyanines studied as well as an azaazulene-based cyanine. These results suggest that the optimization of SHG sensitivity can occur using both approaches taken.

CHAPTER 1

INTRODUCTION

1.1.   Introduction

Mankind's fascination with the unseen goes so far back into history that clear records are hard to come by. The ancient Greeks and Romans understood that certain materials could magnify an object such that it appears larger than in real life. It was Euclid in ca. 300 BC that first described an angular dependence of the refraction of light resulting in either magnification or reduction of an image. There are comments recorded from Seneca (ca. 62 AD) that a glass ball filled with water could make obscure text more visible.[1] The dark ages lead to a near standstill in scientific discovery and inquest in optics. The only real advancement during this time was in the eleventh century, when Ibn al-Haytham wrote a book on optics which described how vision worked and transformed the way we think of optics and light. Strangely enough, he saw no practical reasons to pursue advancements in optical magnification.[1]

Jumping ahead to the 1600's and Galileo's fascination with optics, moves to a time period of rapid discovery in microscopy. Galileo's contributions to microscopy may have been a bit accidental as he discovered that he could focus his telescopes on near objects, and many of his early experiments with magnification of near objects were in an attempt to prove the stability and superiority of his telescope designs.[1] Our entrance

1

into modern microscopy was made possible by observations from Robert Hooke and later by Antoni van Leeuwenhoek around the turn of the 18th century. In the intervening years, we have seen advancements in nearly every aspect of microscopy, including different light sources, optics, orientations, materials, and even the optical processes used. Microscopy has allowed us to better understand the world, and has become a vital tool in numerous aspects of modern life.

One of the most important applications for microscopy is the investigation and understanding of how cells function and interact. This field has flourished with the advancement of fluorescence microscopy and the invention of two-photon fluorescence microscopy (TPM) by Denk et al. in the early 1990s[2-3]. TPM offers some distinct advantages, as will be discussed further in chapters 2 and 3. In brief, the biggest advantages of TPM are the spatial resolution, as the fluorescence signal falls off with the forth power of the distance to the focal point[4]. In the time since these two major milestones, fluorophores sensitive to a myriad analytes have been developed including Ca(II)[5-6], Na(I)[7], Zn(II)[8-9], Ag(I)[10], Hg(II)[11], and Cu(I)[12], just to name a few. There has also been significan work to optimize these metal ion sensitive probes for TPM applications by changing the design of the fluorophores to dictate charge transfer characteristics.[9, 13] In addition to developing probes sensitive to metal ions, pH and potential sensitive probes have been developed following the pioneering work by Loew et al.[14-19]

Another major breakthrough in the field of biological sensing involves the use of chromophores with strong nonlinear optical (NLO) properties for sensing of potential and pH changes in cells and imaging them in general. One of the most famous recent

advances in sensing using NLO techniques is known as the SpectroPen[20], which uses a hand held laser and collection system to excite the fluorescence or Raman activity of nonlinear optical chromophores used as reporter molecules. The reporters bind to cancer cells and the pen allows surgeons to more accurately determine the amount of tissue to be removed. While these reporters, themselves, are not responding to a change in field or pH, they have been designed for their strong nonlinearities and specifically their interaction with surface plasmons on gold nanoparticles.
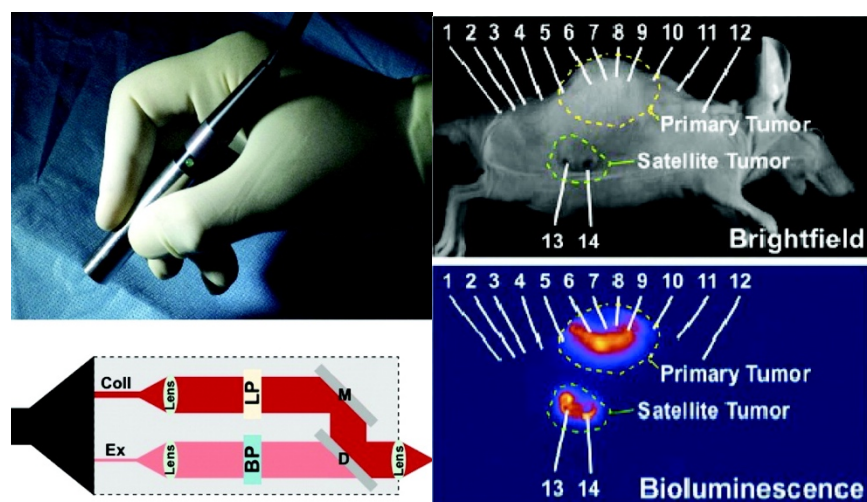
Figure 1.1. SpectroPen for use in the detection of cancer by utilizing nonlinear optical properties of reporter probes. Adapted with permission from Mohs, A.M., et al., *A Handheld Spectroscopic Device for In Vivo and Intraoperative Tumor Detection: Contrast Enhancement, Detection Sensitivity, and Tissue Penetration.* Analytical chemistry, 2010. **82**(21): p. 9058. Copyright (2010) American Chemical Society.

Second-harmonic generation (SHG) has also shown immense promise in high resolution biological imaging.[21-23] SHG is a nonlinear optical phenomenon where two photons of light are converted to a single photon at half the wavelength. The ability of a chromophore to facilitate SHG is related to its second order susceptibility to an electric

field, which will be described in greater detail in later chapters.[22] Not only does aqueous media, such as in biological tissues, provide almost zero background SHG signal, but the spatial and intensity requirements of TPM still remain true. In addition to these factors, SHG response is also sensitive to changes in potential, making it an ideal technique for investigating the interactions between neurons[23-24], as will be discussed in chapters 5 and 6.
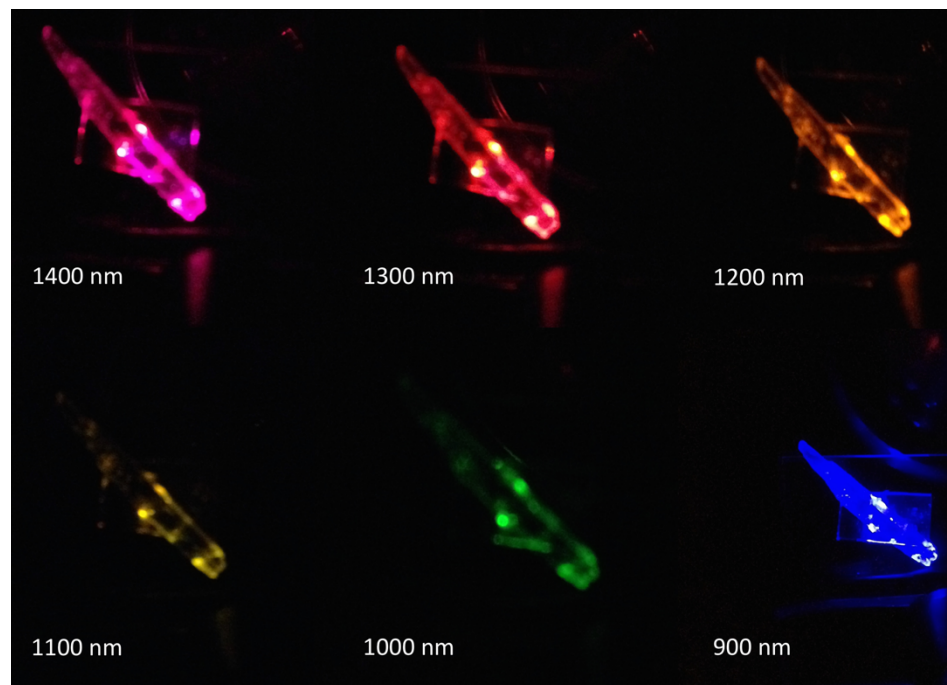
Figure 1.2. Urea crystal exhibiting second harmonic generation at various wavelengths during the development of our setup.

The detection of action potentials in neurons and specifically in networks of neurons is of particular import for the investigation of neurodegenerative diseases. We know how neurons function and we know how they become affected during the course of a neurodegenerative disease. What is still necessary to investigate is the way the neurons

communicate in a network in real time and how this communication is altered of hindered by disease.[25]

The work herein focuses on the structural and environmental factors that affect the target chromophores for sensing applications. In chapter 2, the various nonlinear optical properties will be discussed that are important for all of the subsequent chapters. Chapter 3 will focus on the synthesis of a strong two-photon absorbing Ca(II) sensor and on the effects of the surfactant charge on a ratiometric Zn(II) sensor encapsulated in surfactant micelles. Chapter 4 discusses the structural and electronic factors influencing the strong nonlinear optical properties of a series of donor-acceptor polyenes prepared for this investigation. Chapter 5 looks at various approaches for the estimation of membrane potential sensitivity in terms of a chromophore's nonlinear optical properties. Finally chapter 6 applies potential sensors to membrane analogs to better investigate the potential sensitivity of target chromophores in relevant environments and using neuron scale potential differences.

1.2. References

[1]   Bardell, D., The Invention of the Microscope. *Bios* **2004,** *75* (2), 78-84.

[2]   Denk, W.; Strickler, J. H.; Webb, W. W., Two-Photon Laser Scanning Fluorescence Microscopy. *Science* **1990,** *248* (4951), 73-76.

[3]   So, P. T. C.; Dong, C. Y.; Masters, B. R.; Berland, K. M., Two-Photon Excitation Fluorescence Microscopy. *Annual Review of Biomedical Engineering* **2000,** *2* (1), 399-429.

[4]   Diaspro, A.; Bianchini, P.; Vicidomini, G.; Faretta, M.; Ramoino, P.; Usai, C., Multi-photon excitation microscopy. *BioMedical Engineering OnLine* **2006,** *5*, 36-36.

[5]   Kuba, K.; Nakayama, S., Two-photon laser-scanning microscopy: tests of objective lenses and Ca2+ probes. *Neuroscience Research* **1998,** *32* (3), 281-294.

[6]   Minta, A.; Kao, J. P.; Tsien, R. Y., Fluorescent indicators for cytosolic calcium based on rhodamine and fluorescein chromophores. *Journal of Biological Chemistry* **1989,** *264* (14), 8171-8178.

[7]   Minta, A.; Tsien, R. Y., Fluorescent indicators for cytosolic sodium. *Journal of Biological Chemistry* **1989,** *264* (32), 19449-19457.

[8]   Bronson, R. T.; Bradshaw, J. S.; Savage, P. B.; Fuangswasdi, S.; Lee, S. C.; Krakowiak, K. E.; Izatt, R. M., Bis-8-hydroxyquinoline-Armed Diazatrithia-15-crown-5 and Diazatrithia-16-crown-5 Ligands: Possible Fluorophoric Metal Ion Sensors. *The Journal of Organic Chemistry* **2001,** *66* (14), 4752-4758.

[9]   Sumalekshmy, S.; Henary, M. M.; Siegel, N.; Lawson, P. V.; Wu; Schmidt, K.; Brédas, J.-L.; Perry, J. W.; Fahrni, C. J., Design of Emission Ratiometric Metal-Ion Sensors with Enhanced Two-Photon Cross Section and Brightness. *Journal of the American Chemical Society* **2007,** *129* (39), 11888-11889.

[10]   Huang, C.; Peng, X.; Lin, Z.; Fan, J.; Ren, A.; Sun, D., A highly selective and sensitive two-photon chemosensor for silver ion derived from 3,9-dithia-6-azaundecane. *Sensors and Actuators B: Chemical* **2008,** *133* (1), 113-117.

[11]   Huang, C.; Fan, J.; Peng, X.; Lin, Z.; Guo, B.; Ren, A.; Cui, J.; Sun, S., Highly selective and sensitive twin-cyano-stilbene-based two-photon fluorescent probe for mercury (ii) in aqueous solution with large two-photon absorption cross-section. *Journal of Photochemistry and Photobiology A: Chemistry* **2008,** *199* (2), 144-149.

[12]   Morgan, M. T.; Bagchi, P.; Fahrni, C. J., High-contrast fluorescence sensing of aqueous Cu(i) with triarylpyrazoline probes: dissecting the roles of ligand donor strength and excited state proton transfer. *Dalton Transactions* **2013,** *42* (9), 3240-3248.

[13]   Sumalekshmy, S.; Fahrni, C. J., Metal-Ion-Responsive Fluorescent Probes for Two-Photon Excitation Microscopy. *Chemistry of Materials* **2011,** *23* (3), 483-500.

[14]   Bouevitch, O.; Lewis, A.; Pinevsky, I.; Wuskell, J. P.; Loew, L. M., Probing membrane potential with nonlinear optics. *Biophysical Journal* **1993,** *65* (2), 672-679.

[15]   Hassner, A.; Birnbaum, D.; Loew, L. M., Charge-shift probes of membrane potential. Synthesis. *The Journal of Organic Chemistry* **1984,** *49* (14), 2546-2551.

[16]   Loew, L. M.; Benson, L.; Lazarovici, P.; Rosenberg, I., Fluorometric analysis of transferable membrane pores. *Biochemistry* **1985,** *24* (9), 2101-2104.

[17]   Loew, L. M.; Cohen, L. B.; Dix, J.; Fluhler, E. N.; Montana, V.; Salama, G.; Jian-young, W., A naphthyl analog of the aminostyryl pyridinium class of potentiometric membrane dyes shows consistent sensitivity in a variety of tissue, cell, and model membrane preparations. *The Journal of Membrane Biology* **1992,** *130* (1), 1-10.

[18]   Millard, A. C.; Jin, L.; Wei, M.-d.; Wuskell, J. P.; Lewis, A.; Loew, L. M., Sensitivity of Second Harmonic Generation from Styryl Dyes to Transmembrane Potential. *Biophysical Journal* **2004,** *86* (2), 1169-1176.

[19]   Montana, V.; Farkas, D. L.; Loew, L. M., Dual-wavelength ratiometric fluorescence measurements of membrane potential. *Biochemistry* **1989,** *28* (11), 4536-4539.

[20]   Mohs, A. M.; Mancini, M. C.; Singhal, S.; Provenzale, J. M.; Leyland-Jones, B.; Wang, M. D.; Nie, S., A Handheld Spectroscopic Device for In Vivo and Intraoperative Tumor Detection: Contrast Enhancement, Detection Sensitivity, and Tissue Penetration. *Analytical chemistry* **2010,** *82* (21), 10.1021/ac102058k.

[21]   Reeve, J. E.; Anderson, H. L.; Clays, K., Dyes for biological second harmonic generation imaging. *Phys Chem Chem Phys* **2010,** *12* (41), 13484-98.

[22]   Theer, P.; Denk, W.; Sheves, M.; Lewis, A.; Detwiler, P. B., Second-Harmonic Generation Imaging of Membrane Potential with Retinal Analogues. *Biophysical Journal* **2011,** *100* (1), 232-242.

[23]   Peterka, D. S.; Takahashi, H.; Yuste, R., Imaging voltage in neurons. *Neuron* **2011,** *69* (1), 9-21.

[24]   Nuriya, M.; Jiang, J.; Nemet, B.; Eisenthal, K. B.; Yuste, R., Imaging membrane potential in dendritic spines. *Proc Natl Acad Sci U S A* **2006,** *103* (3)*,* 786-90.

[25]   Nemet, B. A.; Nikolenko, V.; Yuste, R. In *Second harmonic imaging of membrane potential of neurons with retinal*, SPIE: 2004; p 9.

CHAPTER 2

NONLINEAR OPTICAL RESPONCES, CHARACTERIZATION, AND SENSING METHODOLOGIES

2.1 Introduction

As discussed previously, organic molecules can be tailored to optimize their nonlinear optical responses for sensing applications. In order to understand how modifications to a chromophores structure will impact its NLO response, it is important to understand these nonlinearities. In this chapter, a qualitative description of second and third order effects and how changes in these NLO responses give rise to sensing responses is presented. In addition, several characterization techniques including: hyper-Rayleigh scattering, two-photon absorption, and z-scan will be discussed.

2.2 Second-Order Nonlinear Effects

2.2.1. Theoretical Framework

When an electromagnetic field (or optical field) interacts with molecule or atom, the electrons of the species will distort in response to the field. This distortion results in an uneven distribution of electrons around the molecule or atom, known as an induced dipole,

μ. The scale of the distortion or the magnitude of the induced dipole is dependent on an intrinsic property of the molecule or atom: polarizability.

The interaction of the molecule with an optical field can be simply described as

$$\mu(\omega) = \alpha \cdot E(\omega),$$
(Eq. 2.1)

where **μ** and **E** are frequency dependent vectors for the induced dipole and the optical field respectively and α is the linear polarizability of the molecule.[1] This simple relationship holds for molecules interacting with a weak optical field. When the incident field becomes intense enough, induced polarization's response is no longer linear with respect to the applied field. The approximation of the induced dipole above is no longer valid for this nonlinear response. In these situations, the induced dipole can be expressed as a Taylor series expansion in E[2]:

$$\mu_i = \mu_0 + \alpha_{ij}E_j + \beta_{ijk}E_jE_k + \gamma_{ijkl}E_jE_kE_l + \dots ,$$
(Eq. 2.2)

where μ is the ground state dipole moment, α is the linear polarizability of the molecule, β is the first-order hyperpolarizability, and γ is the second-order hyperpolarizability. For our purposes, the parameters of the most import are the hyperpolarizability and the second hyperpolarizability, β and γ respectively.

On a macroscopic scale, the induced dipole moment impacts that of surrounding molecules resulting in a macroscopic polarization, **P**, which is related to the induced dipole by:

$$\mathbf{P} = N\langle\mu\rangle ,$$
(Eq. 2.3)

where N is the number density of microscopic induced dipoles (μ).

The polarization can be similarly expanded using a Taylor series as follows

$$\mathbf{P} = \mathbf{P_0} + \chi^{(1)}E + \frac{1}{2!}\chi^{(2)}E \cdot E + \frac{1}{3!}\chi^{(3)}E \cdot E \cdot E + \dots \qquad \text{(Eq. 2.4)}$$

In the above expansion, $\chi^{(n)}$ is the *n*-th order susceptibility. For the purposes of this work, we mostly consider the microscopic polarizabilities. It is important to note, however, that for one of the main processes under investigation, Second Harmonic Generation (SHG), is typically thought of from a bulk or macroscopic perspective. In that case the actual measurable phenomenon is dependent on the second and third order susceptibilities $\chi^{(2)}$ and $\chi^{(3)}$ respectively and their interaction with an electric field.

2.2.2. Introduction to Hyper-Rayleigh Scattering

The measurement of the first hyperpolarizability, β, is typically accomplished by one of two methods: Electric Field Induced Second Harmonic Generation (EFISH) or by Hyper-Rayleigh scattering (HRS). EFISH is the traditional way to measure β but is plagued with numerous issues that limit its scope. Hyper-Rayleigh scattering, on the other hand, allows for the direct measurement of β, even of compounds which are centrosymmetric or are ionic, two classes of molecules which EFISH is incompatible.

Hyper-Rayleigh Scattering allows for a direct measurement of β. For a dilute solution, the indices of refraction for the solution and the neat solvent are assumed to equal, allowing for the assumption that the reflection and refraction at the cuvette walls will also be equal. The following expressions can be derived for the HRS signals, $S^{(2\omega)}$, of the neat solvent and the dilute solution respectively.

$$S^{(2\omega)}_{solvent} \propto N_{solvent} \langle \beta^2_{solvent} \rangle \left(P^{(\omega)} \right)^2 \qquad \text{(Eq. 2.5)}$$

$$S_{solution}^{(2\omega)} \propto \left(N_{solute} \langle \beta_{solute}^2 \rangle + N_{solvent} \langle \beta_{solvent}^2 \rangle \right) \left(P^{(\omega)} \right)^2 \qquad \text{(Eq. 2.6)}$$

As is shown above the HRS signals are linearly proportional to the number densities, N, and quadratically dependent on the first hyperpolarizability, β, and the power of the incident beam, $P^{(\omega)}$. In the above expressions, $\langle \beta^2 \rangle$ is the orientational average of the β tensor components.

As is shown above, the HRS signal has a quadratic dependence on the power of the incident beam. In order to achieve an intensity at the sample sufficiently high enough to see an appreciable HRS signal, the incident beam must be tightly focused inside the sample cell. This necessary sampling geometry allows for additional higher-order processes such as hyper-Raman scattering, two-photon fluorescence (2PF), supercontinuum generation, self-(de)focusing, and dielectric breakdown. In order to ensure that the collected signal is indeed hyper-Rayleigh scattering and not a combination of processes, it is absolutely vital to collect the spectrum of the scattered light. The resulting spectra can be processed in a way to eliminate the effects of these higher order effects, particularly 2PF.

2.2.3. Calibration and Referencing of HRS Measurements

As is discussed briefly in section 2.2.2 a target chromophore's HRS response is directly proportional to the square of the first hyperpolarizability. The determination of β from HRS measurements is more complicated that it appears on the surface. This is in large part because of the incoherent nature of the scattered light generated by hyper-Rayleigh scattering. Attempting an absolute measurement, which would require a means of collecting all of the scattered light, which is not practical for our purposes. Instead, HRS

measurements can be made referentially, ideally in reference to a compound which is stable, readily available, and which has a generally well accepted first hyperpolarizability.

As will be discussed in the next section, HRS measurements are typically referenced in one of two ways, either internally by comparing to the first hyperpolarizability of the neat solvent or externally to a different chromophore with known hyperpolarizability. Referencing HRS measurements to the hyperpolarizability of the sample's solvent is an ideal case, as the dilute sample solution and the neat solvent are already assumed to be identical in refractive index and the HRS signal for the neat solvent is always measured in order to subtract the solvent response from that of the solution.

The majority of the work presented here is based on the measurement of target dyes in various solvents, and therefore, it is unreasonable to reference all measurements to a single solvent nonlinearity, as the beam focusing and collection of the HRS signal is dependent on the refractive index of the sample being measured. In addition, all of the studies conducted in this thesis are aimed at the eventual use of the target chromophores in biological systems, and therefore the possible wavelengths used for measurements are limited by the biological window[3] or the wavelength range over which biological environments have minimal absorption. While the biological window can have many definitions and ranges based on application, such as taking the absorption of fat cells or (de)oxygenated blood into account. In our preliminary consideration, we have taken the biological window to be based simply on the absorption of water, which is approximately between 250 – 1000 nm. Whenever the absorption of a chromophore of interest required, the incident wavelength was changed to minimize the absorption of the incident light, which would cause heating in the sample, or reabsorption of the scattered light. Additional

wavelengths outside of our simplistic biological window were selected with the second (1000 – 1350 nm) and third (1550 – 1870 nm) biological windows[3-4] in mind.

Taking the biological window into account, the next consideration is the output of the laser system. Figure 2.1 shows the output of the TOPAS-C used in all of our experiments as a function of wavelength. The first biological window and the second harmonic of the signal and idler beams overlap quite well. Unfortunately, the peak power of this region for our system is 800 nm. This is an issue because the TOPAS input is 800 nm and it has significant issues with output between 780 nm and 820 nm (Figure 2.1 was recorded when the TOPAS was installed in its current location in 2005).
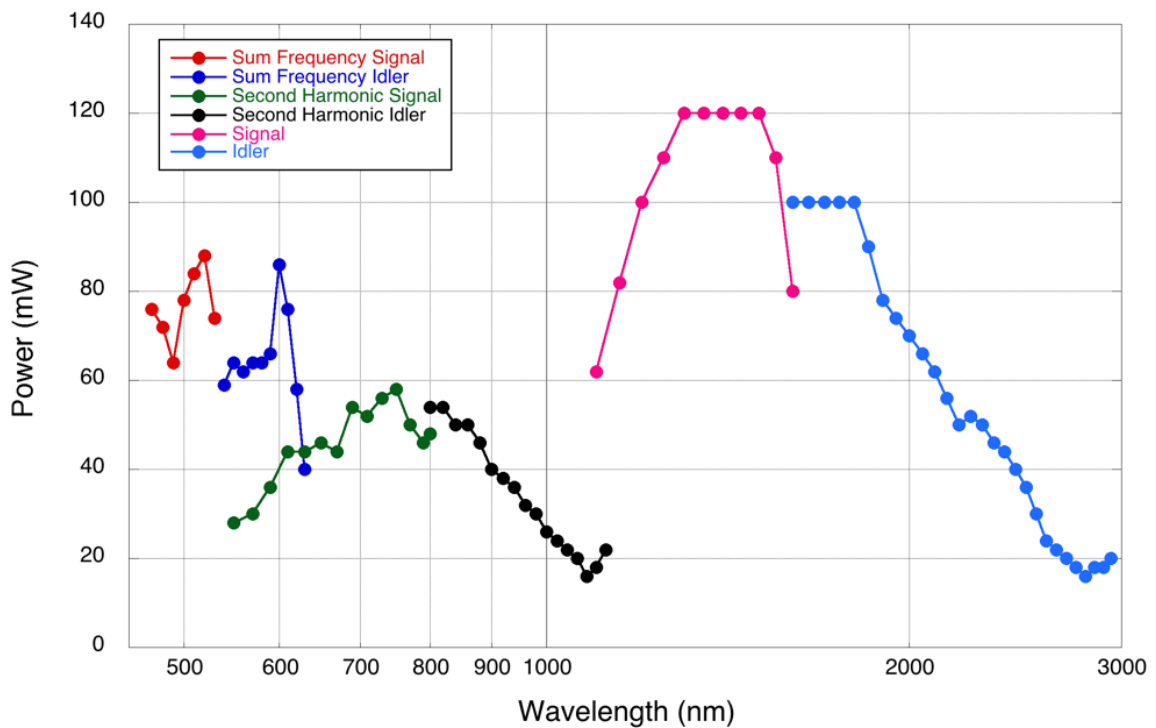
Figure 2.1. Tuning curve for the TOPAS-C by Light Conversion.

For these reasons as well as spectral profile of the output, most experiments were conducted at 900 nm. Though it is a slight decrease from 850 nm, it has much better stability and a narrower bandwidth.

In order to ensure that the HRS signals are consistent in different media and at different wavelengths, the resulting HRS signals of the relevant neat solvents are compared by taking into account local field factors and differences in focusing and collection geometry. The solvent hyper-Rayleigh scattering signal for a gaussian beam that is tightly focused in at least one direction can be described as:

$$S_{solvent}^{(2\omega)} \propto n_\omega \frac{1}{n_{2\omega}^2} T_\omega^2 T_{2\omega} f_\omega^4 f_{2\omega}^2 N \langle \beta_{solvent}^2 \rangle \left(P^\omega \right)^2, \tag{Eq. 2.7}$$

where T_ω and $T_{2\omega}$ are transmission factors and f_ω and $f_{2\omega}$ are local field factors for the incident and second harmonic wavelengths. The transmission factors can typically be neglected as experiments are designed in such a way that solvent absorption is negligible. The local field factors (Lorentz-Lorenz), shown in Eq. 2.8, are spherical and dependent on the dielectric constant, ε_ω.

$$f_\omega = \frac{\varepsilon_\omega + 2}{3} \tag{Eq. 2.8}$$

The refractive indices of the neat solvents at the incident and second harmonic wavelengths are calculated using the one-term Sellmeier dispersion formula:

$$n(\lambda)^2 = 1 + \frac{A_1 \lambda^2}{\left(\lambda^2 - \lambda_1^2 \right)}, \tag{Eq. 2.9}$$

where λ_1 and A_1 are fitting parameters based on experimental valued from the literature as is described by Campo *et al* in optics express[5].

As is noted in the above reference, the choice of solvent is quite crucial for HRS studies. There are a myriad factors to consider such as absorption or reabsorption of the incident or scattered light respectively by the solvent, as well as the effects that the solvent may have on the analyte of choice. Further discussion of the solvent effects on photophysical properties will be discussed in chapters 4 and 5. Figure 2.2, below shows the UV-VIS-NIR absorbance spectra for various solvents with the potential for use in HRS experiments.
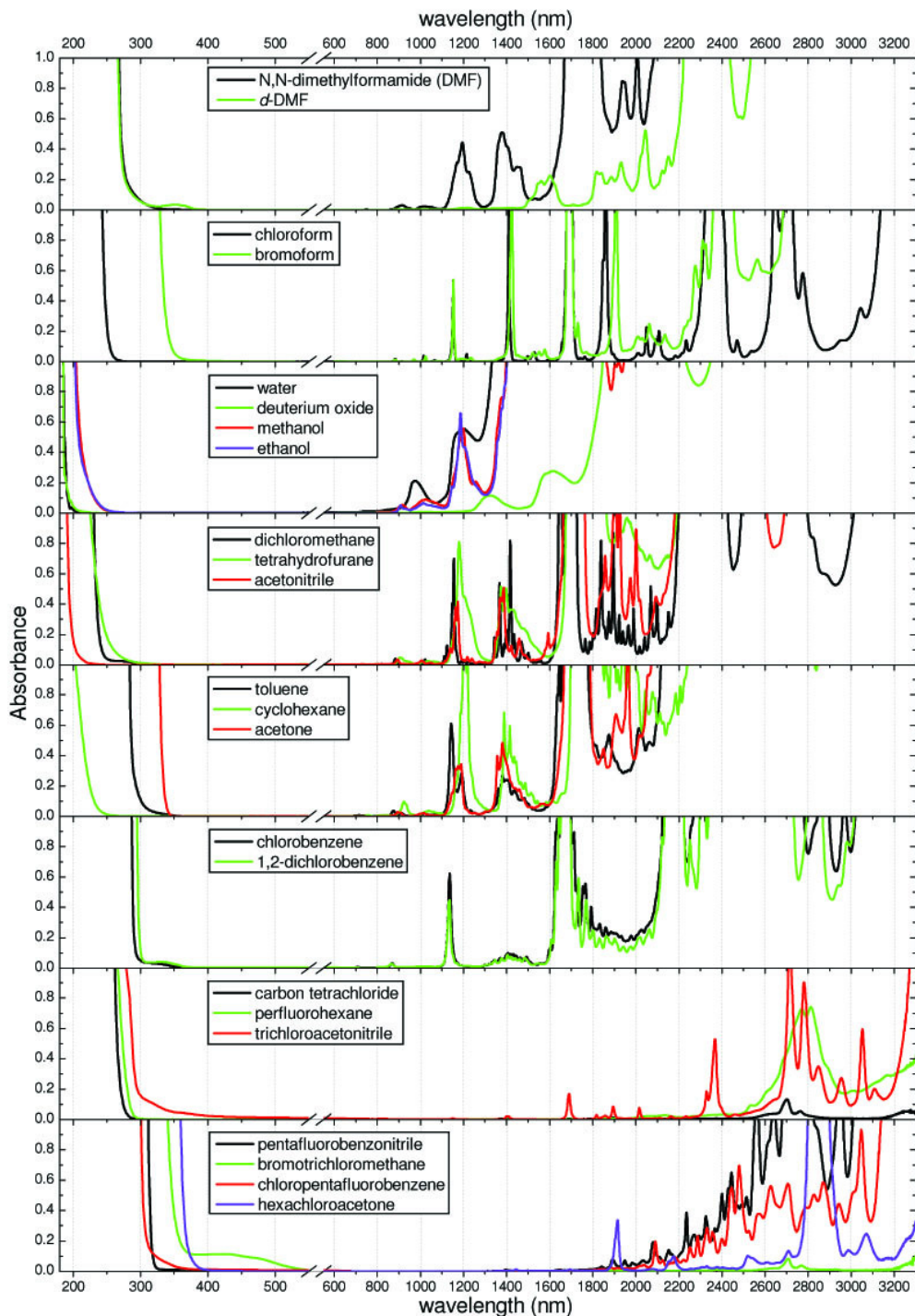
Figure 2.2. UV-VIS-NIR absorption spectra of various solvents, measured in a 1 cm cuvette as received. Figure reproduced with permission from Jochen Campo, Filip Desmet, Wim Wenseleers, Etienne Goovaerts, "Highly sensitive setup for tunable wavelength hyper-Rayleigh scattering with parallel detection and calibration data for various solvents," Opt. Express 17, 4587-4604 (2009)

2.2.3.1. Internal vs External Referencing of HRS Signals

As was stated earlier, referencing HRS measurements to the hyperpolarizability of the sample's solvent is the ideal case, as the dilute sample solution and the neat solvent are already assumed to be identical in refractive index and the HRS signal for the neat solvent is always measured in order to subtract the solvent response from that of the solution. The most common solvent used as a reference for HRS measurements in the literature is that of chloroform, and the most commonly cited value for the first hyperpolarizability of chloroform is 0.49 x 10^{-30} esu at 1064 nm, reported by Zyss in 1987[6]. Although this is the most common value cited, there is significant controversy over its accuracy[5]. The other most commonly cites value is that of Shelton in 1998, which was measured by HRS at 10.8 ± 0.5 au,[7] which roughly converts to 0.16 x 10^{-30} esu. That said, if a better representative value should arise, these reported HRS values need only to be scaled accordingly.

For dilute solutions, the refractive indices of the solution and the neat solvent are assumed to be equivalent. This leads to identical focusing of the beam inside the cell, as well as the same refraction and reflection at the cuvette walls for the neat solvent and the solution. This, and the use of spherical local field factors allows the refractive indices, local field factors, and transmission factors to cancel out. The resulting expression for the HRS signal, $S^{(2\omega)}$, of the neat solvent and dilute solution are shown above in eq. 2.3 and 2.4.

Application of an internal solvent reference is essentially the same as looking at the contributions from the dye divided by the contributions from the solvent. Therefore, it is necessary to subtract the contribution from the solvent out of the signal measured from the solution.

$$\frac{S_{dye}^{(2\omega)}}{S_{solvent}^{(2\omega)}} = \frac{S_{solution}^{(2\omega)} - S_{solvent}^{(2\omega)}}{S_{solvent}^{(2\omega)}} \frac{N_{dye}}{N_{solvent}} \frac{\langle \beta_{dye}^2 \rangle}{\langle \beta_{solvent}^2 \rangle} \qquad \text{(Eq. 2.10)}$$

Rearranging to solve for $\langle \beta_{dye}^2 \rangle$ gives the expression for the hyperpolarizability of the dye as a function of the solvent hyperpolarizability.

$$\langle \beta_{dye}^2 \rangle = \frac{N_{solvent}}{N_{dye}} \frac{S_{solution}^{(2\omega)} - S_{solvent}^{(2\omega)}}{S_{solvent}^{(2\omega)}} \langle \beta_{solvent}^2 \rangle \qquad \text{(Eq. 2.11)}$$

Similarly, the external referencing method also looks at the signal of the chromophores of interest (or reference) less the respective solvent signal. If the interrogated chromophore and the reference compound are dissolved in different solvents, the following describes the external referencing method:

$$\frac{S_{dye}^{(2\omega)}}{S_{solvent}^{(2\omega)}} = \frac{S_{solution}^{(2\omega)} - S_{solvA}^{(2\omega)}}{S_{ref}^{(2\omega)} - S_{solvB}^{(2\omega)}} \frac{N_{dye}}{N_{ref}} \frac{\langle \beta_{dye}^2 \rangle}{\langle \beta_{ref}^2 \rangle} \qquad \text{(Eq. 2.12)}$$

Again, solving for the $\langle \beta_{dye}^2 \rangle$ gives the hyperpolarizability as a function of a known hyperpolarizability value, this time the reference compound.

$$\langle \beta_{dye}^2 \rangle = \frac{N_{ref}}{N_{dye}} \frac{S_{solution}^{(2\omega)} - S_{solvA}^{(2\omega)}}{S_{ref}^{(2\omega)} - S_{solvB}^{(2\omega)}} \langle \beta_{ref}^2 \rangle \qquad \text{(Eq. 2.13)}$$

2.2.3.2. Common Dyes Used as External HRS References

External referencing can be very useful when the desired solvent does not have strong enough HRS response to detect. There are numerous dyes that have been used as external references, but among them, the most common are disperse red 1 (DR-1) and *para*-nitroaniline (pNA).
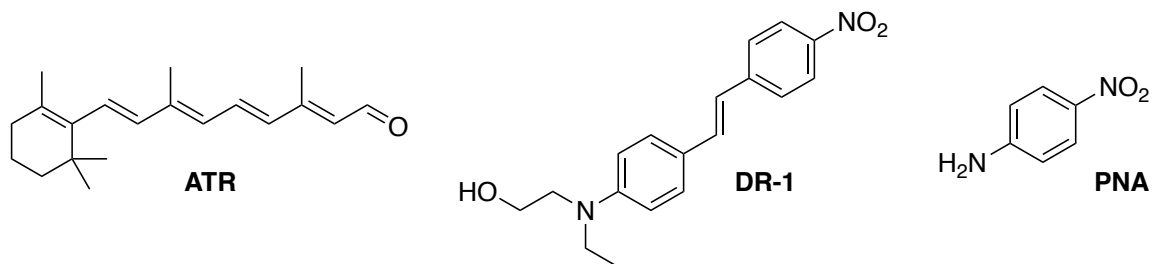
Figure 2.3. Chemical structures for HRS Standards

Table 2.1. Reference Hyperpolarizabilities for both internal and external reference techniques

Compound	Wavelength (nm)	β (esu)	Ref.
CHCl$_3$	1064	0.49 x 10^{-30}	[6]
CHCl$_3$	1064	0.16 x 10^{-30}	[7]
pNA (in CHCl$_3$)	1064	22.7 x 10^{-30}	[7]
DR-1 (in CHCl$_3$)	1650	160 x 10^{-30}	[5]

2.2.4. Units of Second-Order Nonlinear Optical Response

Hyperpolarizabilities reported in the literature are typically reported using the cgs unit system in esu. In order to use the measured hyperpolarizabilities to estimate voltage sensitivity, they must be converted into the SI system as follows:

$$\beta \left[\frac{C \cdot m^3}{V^2} \right] = \left(\frac{4\pi\varepsilon_0}{3} \times 10^{-6} \right) \beta \left[esu \right]$$

(Eq. 2.14)

2.3 Third-Order Nonlinear Optical Response

2.3.1. Nonlinear Refraction

The nonlinear refractive index is related to $\chi^{(3)}$ as follows:

$$n_2 = \frac{3}{4\varepsilon_0 n_0(\omega)^2 c} \text{Re}\left[\chi^{(3)}\right],$$

(Eq. 2.15)

where ε_0 is the permittivity of free space, $n_0(\omega)$ is the frequency dependent linear refractive index, and c is the speed of light in a vacuum. This nonlinear refraction is observed as an intensity-dependent change in refractive index. This refractive index change gives rise to the aforementioned phase change:

$$\Delta\phi = \frac{2\pi}{\lambda_0} n_2 IL.$$

(Eq. 2.16)

In the above equation, λ_0 is the wavelength, I is the intensity of the incoming light and L is the length of the nonlinear material. The sign of the nonlinear refraction determines if the resulting phase change causes the beam to focus (positive n_2) or diverge (negative n_2). The sign of the nonlinear refractive index will play an important role in determining the sign of the predicted SHG sensitivity in Chapter 4.

2.3.2. Two-Photon Absorption

Two-photon absorption (2PA) is an optical transition in which a molecule absorbs two photons of light simultaneously, resulting in excitation to a higher lying state. In order for this to occur, the sum of the energies of the two simultaneously absorbed photons must be equal to the transition energy. The process of 2PA is described by a 2PA coefficient (β) which is related to $\text{Im}[\chi^{(3)}]$ as follows:

21

$$\beta_{2PA} = \frac{3\omega}{2\varepsilon_0 n_0(\omega)^2 c^2} Im\left[\chi^{(3)}\right]. \qquad \text{(Eq. 2.17)}$$

The ability of a molecule to undergo 2PA is described by a molecules 2PA cross section, δ, which is given by:

$$\delta = \frac{4\pi^2 3\hbar\omega^2}{n^2 c^2} L^4 Im\left[\gamma\right]. \qquad \text{(Eq. 2.18)}$$

The relationship between β and δ can be described in terms of the photon energy and the number density of the chromophores in the sample:

$$\delta = \frac{\beta_{2PA} E_{ph}}{N}. \qquad \text{(Eq. 2.19)}$$

As is shown in Figure 2.4, this process can happen in two main ways: degenerate and non-degenerate.

One-Photon Absorption **Two-Photon Absorption**
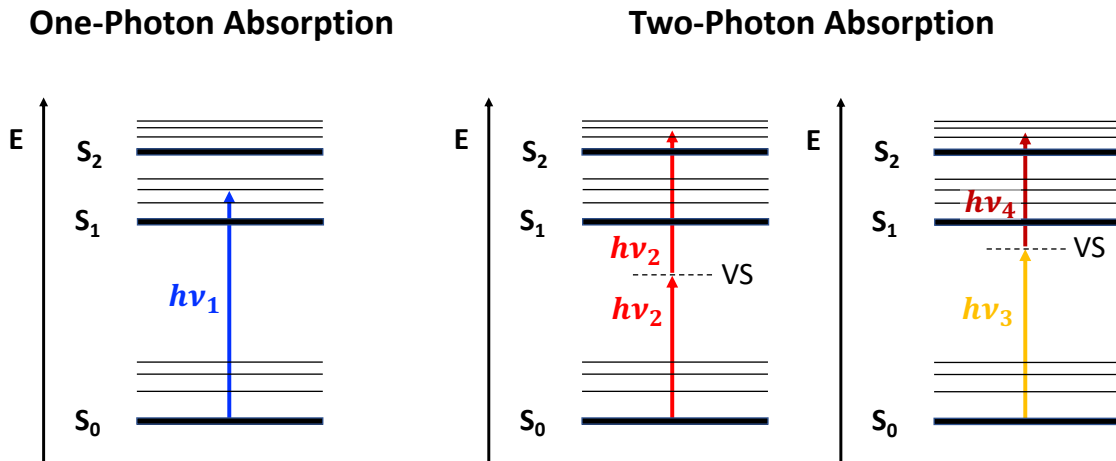
Figure 2.4. Jablonski diagrams showing 1PA (left), degenerate (middle), and non-degenerate (right) two-photon excitation of a molecule from its singlet ground state (S_0) to a singlet excited state (S_n). For the 2PA processes the dashed line represents a virtual state (VS).

In the above figure, $h\nu_n$ corresponds to the energy differences shown by the arrows of matching color. As an illustrative example, assuming that all three Jablonski diagrams above are showing the same idealized energy levels, if the wavelength required for the 1PA (blue) is 400 nm, then the wavelength required for the degenerate 2PA (red) would be 800 nm for each photon. The non-degenerate case is less straight forward. The equivalent 1PA transition for the non-degenerate two-photon absorption (ND2PA) is

$$\frac{1}{\lambda_{1PA}} = \frac{1}{\lambda_3} + \frac{1}{\lambda_4},\qquad\text{(Eq. 2.20)}$$

where λ_3 and λ_4 correspond to ν_3 and ν_4 from Figure 2.4 and can be any values that satisfy the above equation. In this example, one set of wavelengths, whose transition energy would add to equal that of a 400 nm photon, are 1200 nm and 600 nm.

While we typically think of 2PA as a simultaneous process, the process can best be described as the absorption of the first photon causes a perturbation in the wavefunction of the ground state. If the second photon interacts with this perturbed state before it dissipates, the transition to the higher lying state is achieved. Since the lifetime of this perturbed state is quite short, successful two-photon transitions require very high photon fluxes. This fact gives rise to one of the biggest advantages of 2PA processes, spatial resolution.

In this dissertation, the two main methods for the measurement of 2PA are two-photon induced fluorescence (TPIF) and non-degenerate two-photon absorption (ND2PA), which are described in the following sections.

2.3.3. Units of Third-Order NLO Parameters

For convenience in calculations, the units of $\chi^{(3)}$ are expressed using the cgs unit system as *esu* which is equivalent to a cm²statvolt⁻². Later, in chapter 5 it will be necessary to express $\chi^{(3)}$ and γ in terms of SI units to predict the voltage sensitivity of our target NLO compounds. The conversion from cgs to SI for $\chi^{(3)}$ is:

$$\chi^{(3)}\left[\frac{m^2}{V^2}\right]=\left(\frac{4\pi}{9}\times 10^{-8}\right)\chi^{(3)}\left[\frac{cm^2}{statvolt^2},esu\right].$$
(Eq. 2.21)

The third order susceptibility, $\chi^{(3)}$ is converted to the microscopic nonlinearity, γ, by the following conversion (in SI units):

$$\gamma\left[\frac{Cm^4}{V^3}\right]=\frac{\varepsilon_0}{NL^4}\chi^{(3)},$$
(Eq. 2.22)

where L is the Lorentz local field factor as shown in Eq. 2.23.

$$L=\frac{n_0^2+2}{3}$$
(Eq. 2.23)

2.4 Characterization Techniques

2.4.1. Measuring Second-Order Nonlinear Optical Properties: Hyper-Rayleigh Scattering

2.4.1.1. Femtosecond HRS Setup

Hyper-Rayleigh scattering (HRS) measurements were conducted on a home-built Hyper-Rayleigh scattering / two-photon induced fluorescence setup. The light source for the HRS measurements consisted of a regeneratively amplified Ti:Sapphire laser (Solstice, Spectra-Physics, 800 nm, 3.7 W average power, 100-fs pulse width, 1 kHz repetition rate). The amplified laser is used to pump a computer controlled optical parametric amplifier

(OPA) (TOPAS-C, Light Conversion). The OPA can be continuously tuned from 1100 – 2600 nm (FWHM 10 – 30 nm) and the second harmonic of the OPA can be used in the range of 550 – 1100 nm (~30 mW average power). The range of excitation energy, at the sample, varies between 2 – 12.5 μJ and is limited below the onset of higher order nonlinear optical effects such as white-light generation. Before entering the sample enclosure, the beam is filtered using appropriate long pass filters (typically 850 nm long pass) to remove stray 800 nm light. The beam then passes through two orthogonally oriented cylindrical lenses and into the sample cell (1 cm path length, Special Optical Glass, Sterna Cells). The cell holder is attached to a movable stage allowing the cuvette to be positioned such that the focus of the beam is just next to the wall of the cell, in order to minimize reabsorption. The generated light is collected at a right angle by means of a collection lens (focal length = 8.0 mm, KPA016-C, Newport Corporation) and is passed through appropriate short pass filters needed to remove scattered light from excitation beam as well as two-photon fluorescence from the sample. The filtered light is collected by fiber collimators (F810SMA-543, Thorlabs) and sent through a two-leg fiber bundle (13 fibers per bundle oriented in a line, Leoni) to an imaging fiber adapter (FC-446-030, Princeton Instruments) that is coupled to a monochromator (SpectrPro-150, Acton). The HRS signal is detected on a liquid nitrogen cooled CCD camera (LN/CCD-1100PB, Roper Scientific, controller: ST-133, Roper Scientific).
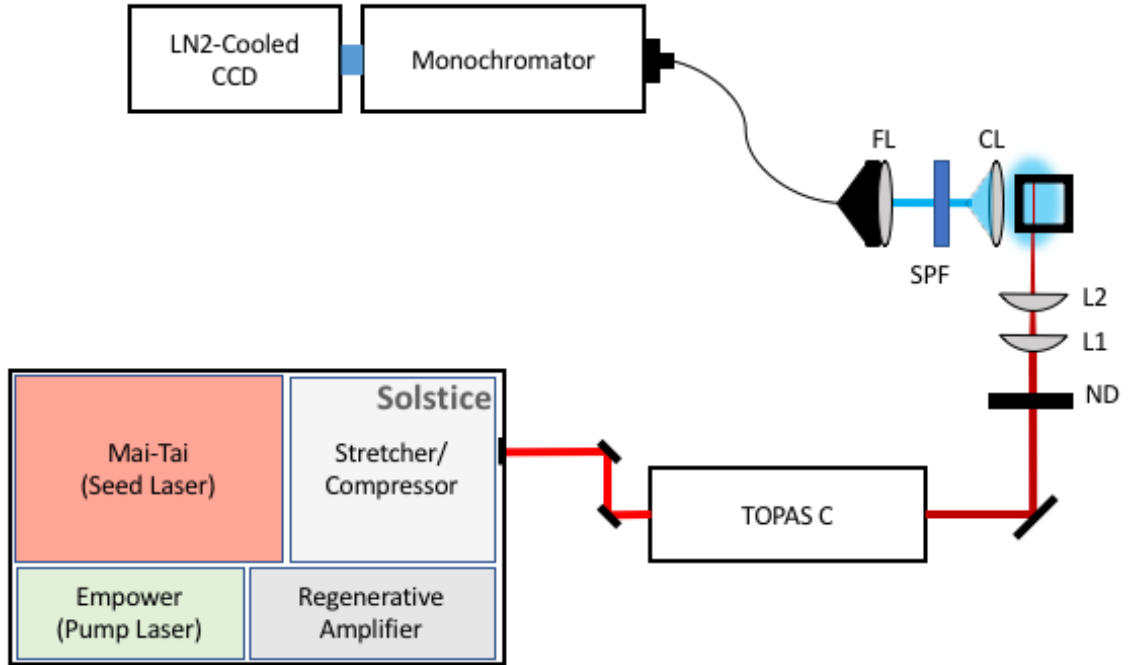
Figure 2.5. Optical setup for variable wavelength femtosecond Hyper-Rayleigh scattering experiments. ND: gradient neutral density filter wheel, L1: horizontally oriented cylindrical lens, L2: vertically oriented cylindrical lens, CL: collection lens, SPF: short-pass filter, FL: focusing lens and fiber couple.

2.4.1.2. Picosecond HRS Setup

Picosecond HRS measurements were conducted on the same home-built Hyper-Rayleigh scattering / two-photon induced fluorescence setup (Figure 2.6). The light source for the HRS measurements was the same regeneratively amplified Ti:Sapphire laser (Solstice, Spectra-Physics, 800 nm, 3.7 W average power, 100-fs pulse width, 1 kHz repetition rate). The amplified laser is used to pump a computer controlled second-harmonic bandwidth compressor (SHBC, Light Conversion) which compresses the bandwidth of the femtosecond pulses and outputs picosecond pulses. The SHBC then

pumps an optical parametric amplifier (TOPAS-400, Light Conversion) . The OPA can
be continuously tuned from 480 – 2400 nm (FWHM = 4 nm).
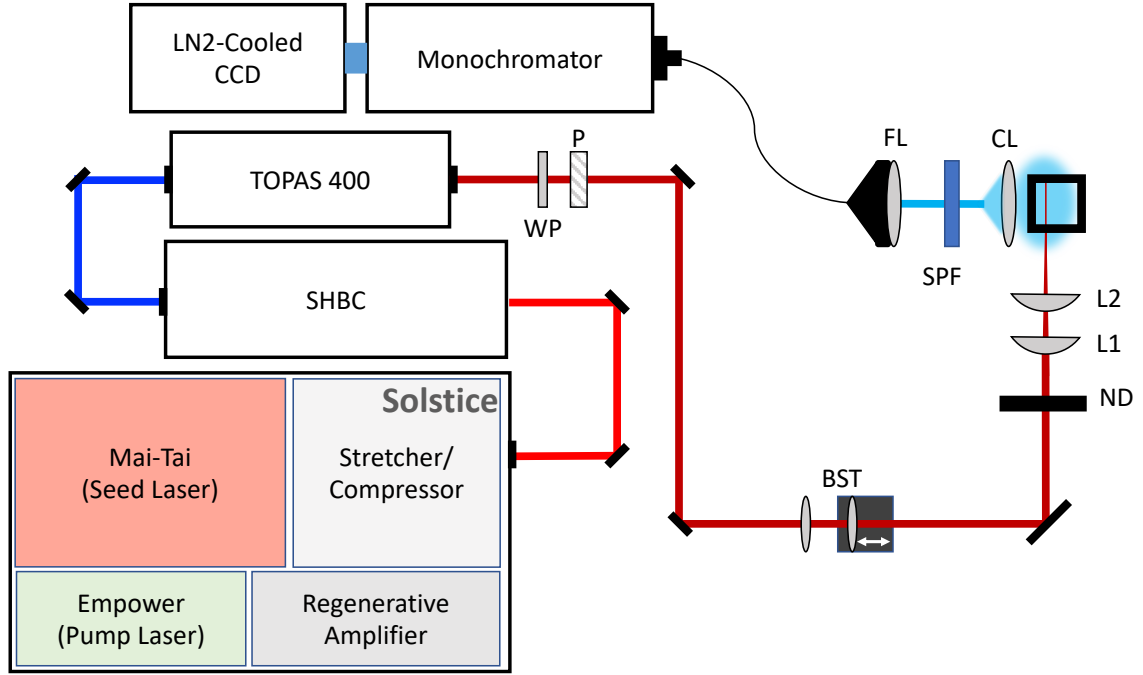
Figure 2.6. Optical setup for variable wavelength picosecond Hyper-Rayleigh scattering
and Hyper-Raman scattering experiments. WP: half waveplate, P: polarizer, BST: beam
shaping telescope, ND: gradient neutral density filter wheel, L1: horizontally oriented
cylindrical lens, L2: vertically oriented cylindrical lens, CL: collection lens, SPF: short-
pass filter, FL: focusing lens and fiber couple

The TOPAS-400 differs from the TOPAS-C amplifiers by the lack of a berek
which makes all polarization vertical. To correct for this, a half-wave plate and polarizer
are set up after the output of the TOPAS-400. To limit beam divergence, a beam shaping
telescope was added into the path of the light before the sample. This addition increased
the power at the sample by nearly 50 %. After the beam shaping telescope, the two setups

are identical. The difference in the bandwidth of the output in the fs-HRS and the ps-HRS

setups is quite dramatic and is shown in
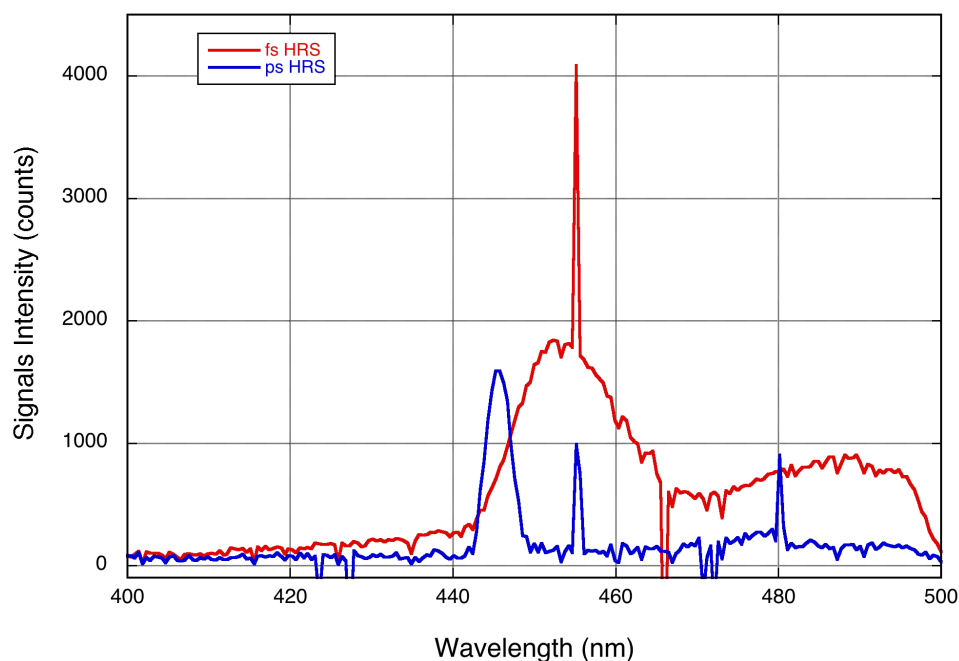
Figure 2.7. Comparison of fs-HRS (red trace) and ps-HRS (blue trace) setups at 900 nm excitation. The sample was TCF[1] (~10 µM in CHCl$_3$) and was excited at 900 nm (~10 µJ) for 250 s. Difference in peak centroid is due to the variations in the tuning curves for the respective optical parametric amplifiers.

2.4.1.3. Data Processing for HRS Measurements

Due to the exceedingly long integration times (50 – 500 s) for the HRS measurements,

the data suffers from being contaminated the detector response to cosmic rays. Another

issue to contend with for certain chromophores is the presence of a distorted baseline due

to multiphoton induced fluorescence (MPF). Show in Figure 2.8, are plots of HRS data

for a solution of TCF[2] (9.14 µM in acetonitrile, structure described in chapter 4) and

acetonitrile at each step of the post measurement processing. It is worth pointing out that

the HRS signal is around 25 – 30 nm (FWHM) this is quite broad but is a result of the fs-

pulsed source.
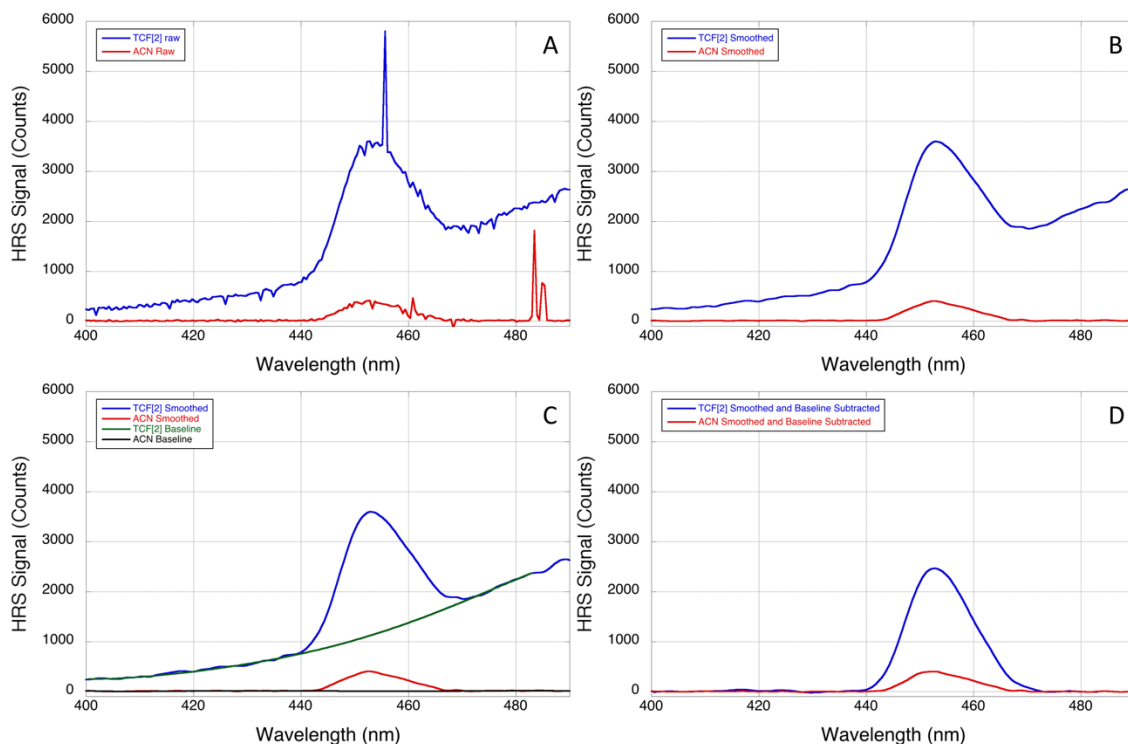
Figure 2.8. Example of HRS data processing. A) raw HRS data including cosmic rays B)
MATLAB based smoothing using the robust Loess fitting method C) Polynomial fit of
the multiphoton induced fluorescent background and D) the baseline fit from C is
subtracted from the raw spectrum in A and the resulting baseline corrected spectrum is
again smoothed with the robust Loess method. Blue trace in all four plots is the HRS
signal from TCF[2] (9.14 µM in acetonitrile). Red trace is the HRS signal from neat
acetonitrile. Both spectra were acquired using the homebuilt HRS setup outlined in
Chapter 2, and are acquired for 250 s at 900 nm (7.20 µJ) using a 500 nm short pass filter
and KG-5 heat absorbing Schott glass filter (<10% transmission above 775 nm and nearly
0% transmission between 850 – 1000 nm)

2.4.2. Measuring Third-Order Nonlinear Optical Properties: Z-Scan

The Z-scan technique is a well-established and popular method for characterizing

third-order nonlinearities.[8-9] One of the major advantages of the Z-scan experiment is

that it can simultaneously measure the nonlinear refraction, related to the real part of $\chi^{(3)}$, and the nonlinear absorption, related to the imaginary part of $\chi^{(3)}$. In addition, the sign of the nonlinear refraction can also be measured. This is particularly useful for determining the sign of the SHG potential sensitivity in Chapter 4 of this thesis.

Z-scan operates on the self-focusing and self-defocusing phenomena caused by an intensity dependent phase change as a result of a changing refractive index. The nonlinear refractive index is related to $\chi^{(3)}$ as follows:

$$n_2 = \frac{3}{4\varepsilon_0 n_0(\omega)^2 c} \mathrm{Re}\left[\chi^{(3)}\right] \qquad \text{(Eq. 2.24)}$$

Where ε_0 is the permittivity of free space, $n_0(\omega)$ is the frequency dependent linear refractive index, and c is the speed of light in a vacuum. This nonlinear refraction is observed as an intensity-dependent change in refractive index, which is determined by the difference in peak and valley transmittance (ΔT) of the closed aperture scan (see Figure 2.10).[10] This refractive index change gives rise to the aforementioned phase change. The change in transmittance and phase are related by equations 2.25 and 2.26.

$$\Delta T = 0.406(1-S)^{0.27}|\Delta\phi| \qquad \text{(Eq. 2.25)}$$

$$\Delta\phi = \frac{2\pi}{\lambda_0} n_2 IL \qquad \text{(Eq. 2.26)}$$

In the above equations, S is the aperture transmittance, λ_0 is the wavelength, I is the intensity of the incoming light and L is the length of the nonlinear material. The sign of the nonlinear refraction determines if the resulting phase change causes the beam to focus or diverge.

2.4.2.1. Femtosecond Z-Scan Setup

Z-scan measurements were conducted on a home-built Z-scan setup. The light source was the same as for the fs-HRS measurements consisted of a regeneratively amplified Ti:Sapphire laser (Solstice, Spectra-Physics, 800 nm, 3.7 W average power, 100-fs pulse width, 1 kHz repetition rate). The amplified laser is used to pump a computer controlled optical parametric amplifier (OPA) (TOPAS-C, Light Conversion). The OPA can be continuously tuned from 1100 – 2600 nm (FWHM 10 – 30 nm) and the second harmonic of the OPA can be used in the range of 550 – 1100 nm (~30 mW average power). Because beam shape is at a premium, the setup includes a beam shaping telescope which focuses the incoming light through a 50 μm pinhole. The gaussian shape of the beam was measured using a CCD camera beam profiler.

Once shaped and into the setup, the beam is split and a tiny portion sent to a reference detector (D1, Figure 2.9). The remaining light passes through a focusing lens (150 mm local length) and then through the sample. A beam splitter sends roughly 50% of the light through to the open and closed aperture detectors (D2 and D3 respectively). As per Sheik-Bae et al.[9], the closed aperture was set to allow 40% of the light to pass. The gaussian shape of the beam was determined using knife-edge beam scans in both the x- and y- directions to measure the beam waste. The beam was considered usable if the gaussian shape of the beam fit with in : $1.0 < M^2 < 1.1$ as determined by our beam scan. The Rayleigh range was typically in the range of 3.5 – 6 mm. Prior to every Z-scan measurement, reference scans of fused silica, ZnSe, and ZnS (1 mm thickness for all). Reference nonlinearities for these references are listed in Table 2.2. The resulting

reference nonlinearities were used to generate a correction factor to account for potential

biases and non-ideal beam quality.
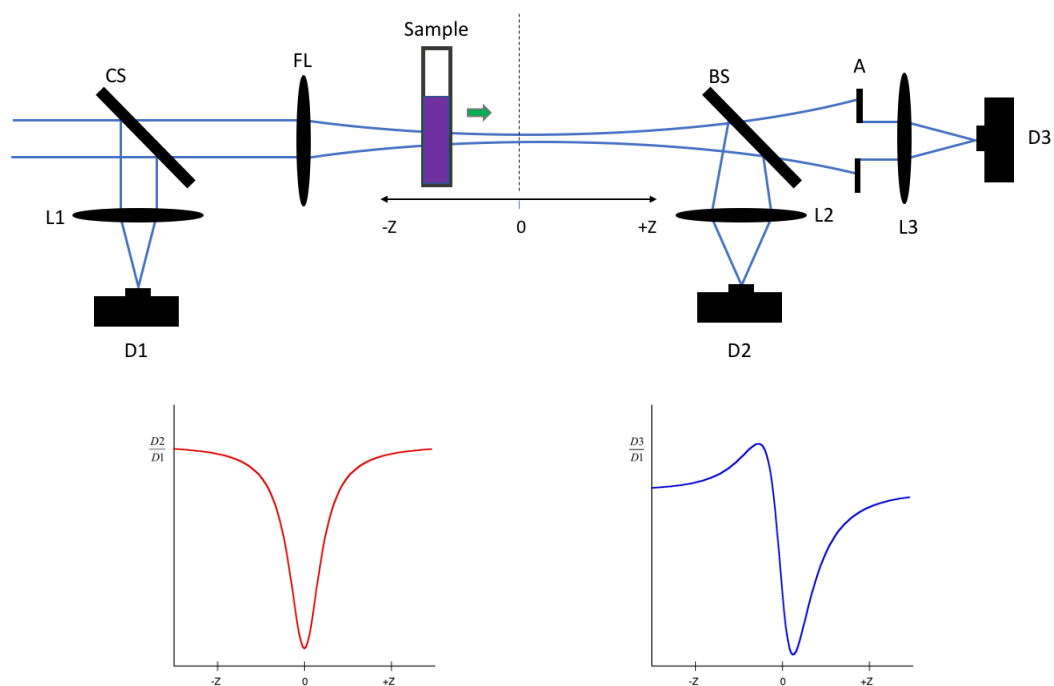
Figure 2.9. Top) Optical Setup for Femtosecond Z-Scan. **FL**: focusing lens, **D1**: reference detector, **D2**: open aperture detector, **D3**: closed aperture detector, **L1 – L3**: focusing lenses, **A**: aperture, **BS**: beam splitter, and **CS**: glass cover slip. Dashed line represents the focal plane, and the sample is translated through the focal plane along the z-axis. Bottom) Typical Z-scan signals: the open aperture signal (D2/D1, Red trace) and closed aperture signal (D3/D1, Blue trace)
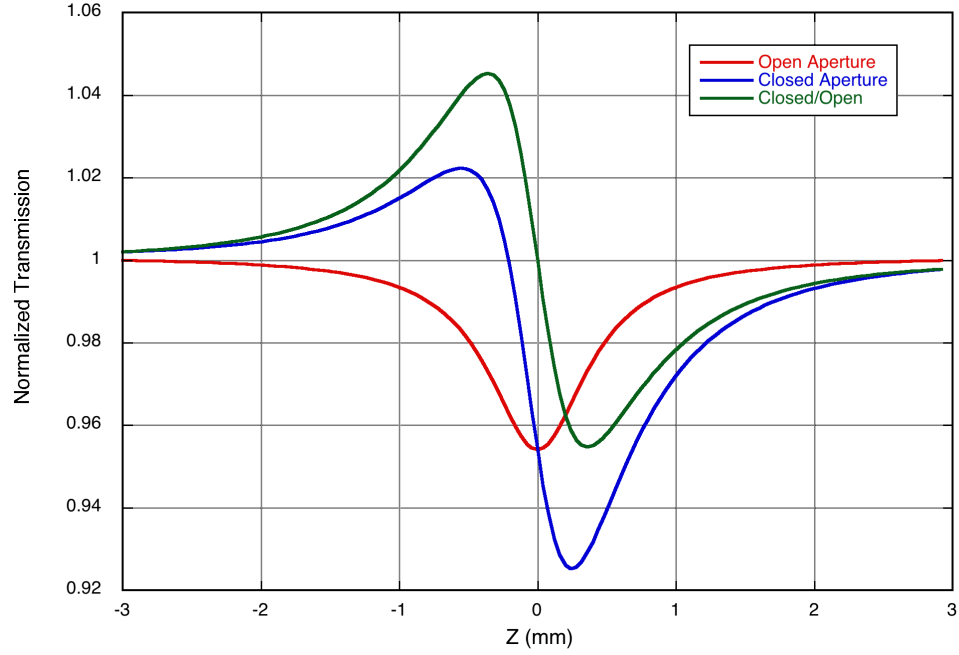
Figure 2.10. Z-scan data after processing. The closed aperture signal (blue trace) is affected by both nonlinear absorption and nonlinear refraction and therefore must be divided by the open aperture signal (red trace) leaving only the results of nonlinear refraction (green trace).

In solution, the errors for γ measurements by Z-scan are estimated to be about 8 – 12% depending the signal. For our purposes, the errors would be slightly elevated by the need to extrapolate the reference nonlinearities from their literature values at 1300 and 1550 nm to 900 nm (or 1250 nm) for the vast majority of the measurements in this work.

2.4.2.2. Calibration and References of Z-Scan Apparatus

Z-scan measurements were calibrated against the three semiconductors listed below on a daily basis.

Table 2.2 Nonlinear optical properties of reference samples.

Standard	λ (nm)	Thickness (μm)	n_0	n_2 (m^2/W)	Ref.
Fused Silica	1300	1000	1.45	2.63×10^{-20}	[11]
	1550		1.45	2.63×10^{-20}	
ZnSe	1300	1016	2.468	1.34×10^{-18}	[12-13]
	1550		2.457	1.18×10^{-18}	
ZnS	1300	1016	2.278	6.14×10^{-19}	[12]
	1550		2.271	5.77×10^{-19}	

2.4.2.3. Two-Photon Induced Fluorescence Measurements

Most 2PA spectra recorded in this work were recorded using our fs-HRS/TPEF setup. The excitation source is the same as previous measurements. In accordance with in Figure 2.11. For our purposes, measurements were referenced to coumarin 540A, rhodamine 610, and/or styryl 9M. the description of our TPEF setup by Makarov et al.[14], all samples were recorded in reference to one or two of the standards established in his two papers[14-15] and shown in Figure 2.11. For our purposes, measurements were referenced to coumarin 540A, rhodamine 610, and/or styryl 9M.
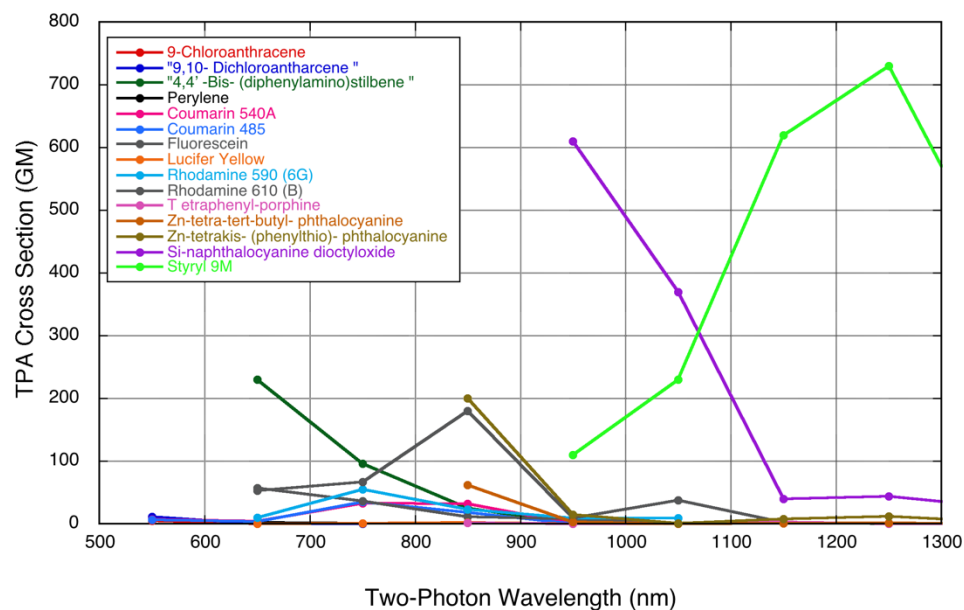
Figure 2.11. 2PA standards as measured on our setup and as described by Makarov et. al[15]
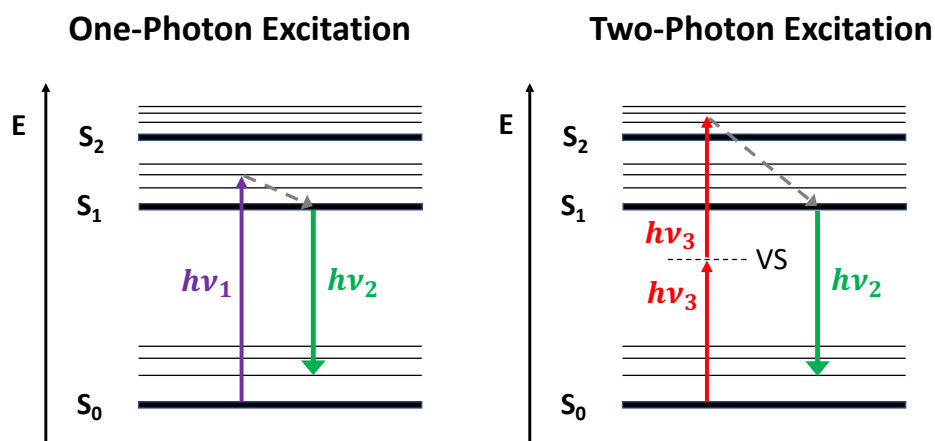
Figure 2.12. Jablonski diagrams comparing fluorescence resulting from 1PA (left) and 2PA (right) excitations.

2.5 References

[1]   Sutherland, R. L., *Handbook of Nonlinear Optics*. 2nd Ed. ed.; CRC Press: Boca Raton, 2003.

[2]   Sun, S.-S.; Dalton, L. R., *Introduction to organic electronic and optoelectronic materials and devices*. CRC Press: 2016.

[3]   Smith, A. M.; Mancini, M. C.; Nie, S., Second window for in vivo imaging. *Nature Nanotechnology* **2009,** *4*, 710.

[4]   Hemmer, E.; Benayas, A.; Légaré, F.; Vetrone, F., Exploiting the biological windows: current perspectives on fluorescent bioprobes emitting above 1000 nm. *Nanoscale Horizons* **2016,** *1* (3), 168-184.

[5]   Campo, J.; Desmet, F.; Wenseleers, W.; Goovaerts, E., Highly sensitive setup for tunable wavelength hyper-Rayleigh scattering with parallel detection and calibration data for various solvents. *Opt. Express* **2009,** *17* (6), 4587-4604.

[6]   Kajzar, F.; Ledoux, I.; Zyss, J., Electric-field-induced optical second-harmonic generation in polydiacetylene solutions. *Physical Review A* **1987,** *36* (5), 2210-2219.

[7]   Kaatz, P.; Shelton, D. P., Spectral features of hyper-Rayleigh scattering in chloroform-d. *Optics Communications* **1998,** *157* (1), 177-181.

[8]   Balu, M.; Hales, J.; Hagan, D. J.; Stryland, E. W. V., White-light continuum Z-scan technique for nonlinear materials characterization. *Opt. Express* **2004,** *12* (16), 3820-3826.

[9]   Sheik-Bahae, M.; Said, A. A.; Wei, T.; Hagan, D. J.; Stryland, E. W. V., Sensitive measurement of optical nonlinearities using a single beam. *IEEE Journal of Quantum Electronics* **1990,** *26* (4), 760-769.

[10]   Stryland, E. W. V.; Sheik-Bahae, M. In *Z-scan technique for nonlinear materials characterization*, Optical Science, Engineering and Instrumentation '97, SPIE: 1997; p 24.

[11]   Milam, D., Review and assessment of measured values of the nonlinear refractive-index coefficient of fused silica. *Appl. Opt.* **1998,** *37* (3), 546-550.

[12]   Krauss, T. D.; Wise, F. W., Femtosecond measurement of nonlinear absorption and refraction in CdS, ZnSe, and ZnS. *Applied Physics Letters* **1994,** *65* (14), 1739-1741.

[13]   Hutchings, D. C.; Wherrett, B. S., Theory of the dispersion of ultrafast nonlinear refraction in zinc-blende semiconductors below the band edge. *Physical Review B* **1994,** *50* (7), 4622-4630.

[14]   Makarov, N. S.; Campo, J.; Hales, J. M.; Perry, J. W., Rapid, broadband two-photon-excited fluorescence spectroscopy and its application to red-emitting secondary reference compounds. *Opt. Mater. Express* **2011,** *1* (4), 551-563.

[15]   Makarov, N. S.; Drobizhev, M.; Rebane, A., Two-photon absorption standards in the 550–1600 nm excitation wavelength range. *Opt. Express* **2008,** *16* (6), 4029-4047.

CHAPTER 3

METAL ION SENSORS WITH ENHANCED TWO-PHOTON ABSORPTION

CROSS-SECTION IN BIOLOGICALLY RELEVANT ENVIRONMENTS

3.1. Introduction

Two-photon laser scanning microscopy or more commonly two-photon excitation
microscopy (TPEM) has drastically expanded the capabilities and usability of
fluorescence microscopy imaging and sensing applications in biological systems[1-4] and
three-dimensional imaging[2, 4-5]. Before their wide utilization, the efficacy of optical
microscopy techniques was bound by the diffraction limit. In diffraction-limited
microscopy, only features, which are spatially separated by more than incident
wavelength divided by twice the numerical aperture of the lens, could be resolved.[6]
Numerous applications such as stimulated emission depletion microscopy can utilize two-
photon induced fluorescence for super resolution microscopy.[6] TPEM operates on the
ability of the two-photon absorbing fluorophore to access excited states by
simultaneously absorbing two photons of half the excitation energy necessary for steady
state excitation.[2] The three-dimensional spatial resolution arises from the dependence
of the probability of the two-photon absorption (TPA) process on the square of intensity
of the incident laser beam.[7-8] In biological environments, among others, the longer
wavelength excitation needed for TPEM also has added benefits of increased depth of

penetration, decreased photo-degradation, and reduced background autofluorescence of biological media.[9-10] The probability of two-photon absorption for a chromophore is defined by its two-photon absorption cross-section[8], δ, and is given in Göppert-Mayer (1 GM = 1 x 10^{-50} cm^{4}s/photon). The cross-section can be described for a quadripolar chromophore and a dipolar chromophore by:

$$\delta^{dipole} = \frac{2\pi L^4}{5\varepsilon_0^2 n^2 c^2 h} \frac{(\Delta\mu)^2 M_{01}^2}{\Gamma} \qquad \text{(Eq. 3.1)}$$

$$\delta^{quad} = \frac{2\pi h v^2 L^4}{5\varepsilon_0^2 n^2 c^2} \frac{M_{01}^2 M_{12}^2}{(E_{01} - hv)\Gamma} \qquad \text{(Eq. 3.2)}$$

respectively, where L is a local field factor and defined by L = (n^2 + 2)/3, Δμ is the change in permanent dipole moments, E_{01} is the transition energy, M_{01} is the transition dipole moment, ε_0 is the permittivity of free space, n is the refractive index of the medium, c is the speed of light, h is Planck's constant, and Γ is the damping factor, which accounts for the bandwidth.[1, 11-12]

In general, the goal of using fluorescent probes is to determine the concentration, either quantitatively or relatively, of an analyte by fluorescence spectroscopy. It is therefore necessary to correlate the fluorescence response with the concentration of analyte. For fluorophores that respond with a change of intensity at one wavelength (turn-on or turn-off sensors), the correlation between analyte concentration and fluorescence for a simple 1:1 stoichiometry can be described as:

$$\left[M^{n+} \right] = K_d \left(\frac{F - F_{min}}{F_{max} - F} \right), \qquad \text{(Eq. 3.3)}$$

39

where F is the recorded fluorescence intensity, F_{min} is the fluorescence intensity of the completely unbound sensor, F_{max} is the intensity when the sensor is saturated, and K_d is the dissociation constant.[13] The parameters F, F_{max}, and F_{min} are assumed to be recorded in the same instrument at the same relative time so that there is no variation in excitation intensity or other instrument factors.[14] This requirement makes the change in fluorescence intensity at a single wavelength harder to implement effectively as it requires calibration measurements. Applications such as sensing arrays and quantitative concentration determination from microscopy are exceedingly difficult to calibrate effectively.[14]

In applications where fluorescence calibration is impractical, fluorescent sensors, which undergo a shift in the fluorescence maximum upon binding, offer distinct advantages. The ratio of fluorescence intensities at two wavelengths can be used to determine the analyte concentration. This ratio is independent of dye concentration, path length or sensitivity of the instrument.[1, 13] The analyte concentration can be determined by:

$$\left[M^{n+} \right] = K_d \left(\frac{R - R_{min}}{R_{max} - R} \right) \left(\frac{S_f}{S_b} \right), \qquad \text{(Eq. 3.4)}$$

where, as before, K_d is the dissociation constant, R is the ratio of fluorescence intensities, R_{max} and R_{min} are the limiting values of R for when the sensor is saturated and free respectively, S_f and S_b are the instrument correction factors measured in the absence of analyte and saturated analyte.[1] The above equation can be simplified by choosing the isoemissive point as one of the detection wavelengths, which removes the necessity of the instrument correction factors from the equation.[13-14]

3.2. Background

In order for a chromophore to be used as a fluorescent metal-ion probe, it is necessary for the binding event to alter the absorbance or fluorescence response of the sensor. Dyes satisfying this requirement can then be sorted in to one of two groups based on the change in fluorescence caused by the binding event. In Figure 3.1, fluorophore **BAPTA-BSB** exhibits a change in the fluorescence intensity with calcium ion binding whereas fluorophore **SL-35** shows a shift in the peak emission upon zinc ion binding.[1] Some dyes in the first group, such as **BAPTA-BSB**, can be optimized to have large two-photon absorption (TPA) cross-sections.[11] When compared to **SL-35**, dye **BAPTA-BSB** has a larger length of conjugation which increases the extent of intramolecular charge transfer (ICT).[11] In addition, the electronic structure of **BAPTA-BSB** is of the general form donor- conjugated bridge-donor (D-π-D), which has been shown to have an enhanced two-photon cross-section due to symmetric charge transfer.[7, 11] In their unbound states, the TPA cross-section of **BAPTA-BSB** is a little more than an order of magnitude larger than that of **SL-35.**[15]
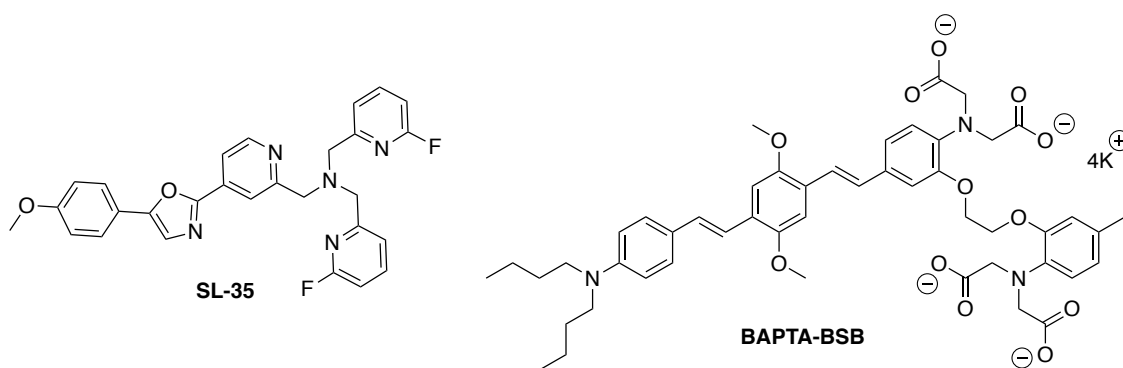
Figure 3.1. Structures of the metal-ion responsive probes described.

Although the TPA cross-section for **SL-35** may be smaller, its utility in metal ion sensing far surpasses that of **BAPTA-BSB**. The main difference is in the nature of the

metal chelating domain. The Ca(II) binding moiety for **BAPTA-BSB**, 1,2-bis-(2-aminophenoxy)ethane-N,N,N',N'-tetraacetic acid (BAPTA), acts as a π-electron donor in the unbound state. Upon binding of Ca(II), the BAPTA moiety is rendered less effective at electron donation.[16] The decrease in donating ability causes a slight blue shift in both absorbance and emission.[13] Binding also diminishes the symmetric ICT, but makes the binding moiety slightly electron accepting. The summation of these effects slightly increases the TPA cross section of **BAPTA-BSB-Ca(II)** compared to that of **BAPTA-BSB**.[15] The net result is slightly stronger emission for **BAPTA-BSB-Ca(II)** at nearly identical λ_{max}. In contrast, the tris(picolyl)amine Zn(II) binding domain functions as the π-electron acceptor in **SL-35**. When Zn(II) binds, the tris(picolyl)amine-Zn(II) becomes a better electron accepting group, leading to an increase in ICT. The increase in the charge transfer will cause a red shifted peak emission and an increased cross-section.[15] This spectral shift is ideal for ratiometric measurements, where the concentration of analyte is determined by the ratio of the bound and unbound states.[14] The use of ratiometry accounts for sample variation and other hard to eliminate sources of error such as photobleaching.[13]

3.3. Synthesis

Compound 1 was synthesized from BAPTA aldehyde[13, 16] and (E)-diethyl 4-(4-(dibutylamino)styryl)-2,5-dimethoxybenzylphosphonate by the Horner-Waddsworth-Emmons reaction as is shown below:
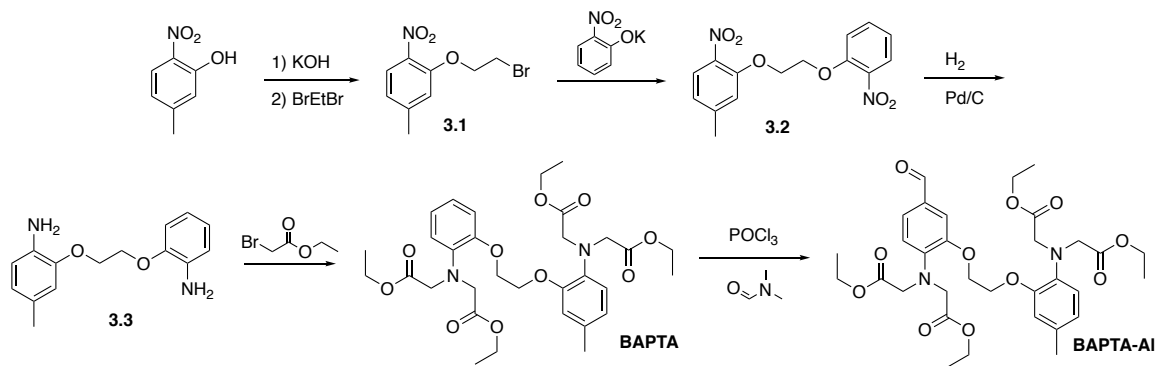
Scheme 3.1. Synthesis of **BAPTA-Al**
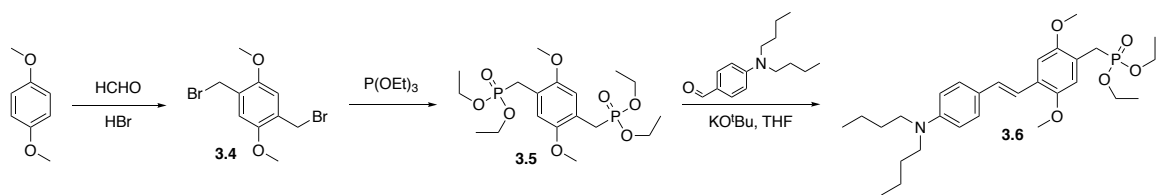
Scheme 3.2. Synthesis of Phosphonate **3.6**
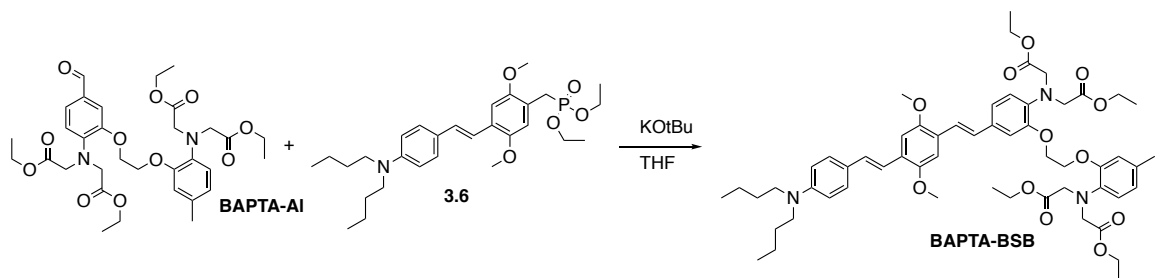
Scheme 3.3. Synthesis of **BAPTA-BSB**

3.4. Results and Discussion

3.4.1. Two-Photon Cross Section of BAPTA-BSB

The design of compound **BAPTA-BSB** emphasized a structure with a large TPA

cross section. The D-π-D structure favors symmetric charge transfer from the donor

groups to the center.[7, 11] The TPA cross section was measured by the two-photon induced fluorescence method[17]. As can be seen in figure 2, the δ_{max} of the tetraethyl ester analog of **BAPTA-BSB** is 412 GM in toluene.
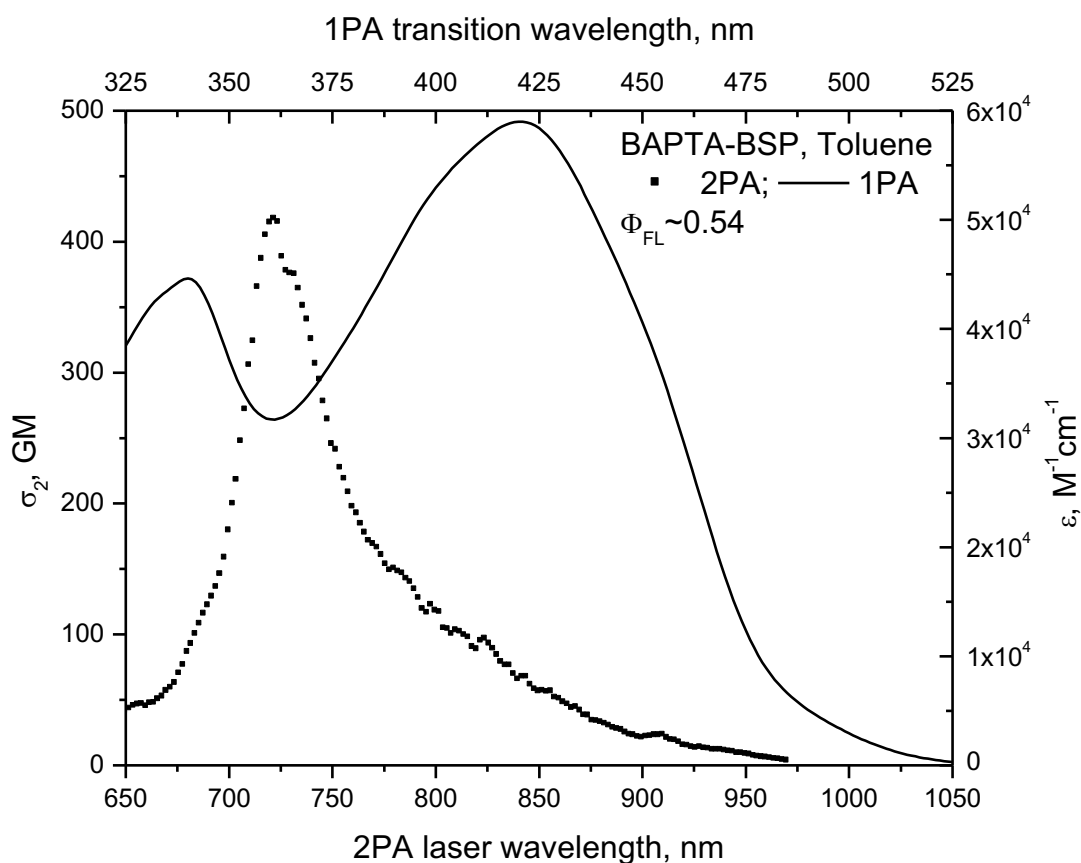
Figure 3.2. One-photon and two-photon absorption spectrum of BAPTA-BSB in toluene.

The TPA cross section is expected to be different when in the tetra acetic acid form, but limitations of fluorescence signal have impeded characterization of **BAPTA-BSB** in aqueous media.

3.4.2. Determination of Critical Micelle Concentrations of Surfactants in a Biologically Relevant Buffer

The critical micelle concentration (CMC) is the concentration of surfactant, above which micelles form spontaneously[18]. A surfactant's CMC is sensitive to a myriad factors including ionic strength of electrolytes[19-20], buffer pH[21], temperature[22-23], and both organic and inorganic additives[20]. It is necessary to determine the CMC for each surfactant in the desired buffer.

The fluorescence spectrum of pyrene shows fine structure due to vibrational bands (Figure 3.4). The intensities of the vibrational bands are dependent on solubilizing medium[24-25]. The ratio of intensities for peak I (373 nm) and peak III (384 nm) provides a quantitative description of the polarity of the surrounding media[25]. This characterization has limiting values of 0.6 for hexanes to 1.8 for pure water.
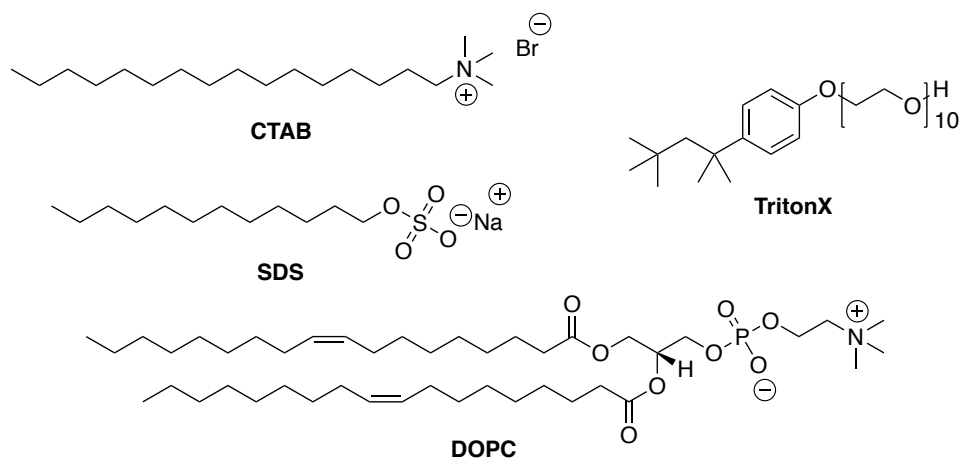
Figure 3.3. Chemical Structures of Studied Surfactants
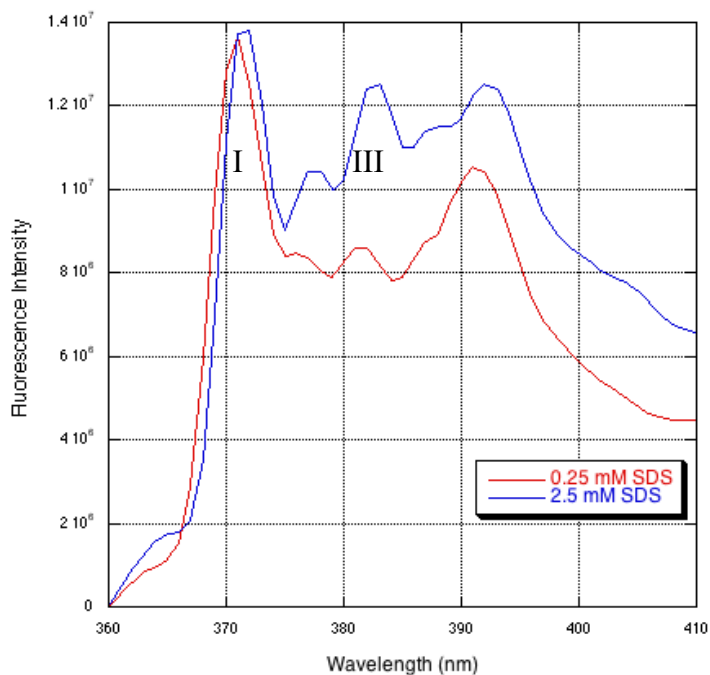
Figure 3.4. Dependence of Vibrational Band Intensities on Solvation. Pyrene (2 µM) in surfactant solutions of varying concentrations were prepared immediately prior to measurement. Samples were excited at 344 nm.

The CMC of SDS, CTAB, and TritonX-100 (Figure 3.3) were determined by the pyrene-fluorescence method (Figure 3.4). The CMC is determined from the sharp change in I_I/I_{III} when the surfactant concentration is great enough to spontaneously form micelles[24-25] (Figure 3.5). This method slightly underestimates the CMC, so the CMC is taken as the midpoint of the change in peak ratio (Table 3.1).

Table 3.1. Critical micelle concentrations of SDS, TritonX, and CTAB in 50 mM PIPES buffer at pH 7.2 with 0.1 M NaCl at pH 7.2 and 25 ˚C. Total ionic strength was 150 mM as determined by the pyrene fluorescence method.

Surfactant	CMC (µM)
SDS	1150
TritonX	250
CTAB	100
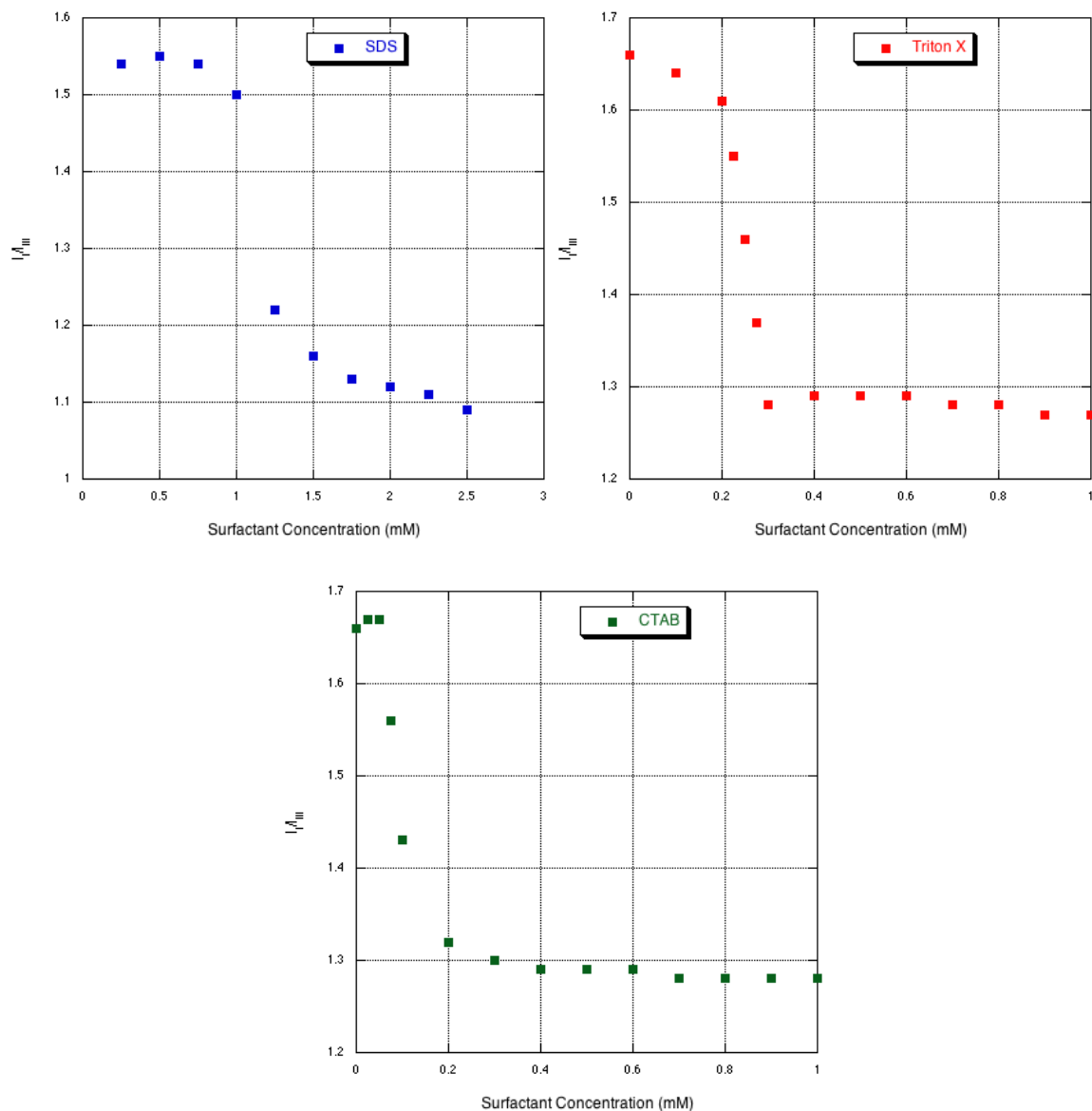
Figure 3.5. CMC Determination of Surfactants in 50 mM PIPES Buffer at pH 7.2. Solutions of pyrene (2 µM) in surfactant solutions of varying concentrations were prepared immediately prior to measurement. Samples were excited at 344 nm. All samples were prepared and measured at 25 ˚C.

3.4.3. Formation of Phosphatidylcholine Vesicles

While they form spontaneously, a key aspect of using vesicles as a membrane analog is to form them in such a way that it is possible to control the size, shape, and number of lamellae present. There are countless methods for the formation of lipid vesicles and these methods are typically specific to the size of the desired vesicle. Small unilamellar vesicles (SUV) are commonly produced by sonication, medium unilamellar vesicles (MUV) by extrusion, and giant unilamellar vesicles (GUV) by either extrusion or by electroformation.[26] The electroformation of lipid bilayers typically is accomplished by applying an electric field across two electrodes which are immersed in a mixture of the lipids of interest and aqueous buffer.[26-28]

An alternative method, first described in the early 1970s, involves the injection of an ethanolic solution of phospholipids into the buffer of interest.[29-31] This method offers some significant advantages in terms of a ease of preparation and tunability of the vesicle size based on the concentration.

The formation of phosphatidyl choline vesicles will be discussed in more detail in Chapter 6. Advancement in the formation of consistent vesicles for that project actually allowed for their translation to this project.

3.4.4. Incorporation of Zn(II) sensor into Micelles and Vesicles.

The incorporation of **SL-35** into the vesicles was done qualitatively by the absorption spectra. As is shown in Figure 3.6, there is a dramatic increase in absorbance once micelle bound. In typical samples, **SL-35** was incorporated into the micelles in less than 5 minutes as is evidenced by a lack of change in absorbance spectra.
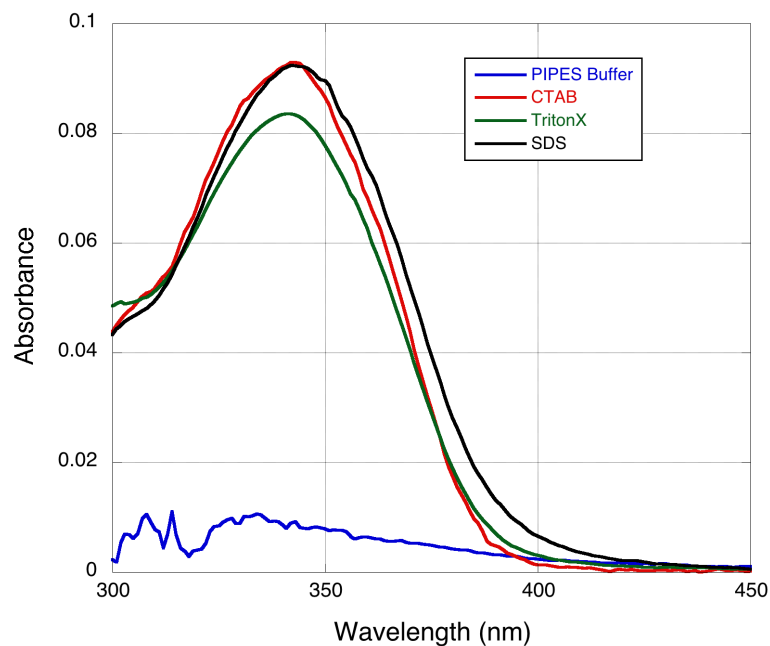
Figure 3.6. Absorbance of SL-35 free and incorporated in to micelles. All samples were prepared and measured at 25 ˚C.

Interestingly, DLS studies of free **SL-35** in PIPES buffer show that the dye forms nanoparticles in water. These dye particles appear to aggregate in buffer if left to stir overnight, as is seen in Figure 3.7.
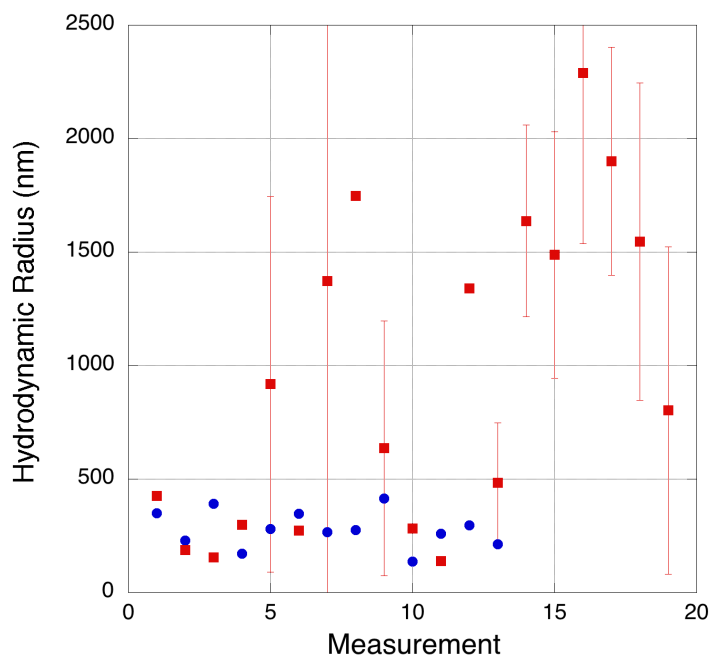
Figure 3.7. Particle size of **SL-35** in PIPES buffer at pH 7.2 after stirring for 10 minutes (blue circles) and after stirring overnight (red squares). All samples were prepared and measured at 25 ˚C. Error bars represent the polydispersity as measured by DLS.

3.4.5. Spectroscopic characterization of SL-35 in the free and Zn(II) bound state

Although the local environment around the **SL-35** molecules is reasonably similar in amongst the micellular samples, the minor differences in the structures of the surfactants give rise to sizeable changes in the absorbance and emission spectra of **SL-35**, as can be seen in Figure 3.8. In particular, the effects of binding Zn(II) are different in the different micelles. In CTAB and in Triton-X micelles, there is only a minimal change ($\leq$ 10 nm) in absorbance maxima but a very large change in fluorescence maxima of SL-35 in the free and Zn(II) bound state. In both CTAB and Triton-X micelles, the bingind of zinc ions results in a stokes shift change of roughly 2500 cm^{-1}. Zn(II) binding of **SL-35** in SDS micelles results in comparable changes in both absorbance and fluorescence maxima.

50
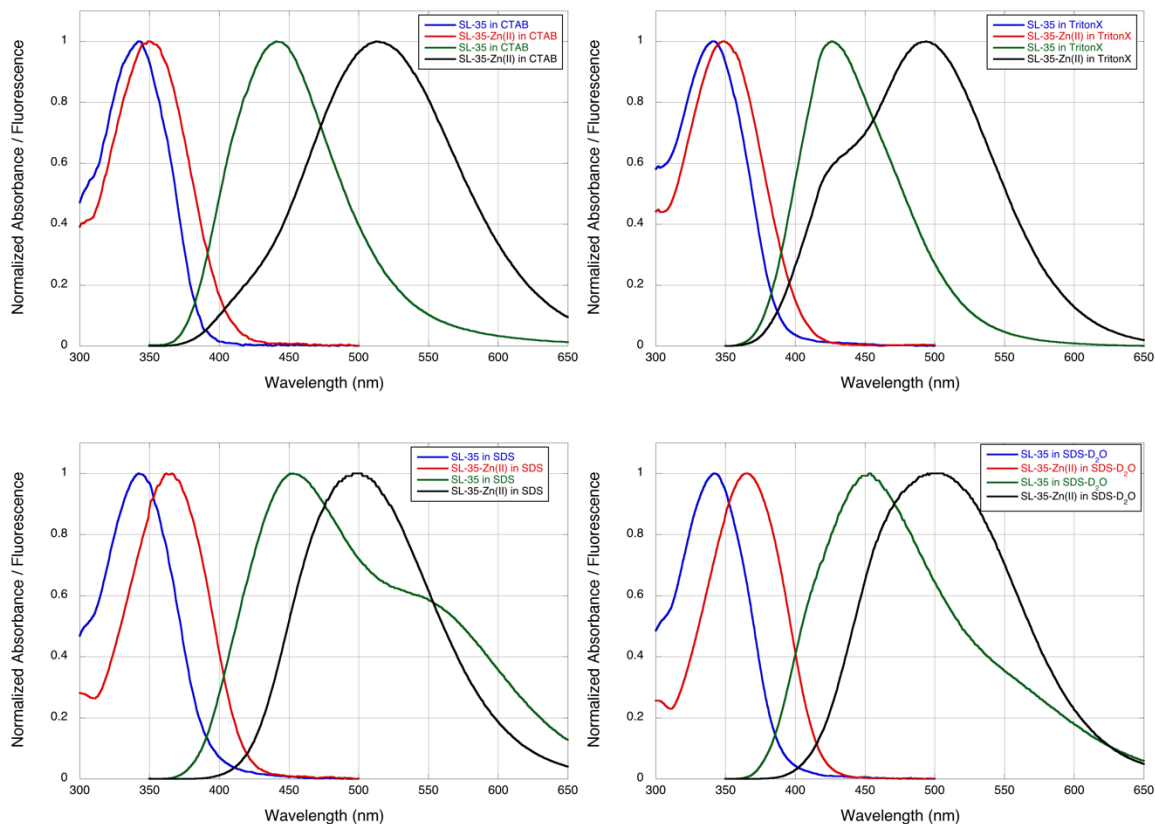
Figure 3.8. Normalized absorbance and fluorescence spectra of **SL-35** in micelles. Normalized absorbance in the unbound (blue traces) and Zn(II) bound (red traces) and normalized fluorescence spectra for the unbound (green traces) and Zn(II) bound (black traces) in CTAB (top left), TritonX-100 (top right), SDS (bottom left), and SDS-D$_2$O (bottom right)

Table 3.2. Tabulated results of spectroscopic characterization of **SL-35** in micelles with and without Zn(II).

| Surfactant | Dye | Absorbance | | Fluorescence | | Stokes Shift |
		λ_{max} (nm)	ε x10^{-3} (Lmol^{-1}cm^{-1})	λ_{max} (nm)	Φ_f	(cm^{-1})
CTAB	SL-35	341	20.3	442	0.32	6673
	SL35-Zn(II)	350	24.4	513		9064
TritonX	SL-35	341	20.4	426	0.33	5847
	SL35-Zn(II)	349	20.6	494		8381
SDS	SL-35	344	18.4	452	0.40	6978
	SL35-Zn(II)	365	20.0	498		7308

51

3.4.6. Titration of Micelle and Vesicle Encapsulated Zn(II) sensor with Zinc Trifluoromethanesulfonate

The binding dynamics of **SL-35** when encapsulated in micellular environments was investigated by both UV-Vis and fluorometric titrations with Zn(II). The response of **SL-35** was measured as a function of Zn(II) concentration in micelles composed of CTAB (Figure 3.9), Triton-X (Figure 3.10), and SDS (Figure 3.11).
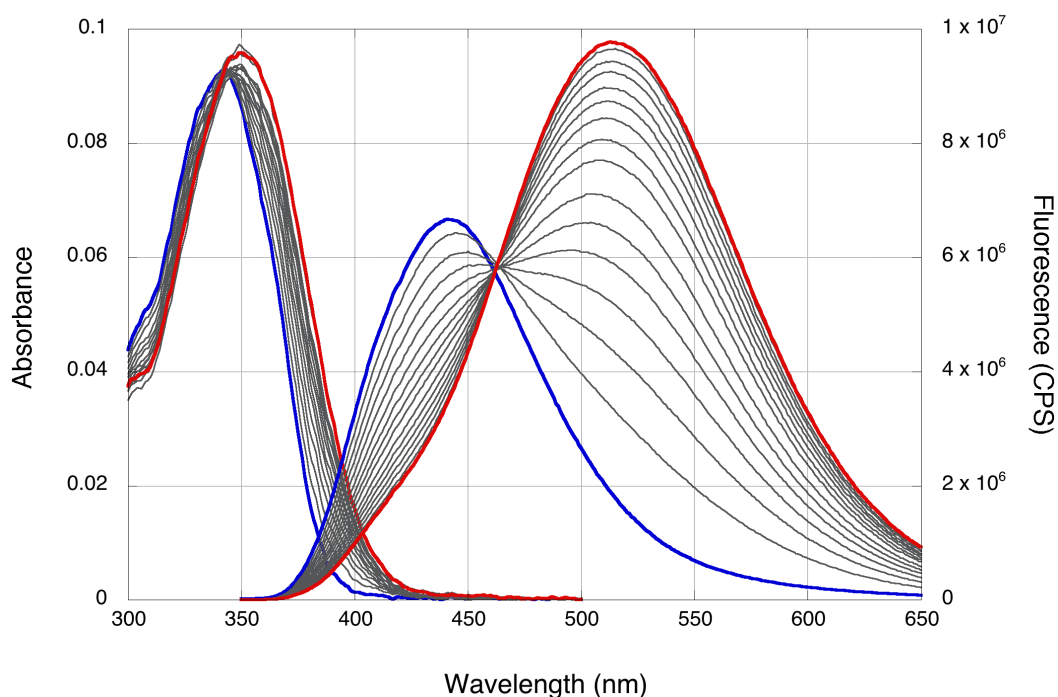
Figure 3.9. Absorbance and Fluorescence Titration of **SL-35** (5 µM) in CTAB vesicles with Zn(OTf)$_2$. Zn(II) concentrations range from 0 µM (blue trace) to 300 µM (red trace). All samples were prepared and measured at 25 ˚C.
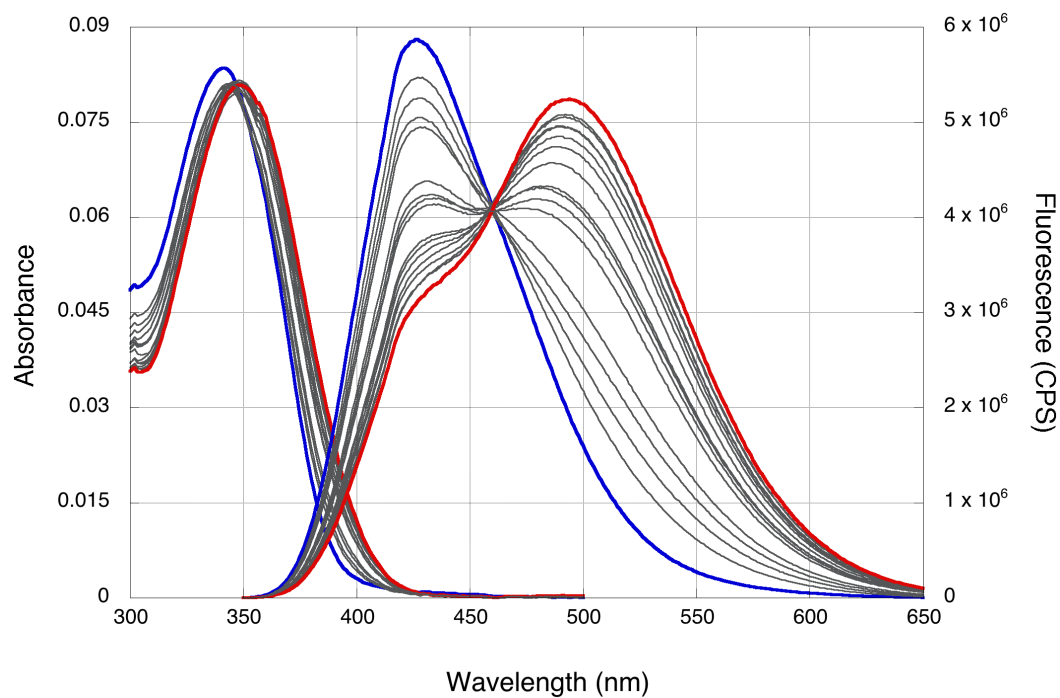
Figure 3.10. Absorbance and Flurescence Titration of **SL-35** (5 µM) in TritonX-100 vesicles with Zn(OTf)$_2$. Zn(II) concentrations range from 0 µM (blue trace) to 200 µM (red trace). All samples were prepared and measured at 25 ˚C.
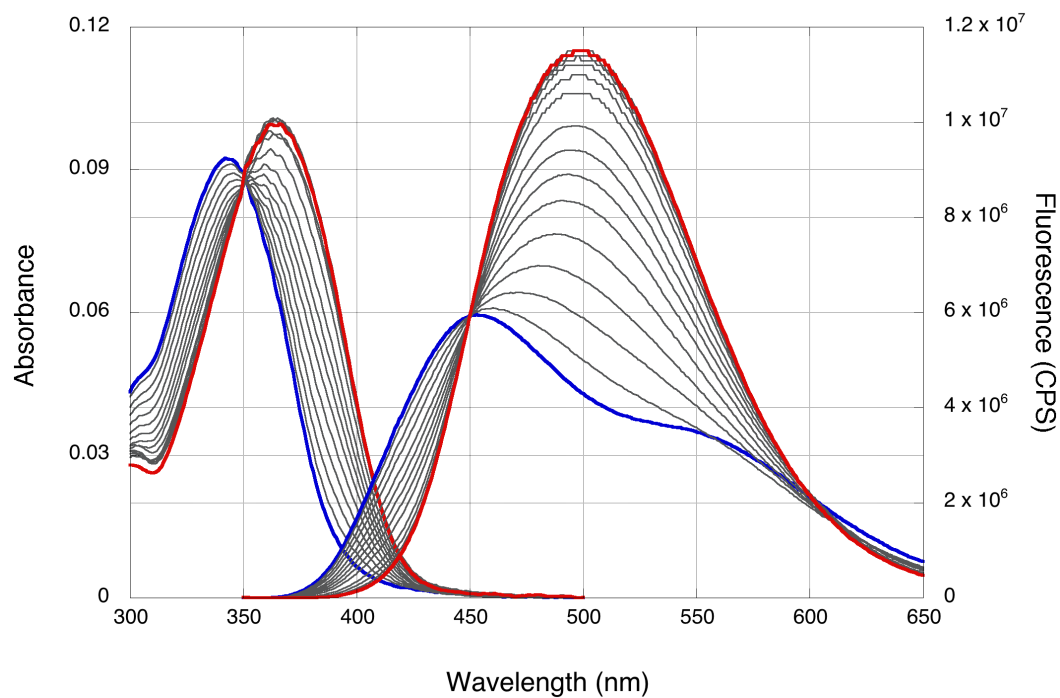
Figure 3.11. Absorbance and Fluorescence Titration of **SL-35** (5 µM) in SDS vesicles with Zn(OTf)$_2$. Zn(II) concentrations range from 0 µM (blue trace) to 7.5 µM (red trace).

The Zn(II) titration of **SL-35** in SDS micelles in PIPES buffer at pH 7.2 shows a

shoulder at longer wavelengths. To determine if the shoulder is due to a protonation event

in the unbound sensor, SDS micelles were prepared in equivalent PIPES buffer in

deuterium oxide. The change to heavy water resulted in the near disappearance of the

shoulder in the unbound dye. The slight residual shoulder could be due to the buffer, in

which hydrogen was not replaced with deuterium. To see if there were isotope effects on

the kinetics of Zn(II) binding, **SL-35** was titrated with $Zn(OTf)_2$ in SDS-D_2O micelles

(Figure 3.12).
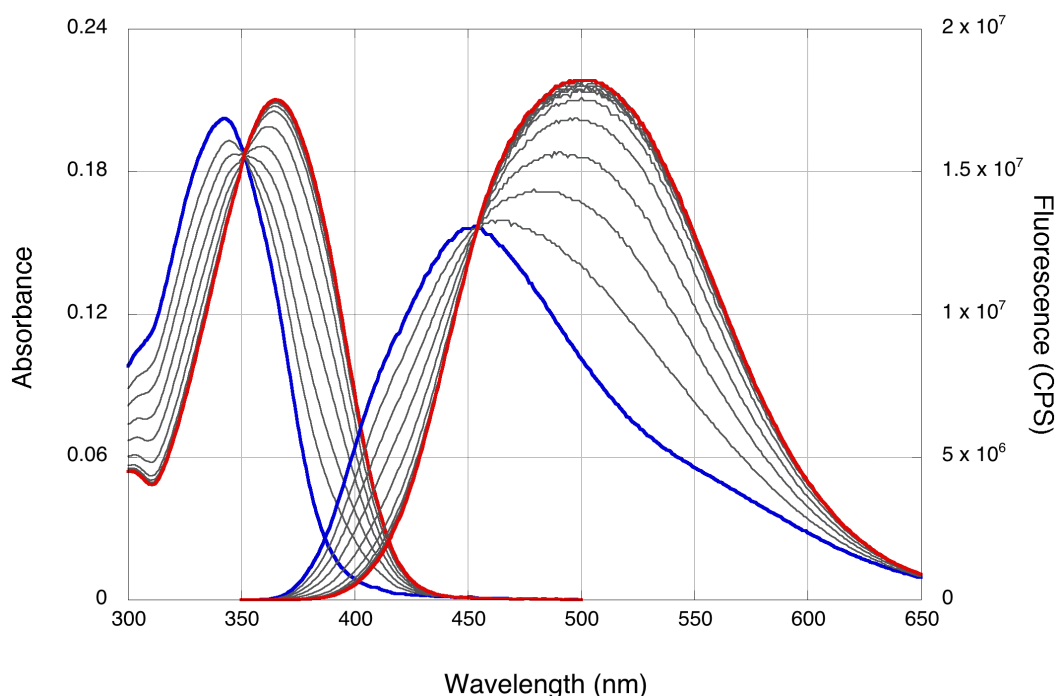
Figure 3.12. Absorbance and Fluorescence Titration of SL-35 (5 µM) in SDS vesicles
prepared in D_2O with $Zn(OTf)_2$. Zn(II) concentrations range from 0 µM (blue trace) to
22.5 µM (red trace). All samples were prepared and measured at 25 ˚C.

The Zn(II) titration, when performed in D_2O shows a dramatic reduction in the

shoulder of the emission spectrum of free **SL-35** in SDS micelles. This shoulder

represents an excited state protonation of the free **SL-35** dye in SDS micelles. This excited state protonation essentially vanishes with the addition of $Zn(OTf_2)$, and in deuterated buffer, the excited state protonation is diminished due to the activity of deuterium relative to that of protium. In D_2O, the logarithmic binding equilibrium is nearly 10 % larger than in aqueous buffer.

3.4.7. Comparison of Zn(II) complexing in differently charged micellular environments

The binding equilibrium can be described in terms of a formation constant (β) as follows for a generalized complex:

$$n \, L + m \, M \rightleftharpoons M_m L_n. \qquad \text{(Eq. 3.5)}$$

In the above equation, n and m are the stoichiometric coefficients for the Ligand (L) and Metal (M) in the reaction respectively. For the generalized equilibrium, a formation constant (β) can be written as:

$$\beta = \frac{\left[M_m L_n\right]}{\left[L\right]^n \left[M\right]^m}. \qquad \text{(Eq. 3.6)}$$

This formation constant relates the order of the reaction with the concentration of each species at equilibrium. The larger the number, the further to the right the equilibrium lies in Eq 3.5. For binding of **SL-35** to Zn(II) the equilibrium can be written as:

$$SL35 + Zn^{2+} \rightleftharpoons SL35\text{-}Zn^{2+}. \qquad \text{(Eq. 3.7)}$$
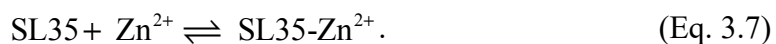
Table 3.3. Cumulative formation constants as calculated by SPECFIT32 using spectra from spectrophotometric and spectrofluorometric titrations of **SL-35** with Zn(OTf)$_2$ in surfactants of varying surface charge

Surfactant	log(β)	
	Absorbance	Fluorescence
CTAB	3.6	3.8
TritonX-100	4.3	4.3
SDS	7.3	7.2
SDS in D$_2$O	8.0	7.7

As expected, the surface charge of the micelle has a noticeable impact on the binding equilibrium. In negatively charged micelles, SDS, the electrostatic attraction between the surface of the micelle and the positively charged zinc ion causes the formation constant to rise significantly. Conversely, a positively charged micelle leads to a reduction in the formation constant of the **SL-35-Zn(II)** complex. TritonX-100 is a neutral surfactant and as expected, its equilibrium is intermediate between the SDS and CTAB. The effects of the surface charge can also be seen in the concentration of zinc ions needed to saturate the dye.

3.5. Conclusions

In summary, **BAPTA-BSB** was synthesized by a HWE reaction between BAPTA aldehyde and a dibutylamino styryl phosphonate. The center ring of **BAPTA-BSB** is substituted with two methoxy groups for tuning the intramolecular charge transfer which should result in a larger two photon absorption cross section. This work builds off of the

thesis work of Dr. Stephanie J. K. Pond, formerly of our group. Her work used a similar chromophore which was substituted with cyano groups on the center ring. In organic solution the dye ester showed enormous δ of 1700 GM. The problem with this dye was that it was prone to pretty extreme fluorescence quenching at higher concentrations. Un like its cyano- substituted counterpart, BAPTA BSB exhibits fluorescence in the solid state, however this comes at a cost. The maximum cross section measured for BAPTA-BSB was around 425 GM. The 2PA cross section was measured as the tetra ester form of the dye. Before being used for Ca(II) sensing, these esters need hydrolyzed to give the free deprotonated acid.

In the second half of this chapter, the sensing of Zn(II) by a ratiometric sensor, **SL-35** was assessed in the presence of micelles with varying surface charge. As expected, the binding of Zn(II) to **SL-35** can be modulated by the surface charge of the lipid structure. SDS, a negatively charged surfactant, enhanced the ability of **SL-35** to sense Zn(II) at lower concentrations. Conversely, when encapsulated in CTAB, a positively charged surfactant, the electrostatic repulsion between the micelle and the analyte caused the sensitivity of **SL-35** to suffer. In fact, changing from CTAB to SDS caused a nearly four orders of magnitude increase in the rate of the complexation. Also of note is that in SDS the fluorophore is susceptible to an excited state protonation that competes with the binding to Zn(II), initially.

3.6. Experimental Details

3.6.1. Synthesis

<u>2-(2-bromoethoxy)-2-nitrobenzene (**3.1**)</u>

2-nitrophenol (5.57 g, 40.0 mmol), K_2CO_3 (11.06 g, 80 mmol), and 1,2-dibromoethane

were dissolved in acetonitrile (120 mL). The reaction mixture heated to reflux with

stirring for 3 hr. Once cooled, the product was filtered and washed with DCM until the

filtrate was colorless. Filtrate was rotovaped to dryness, and the residue was twice

recrystallized from methanol to give **3.1** as yellow crystals (7.13 g, 67%). ^{1}H NMR

(CDCl$_3$, 400 MHz) δ 7.83 (dd, $J = 8.3$, 1.7 Hz, 1H), 7.56 (ddd, $J = 8.3$, 7.6, 1.7 Hz, 1H),

7.08 (m, 2H), 4.14 (t, $J = 6.5$ Hz, 2H), 3.67 (t, $J = 6.5$ Hz, 2H).

4-methyl-1-nitro-2-(2-(2-nitrophenoxy)ethoxy)benzene (**3.2**)

5-methyl-2-nitrophenol (7.65 g, 49.7 mmol) and potassium carbonate (14.0 g, 100 mmol)

were combined with DMF (50 mL) and heated to 45 ˚C with stirring. The mixture

quickly turned orange. After 30 min **3.1** (10.49 g, 39.7 mmol) was added and the reaction

mixture brought to reflux. After 3 hours the mixture was cooled, and 400 mL of water

was added, resulting in precipitation. The precipitate was collected by filtration and

washed with 10% NaHCO$_3$ and water. The air-dried crude was recrystallized from

ethanol (containing 0.4% AcOH) to give **3.2** (11.51 g, 91%) as a powder. ^{1}H NMR

(CDCl$_3$, 400 MHz) δ 7.83(dd, $J = 8.1$, 1.7 Hz, 1H), 7.78 (d, $J = 8.3$ Hz, 1H), 7.57 (ddd, J

$= 8.5$, 7.4, 1.7 Hz, 1H), 7.23 (m, 1H), 7.10 (ddd, $J = 8.1$, 7.5, 1.1 Hz, 1H), 7.02 (s, 1H),

6.87 (d, $J = 8.3$ Hz, 1H), 4.53 (m, 4H), 2.44 (s, 3H).

2-(2-(2-aminophenoxy)ethoxy)-4-methylaniline (**3.3**)

In a pressure vessel, was combined **3.2** (11.50 g, 36.1 mmol), 10 % Pd/C (1.5 g) and

ethanol (230 mL). The apparatus was charged with 50 PSI of H2 and agitated overnight.

The following day the pressure in the bottle had dropped to 31 PSI and the reaction vessel

was vented. The product mixture was transferred to a boiling flask and refluxed for 1 hour before filtering hot. Product recrystallized from ethanol to give **3.3** as shiny off-white flakes (7.53 g, 81%). ^{1}H NMR (CDCl$_3$, 400 MHz) δ 6.87 – 6.80 (m, 2H), 6.741 (m, 4H), 4.36 (s, 4H), 3.72 (br. S, 4H), 2.26 (s, 3H) ppm.

Tetraacetate-BAPTA (**BAPTA**)

3.3 (3.01 g, 11.6 mmol), Na$_2$HPO$_4$ (8.70, 58.1 mmol), NaI (0.66 g, 4.4 mmol), ethyl bromoacetate (7.15 mL, 64.5 mmol) were dissolved in acetonitrile (20 mL) and brought to reflux under nitrogen. After 18 h, product mixture was removed from heating and allowed to cool. The resulting product slurry was partitioned between toluene and water. The aqueous fractions were again extracted with toluene and the organic fractions were combined, dried over magnesium sulfate, evaporated and recrystallized from methanol to give **BAPTA** (5.44 g, 79%). ^{1}H NMR (CDCl$_3$, 400 MHz) δ 6.92 – 6.64 (m, 7H), 4.12 (d, $J = 13$ Hz, 8H), 4.04 (q, $J = 7.5$ Hz, 4H), 4.02 (q, $J = 7.5$ Hz, 4H), 2.25 (s, 3H), 1.13 (td, $J = 7.2, 2.5$ Hz, 12H).

BAPTA-Aldehyde

BAPTA (2.50 g, 4.25 mmol) was dissolved in a 10% mixture of pyridine in DMF, and the resulting reaction mixture cooled in an ice bath. Once cooled, POCl$_3$ (3.2 mL, 34.0 mmol) was added dropwise. The mixture was stirred for 10 min before removing from the ice bath and allowing to stir and warm for another 10 min before being heated to 70 ˚C for 1h with stirring. The reaction mixture was removed from the heat and allowed to stir overnight at rt. DCM was added to the product mixture and then poured over ice to

59

quench. The product was extracted from the aqueous mixture with DCM. All organic fractions were combined, dried over magnesium sulfate and rotovaped to dryness. Product was twice recrystallized from IPA to give **BAPTA-Al** (0.81 g 30 %).

1,4-bis(bromomethyl)-2,5-dimethoxybenxene (**3.4**)

1,4-dimethoxybenzene (7.51 g, 54.3 mmol), paraformaldehyde(3.28 g, 108 mmol), AcOH (61 mL), and HBr (33% in AcOH, 28 mL, 108 mmol) were mixed together under nitrogen. The mixture was heated to 50 ˚C and stirred for 1 h, after which there was visible precipitation. The product was hydrolysed in water (150 mL), then collected by filtration. The resulting product was resuspended in chloroform and brought to reflux for about 15 min. After cooling the product was again collected by filtration and washed with water and methanol to give **3.4** as a white powder (9.29 g, 53 %). ^{1}H NMR (CDCl$_3$, 400 MHz) δ 6.87 (s, 2H), 4.53 (s, 4H), 3.87 (s, 6H).

Tetraethyl (2,5 -dimethoxy-1,4-phenylene)bis(methylene)diphosphonate (**3.5**)

3.4 (9.25 g, 28.5 mmol) was combined with triethylphosphite (50 mL, 85.6 mmol) and brought to reflux with stirring. After 46 hrs, product mixture allowed to cool and was diluted in chloroform (100 mL) the product solution was thrice washed with saturated brine and the organic fractions combined, dried over magnesium sulfate and concentrated on the rotovap. Product was allowed to crystallize after removing from the rotovap. The crystalline product was collected by filtration and washed with hexane to give **3.5** as a white crystalline solid (10.11 g, 81 %) ^{1}H NMR (CDCl$_3$, 400 MHz) δ 6.87 (s, 2H), 4.00 (q, J = 7.17 Hz, 4H), 3.98 (q, J = 7.17 Hz, 4H), 3.76 (s, 6H), 3.18 (d, J = 20.1 Hz, 4H),

1.20 (t, J = 7.1 Hz, 12 H) ppm. ^{13}C NMR (CDCl$_3$, 100 MHz) δ 151.0, 151.0, 119.5, 119.4, 114.1, 61.9, 61.8, 61.8, 56.1, 27.2, 27.1, 25.7, 25.7, 16.3, 16.3,16.2 ppm. ^{31}P NMR (CDCl$_3$, 161.9 MHz) δ 27.55 ppm.

(*E*)-diethyl 4-(4-(dibutylamino)styryl)-2,5-dimethoxybenzylphosphonate (**3.6**)

3.5 (1.65 g, 3.76 mmol) and (N,N-dibutylamino)benzaldehyde (0.86 mL, 3.58 mmol) were dissolved in dry THF (150 mL) under inert atmosphere. To this solution was added a solution of KO^{t}Bu (0.51 g, 3.58 mmol) previously dissolved in dry THF (25 mL), causing an immediate appearance of a vibrant fluorescent yellow. The reaction was stirred for 2 hours before being quenched with water and extracted in toluene. The resulting extracts were combined, dried over magnesium sulfate and evaporated. The residue was redissolved in EtOAc and purified by column chromatography (silica gel, EtOAc) to separate any symmetrically substituted dye formed. Product fractions were combined and concentrated to give an orange oil (1.31 g, 67%).^{1}H NMR (CDCl$_3$, 400 MHz) δ 7.39 (d, J = 8.8 Hz, 2H), 7.20 (d, J = 16.5 Hz, 1H), 7.07 (s, 1H), 6.98 (d, J = 16.5 Hz, 1H), 6.90 (d, J = 2.7 Hz, 1H), 6.61 (d, J = 8.8 Hz, 2H), 4.04 (q, J = 7.2 Hz, 2H), 4.02 (q, J = 7.2 Hz, 2H), 3.86 (s, 3H), 3.83 (s, 3H), 3.30 – 3.21 (m, 6H), 1.57 (p, J = 7.6 Hz, 4H), 1.36 (sx, J = 7.44 Hz, 4H), 1.25 (t, J = 7.1 Hz, 6H), 0.96 (t, J = 7.5 Hz, 6H) ppm.

BAPTA-BSB

3.6 (0.45 g, 0.86 mmol) and **BAPTA-Al** (0.45 g, 0.86 mmol) were combined in 150 mL of THF with stirring. To this solution, was added KO^{t}Bu (100 mg, 0.87 mmol)in 15 mL of THF, which had been previously dissolved over thirty minutes at room temperature.

The reaction was then stirred for 3 hours at room temperature. The reaction was quenched and the product extracted in three times in toluene. The toluene fractions were combined, washed with brine and dried over magnesium sulfate. Toluene was removed on a rotovap and the product was purified by collumn chromatography using ethyl acetate to give a yellow/orange oil (0.71 g, 82%).

3.6.2. Micelle preparation

Surfactants were purchased from Sigma Aldrich (SDS and TritonX-100) or from Fluka (CTAB) and used as received. All buffers were prepared in deionized water (18.0 MΩ, Barnstead Deionizer) and were filtered to remove any particulate.

For experiments investigating only the unbound **SL-35**, micelles were prepared at twice their critical micelle concentrations (2.3 mM for SDS, 500 µM for TritonX, and 200 µM for CTAB) by dissolving desired surfactant in PIPES buffer (50 mM PIPES, 100 mM NaCl, 0.5 mM EDTA, pH 7.2) that had been filtered through a 0.2 µm Supor syringe filter (Pall Corp.) After preparation, micelles were stirred overnight before use. Micelles for Zn(II) binding studies or anything involving the SL-35-Zn(II) comples, micelles were prepared as before but in EDTA-free PIPES buffer buffer (50 mM PIPES, 100 mM NaCl, pH 7.2). Vesicle size was checked using a Wyatt DLS plate reader.

3.6.3. Spectroscopy

Linear absorption measurements were performed using either a UV-Vis-NIR scanning spectrophotometer (UV-3101PC, Shimadzu). Steady state fluorescence measurements were conducted using a scanning spectrofluorometer (Flurolog-2, SPEX).

All spectra were measured in 1 cm quartz cuvettes (Starna cells) with the exception of quantum yield measurements, in which the absorbance was measured in a 10 cm cuvette.

Quantum yield measurements were conducted

3.6.4. Zn(II) Titration

Zn(II) titrations were accomplished in one of two ways. First, the amount of excess Zn(OTf)$_2$ needed to completely complex the SL-35 sensor in each micellular preparation was needed. This was tested with the assumption that there would be no further reaction once the Zn-SL35 complex was formed, so reaction time was not critical. To roughly estimate the range of Zn(II) needed, a large batch (100 mL) of each micelle suspension was prepared in 50 mM PIPES buffer (100 mM NaCl, pH 7.2) at roughly twice the CMC for each surfactant. The micelle suspensions were loaded with dye at 5 µM. Initially 10 µM was used to give less noisy UV-Vis spectra, however, the amount of Zn(OTf)$_2$ needed to complex all 10 µM SL-35 in CTAB caused precipitation. Using a repeating pipettor (Eppendorf, with 10 mL syringe), 2 mL of dye-loaded micelles were placed in separate disposable cuvettes (Brand, UV semi micro). Varying amounts of Zn(OTf)$_2$ in methanol were added to each cuvette to get the desired concentrations. A control was made for each micelle suspension, whose UV-Vis was measured about 30 min after preparation. The control was used to ensure that there was no degradation. The samples were left for several hours (usually long enough to go teach my lab) and their absorbance and fluorescence spectra were measured.

Once a rough idea of the concentration of Zn(II) needed to fully complex the dye was obtained, a single 3 mL sample (usually the left over solution from the previous trials if possible was placed in a quartz cuvette with a micro stir bar. The UV-Vis was equipped

with a stirrer magnet for laser experiments. The initial absorbance and florescence of the

unbound dye in micelles was recorded and then $Zn(OTf)_2$ in methanol was added to the

sample. The sample was allowed to stir in the chamber of the UV-Vis until the

absorbance ceased to change. Once a stable UV-Vis was recorded (usually 5-7 min) the

fluorescence was recorded before a second addition of $Zn(OTf)_2$ was added. The cycle

was repeated until full complexation, or until precipitation occurred. Aliquots of Zn(II)

solution were chosen to give 20-25 evenly spaced data points between free and fully

complexed SL-25. The only exception to this was with CTAB, so much was required that

multiple titrants had to be made to minimize the total amount of methanol added. For this

reason the concentration steps got large as the titration proceeded. Spectra were fit using

a global fitting protocol from SPECFIT/32 for windows.

3.7. References

[1]   Sumalekshmy, S.; Fahrni, C. J., Metal-Ion-Responsive Fluorescent Probes for Two-Photon Excitation Microscopy. *Chemistry of Materials* **2011,** *23* (3), 483-500.

[2]   Pond, S. J. K.; Tsutsumi, O.; Rumi, M.; Kwon, O.; Zojer, E.; Brédas, J.-L.; Marder, S. R.; Perry, J. W., Metal-Ion Sensing Fluorophores with Large Two-Photon Absorption Cross Sections: Aza-Crown Ether Substituted Donor−Acceptor−Donor Distyrylbenzenes. *Journal of the American Chemical Society* **2004,** *126* (30), 9291-9306.

[3]   Dong, C.-Y.; Yu, B.; Hsu, L. L.; Kaplan, P. D.; Blankschstein, D.; Langer, R.; So, P. T. C. In *Applications of two-photon fluorescence microscopy in deep-tissue imaging*, Photonics Taiwan, SPIE: 2000; p 10.

[4]   Denk, W.; Strickler, J. H.; Webb, W. W., Two-Photon Laser Scanning Fluorescence Microscopy. *Science* **1990,** *248* (4951), 73-76.

[5]   Dierolf, V.; Sandmann, C., Confocal two photon emission microscopy: A new approach to waveguide imaging. *Journal of Luminescence* **2003,** *102-103*, 201-205.

[6]   Grotjohann, T.; Testa, I.; Leutenegger, M.; Bock, H.; Urban, N. T.; Lavoie-Cardinal, F.; Willig, K. I.; Eggeling, C.; Jakobs, S.; Hell, S. W., Diffraction-unlimited all-optical imaging and writing with a photochromic GFP. *Nature* **2011,** *478*, 204.

[7]   Rumi, M.; Ehrlich, J. E.; Heikal, A. A.; Perry, J. W.; Barlow, S.; Hu, Z.; McCord-Maughon, D.; Parker, T. C.; Röckel, H.; Thayumanavan, S.; Marder, S. R.; Beljonne, D.; Brédas, J.-L., Structure−Property Relationships for Two-Photon Absorbing Chromophores: Bis-Donor Diphenylpolyene and Bis(styryl)benzene Derivatives. *Journal of the American Chemical Society* **2000,** *122* (39), 9500-9510.

[8]   Rumi, M.; Perry, J. W., Two-photon absorption: an overview of measurements and principles. *Adv. Opt. Photon.* **2010,** *2* (4), 451-518.

[9]   Kuba, K.; Nakayama, S., Two-photon laser-scanning microscopy: tests of objective lenses and Ca2+ probes. *Neuroscience Research* **1998,** *32* (3), 281-294.

[10]   So, P. T. C.; Dong, C. Y.; Masters, B. R.; Berland, K. M., Two-Photon Excitation Fluorescence Microscopy. *Annual Review of Biomedical Engineering* **2000,** *2* (1), 399-429.

[11]   Albota, M.; Beljonne, D.; Brédas, J.-L.; Ehrlich, J. E.; Fu, J.-Y.; Heikal, A. A.; Hess, S. E.; Kogej, T.; Levin, M. D.; Marder, S. R.; McCord-Maughon, D.; Perry, J. W.; Röckel, H.; Rumi, M.; Subramaniam, G.; Webb, W. W.; Wu, X.-L.; Xu, C., Design of Organic Molecules with Large Two-Photon Absorption Cross Sections. *Science* **1998,** *281* (5383), 1653.

[12]   Barzoukas, M.; Blanchard-Desce, M., Molecular engineering of push–pull dipolar and quadrupolar molecules for two-photon absorption: A multivalence-bond states approach. *The Journal of Chemical Physics* **2000,** *113* (10), 3951-3959.

[13]   Grynkiewicz, G.; Poenie, M.; Tsien, R. Y., A new generation of Ca2+ indicators with greatly improved fluorescence properties. *Journal of Biological Chemistry* **1985,** *260* (6), 3440-3450.

[14]   Demchenko, A. P., The Concept of λ-Ratiometry in Fluorescence Sensing and Imaging. *Journal of Fluorescence* **2010,** *20* (5), 1099-1128.

[15]   Sumalekshmy, S.; Henary, M. M.; Siegel, N.; Lawson, P. V.; Wu; Schmidt, K.; Brédas, J.-L.; Perry, J. W.; Fahrni, C. J., Design of Emission Ratiometric Metal-Ion Sensors with Enhanced Two-Photon Cross Section and Brightness. *Journal of the American Chemical Society* **2007,** *129* (39), 11888-11889.

[16]   Minta, A.; Kao, J. P.; Tsien, R. Y., Fluorescent indicators for cytosolic calcium based on rhodamine and fluorescein chromophores. *Journal of Biological Chemistry* **1989,** *264* (14), 8171-8178.

[17]   Makarov, N. S.; Campo, J.; Hales, J. M.; Perry, J. W., Rapid, broadband two-photon-excited fluorescence spectroscopy and its application to red-emitting secondary reference compounds. *Opt. Mater. Express* **2011,** *1* (4), 551-563.

[18]   Fuguet, E.; Ràfols, C.; Rosés, M.; Bosch, E., Critical micelle concentration of surfactants in aqueous buffered and unbuffered systems. *Analytica Chimica Acta* **2005,** *548* (1), 95-100.

[19]   Corrin, M. L.; Harkins, W. D., The Effect of Salts on the Critical Concentration for the Formation of Micelles in Colloidal Electrolytes1. *Journal of the American Chemical Society* **1947,** *69* (3), 683-688.

[20]   Benito, I.; García, M. A.; Monge, C.; Saz, J. M.; Marina, M. L., Spectrophotometric and conductimetric determination of the critical micellar concentration of sodium dodecyl sulfate and cetyltrimethylammonium bromide micellar systems modified by alcohols and salts. *Colloids and Surfaces A: Physicochemical and Engineering Aspects* **1997,** *125* (2), 221-224.

[21]   Lin, C.-E.; Lin, W.-C.; Chiou, W.-C., Migration behaviour and selectivity of dichlorophenols in micellar electrokinetic capillary chromatography Influence of micelle concentration and buffer pH. *Journal of Chromatography A* **1996,** *722* (1), 333-343.

[22]   Bayrak, Y., Micelle formation in sodium dodecyl sulfate and dodecyltrimethylammonium bromide at different temperatures. *Turk J Chem* **2003,** *27* (4), 487-492.

[23]   Streletzky, K.; Phillies, G. D. J., Temperature Dependence of Triton X-100 Micelle Size and Hydration. *Langmuir* **1995,** *11* (1), 42-47.

[24]   Dominguez, A.; Fernandez, A.; Gonzalez, N.; Iglesias, E.; Montenegro, L., Determination of Critical Micelle Concentration of Some Surfactants by Three Techniques. *Journal of Chemical Education* **1997,** *74* (10), 1227.

[25]   Goddard, E. D.; Turro, N. J.; Kuo, P. L.; Ananthapadmanabhan, K. P., Fluorescence probes for critical micelle concentration determination. *Langmuir* **1985,** *1* (3), 352-355.

[26]   Pott, T.; Bouvrais, H.; Méléard, P., Giant unilamellar vesicle formation under physiologically relevant conditions. *Chemistry and Physics of Lipids* **2008,** *154* (2), 115-119.

[27]   Politano, T. J.; Froude, V. E.; Jing, B.; Zhu, Y., AC-electric field dependent electroformation of giant lipid vesicles. *Colloids and Surfaces B: Biointerfaces* **2010,** *79* (1), 75-82.

[28]   Estes, D. J.; Mayer, M., Electroformation of giant liposomes from spin-coated films of lipids. *Colloids and Surfaces B: Biointerfaces* **2005,** *42* (2), 115-123.

[29]   Batzri, S.; Korn, E. D., Single bilayer liposomes prepared without sonication. *Biochimica et Biophysica Acta (BBA) - Biomembranes* **1973,** *298* (4), 1015-1019.

[30]   Kremer, J. M. H.; Van der Esker, M. W.; Pathmamanoharan, C.; Wiersema, P. H., Vesicles of variable diameter prepared by a modified injection method. *Biochemistry* **1977,** *16* (17), 3932-3935.

[31]   Zouni, A.; Clarke, R. J.; Holzwarth, J. F., Kinetics of the Solubilization of Styryl Dye Aggregates by Lipid Vesicles. *The Journal of Physical Chemistry* **1994,** *98* (6), 1732-1738.

CHAPTER 4

STRUCTURE-PROPERTY RELATIONSHIPS AND SOLVATOCHROMIC

BEHAVIOR OF DONOR-ACCEPTOR POLYENES

4.1. Introduction

In a conjugated molecule terminated by an electron-donating group (D) and an electron-accepting group (A), the electrons of the π-system will be arranged such that the internal potential energy is minimized. The uneven distribution of charge results in a permanent dipole moment, μ_0. Upon application of an electric field (E) to the aforementioned conjugated donor-acceptor molecule, there will be a reorganization of the electrons of the π-system resulting in a polarization as defined as[1-3]:

$$\mu = \mu_0 + \alpha_0 E + \frac{1}{2!}\beta_0 E^2 + \frac{1}{3!}\gamma_0 E^3 + ... \qquad \text{(Eq. 4.1)}$$

In the above expansion, α_0 is the linear polarizability and is related to the first derivative of the dipole moment with respect to E. The higher order coefficients in the expansion, β_0 and γ_0, are descriptors of nonlinear optical response at high field intensity and are know as the first and second hyperpolarizabilities.[1] By definition, the dipole moment is the product of effective charge of the molecule and the effective distance over which that charge is separated.[4-5] As such, the dipole moment, and its derivatives, must all inherently depend on molecular structure.

4.2. Background

4.2.1. Bond Length Alternation

In molecules containing π-electron donating and accepting groups on opposite ends of the structure, also known as merocyanines, there exists two limiting resonance structures[4, 6] (Figure 4.1). The first structure obeys all of the rules of valence bonding (VB), and the second results from the movement of electrons from the donor-end of the merocyanine to the acceptor group (CT).[4, 7-8] The ground state of the merocyanine can be best expressed as a superposition of the valence-bond and charge-transfer resonance structures.[6, 9] In the valence bond description, the polyene chain is a series of alternating C-C single (r = 1.45 Å) and double (r = 1.33 Å) bonds.[10] In the charge transfer description, the single bonds have become double bonds and vice versa. The ground state structure is a superposition of these limiting wave functions, which yields a polyene chain of bond lengths representative of the contribution of the CT resonance structure.[6]
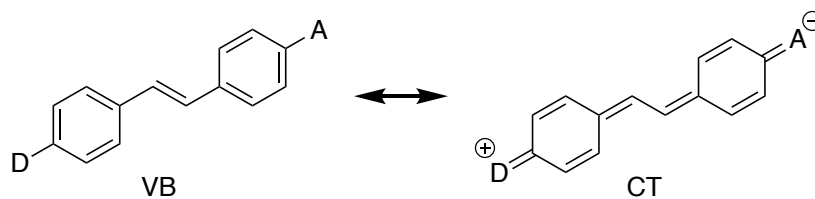
Figure 4.1. Limiting resonance structures of generic conjugated donor-acceptor compound

Bond Length Alternation (BLA, q_0) is defined as the difference in average bond lengths of single bonds and double bonds.[6, 11-13] By convention, the limiting value of BLA for a simple polyene is $q_{VB} = 0.11$ Å and for its corresponding zwitterion the limiting

value of BLA is q_{CT} = -0.11 Å.[6] If the contribution of the CT configuration on the ground state is defined as *f*, then the equilibrium BLA parameter, q_0, can be defined as[5, 8]:

$$q_0 = q_{VB} - f(q_{VB} - q_{CT}).$$
(Eq. 4.2)

BLA can thusly serve as a descriptor of symmetry as well as the contribution of the charge transfer resonance structure.

Directly in between the two extremes of the valence bonding and charge-transfer resonance structures, the BLA passes through 0 Å. This point is known as the cyanine limit. As is described by Bourhill *et al,* at the cyanine limit, the ground state dipole moment, μ, and the first hyperpolarizability are both equal to zero[14].

When looking at the chemical and electronic structures of conjugated chromophores, it is important to recognize that the bond length alternation (BLA) and bond order alternation (BOA) are very similar properties, but they are not the same. BLA is defined as the difference in the average *length* of the single bonds and the average *length* of the double bonds. BOA on the other had is the difference in the average bond order between doubly bound carbons and singly bound carbons. BLA is a measure of the geometric structure of a molecule, whereas BOA is a measurement of the electronic structure.[15] Although they may seem equivalent, there are situations in which the geometric and electronic structures of a molecule differ. Importantly, Gieseking et al point out that since BOA is a measure of the electronic structure of a molecule, it will always be a good predictor of nonlinearities. This holds true even for situations in which the geometric and electronic structures differ.
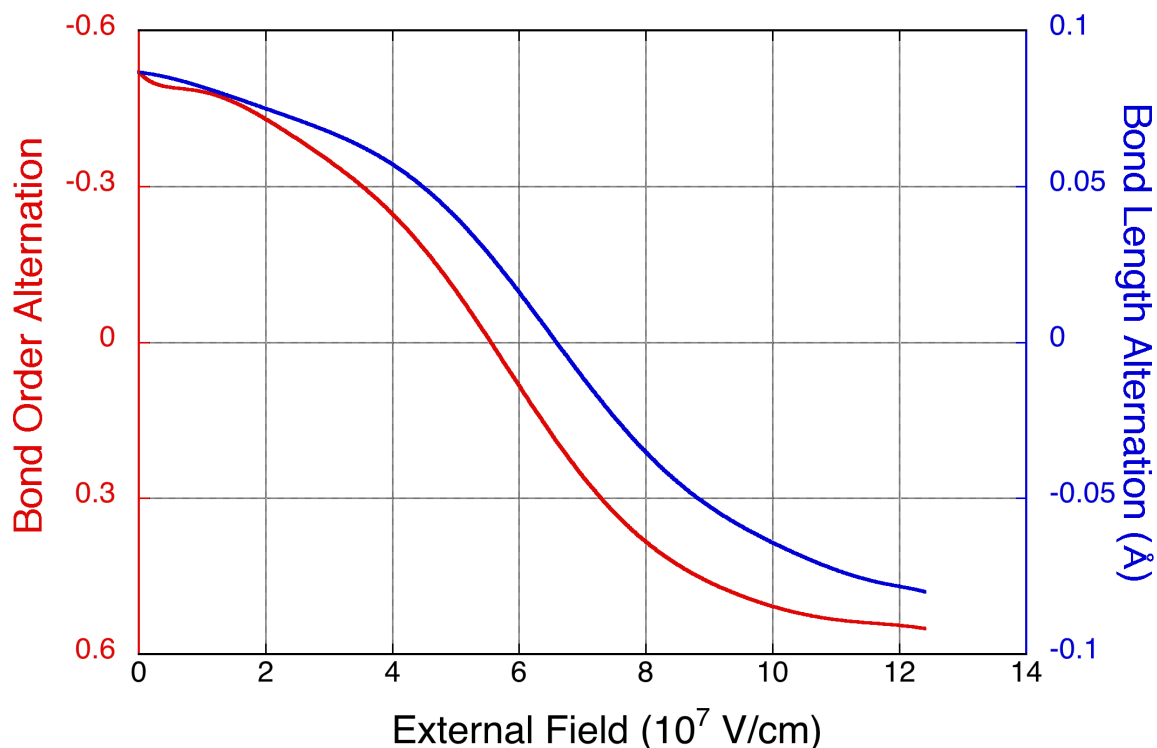
Figure 4.2. Comparison of bond order alternation (BOA, red trace) and Bond length alternation (BLA, blue trace). Data extracted from previously published work from the Bredas Group[16]

4.2.2. Solvatochromism

Solvatochromism is a phenomenon in which solutions of a given chromophore in solvents of varying polarity result in a change in spectroscopic properties.[17] Solvatochromism is typically described as being either positive or negative depending on if the absorbance shifts to lower energies (bathochromic shift or red shift) or to higher energies (hypsochromic shift, blue shift), respectively, with increasing solvent polarity.[18] Reverse solvatochromism occurs when the solvatochromic behavior of a chromophore changes from positive to negative or vice versa with increasing polarity. As is apparent from these descriptors of solvatochromism, a robust description of solvent

polarity is crucial for describing solvatochromism.[17] Numerous attempts have been

made at describing solvent polarity which have resulted in numerous solvent polarity

scales.

Solvent effects were first described by in 1896 by Claisen and Knorr with their

independent discovery of 1,3-diketones. These solvent effects were described based on

the solvent's ability to affect the keto-enol equilibrium.[18] In the time since, solvent

effects have been investigated for seemingly every process and from every angle. One of

the most important is the π^* scale of Kamlet et al. which is based upon the ability of a

solvent to affect the electronic transition from p - π^* or π - π^* orbitals. It is also very

important because it clearly delineates solvents as non-hydrogen bonding, hydrogen bond

acceptors, hydrogen bond donors, Amphiprotic hydrogen bonding, or aromatic. [19]

There are far too many polarity scales than it is possible to discuss in a reasonable

manner. It is, however, important to briefly discuss the polarity scales of import in this

dissertation.

The $E_T(30)$ solvent polarity scale and its normalized counterpart E_T^N were

developed by Prof. Christian Reichardt of Phillips University of Marburg is based on the

transition energy of a strongly negative solvatochromic pyridinium phenolate betaine dye

which was originally called dye 30.[18, 20] The $E_T(30)$ polarity scale is calculated from

the molar electronic transition energy of the dye 30 betaine dye dissolved in the solvent

under analysis according to the following equation:

$$E_T\left(30\right) = \frac{hcN_A}{\lambda_{max}} = \frac{28591 \text{ kcal} \cdot \text{nm} \cdot \text{mol}^{-1}}{\lambda_{max}}, \qquad \text{(Eq. 4.3)}$$

where h is Planck's constant in kcal, c is the speed of light in nm, N_A is Avogadro's

number, and λ_{max} is the wavelength of peak absorbance for the longest wavelength

charge-transfer absorption ($\pi - \pi^*$) of dye 30. The $E_T(30)$ values are put into a more convenient form by normalizing them using TMS and water as nonpolar and polar extremes according to the following equation:

$$E_T^N = \frac{E_T(\text{solvent}) - E_T(\text{TMS})}{E_T(\text{water}) - E_T(\text{TMS})}.$$

(Eq. 4.4)

Solvatochromism can also be thought of as an electric field resulting of solvation. The molecular model of solvation[21] describes a solution as consisting of three main components: the solute, the primary solvation shell, and the bulk solvent. The primary solvent shell can be defined as any arrangement of solvent molecules around a solute that differs from the bulk solvent.[21-22] This arrangement of solvent molecules is induced by the polarization of the solvent molecules by the polar solute molecule. Once polarized, electrostatic interactions between the solvent and solute molecules. The Onsager reaction field theory describes the electric field that results from this polarization and organization of solvent molecules around a polar solute. This resultant electric field, or reaction field, can be described in terms of the dielectric constant of the media (ε), the dipole moment of the solute (μ), and the radius of the spherical cavity created by the solvent around the solute (a)[23]:

$$R = \frac{1}{4\pi\varepsilon_0} \frac{2(\varepsilon - 1)}{2\varepsilon + 1} \frac{\mu}{a^3}.$$

(Eq. 4.5)

As is shown in the equation above, the reaction field is dependent on the solute's size and dipole moment, this means that two different solutes in the same solvent can have very different reaction fields. The reaction field is also a product of the $2(\varepsilon-1)/(2\varepsilon+1)$ term, which can be used as a polarity scale by itself, because without the aid of quantum calculations, the cavity radius and dipole moment are taken as static.

4.3. Synthesis

4.3.1. Synthesis of Donor-Acceptor Polyenes

Charge transfer between the π-electron donating 4-(dimethylamino)phenyl group to the π-electron accepting groups will cause a loss of aromaticity on the phenyl ring. This can be compensated for by very strong electron accepting groups such as dicyanovinyl (DCV), 1,3-indanedione (ID), diethyl-thiobarbituric acid (TB), tricyanodihydrofuran (TCF) acceptors.[13] [refs] The thiobarbituric acid, in particular, gains aromatic stabilization upon charge separation[13]. While all five acceptor groups and the aldehyde will stabilize the charge-separated form, the stronger acceptor groups will have more of a contribution from the charge-separated resonance form in the ground state. In addition, because the charge-separated form is stabilized the absorption maxima of the charge-transfer band will be red-shifted proportionally to the acceptor strength.[24]

4.1.1.1. Synthesis of ((1,3-dioxolanyl)methyl)triphenyphosphonium Bromide for stepwise extension of conjugated aldehydes

In this study, a series of donor-acceptor polyenes was prepared to determine the effects on chain length and acceptor strength on NLO properties. This study emphasized characterization of bond length alternation (BLA) and hyperpolarizability (β). In order to neglect the effects of the aromatic π-donor, 4-(dimethylamino)phenyl group was used as the donor for all polyenes in the series.
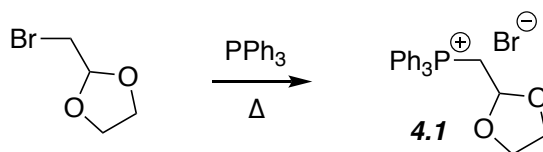
Scheme 4.1. Synthesis of ((1,3-dioxolanyl)methyl)triphenyphosphonium Bromide.

A homologous series of 4-(dimethylamino)phenyl polyeneals were prepared by Wittig oxyprenylation using an acetal protected phosphonium salt, followed by deprotection of the aldehyde (Scheme 4.2).[13, 25-26] Polyeneals were prepared in near quantitative yields using ((1,3-dioxolanyl)methyl)triphenylphosphonium bromide, synthesized according to Scheme 4.1. The commercially available salt gave low yield in all three attempts (30 – 50%). In an attempt to increase yield and reduce cost, the phosphonium salt was prepared by a simple Arbuzov reaction between 2-bromomethyl-1,3-dioxolane and triphenyl phosphine. The reaction proceeds quite well under solvent free conditions. Once heated, the triphenylphosphine completely dissolved in 2-bromomethyl-1,3-dioxolane. Vigorous stirring was crucial for the solvent free reaction as it kept the product mixture moving while the reaction proceeded. When stirring was not sufficient, the phosphonium salt crashed out after heating for about 3 hours and product discoloration began to occur at the bottom of the flask limiting both yield and ease of purification. The phosphonium bromide salt readily recrystallizes from a wide variety of solvents. While great for purification, crystals of the phosphonium salt proved to diminish the rate and yield of the subsequent Wittig reaction. This is most likely due to the limited solubility of the salt in polar aprotic solvents. To increase the rate and the yield, the surface area of the phosphonium salt was dramatically increased by redissolving in a small amount of DCM and reprecipitated in vigorously stirred ether. Both recrystallization and reprecipitation

were necessary for the subsequent Witting reactions to give near quantitative yields, and both were easily accomplished in a few hours time.

4.1.1.2. *Stepwise Vinylogous Extension of 4-(dimethylamino)benzaldehyde*

As mentioned previously, extended aldehydes (***Al[n-1]***) were synthesized by a stepwise vinylogous extension by Wittig reaction between each shorter 4-(dimethylamino)phenyl-terminated aldehyde (***Al[n]***) and ((1,3-dioxolanyl)methyl)triphenyphosphonium Bromide (***4.1***) followed by deprotection (Scheme 4.2).[13, 26] Early attempts purified the resulting protected aldehyde before deprotection, but suffered from quite low yields. Yields were then increased by extracting the protected aldehyde but not purifying it before deprotection. Finally, a one-pot extension and deprotection gave near quantitative yields. For the one-pot method, it is extremely important to cool with an ice bath both before quenching with water and before the addition of concentrated hydrochloric acid for deprotection. The resulting heat from neutralization/acidification can cause the reaction mixture to boil. The resulting deprotected product was typically purified by a quick recrystallization, this method did not require the purification by column chromatography which could be a major factor for the increased yield.
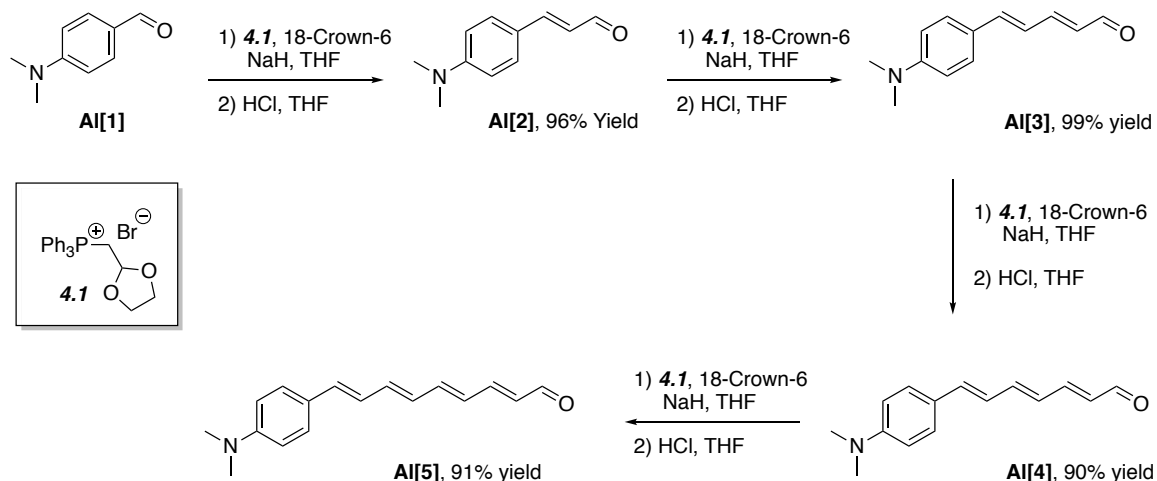
Scheme 4.2. Stepwise Vinylogous Extension of 4-(dimethylamino)bezaldehyde.

4.1.1.3. Attachment of Strong π-Acceptors by Knovenagel Condensation

Acceptor groups were attached to the polyene framework by Knovenagel condensation (Scheme 5) of **Al[n]** with malononitrile (for **DCV[n]** derivatives), 1,3-diethyl-2-thiobarbituric acid (for **TB[n]** derivatives), 2-(3-cyano-4,5,5-trimethyl-5*H*-furan-2ylidene)malononitrile (**TCF,** Scheme 4.3, for **TCF[n]** derivatives), and 1,3-indanedione (for **ID[n]** derivatives). Most D-A D-A polyenes were purified by recrystallization, as column chromatography proved quite difficult.
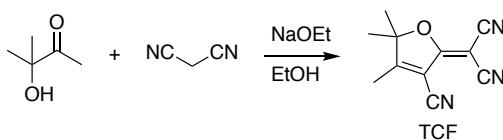
Scheme 4.3. Synthesis of tricyanofuran (TCF) acceptor group
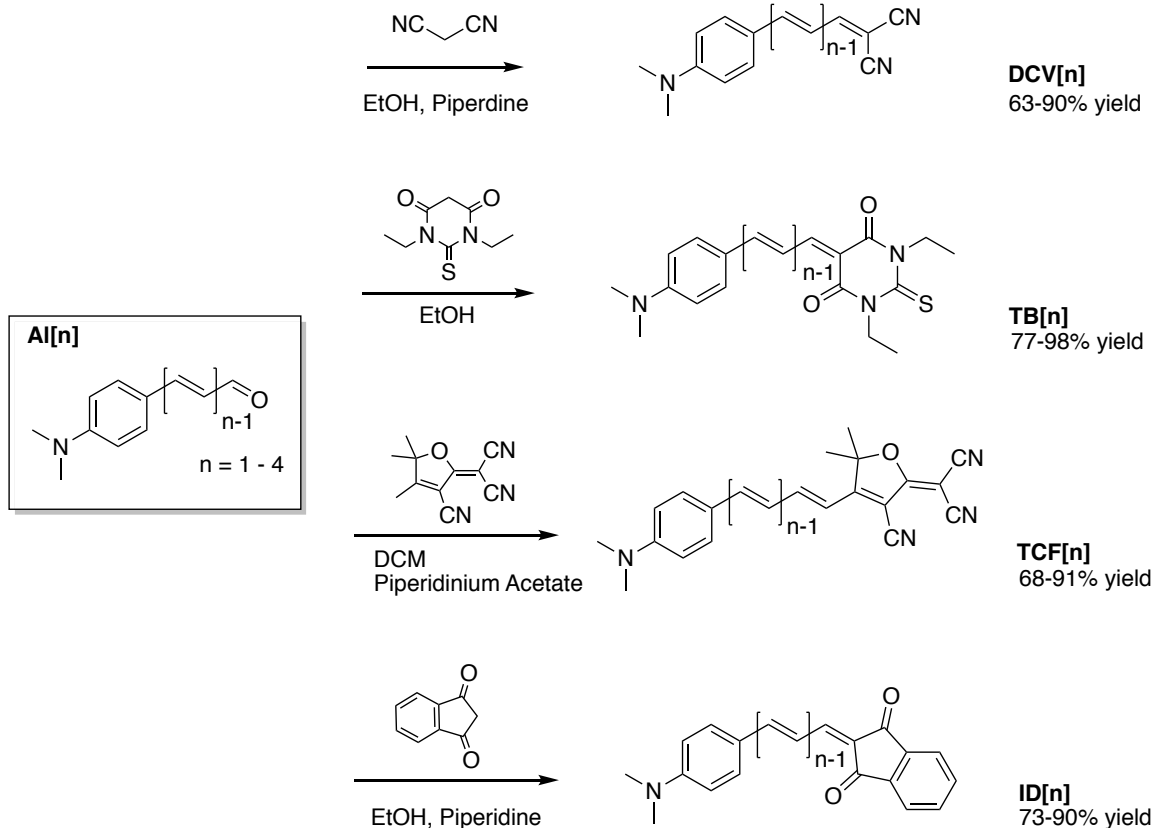
Scheme 4.4. Synthesis of donor-acceptor polyenes by Knovenagel Condensation

4.4. Results and Discussion

4.4.1. Description of Acceptor Strength

The absolute strength of strong π-electron donating and accepting groups is a very challenging thing to quantify. That said, if the solvent, donor strength, and length of conjugation are all kept constant, then the acceptor strength of each acceptor can be approximated relative to the others by the bathochromic shift in absorbance. [need ref] If the acceptor strength is greater, there will be more of a contribution from the charge transfer resonance contributor and thusly a lower energy C-T absorption band.
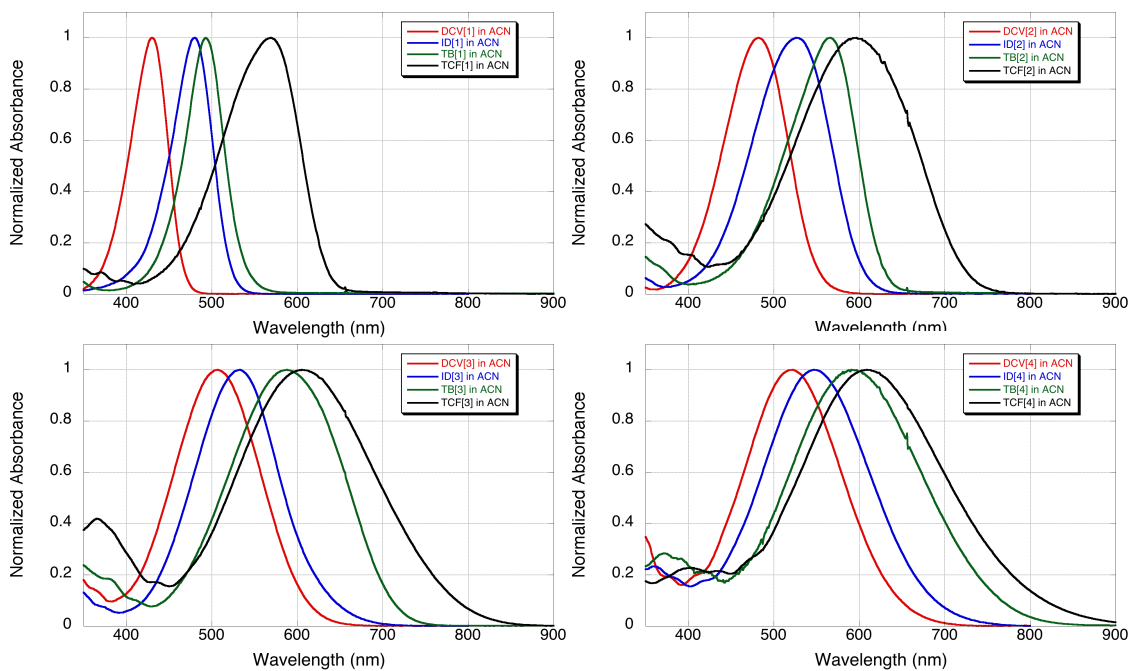
Figure 4.3. Normalized electronic absorption of donor-acceptor polyenes grouped by length of conjugation. All spectra were recorded in acetonitrile.

Based on the absorption maxima of the D-A polyene series (Figure 4.3) in acetonitrile, the acceptor strength in order of increasing strength is as follows:

$$DCV < ID < TB < TCF$$

It is of note that the relative strength of the TB and TCF acceptors becomes much more comparable as the polyene is extended.

Table 4.1. Absorption maxima of donor-acceptor series in acetonitrile. Number of double bonds represents the total number of double bonds between donor an acceptor and is equal to the n+1 repeating units in Scheme 4.4 and is analogous to length of conjugation.

Double Bonds	λ_{max} (nm) in Acetonitrile			
[n]	DCV[n]	ID[n]	TB[n]	TCF[n]
1	430	480	493	569
2	482	526	565	596
3	507	533	588	606
4	520	548	593	608

4.4.2. Bond Length Alternation from X-Ray Crystallography
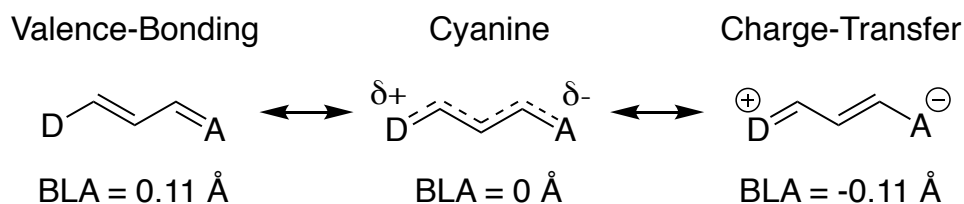
Figure 4.4. Extremes of bond length alternation as a description of Valence Bond – Charge Transfer theory

Bond Length Alternation is defined as the difference in average bond lengths of single bonds and double bond.[6, 11-13]By this convention, the limiting value of BLA for a simple valence bonded polyene is 0.11 Å and for its corresponding charge-transferred resonance structure, the limiting value of BLA is -0.11 Å.[6] The extremes of the BLA continuum are shown in Figure 4.4 and the limiting resonance structures for a representative chromophores are shown in Figure 4.5.
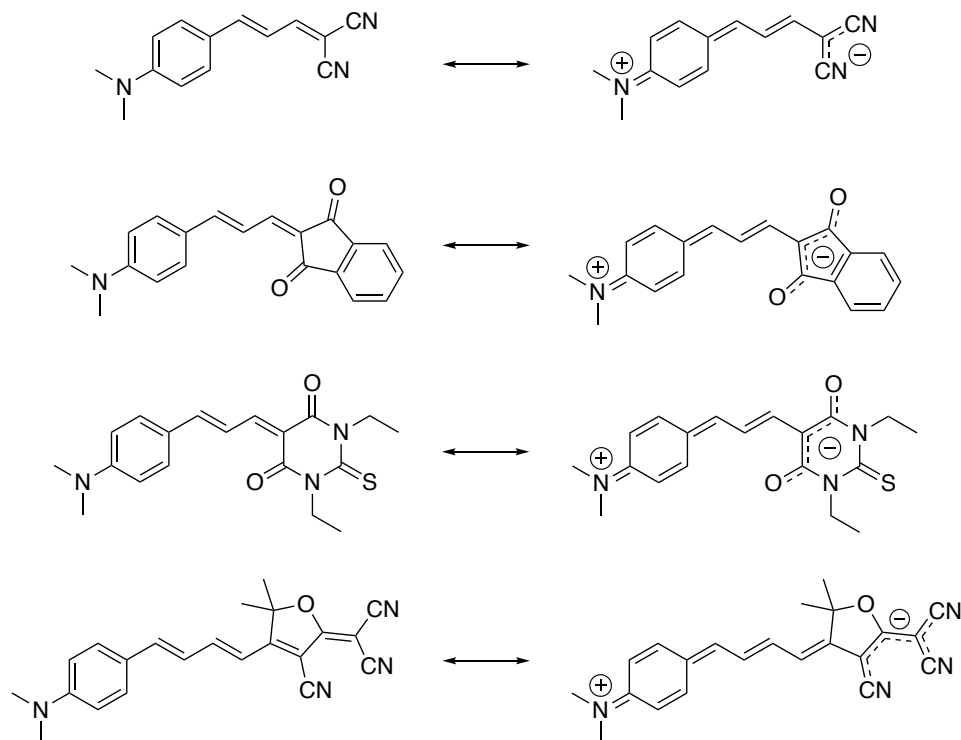
Figure 4.5. Limiting resonance structures for the D-A polyene series. From top to bottom the representative compounds are DCV[2], ID[2], TB[2], and TCF[2].

Diffraction quality single crystals were grown by three main methods, the most common of which was vapor diffusion. New attempts at crystal growth were dictated by solubility, and solvents systems were chosen based on the solvent having a lower boiling point than that of the nonsolvent where ever possible. This method allowed for crystallization to be induced by slow evaporation of the solvent and/or by the vapor diffusion of the nonsolvent. Crystallization by vapor diffusion offered an insight into which of the two factors were impacting crystallization the most. Typically, if nucleation began towards the top of the sample, the decrease in solubility due to the nonsolvent was the most prevalent factor in crystallization, while nucleation at the bottom of the vial likely indicated that the concentration of the sample was the driving force. This insight allowed for

insightful tailoring of the solvent system to produce larger better-quality crystals, typically by adjusting the solvent system to slow down crystallization.

The second most effective crystallization protocol was that of solvent layering. This was particularly useful in getting large single crystals of the shorter D-A polyenes. The most common solvent system for solvent layering was layering cold ethanol on top of a nearly saturated solution of chromophore in dichloromethane. TB[2] was particularly suited to solvent layering and numerous centimeter and half centimeter long rectangular crystals were grown.

When neither vapor diffusion nor solvent layering was effective for growing crystals, slow cooling and slow evaporation were used. The TCF[n] series in particular was best grown from slow cooling of nearly saturated solutions in acetonitrile. The cooling was slowed by submerging sealed vials of hot solution in boiling water in a large (2 liter) vacuum Dewar flask. After the temperature equilibrated, typically over 3-5 days, TCF[1], TCF[2], and TCF[4] all gave great quality rectangular prisms. The resulting TCF[n] crystals were incredibly difficult to redissolve, necessitating crushing before use.

For a few of the D-A polyenes, the difficulty of growing crystals was dramatically larger. ID[2] in particular very easily gave thin fragile actinic crystals by all crystallization methods attempted. Frustratingly, none have been of diffraction quality to date. A sample of these crystals was able to do both second harmonic generation and two photon fluorescence at 1200 nm.

X-Ray diffraction and crystal structure determination were done by Georgii Bogdanov, Sergei Rigin and Evgheni Jucov in Dr. Tatianna Timofeeva's research group at New Mexico Highlands University. Interestingly, the DCV[n] and TCF[n] series showed

the expected overall trend of increasing BLA with increasing length, and a decrease in the

ΔBLA with each additional double bond as is shown in Figure 4.6. As the length of the

conjugated chain increases, it is expected that the ability for charge transfer to occur down

the entire length of the chain will decrease. This critical length at which the molecule is too

long for charge transfer over the entire length of the chain should also be dependent on the

strength of the donor and acceptor groups.
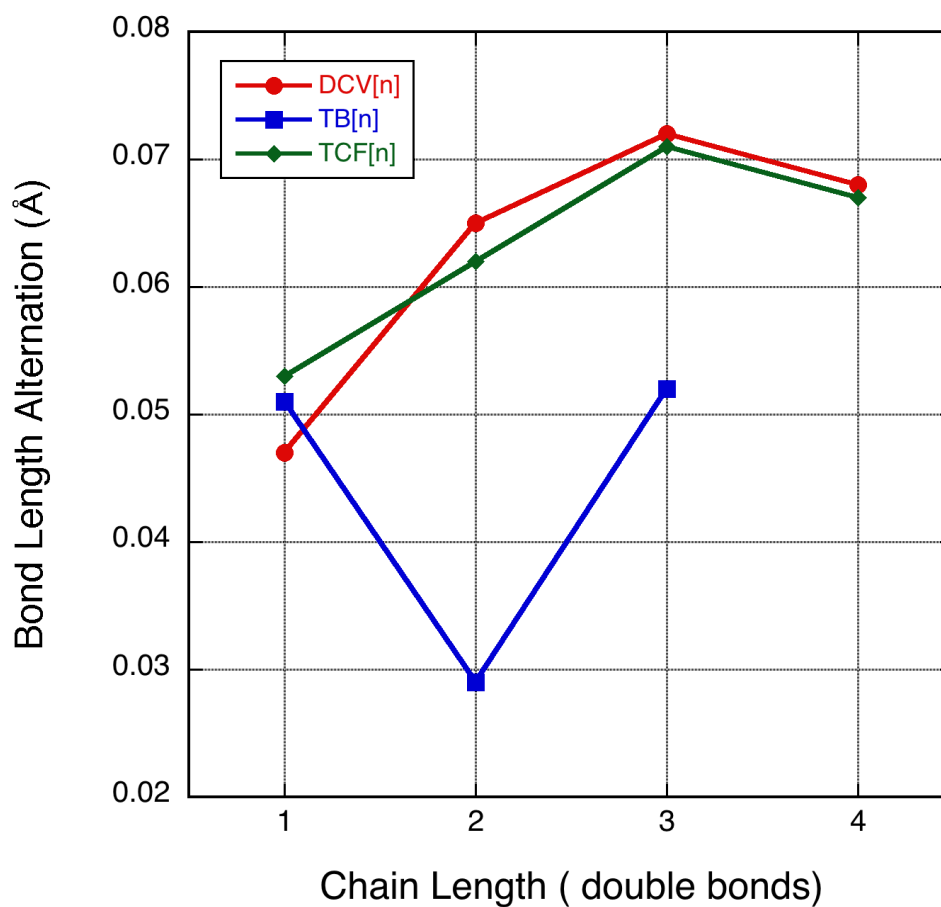
Figure 4.6. Bond length alternation as determined from crystal structures. Crystal structures determined by Georgii Bogdanov, Sergei Rigin and Evgheni Jucov in Dr. Tatianna Timofeeva's research group at New Mexico Highlands University.

Since all of the donor groups are the same, a 4-(dimethylamino)phenyl group, the critical length should be determined by the relative strength of the acceptor groups[27]. It appears that the critical length for the DCV[n] series occurs at n = 3, as the BLA at n = 4 decreases. While it is hard to make any concrete observations without having a full set from anything but DCV[n], it is expected that the critical length for the DCV[n] series would be the shortest as the dicyanovinyl acceptor group is the weakest of the series. The TB[n] series deviated dramatically from expectation as the BLA value for TB[2] represents a local minimum.
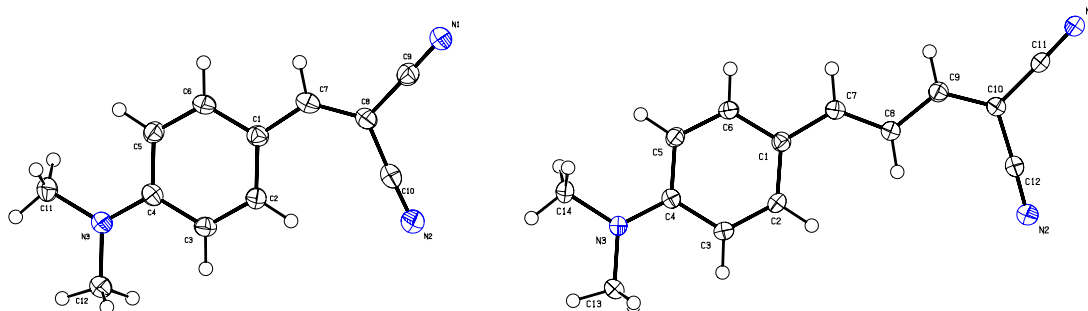
Figure 4.7. Crystal structures of DCV[n] for n = 1 and 2. Images generated using PLATON software package.

The crystal structures of DCV[1] and DCV[2] have been previously reported in the literature [28-29]. That said, all data presented in this chapter are of newly grown crystals that have been measured by the Timofeeva group as previously mentioned.
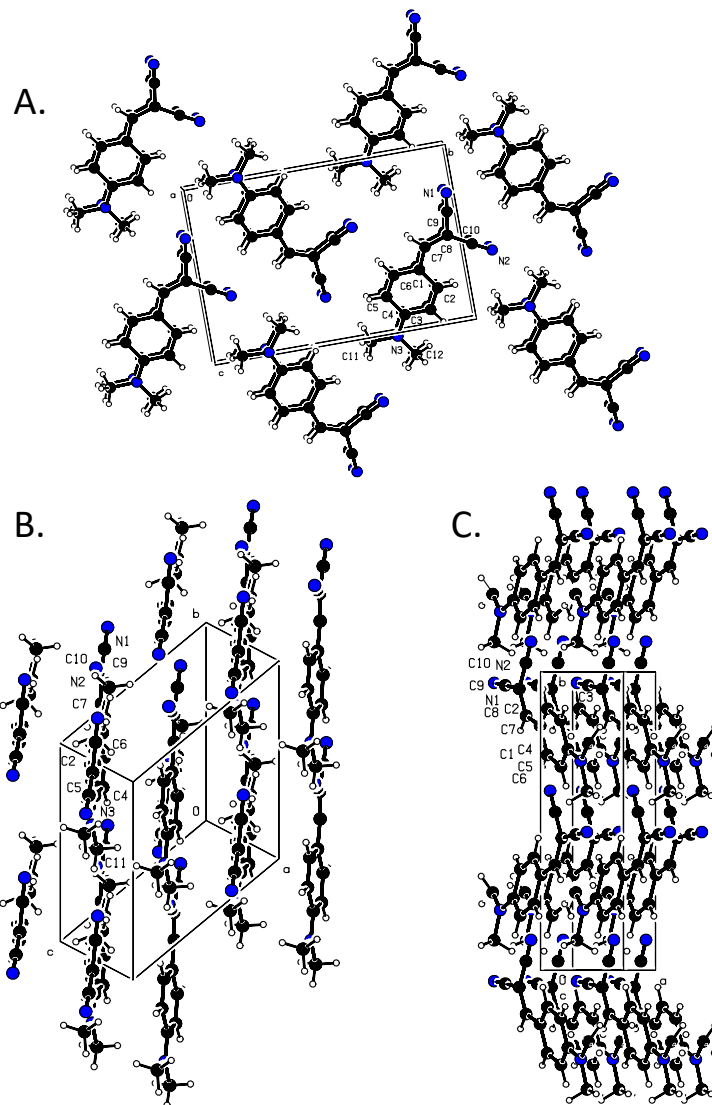
Figure 4.8. Molecular packing of DCV[1] Crystals. A) Packing oriented for minimal overalp, B) packing as viewed along the a face of the crystal, and C) packing as viewed along the x = y = z = 0 direction. Images generated using PLATON software package.
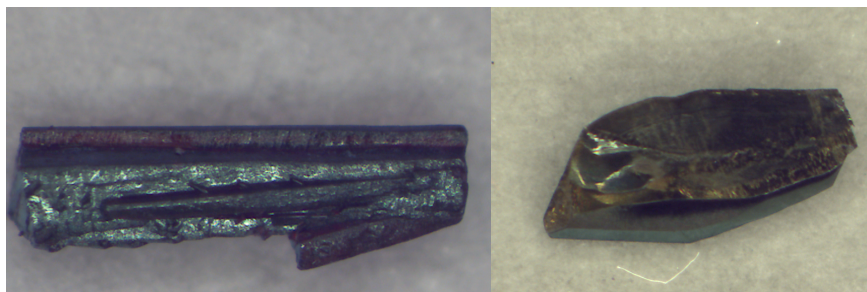
Figure 4.9. Polymorphs of DCV[2]. The crystal on the left is bright red with a green metallic sheen and the crystal on the right appears black with a yellow metallic luster.
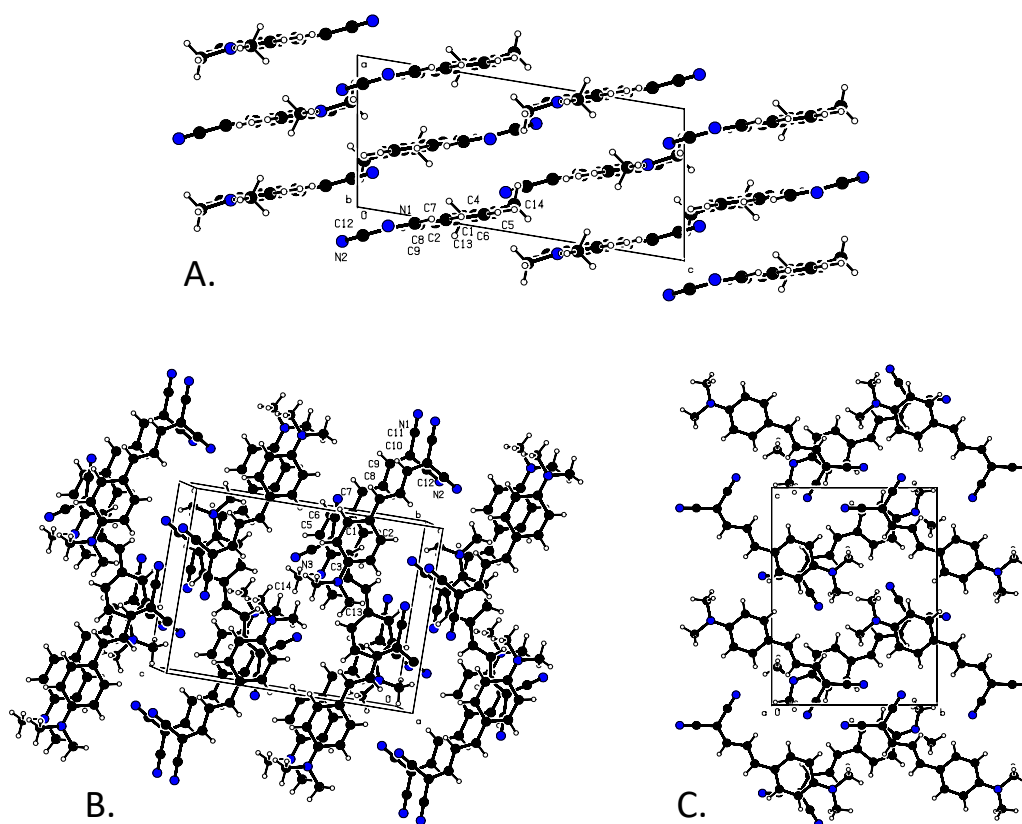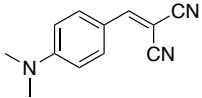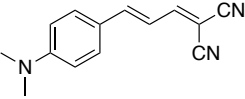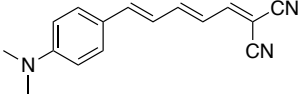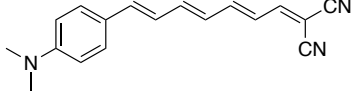
Figure 4.10. Molecular packing of DCV[2] crystals. A) Packing as viewed along the x = z = 90˚, y = 0˚ direction of the crystal B) packing oriented for minimal overlap, and C) packing as viewed along the x = y = 90˚, z = 0˚ direction of the crystal. Images generated using PLATON software package.

Table 4.2. Crystal structure data summary of DCV[n] series for n = 1 – 4.

Label	Structure	a, b, c (Å)	Angles (degrees)	R-factor	Space group	Z
DCV[1]		3.89	90	5.07	$P2_1$	2
		14.00	99.22			
		9.41	90			
DCV[2]		6.94	90	5.44	$P2_1/n$	4
		11.38	99.32			
		15.15	90			
DCV[3]		16.94	90	3.80	$P2_1/c$	8
		7.45	104.98			
		23.03	90			
DCV[4]		13.62	90	4.52	$P2_1/c$	8
		11.65	104.12			
		19.72	90			
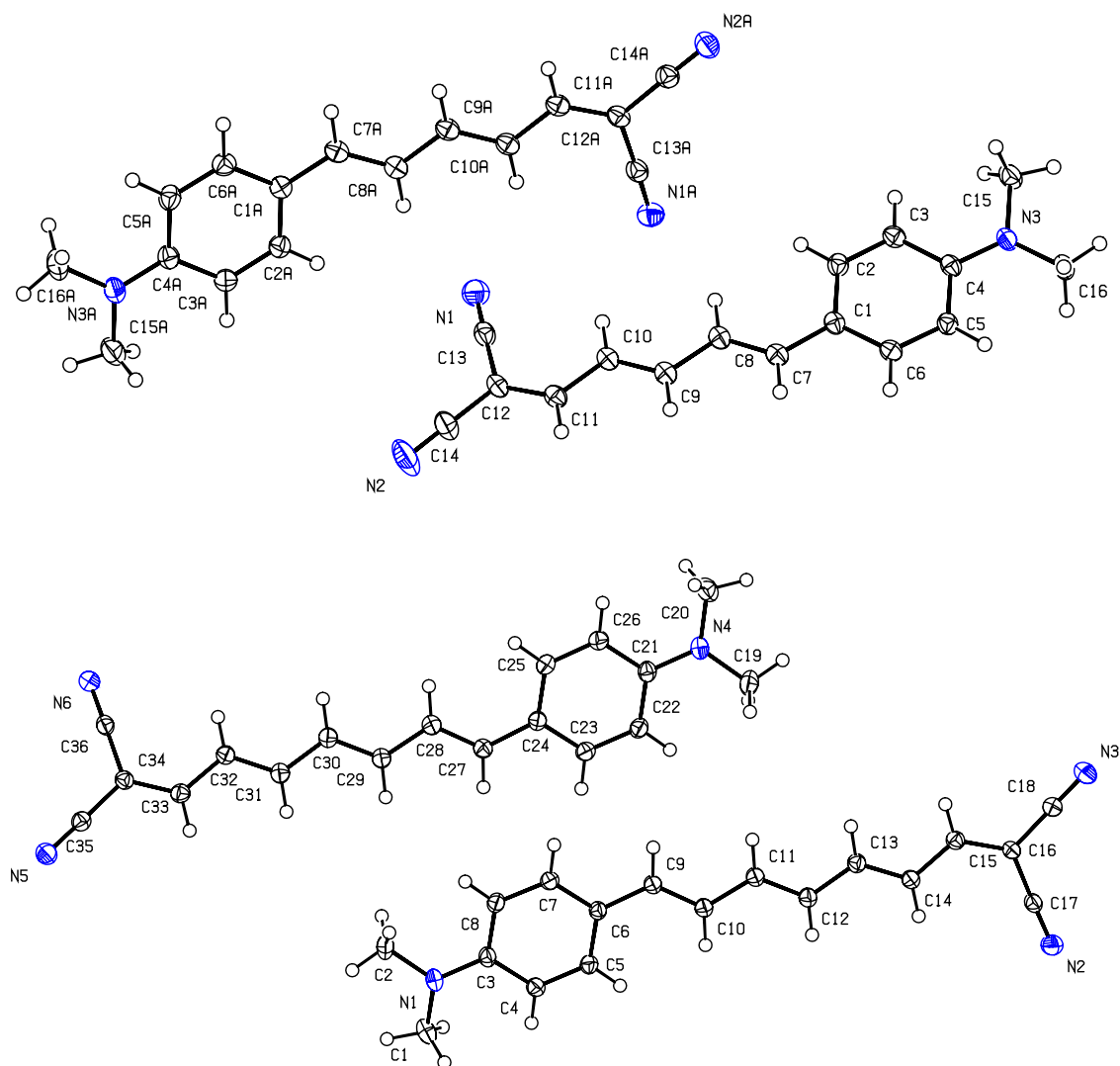
Figure 4.11. Crystal structures of DCV[n] series for n = 3 and 4. Images generated using PLATON software package.

Figure 4.12. Molecular packing of DCV[3] crystals. A) Packing as viewed along the x = z = 90˚, y = 0˚ direction of the crystal B) packing as viewed along the a-face of the crystal, and C) packing as viewed along the x = y = z = 0˚ direction of the crystal. Images generated using PLATON software package.

Figure 4.13. Molecular packing of DCV[4] crystals. A) Packing as viewed along the x = z = 90˚, y = 0˚ direction of the crystal B) packing as viewed along the x = y = 90˚, z = 0˚ direction of the crystal, and C) packing as viewed along the b-face of the crystal. Images generated using PLATON software package.

Figure 4.14. Crystal Structures of TB[n] series for n = 1 - 3. Image generated using the PLATON software package.

Table 4.3. Crystal structure data summary of TB[n] series for n = 1 – 3.

Label	Scheme	a, b, c (Å)	Angles (degrees)	R-factor	Space group	Z
TB[1]		5.15	83.22			2
		11.51	85.11	6.82	P-1	
		13.85	84.99			
TB[2]		8.18	82.41			2
		9.04	82.91	6.61	P-1	
		12.19	86.88			
TB[3]		9.22	90			
		24.90	110.65	3.58	P2₁/c	4
		9.10	90			
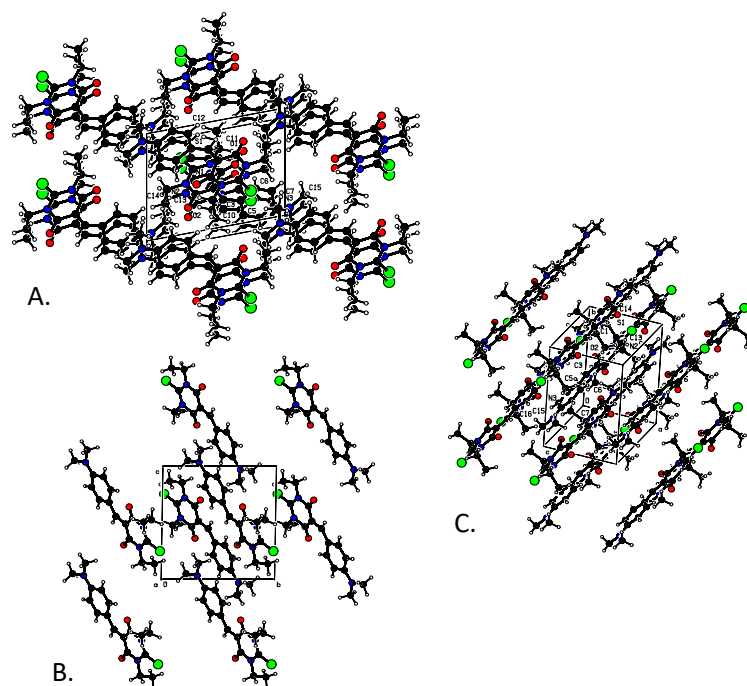
Figure 4.15. Molecular packing of TB[1]a cyrstals. A) Packing as viewed along the x = z = 90°, y = 0° direction of the crystal B) packing as viewed along the x = y = 90°, z = 0° direction of the crystal, and C) packing as viewed along the a-face of the crystal. Images generated using PLATON software package.
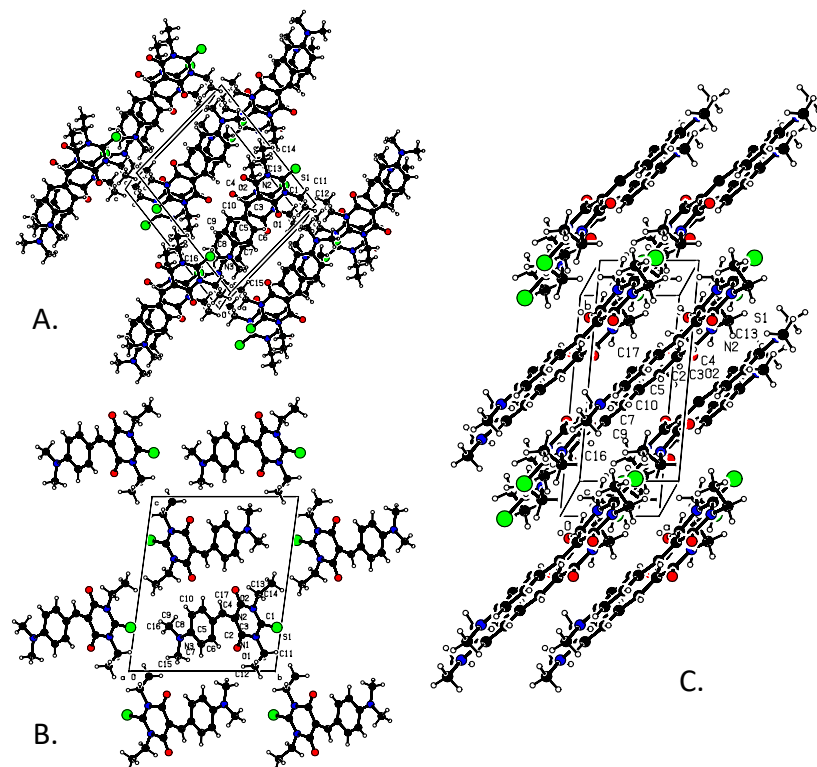
Figure 4.16. Molecular packing of TB[1]b crystals. A) Packing as viewed along the x = z = 90˚, y = 0˚ direction of the crystal B) packing as viewed along the x = y = 90˚, z = 0˚ direction of the crystal, and C) packing as viewed along the a-face of the crystal. Images generated using PLATON software package.
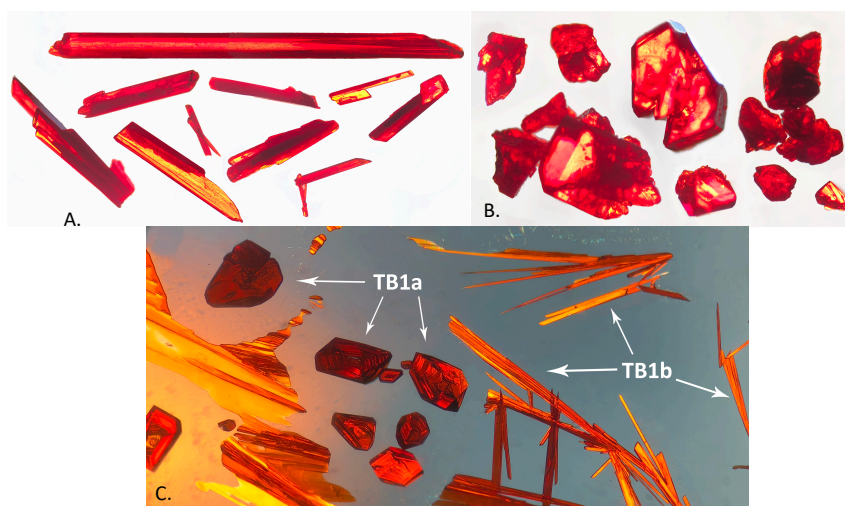
Figure 4.17. Images of TB[1]a and TB[1]b polymorphs. A) TB[1]b crystals, B) TB[1]a crystals, and C) a mixture of polymorphs
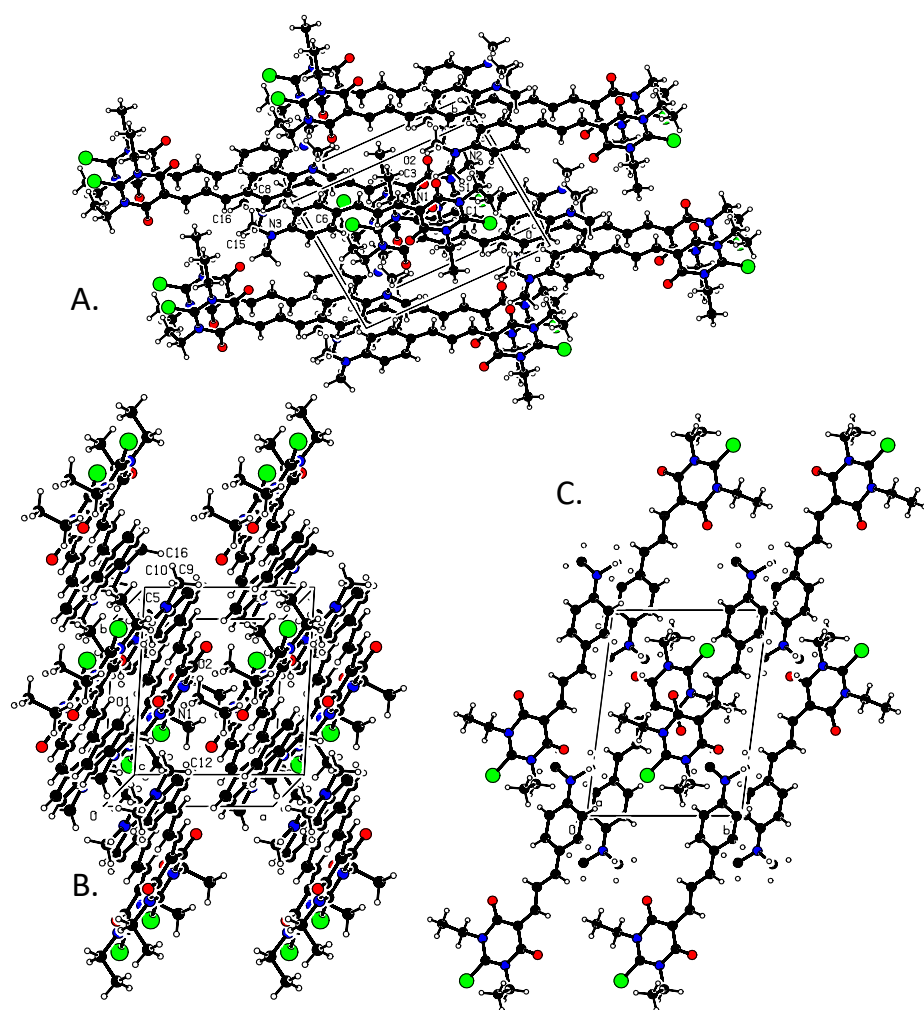
Figure 4.18. Molecular packing for TB[2] crystals. A) Packing as viewed along the x = z = 90˚, y = 0˚ direction of the crystal, B) packing as viewed along unit cell axis of the crystal, and C) packing as viewed along the y = z = 90˚, x = 0˚ direction of the crystal. Images generated using PLATON software package.
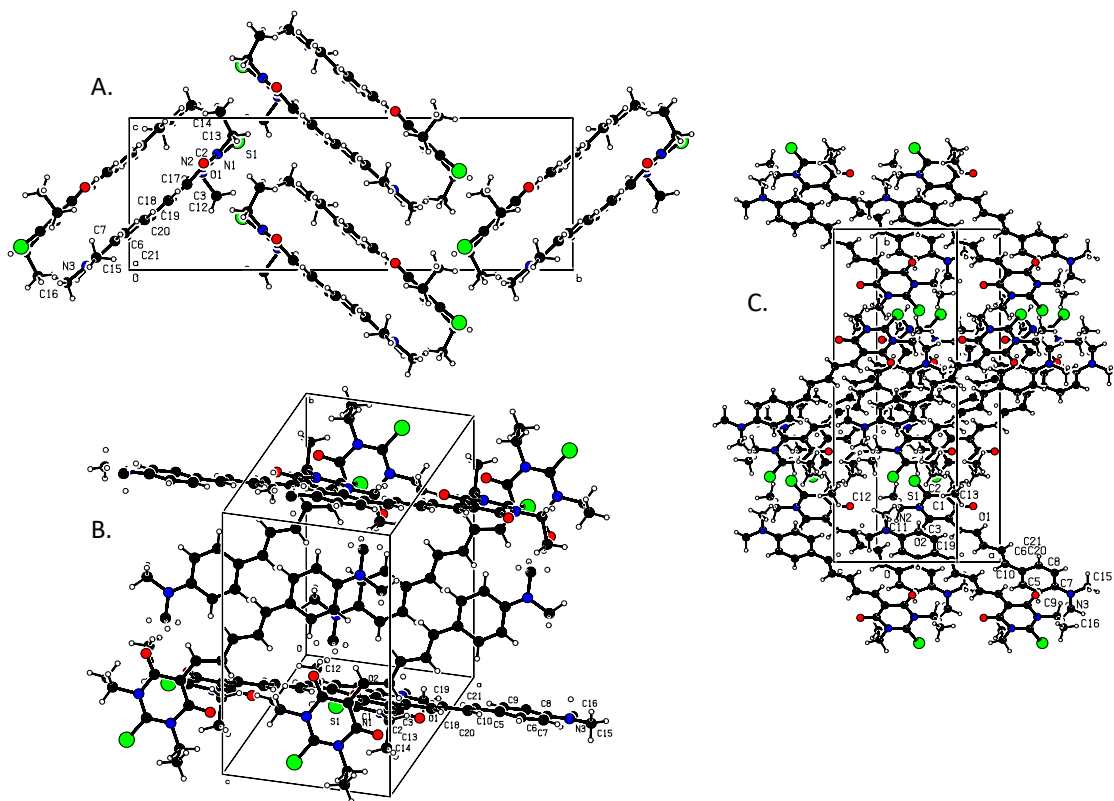
Figure 4.19. Molecular Packing of TB[3] crystals. A) Packing as viewed along unit cell axis of the crystal, B) packing as viewed along the c face of the crystal, and C) packing to give minimal overlap. Images generated using PLATON software package.
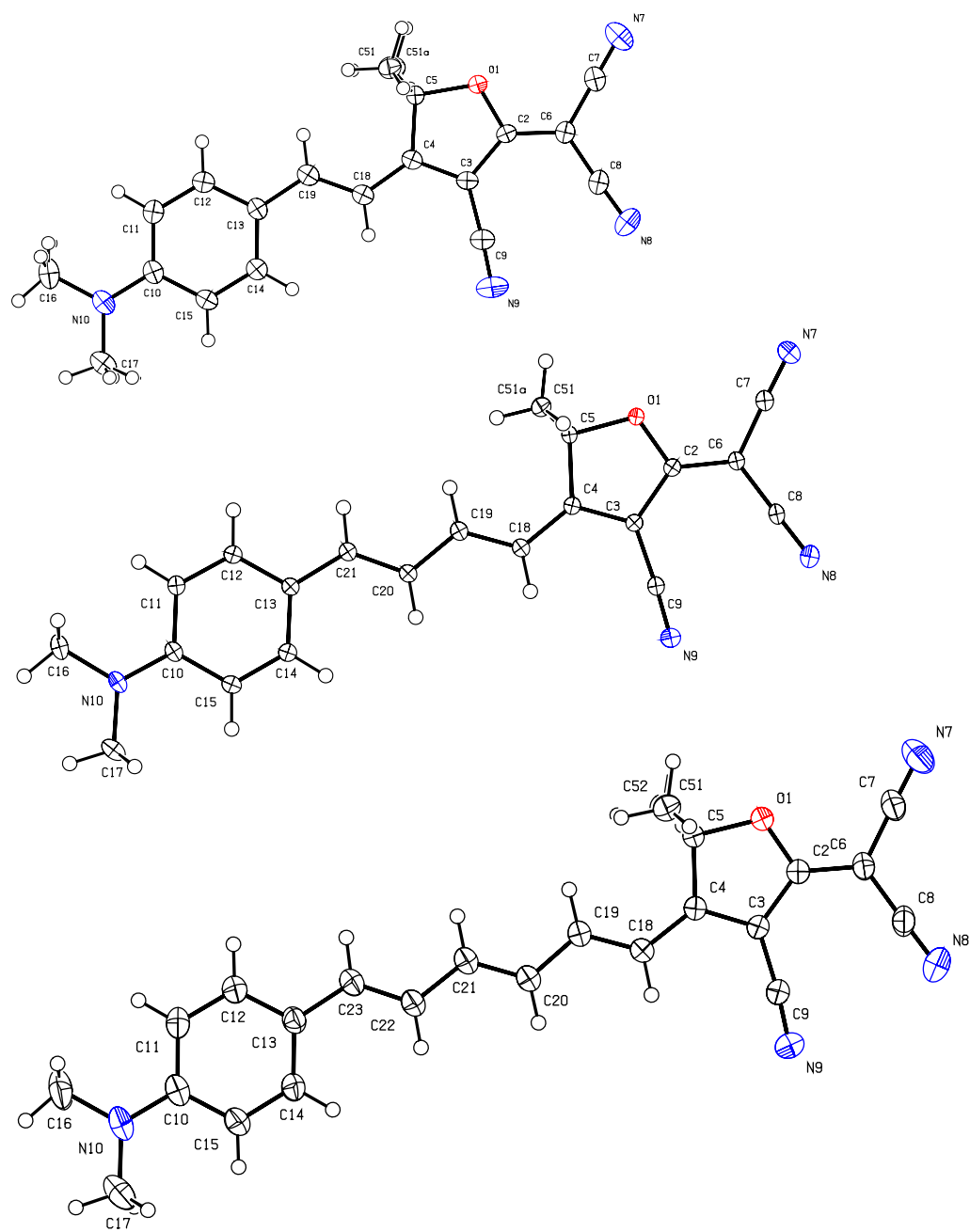
Figure 4.20. Crystal structures of TCF[n], for n = 1- 3. Images generated by Using the PLATON software package.

Figure 4.21. Crystal structure of TCF[4]. Images generated by Using the PLATON software package.

Table 4.4. Crystal structure data summary of TCF[n] series for n = 2 and 4.

Label	Scheme	a, b, c (Å)	Angles (degrees)	Space group	Z
TCF[1]		18.618(3) 6.9885(13) 13.737(3)	90 90 90	Pnma	4
TCF[2]		17.553(3) 6.8670(13) 15.561(3)	90 90 90	Pnma	4
TCF[3]		7.0919(10) 17.289(2) 17.417(3)	90 98.082(2) 90	P2$_1$/c	4
TCF[4]		7.6501(17) 17.26261(4) 18.469(4)	66.11 87.33 85.20	P-1	4

96
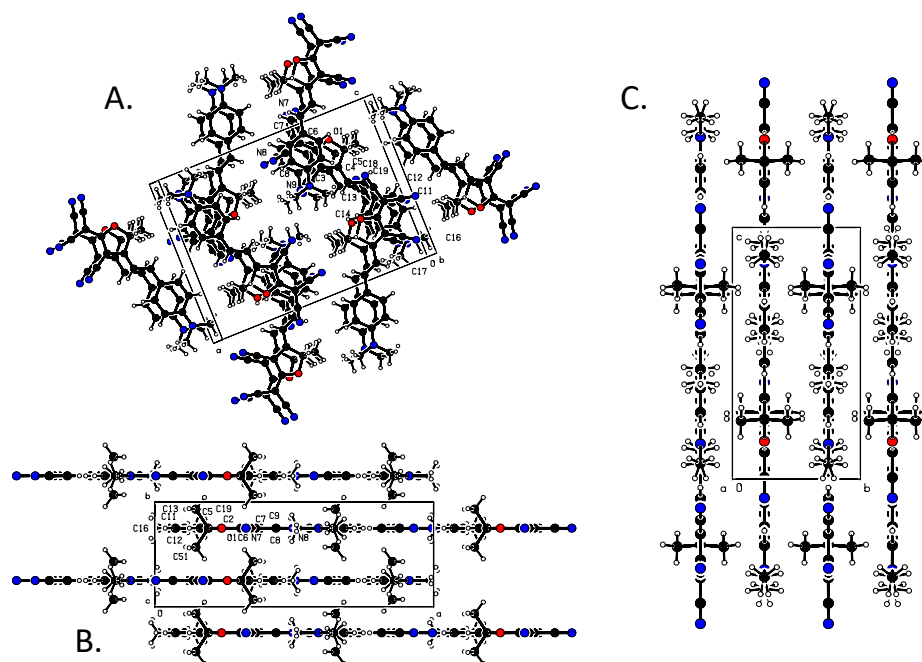
Figure 4.22. Molecular packing of TCF[1] crystals. A) Packing as viewed along the x = z = 90˚, y = 0˚ direction of the crystal B) packing as viewed along unit cell axis direction of the crystal, and C) packing as viewed along the y = z = 90˚, x = 0˚ direction of the crystal. Images generated using PLATON software package.

The crystal structure of TCF[1] shows that the molecules are perfectly planar, with the exception of the methyl groups on the TCF acceptor. As shown in Figure 4.22 – A, the molecules of TCF[1] in adjacent layers are oriented antiparallel to one another.
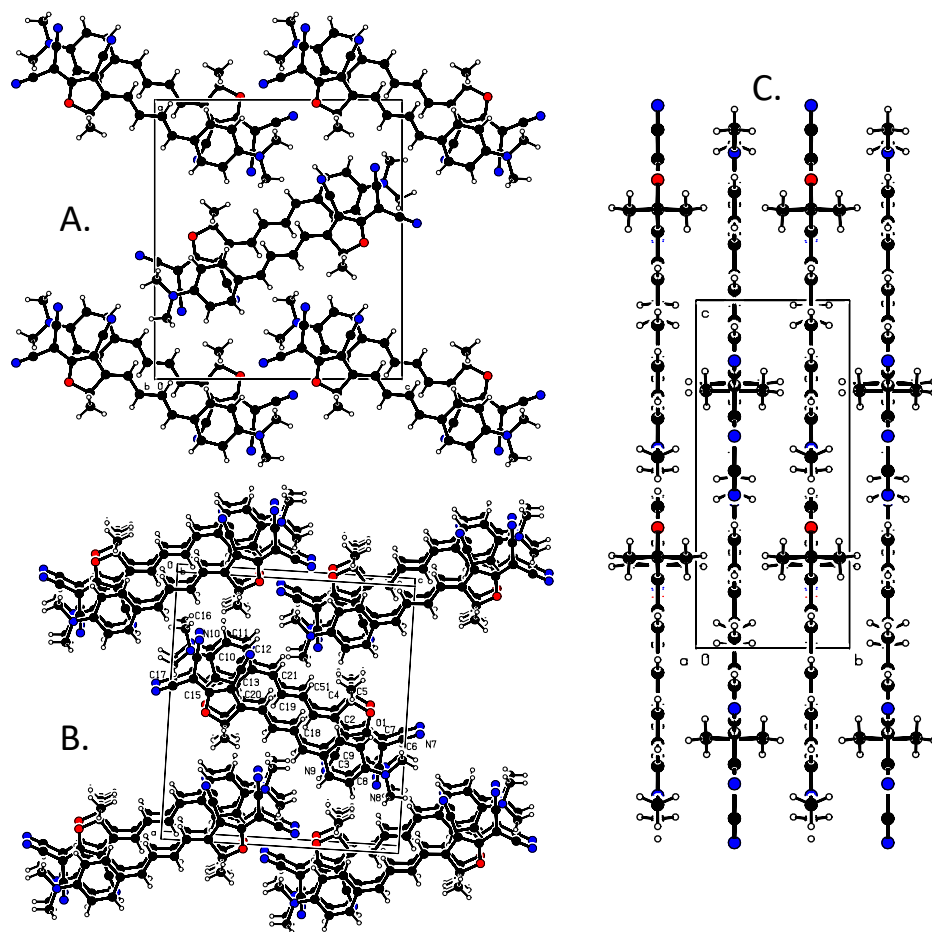
Figure 4.23. Molecular packing of TCF[2] crystals. A) Packing as viewed along the x = z = 90°, y = 0° direction of the crystal B) packing to give minimal overlap, and C) packing as viewed along unit cell axis direction of the crystal. Images generated using PLATON software package.

The crystal structure of TCF[2] also indicates that the molecule is perfectly planar, with the exception of the methyl groups on the TCF acceptor. Most of these compounds are mostly planar, but deviate when you look at the dihedral angle between the donor group and the bridge or the bridge and the acceptor. In the case of TCF[2] these dihedral angles are 0°.
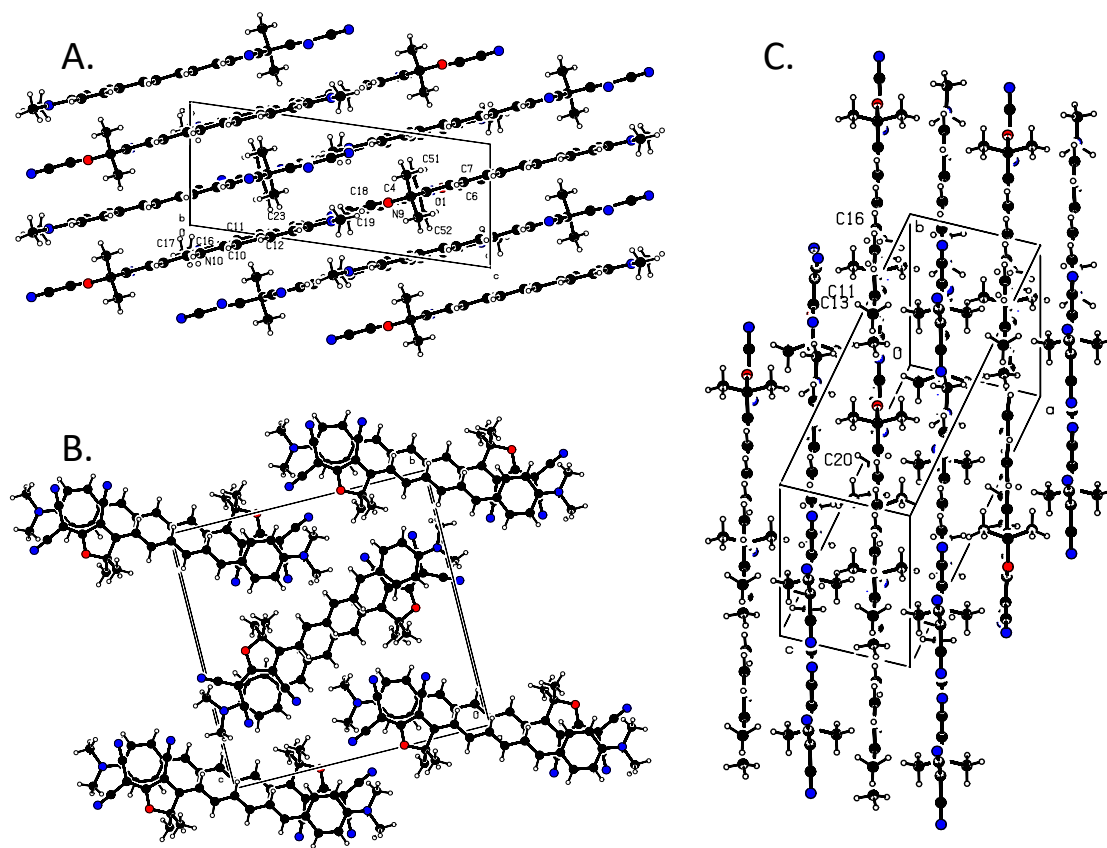
Figure 4.24. Molecular Packing of TCF[3] crystals. A) Packing as viewed along the x = z = 90˚, y = 0° direction of the crystal B) packing to give minimal overlap, and C) packing as viewed along b face of the crystal. Images generated using PLATON software package.
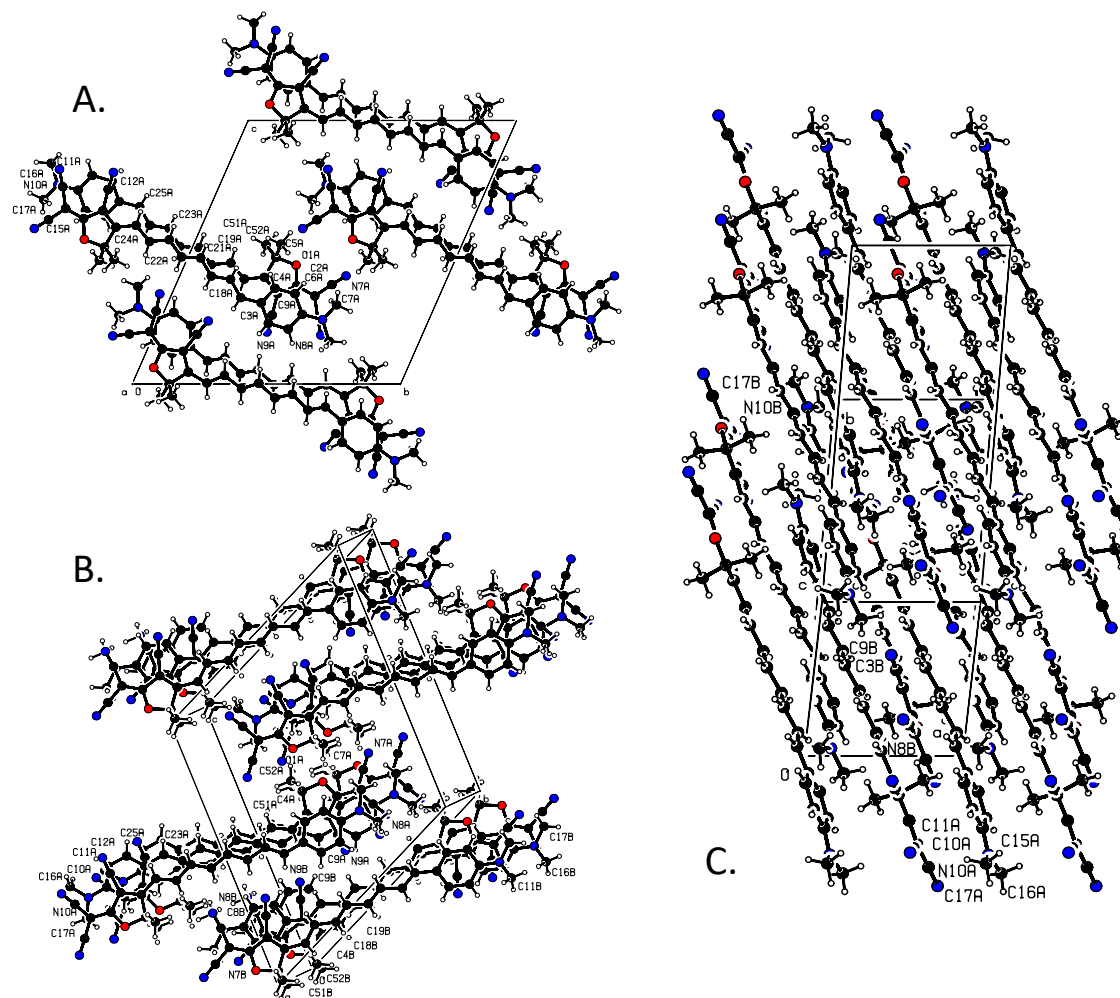
Figure 4.25. Molecular Packing of TCF[4] crystals. A) Packing as viewed along the y = z = 90˚, x = 0˚ direction of the crystal B) packing as viewed along the a face of the crystal, and C) packing as viewed along unit cell of the crystal. Images generated using PLATON software package.

The crystal structure of TCF[4] shows that it exists in to conformations, an *s-cis-* and *s-trans-* conformation about the single bond immediately before the TCF ring. From an orbital overlap/conjugation perspective, the *s-trans* conformer is the ideal case, however DFT calculations performed by Chafin et al. [30] the *s-cis* conformation is approximately 1.3 kcal/mol lower in energy. DFT calculations on another TCF

containing chromophore, FTC, suggest that the difference in energy between the two may

be much smaller, as it is only 0.3 kcal/mol for FTC.[31]
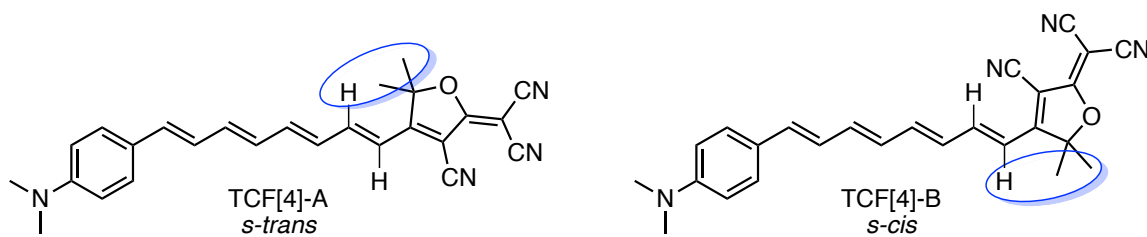
Figure 4.26. Structures of TCF[4] conformers as described in the text and by x-ray crystallography. Superimposed oval indicates the NOE interaction

The crystal structure of TCF[4] shows that the two conformers are present in

nearly equal proportions. Evidence for the *s-cis-* and *s-trans-* conformations of TCF[4] in

solution can be investigated by NMR. Based on the structures of the two conformers,

shown in Figure 4.26, they each will have a different set of protons that interact by the

nuclear Overhouser effect (NOE), a through-space interaction. This NOE interaction can

be interrogated by NMR by 2D-nuclear Overhouser effect spectroscopy of NOESY.

Integrating the NOE cross peaks between the two indicated polyene protons and the

protons of the TCF group allow for an estimate the ratio of *s-trans* to *s-cis* of TCF[4] in

CD_2Cl_2 to be 59 % *s-trans*, 41 % *s-cis*. A similar NOESY analysis of TCF[5] show that

the *s-trans* conformation makes up about 76 % of the sample.

4.4.3. Bond Length Alternation Studies by NMR Spectroscopy

While the BLA determined by crystal structure is a valuable metric for the

electronic structure of donor-acceptor polyenes, and most other NLO materials, the

applicability is slightly limited in scope. Using Raman spectroscopy, Marder *et al*

demonstrated that the local environment in a crystalline lattice is significantly different

from that of a solvent field.[6] Because of this, the BLA calculated from a crystal structure does not accurately represent the electronic structure of a molecule in solution. Bond length alternation has become a very important metric in the field of nonlinear materials, and it is necessary to explore alternatives that give a better picture of the material in the environment in which it will be used. NMR has the potential to be enormously helpful with this issue.

Vicinal proton coupling constants, $^3J_{1H\text{-}1H}$, are representative of the overlap between the molecular orbitals of protons on adjacent carbon atoms. Ordinarily, the orbital overlap is mainly impacted by the dihedral angle between interacting protons, with maxima at 0° and 180° and minimum at 90° (Figure 4.8). This relationship is described by either the Karplus equation or the Bothner-By equation [32-33] (Eq. 4.12 and 4.13 respectively).

$$^3J = J_0 \cos^2 \phi - K \begin{cases} J_0 = 10, & 0° \leq \phi < 90° \\ J_0 = 14, & 90° \leq \phi \leq 180° \end{cases} \qquad \text{(Eq. 4.6)}$$

$$^3J = 7 - \cos \phi + 5 \cos 2\phi \qquad \text{(Eq. 4.7)}$$

In a donor-acceptor polyene chain, all of the protons on adjacent carbons are anti-periplanar to one another, the absolute maximum of the Karplus equation. In this configuration, with the dihedral angle static, the distance between adjacent sp^2 hybridized carbons will impact that orbital overlap and thusly the resulting coupling between their attached protons.
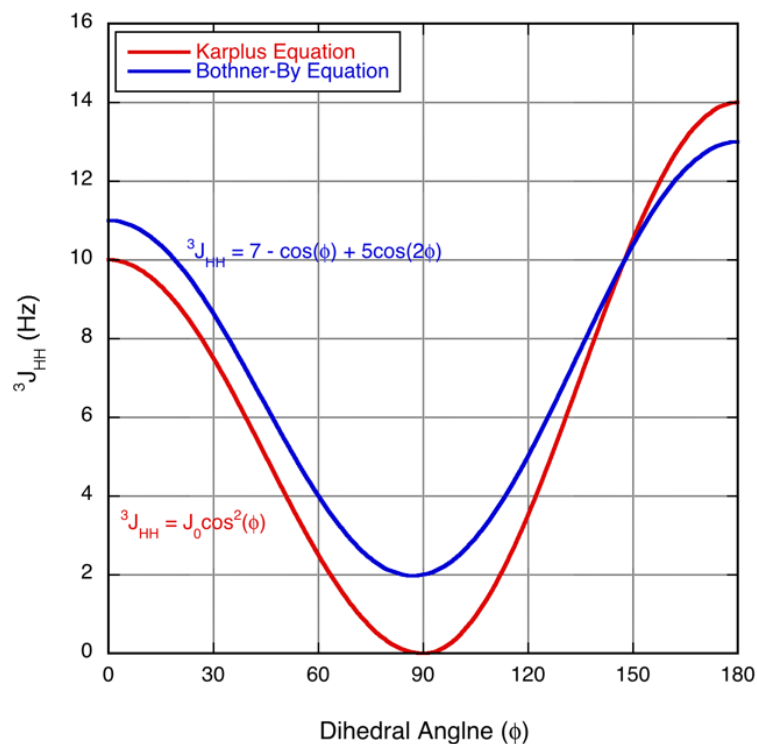
Figure 4.27. Estimation of the dependence of vicinal proton coupling constants on dihedral angle by the Karplus (red trace) and Bothner-By (blue trace) equations.

Vicinal coupling constants in *trans-* double bonds are typically about 16.5 Hz but can range between 12 – 24 Hz.[34] The typical coupling constant between two anti-periplanar protons on sp^2 carbons bound by a single bond is about 10 Hz. These typical values can be taken as the extreme values for a bond length alternation approximation.[35]
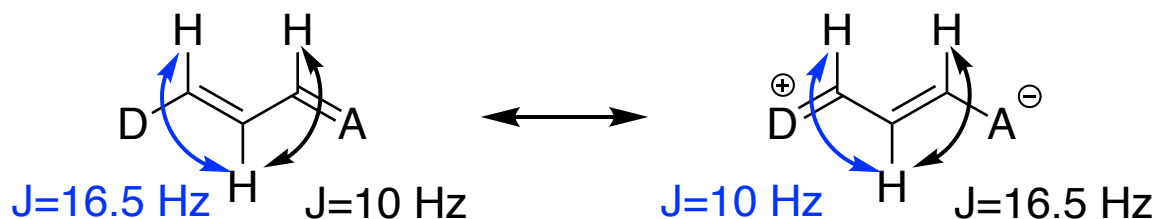
Figure 4.28. Bond length alternation by NMR spectroscopy.

When measure by crystal structure, the formula for bond length alternation is the average single bond length subtracted by the average double bond length. This formula establishes a positive BLA value for the valence bonding structure and a negative BLA for the charge transfer structure. To keep this same convention, the formula for bond length alternation by NMR, ΔJ to avoid confusion, must be flipped so that the valence bonding structure has a positive ΔJ:

$$\Delta J = \overline{J}_{C=C} - \overline{J}_{C-C}. \qquad \text{(Eq. 4.8)}$$

Using this convention, the limiting ΔJ values are 6.5 Hz for the valence bonding structure and -6.5 Hz for the charge transfer contributor.

The extraction of the coupling constants for most of the donor-acceptor polyenes was straight forward. There were a few which were too complicated to extract all of the J values (indicated n.d. in Table 4.5). The NMR Spectra of all of the DA[4] compounds and several others show significant second order effects for the two or three protons along the chain that are adjacent to the donor group. After careful analysis, the second order effects manifest themselves as an ABX spin system[34]. In addition to being ABX, there are two additional factors leading to even more complexity. First, instead of the normal doublet of ABq as described by Reich[34] the X proton is intermediate in distance away from the A and B protons which causes one of the ABq to collapse into a singlet. Second, the X of the ABX system is coupled to an additional proton, typically with a large coupling constant. It is for these two reasons that the spin system will be referred to as an ABMX system.
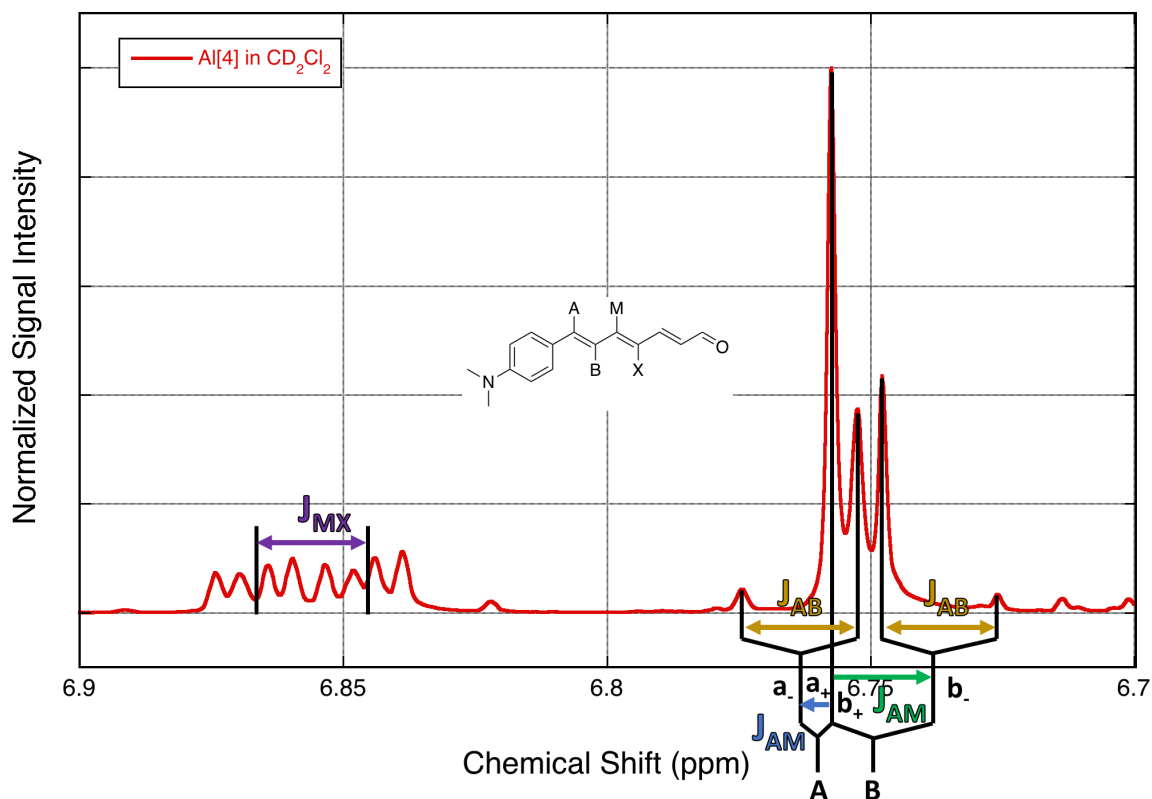
Figure 4.29. ^{1}H NMR spectrum of Al[4] in CD$_2$Cl$_2$ to describe the ABMX spin system. Based on the description of Reich.[34] The inset shows the structure of DCV[4] with the protons in question labeled as A, B, M, and X.

In the above example, The peaks corresponding to the ABq and s can be solved by the following method. In the following equations, the peaks of the ABq are labeled 1 – 4 from left to right and the intervening singlet is labeled as s. The first step is to solve the ABq by first measuring J_{AB} by taking the difference (in Hz) of the first and second peaks as well as the third and fourth.

$$\left|J_{AB}\right| = v_1 - v_2 = v_3 - v_4 \qquad \text{(Eq. 4.9)}$$

Next the center of the ABq is calculated by taking the average of peaks 2 and 3. The difference in the frequencies for protons A and B (Δv) can be calculated as follows:

$$\Delta V_{AB} = \sqrt{(v_1 - v_4)(v_2 - v_3)}.$$ (Eq. 4.10)

Find the position of υ_A and υ_B using the center and the difference between them as follows. This step is necessary because the resonance frequency is actually the center of integration of a multiplet and not simply its center.

$$V_A = V_{center} + \Delta V_{AB}$$
$$V_B = V_{center} - \Delta V_{AB}$$ (Eq. 4.11)

Finally, the chemical shift of protons A and B can be found by dividing the frequency in Hz by the frequency of the spectrometer in MHz. The added complexity for the ABX (or ABMX) spin system is shown in Figure 4.29. In our case, we have solved Eq. 4.9 – 4.11 for the ab- half of the pattern. The ab+ side is the ABq that collapsed in to a singlet (peak s). The actual chemical shift of A and B must be found by subtracting the a- fragment from the a+, and b- from b+. This results in a negative value for the J_{AM}. This negative value actually gives us a tiny bit more information, as coupling through even numbers of bonds is often negative in value.[20] After executing the above method on the ABMX system, the resulting coupling constants are J_{AB} = 15.1 Hz, J_{AM} = -1.8 Hz, J_{BM} = 12.3 Hz, and J_{MX} = 14.2 Hz. The second order effects distort the spectrum to a significant degree. There is actually a small amount of ambiguity in the reporting for this special case where one of the two ABq halves collapses. For an ordinary ABq, it is appropriate to list the $\Delta\delta$ (or $\Delta\upsilon$ in Hz) of the protons corresponding to the A and the B part of the signal as well as the coupling constant. The ratio of $\Delta\upsilon$/J for a second order NMR splitting pattern can describe the extent to which the second order effects are distorting the spectrum. That said, in this case, the peaks that actually resemble an ABq all belong to a single proton. In an attempt to describe the system fully, the reported NMR data lists the collapsed ABq as

$\Delta\delta =$ 0 Hz. While this may not be ideal, it does seem less strange than reporting it as an ABX_1ABq_1s or something of that nature.

Using the above parameters, the expected spectrum of the aforementioned spin system was simulated using the DAISY 1D-spectrum simulation software by Bruker as an application in TopSpin. The simulated spectrum of the spin system and the actual spectrum, shown in Figure 4.30, match quite well. The DAISY simulation slightly overestimated a line broadening factor, so the simulated spectrum appears slightly wider. This may be due to the gaussian window multiplication that was used to sharpen the peaks in leu of and exponential on (default settings) prior to the transform.
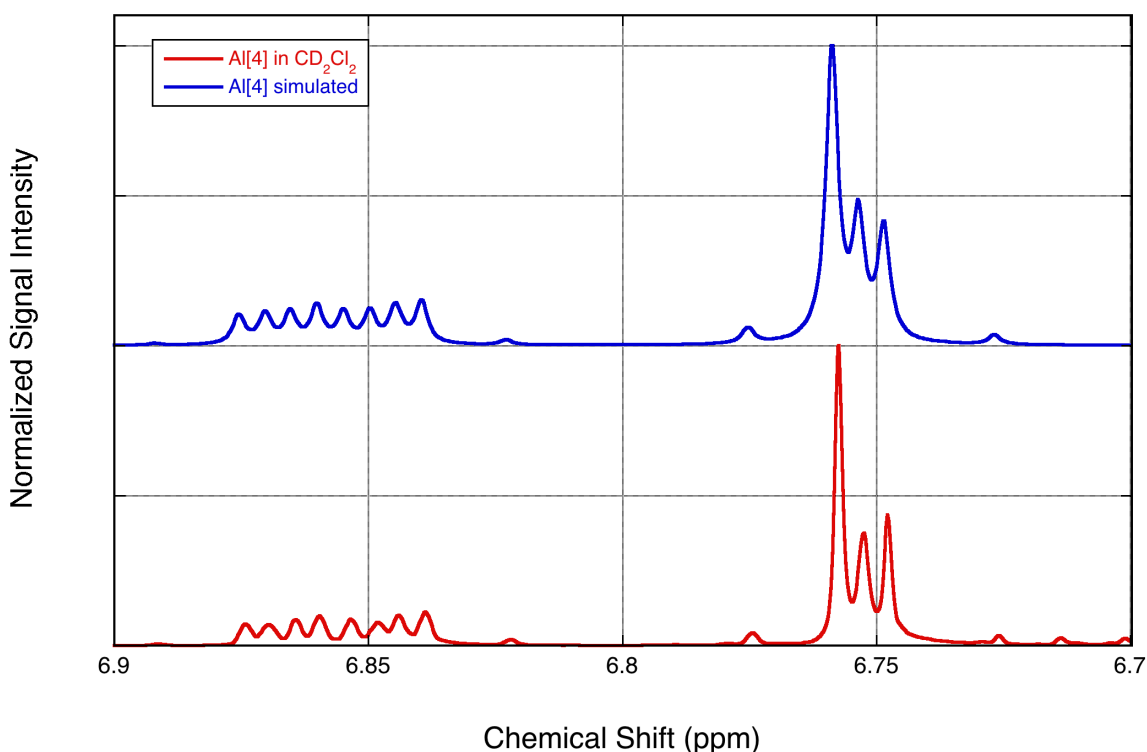
Figure 4.30. ^{1}H NMR spectrum of Al[4] in CD$_2$Cl$_2$ (red trace) and the DAISY simulation (blue trace) using the parameters from solving the ABMX system listed in the text
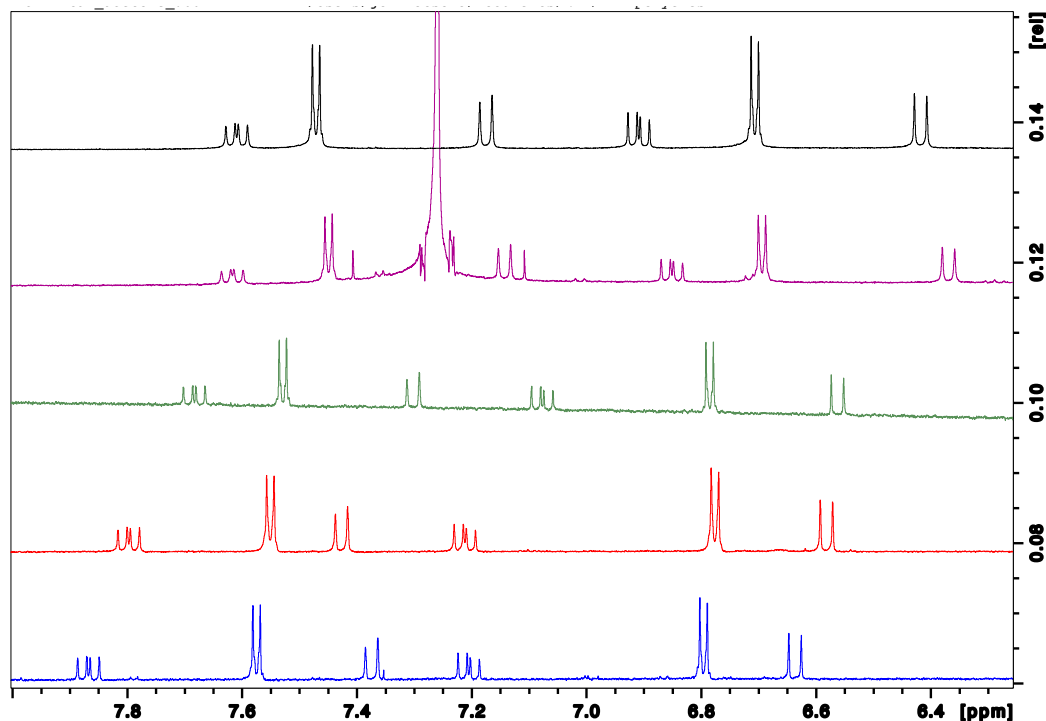
Figure 4.31. 1H NMR spectra of TCF[2] in acetone-d_6 (blue trace), DMSO-d_6 (red trace), acetonitrile-d_3 (green trace), Chloroform-d (purple trace), and dichloromethane-d_2 (black trace) as an example of measuring ΔJ. All spectra were recorded using a Bruker AVIII-HD 700 MHz NMR spectrometer and are referenced to their residual solvent signals.

The coupling constants are not the only aspect of the NMR spectra that change depending on solvent. Figure 4.31 shows the ^{1}H NMR spectra of TCF[2] in acetone-d_6, DMSO-d_6, acetonitrile-d_3, chloroform-d, and dichloromethane-d_2 from the bottom up. All of the spectra have been corrected in reference to their residual solvent peaks[36] which are in reference to TMS. The chemical shifts of the most down field and most upfield resonances shift down field in hydrogen bonding solvents. These protons correspond to the second proton from the acceptor end and the last proton before the TCF group and would be deshielded corresponding to the degree of charge delocalization.

Table 4.5. Vicinal proton coupling constants between adjacent protons on the polyene backbone of the D-A polyenes. NMR spectra were acquired in CD_2Cl_2. Bonds are numbered from donor to acceptor ends. The asterisk indicates the vicinal coupling constant involving an aldehyde proton.

Dye	J_{1-2} (Hz)	J_{2-3} (Hz)	J_{3-4} (Hz)	J_{4-5} (Hz)	J_{5-6} (Hz)	J_{6-7} (Hz)	J_{7-8} (Hz)	J_{8-9} (Hz)	$<\Delta J>$ (Hz)
Al[3]	15.32	10.92	15.02	8.04*					4.25
Al[4]	15.33	10.53	14.49	11.33	15.07	8.00*			4.03
Al[5]	n.d.	n.d.	14.06	11.25	14.68	11.32	15.04	8.01*	3.31‡
DCV[2]	14.82	11.70							3.12
DCV[3]	15.08	11.20	14.14	12.02					3.00
DCV[4]	15.08	12.33	14.22	11.61	14.32	11.89			2.60
TB[2]	14.79	12.51							2.28
TB[3]	15.12	10.97	13.69	12.64					2.62
TB[4]	14.98	13.39	14.24	11.69	14.13	12.64			1.87
TB[5]	14.32	n.d.	n.d.	11.48	14.42	11.62	13.90	12.64	2.30‡
TCF[1]	15.91								--
TCF[2]	15.16	11.21	14.93						3.84
TCF[3]	15.20	11.36	14.24	11.04	15.12				3.65
TCF[4]	n.d.	n.d.	13.42	11.44	14.12	11.50	15.21		2.78‡

‡: BLA estimate based on incomplete assignment of coupling constants
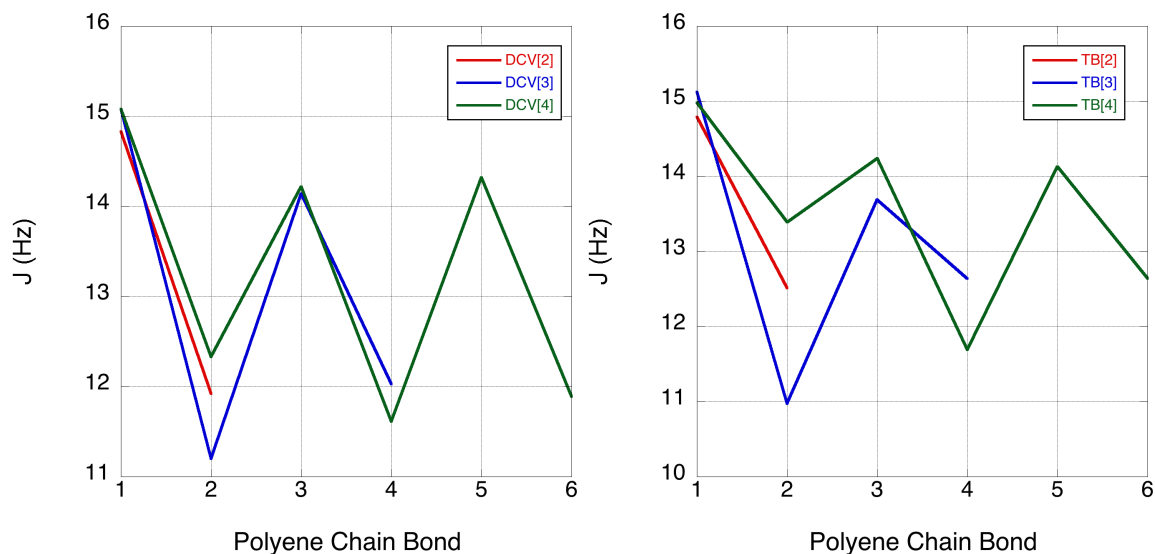
Figure 4.32. Oscillatory behavior of proton coupling constants along polyene chain from donor end to acceptor end for DCV[n] (left) and TB[n] (right) in CD_2Cl_2.

Error! Reference source not found. and Figure 4.32, show the coupling constants measured for each bond of the polyene chain (numbered from donor end to acceptor end). In the DCV[n] series shown in **Error! Reference source not found.**, the oscillatory behavior of the coupling constants remains nearly the same with increasing length. There is a slight but noticeable decrease in coupling in DCV[4] at the donor end. This fits with the expectation that the bond length alternation is increased on the acceptor side of the molecule. In the TB[n] series of Figure 4.32, the change in coupling constants at the donor end is very dramatic in TB[4], resulting in a significant change in ΔJ.
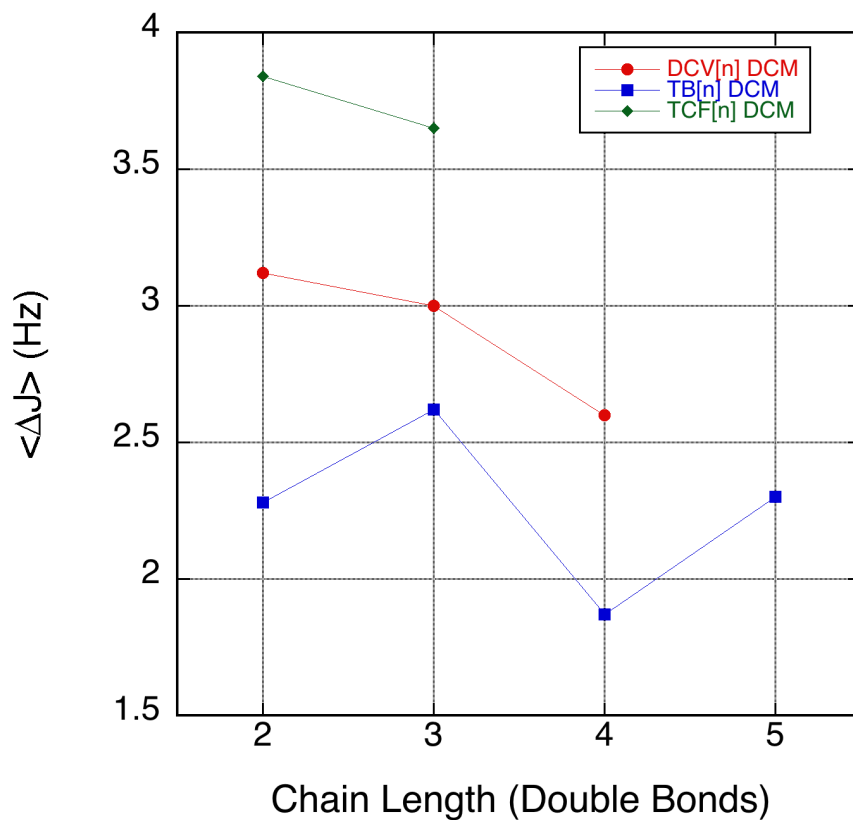
Figure 4.33. Bond length alternation as measured by ^{1}H NMR coupling constants, ΔJ.
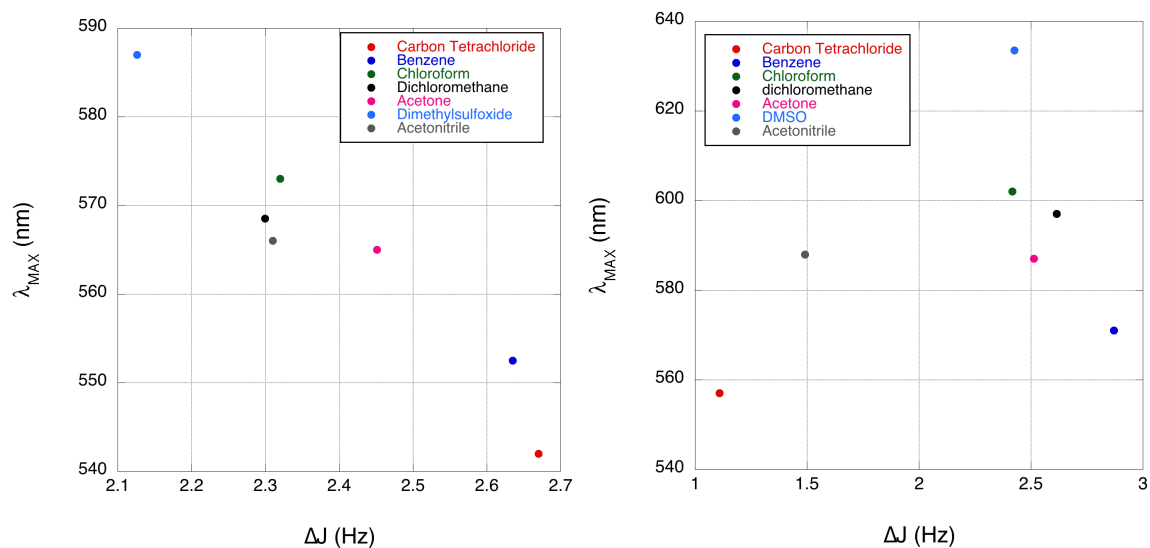
Figure 4.34. ΔJ vs absorbance maxima for Left) TB[2] and Right) TB[3] in various solvents

4.4.4. Steady State Spectroscopic Studies

The electronic spectra of DCV[n], ID[n], TB[n], and TCF[n] series for n = 1 – 4 are shown below in Figure 4.35. The different series of DA compounds show dramatic solubility differences. The TCF[n] series, which have the strongest acceptor groups, are quite difficult to dissolve in most non-chlorinated solvents. The TB[n] series, on the other hand can be dissolved in solvents as nonpolar as benzene and carbon tetrachloride as well as solvents as polar as acetonitrile and DMSO. The DCV[n] and ID[n] series lie in between the extremes represented by TCF[n] and TB[n] series.
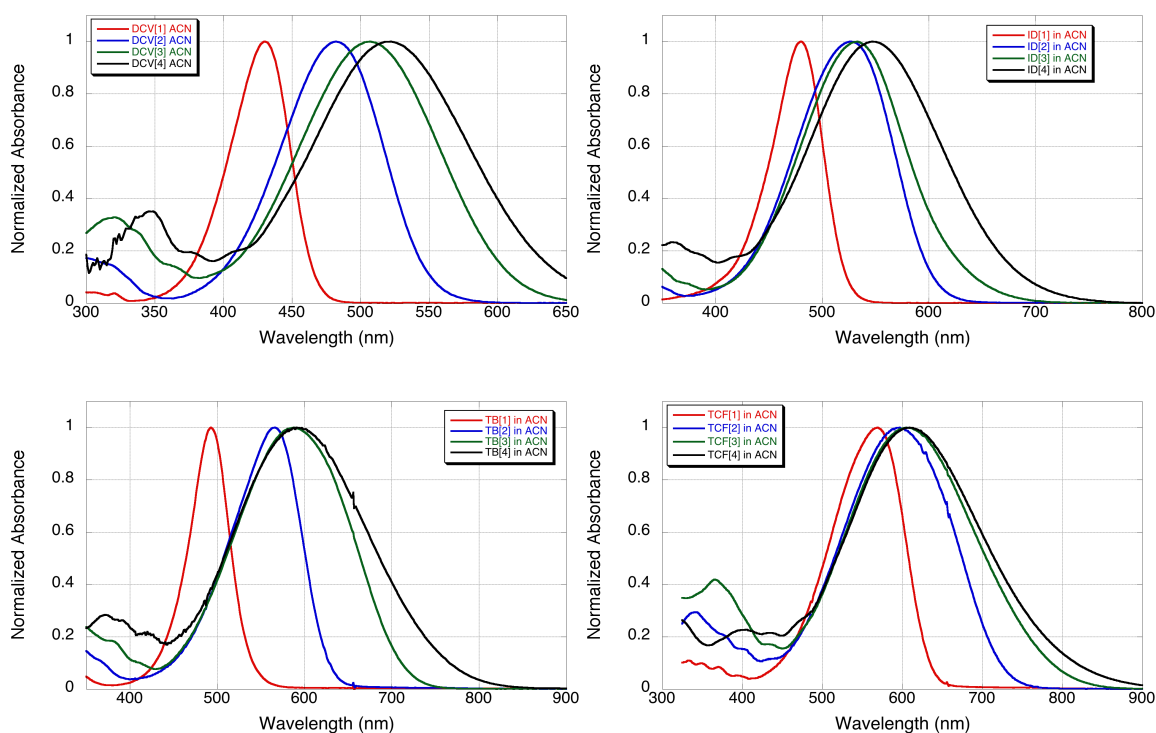
Figure 4.35. Normalized absorbance spectra in acetonitrile for DCV[n] series (top left), ID[n] series (top right), TB[n] series (bottom left), TCF[n] series (bottom right).

Table 4.6. Absorption maxima for the dimethylaminopheny polyenals, DCV[n], ID[n], TB[n], and TCF[n] series in chloroform and acetonitrile. All values are in nanometers

Acceptor	Solvent	Polyene Chain Length (number of double bonds)			
		1	2	3	4
DCV[n]	CHCl$_3$	433	491	525	547
	ACN	426	476	506	528
ID[n]	CHCl$_3$	483	539	547	564
	ACN	480	526	533	549
TB[n]	CHCl$_3$	495	573	602	621
	ACN	493	566	588	591
TCF[n]	CHCl$_3$	577	612	645	657
	ACN	569	595	605	611

4.4.5. Solvatochromism

Many trends in solvatochromism can be described by considering the relative stabilization of the ground and excited states in solvents of differing polarity. For donor-acceptor polyenes, the dominating feature of the absorbance spectrum is the $\pi - \pi^*$ transition that results from charge transfer from donor to acceptor.[18] Positive solvatochromism results when the excited state is stabilized by being dissolved in solvents of greater polarity. This is typical of a compound whose dipole moment is greater in the excited state than in the ground state. By the same logic negative solvatochromism arises when the ground state has a larger dipole moment than that of the excited state.

Electronic transitions occur on a much faster time scale (about 10^{-15} s) than that of vibrations or rotations (about 10^{-12} to 10^{-10} s), and as such, the absorbing molecule remains in essentially the same conformation during the transition. This idea is known as

the Franck-Condon principle.[37-38] The state of the molecule in the short amount of time after the absorbance of light is known as a Franck-Condon state. Another major contributor to solvatochromic behavior is the intramolecular interactions between the Franck-Condon state of the absorber and its environment.

As is shown in Figure 4.37 below, the solvatochromic behavior of the DCV[n] series in toluene, chloroform, and acetonitrile show reversed solvatochromism, where there is a bathochromic shift when the solvent changes from toluene to chloroform, followed by a hypsochromic shift from chloroform to acetonitrile. Similarly, the TB[n] series, shown in Figure 4.38 in benzene, chloroform, acetonitrile, and DMSO, show a particularly strange solvatochromism. There are several spectral shifts as shown in Figure 4.36.
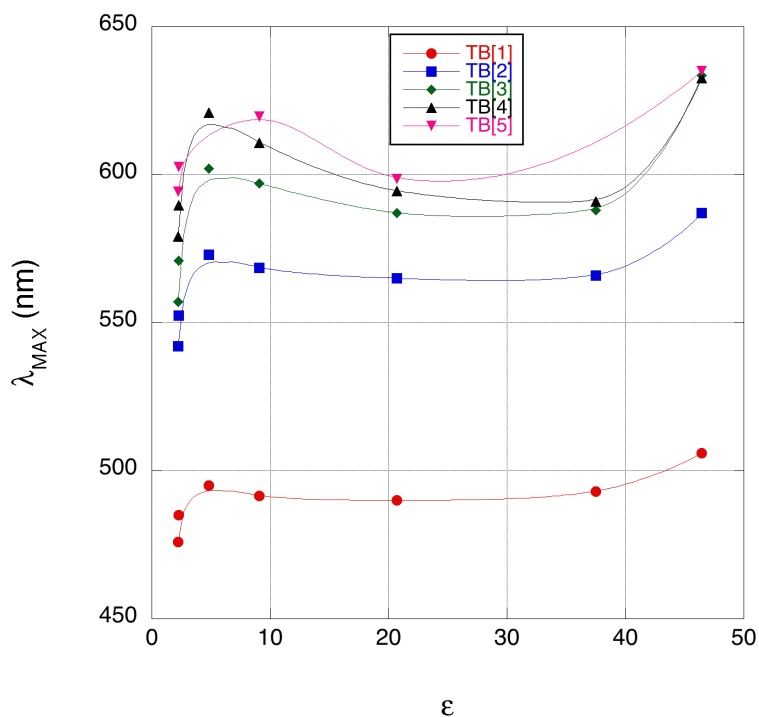
Figure 4.36. Solvatochromism of TB[n] series. Absorbance λ_{max} vs relative permittivity
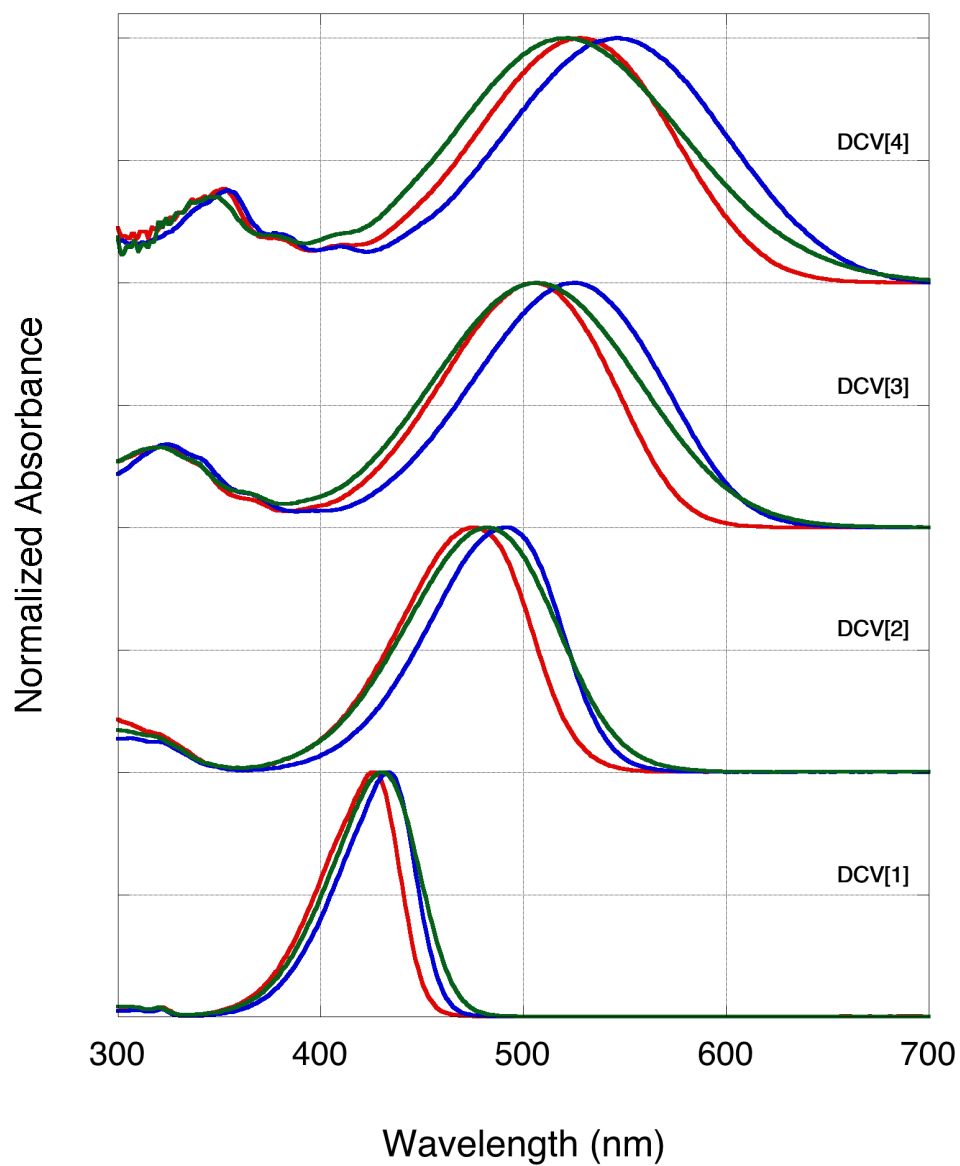
Figure 4.37. Normalized and Stacked absorbance of DCV[1-4] in toluene (red traces), chloroform (blue traces), and acetonitrile (green traces).
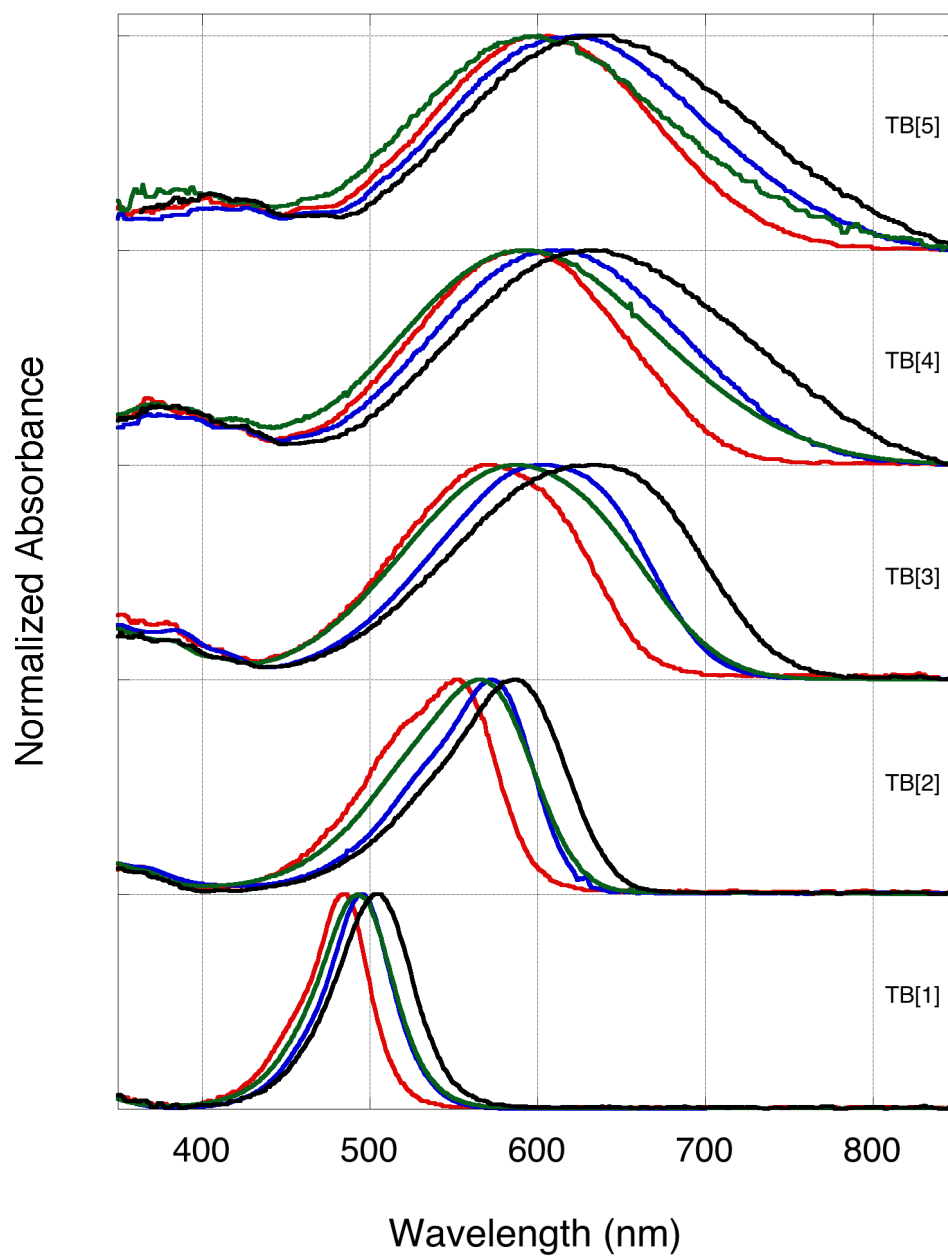
Figure 4.38. Normalized and stacked absorbance spectra of TB[1-5] in benzene (red traces), chloroform (blue traces), acetonitrile (green traces), and DMSO (black traces).

The solvatochromic behavior of the TCF[n] series shows a correlation to the type of solvent interaction present, as can be seen in Figure 4.41.
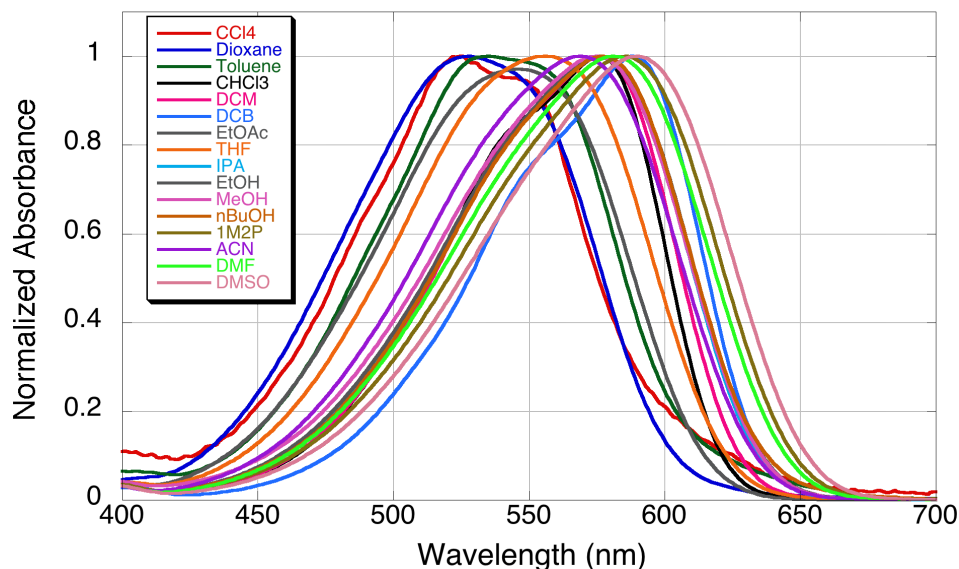
Figure 4.39. Normalized absorbance of TCF[1] in various solvents
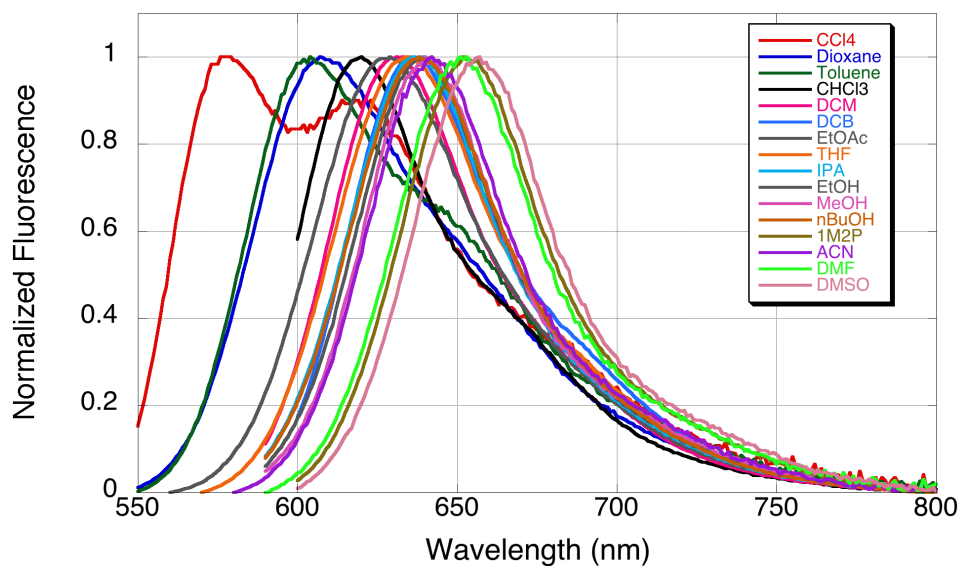
Figure 4.40. Normalized Fluorescence of TCF[1] in various solvents. All samples were excited at their maximum absorbance as shown in Figure 4.39. Emission was recorded starting a minimum of 10 nm longer wavelength than the excitation.
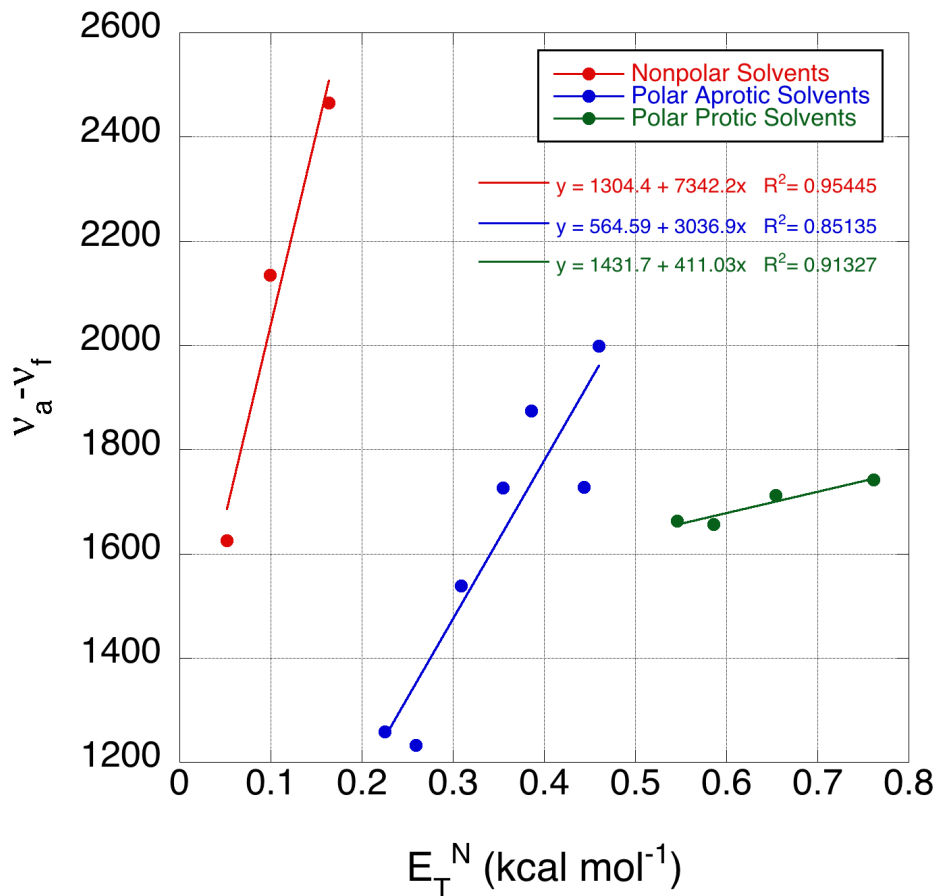
Figure 4.41. Solvatochromic response of TCF[1] in solvents characterized by type

The solvatochromism of TCF[1] can best be described by grouping solvents based on

their properties. As is shown in Figure 4.41, the solvatochromic behavior of TCF[1] can

be divided into nonpolar, polar aprotic and polar protic solvents.

4.4.6. Solvent-Dependent Raman Scattering Cross-Sections

      Another way of assessing the bond order alternation is by Raman scattering. Back

in 1993, Marder et. Al. described the use of Raman scattering as an indicator of bond

length alternation.[6] They showed that for a set of simple of asymmetric polymethines,

the intensity of the Raman bands corresponding to a polyene-like structure (at about 1600 and 1150 cm^{-1}) show a solvent dependence and that the Raman spectra become increasingly similar to that of the solid state in increasingly polar solvents.[5-6]

The probability of Raman scattering is described by the total differential cross section, dσ/dΩ, of a material[39]. The value of the scattering cross section is dependent on measurable quantities such as the laser power (P_0), the number density of the sample (N), the path length (l), and solid angle of collection (Ω) is shown below.

$$\frac{d\sigma}{d\Omega} = \frac{P_R}{P_0 N l \Omega}$$
(Eq. 4.12)

In the above equation, P_R is the integrated Raman intensity for the whole band.[40] Experimentally, donor-acceptor polyenes have very simple Raman spectra. They are generally dominated by two modes, one at 1150 cm^{-1} corresponding to C-C single bond stretching and the other is at about 1600 cm^{-1} corresponding to C=C double bond stretching.[6, 41] The cross sections of these two dominant features depend on the equilibrium geometry of the molecule, and thusly the cross section should also depend on bond length alternation. This correlation between BLA and Raman scattering was shown by Marder and colleagues by showing that the Raman spectra recorded in polar solvents was much more similar to those spectra recorded in solid form than they were to those recorded in nonpolar solvents.[6] RSC values can be determined with greater accuracy by measuring in reference to a well-known and characterized mode, such as the 992 cm^{-1} line in benzene.[39] By measuring benzene in the same setup as the sample of interest, the scattering cross section becomes:

$$\left(\frac{d\sigma}{d\Omega}\right)_i = \left(\frac{d\sigma}{d\Omega}\right)_0 \frac{P_R^i P_L^0 N_0 l_0 n_i^2}{P_R^0 P_L^i N_i l_i n_0^2},$$
(Eq. 4.13)

where the designations i and 0 denotes the sample and the reference respectively. In solution, the three major contributors to the electronic and molecular structure of the polyene chain are the strength of the donor and acceptor groups, the length of the polyene chain, and the polarity of the medium. The effects of the relative strength of the acceptor groups is shown below in Figure 4.42, Figure 4.43, and Figure 4.44, and comparison between the spectra of the same acceptor group demonstrate the effects of chain length. As was mentioned previously, in an ideal polyene, the Raman spectrum is characterized primarily by two modes corresponding to C=C stretching (~1600 cm⁻¹) and *sp²* C-C stretching (~1150 cm⁻¹).
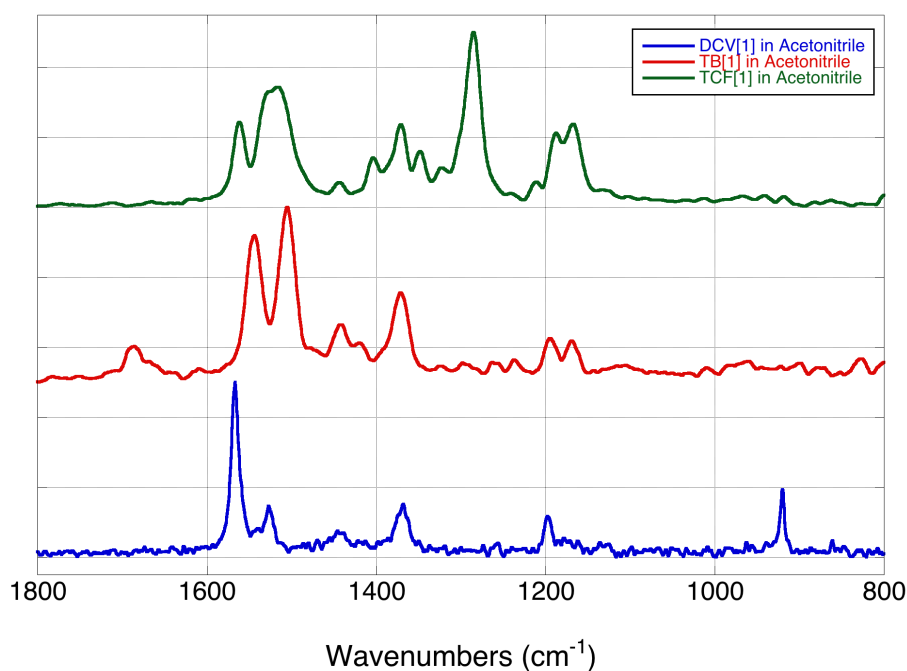
Figure 4.42. Normalized FT-Raman spectra of DCV[1] (blue trace), TB[1] (red trace), and TCF[1] (green trace) in acetonitrile. All concentrations are between 1 – 5 mM. The y-axis is arbitrary, and the spectra are stacked for ease of visual comparison.
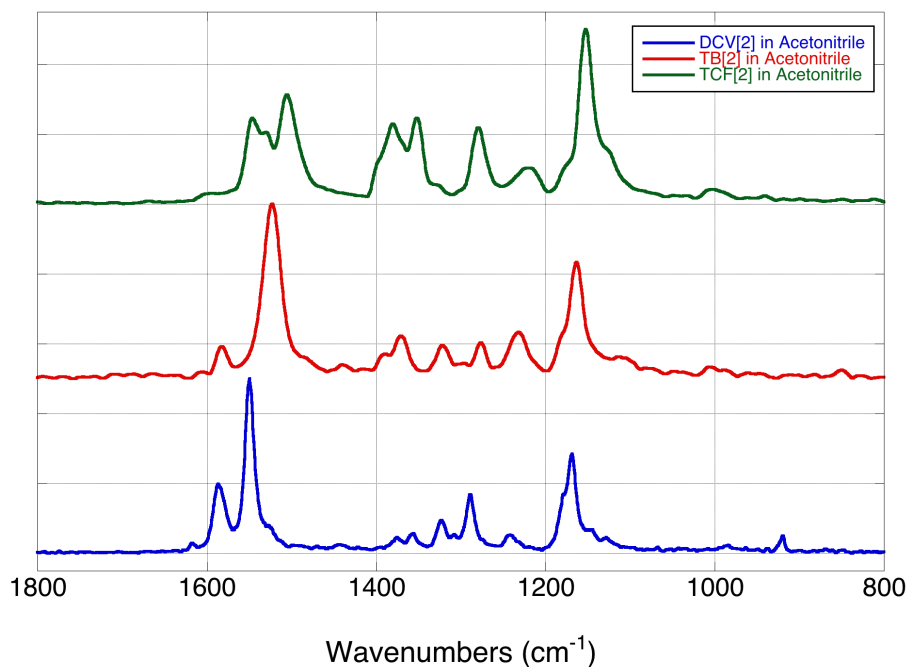
Figure 4.43. Normalized FT-Raman spectra of DCV[2] (blue trace), TB[2] (red trace), and TCF[2] (green trace) in acetonitrile. All concentrations are between 1 – 5 mM. The y-axis is arbitrary, and the spectra are stacked for ease of visual comparison.
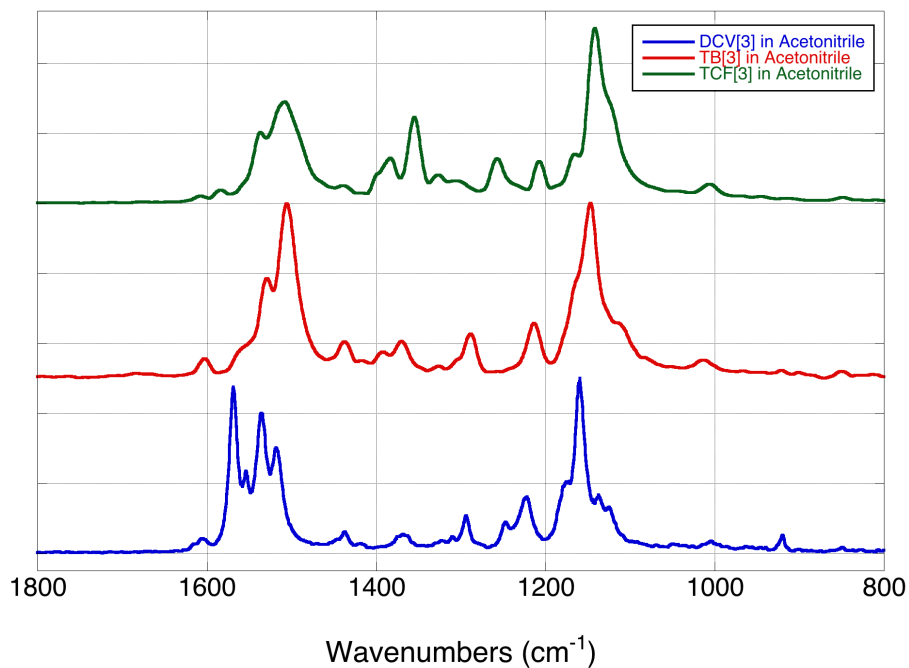
Figure 4.44. Normalized FT-Raman spectra of DCV[3] (blue trace), TB[3] (red trace), and TCF[3] (green trace) in acetonitrile. All concentrations are between 1 – 5 mM. The y-axis is arbitrary, and the spectra are stacked for ease of visual comparison.

With the addition of strong donor and acceptor groups at the terminal positions, the polyene π-electrons will be delocalized along the chain resulting in an overall decrease in intensity of the sp^2 C-C stretching and sp^3 C-C stretching modes and the appearance of intermediate modes. The intensity of the intermediate modes, relative to the C=C and C-C modes increase with increasing acceptor strength. In the three above sets of Raman spectra, the intensity of the modes are in arbitrary units and have been normalized and stacked for ease of viewing. The chromophores of containing the same acceptor group are plotted with the same color trace and are, in order of increasing acceptor strength, DCV[n] (blue traces), TB[n] (red traces), and TCF[n] (green traces). In each of the above series, the TCF[n] compound has a significantly higher contribution from the intermediate bands than from that of TB[n] or DCV[n].

The effects of chain length and solvent are best seen through their effects on the RSC values for the C=C and C-C modes. As the chain length increases there is a sizeable increase in the scattering cross sections of both modes, as is shown in Figure 4.45. The spectra from which these cross sections were calculated were all recorded in acetonitrile and were referenced to the 992 cm^{-1} line of benzene.[39] Similar trends can be seen from the RSCs measured in chloroform and chlorobenzene. This dramatic increase in Raman scattering in longer chromophores can be attributed to an increase in the
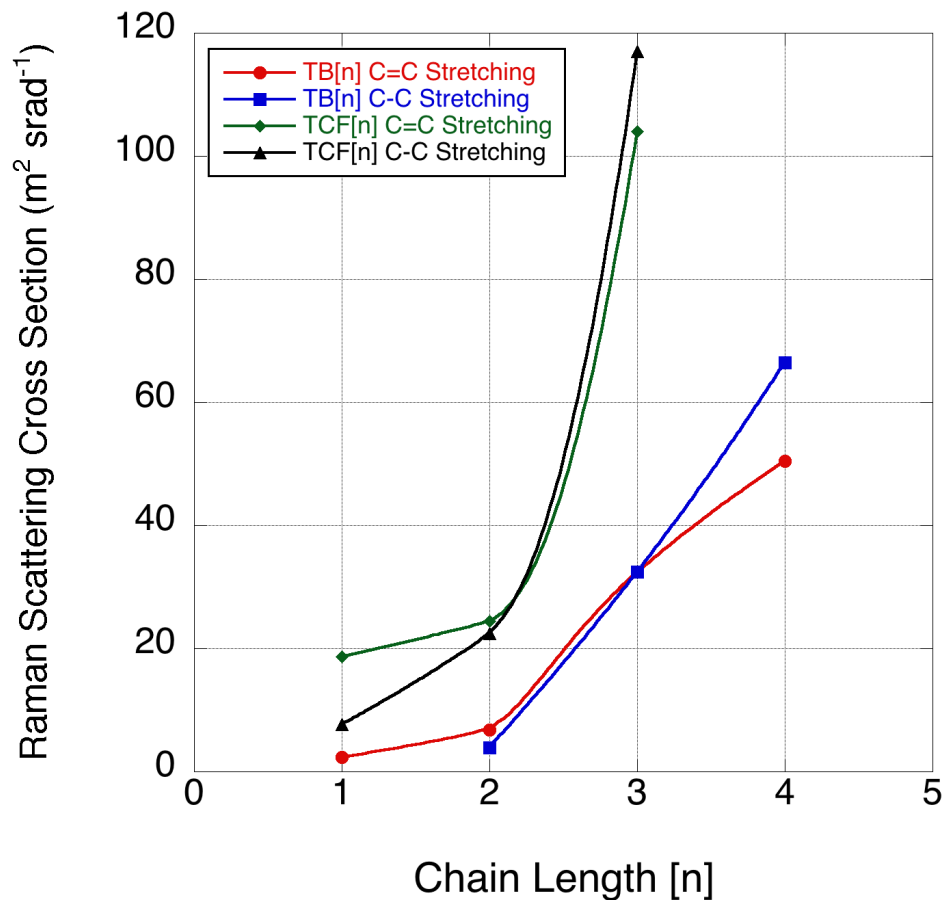
Figure 4.45. Raman Scattering Cross Section dependence on chain length. All Raman spectra used for this figure were recorded in acetonitrile and the RSC measurements are in reference to the 992 cm^{-1} line of benzene.[39] The curve is not a fit of the data, it is merely meant to guide the eye.

4.4.7. Electrochemical Measurements on Select Donor-Acceptor Polyenes

Further evidence for the relative strengths of the π-electron acceptors can be seen through the redox potentials of similarly sized D-A polyenes.[13] In the series of three double bond D-A polyenes shown in Table 4.7, going down the series from DCV[3] to TB[3] to TCF[3], there is a minimal decrease in oxidation potential and a significant increase in reduction potentials (becoming less negative).This is consistent with an increase in acceptor strength along the series, which makes reduction more favorable.

The D-A polyenes show a completely reversible oxidation process and a partially reversible reduction process, as is shown in Figure 4.46, when only swept between 0 V and 1.7 V the oxidation process is reversible, however when swept to -1.9 V the reduction is only partly reversible. The voltammagrams show are both for ID[1] in dry dichloromethane with 0.1 M $^{n}Bu_4NPF_6$ as a support electrolyte, and are representative of the behavior of all of the compounds measured.
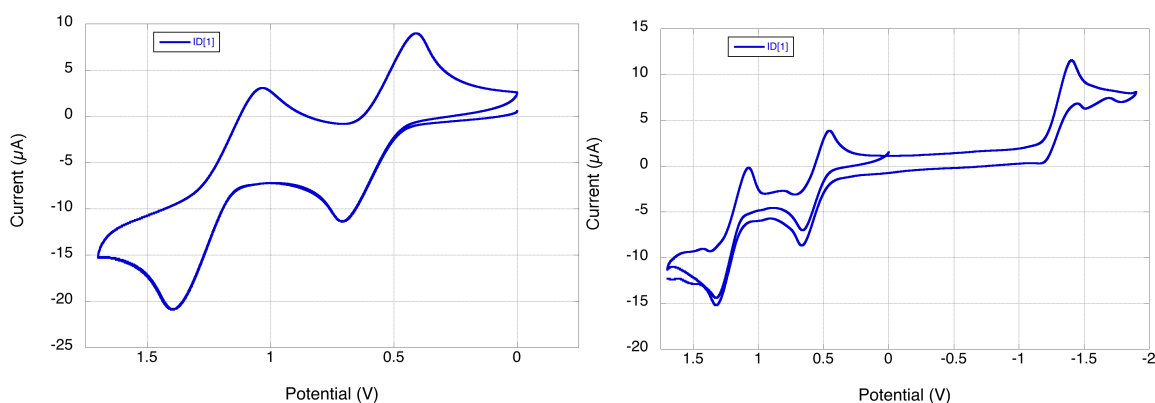
Figure 4.46. Cyclic voltammagrams of ID[1] against $FeCp_2^{+/0}$ (internal reference $E_{1/2}^{+/0} = 0.55$ V vs Ag/AgCl) in dichloromethane with 0.1 M $^{n}Bu_4NPF_6$. Left)The voltage was swept from 0 V to 1.7 V or Right) 0 V to 1.7 V to -1.9 V. CV measurements recorded at 50 mV/s using a BAS Potentiostat using a glassy carbon working electrode, Pt wire aux electrode, and a Ag/AgCl reference electrode.

Table 4.7. Redox potentials of D-A polyenes as determined by CV recorded against $FeCp_2^{+/0}$ (internal reference $E_{1/2}^{+/0} = 0.55$ V vs Ag/AgCl) in dichloromethane with 0.1 M $^{n}Bu_4NPF_6$. CV measurements recorded at 50 mV/s using a BAS Potentiostat using a glassy carbon working electrode, Pt wire aux electrode, and an Ag/AgCl reference electrode.

Dye	$E_{Oxidation}$	$E_{Reduction}$
DCV[3]	0.955	-0.997
TB[3]	0.907	-0.780
TCF[3]	0.852	-0.594

In addition to acceptor strength changes, CV measurements allow for an estimation the energy levels of the highest occupied molecular orbital (HOMO) and the lowest unoccupied molecular orbital (LUMO) and the resulting electronic band gap. This is done by comparing the oxidation and reduction potentials of the compounds of interest to that of the $FeCp_2^{+/0}$ corresponding to -4.4 eV below vacuum level.[42] The band gaps of the D-A polyenes decrease with increasing length in each series.
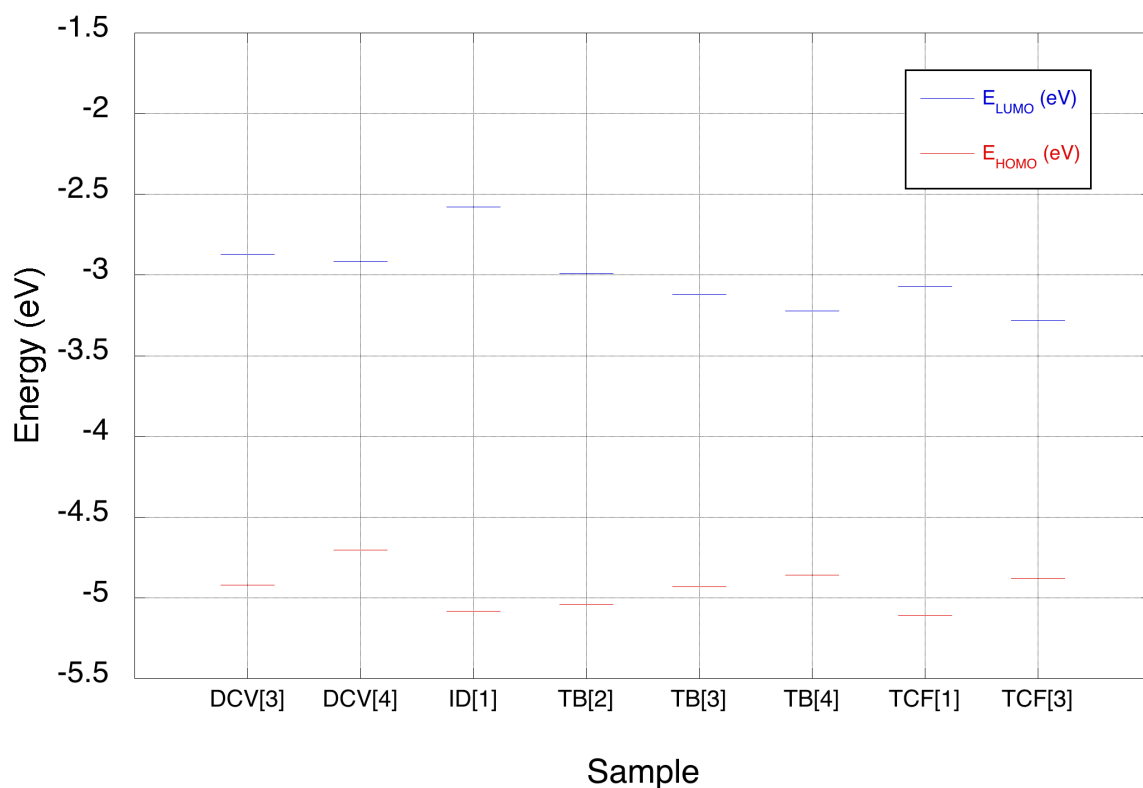
Figure 4.47. HOMO (red bars) and LUMO (blue bars) energy levels of select D-A polyenes

4.4.8. First Hyperpolarizability from Hyper-Rayleigh Scattering in Solution

As is discussed in Chapter 2 (section 2.5.1), hyper-Rayleigh scattering, or HRS, is a useful tool for the direct measurement of first hyperpolarizability, β. It is also very useful because it depends on the instantaneous orientation of molecules and has no requirement for asymmetry. This is particularly well suited to investigating the first hyperpolarizability of cyanines, which should correspond to the lowest SHG signal, but the largest SHG sensitivity ($\Delta I_{SHG}/I_{SHG}$).

While absolute measurements can be taken using an integrating sphere, hyper-Rayleigh scattering measurements are typically taken relative to a sample of known β, typically the solvent used for the measurement.[43] The most commonly referenced solvent β is that of chloroform. Unfortunately, there is considerable disagreement on the actual value of β for chloroform. Throughout this dissertation, the first hyperpolarizability of chloroform at 1064 nm is assumed to be 0.49 x 10^{-30} esu.[44] This value was selected in accordance with comparison of first hyperpolarizabilities of solvents as described by Campo *et at*.[45] Using the undamped two-level model and a simple one term Sellmeier equation for the dispersion of the refractive indices, the first hyperpolarizabilities of the relevant solvents were determined at the experimental wavelengths. It is in reference to these β values that the relative β of the chromophores of interest are measured.

The majority of HRS experiments were conducted at 900 nm. This was due to a few factors, most importantly, the absorption spectrum of relevant media. Water makes up a very large percentage of brain tissue and of neurons, estimated between 68 – 80% by mass. The water has a very small absorption coefficient between 300 – 950 nm, this

transparent region of the electromagnetic spectrum is known as the biological window[46]. The second major consideration is the light source. Our amplified femtosecond system has an average output of 3.7 W at 800 nm. This 800 nm beam is routed into an optical parametric amplifier (TOPAS-C, Light Conversion) which is tunable between 1100 – 2900 nm. Additional regions in the visible and near IR accessible through second harmonic generation (550 – 1120 nm) and sum frequency generation (470 – 630 nm). The power and beam shape of the laser are much better quality below 700 nm, however the chromophores of interest all absorb in the 400 – 800 nm range. Taking the absorption of the chromophores and the biological window into account, 900 nm represents a good compromise as both incident and scattered frequencies are within the biological window, and the TOPAS-C output and beam shape degrade rapidly above 900 nm.

Table 4.8. Solvent dependent hyperpolarizability of D-A polyenes.

Dye	Solvent	$\beta \times 10^{-48}$ $[C\ m^3\ V^{-2}]$	Dye	Solvent	$\beta \times 10^{-48}$ $[C\ m^3\ V^{-2}]$
TB[1]	ACN	3.9	TCF[1]	ACN	6.1
	DMF	2.0		DMF	4.5
TB[2]	ACN	5.8	TCF[2]	ACN	7.8
	DMF	4.5		DMF	11.5
TB[3]	ACN	9.6	TCF[3]	ACN	11.3
	DMF	7.2		DMF	7.2
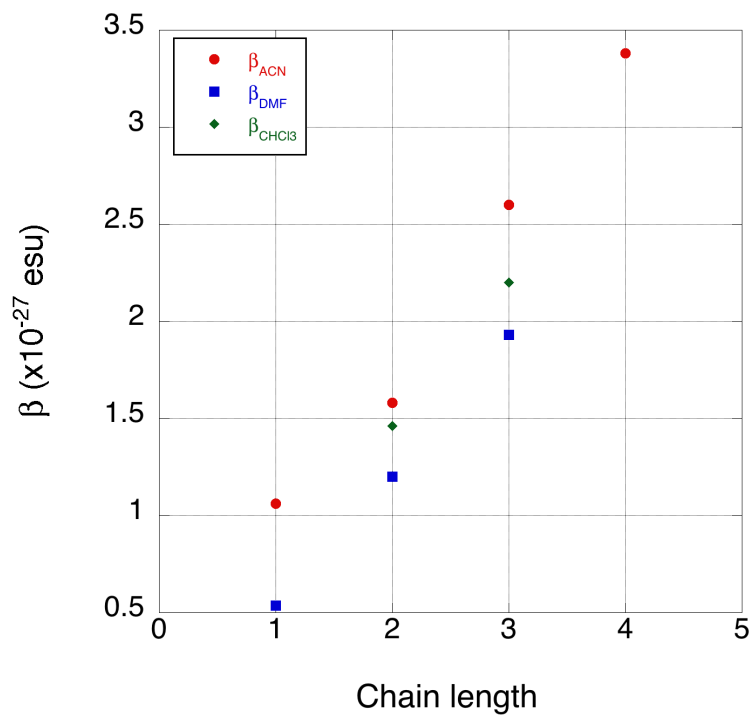
Figure 4.48. Solvent dependent first hyperpolarizabilities of the TB[n] series.
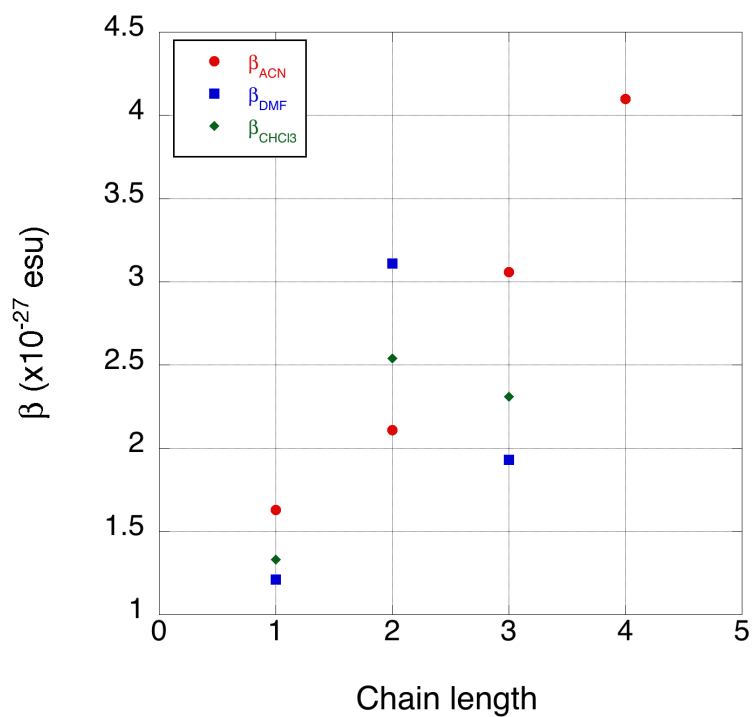
Figure 4.49. Solvent dependent first hyperpolarizabilities of the TCF[n] series.

4.5. Conclusions

In summary, the series of D-A polyenes described above is effective for investigating the effects of acceptor groups on the NLO characteristics of the merocyanine class of molecules. These dyes have such a broad applicability to the numerous projects in our group that at one point every active project in our group except for the high energy density nanocomposites project was using some or all of the D-A polyene series. The spectroscopic and electrochemical measurements suggest that the acceptor strengths of the series are as follows

$$DCV < ID < TB < TCF$$

Though TCF is the stronger acceptor in all of our measurements than the TB derivatives, this impact decreases with increasing length. Also, of note that for practical device applications, where solubility is a factor, the TCF chromophores will have issues. The range of solvents in which our TCF chromophores (longer than TCF[1]) are substantially soluble is incredibly limited, primarily chloroform, bromoform, and dichloromethane. TB[n] series, on the other hand, is quite soluble in a vast array of solvents including very non-polar solvents such as benzene and carbon tetrachloride and very polar aprotic solvents such as acetonitrile and DMSO. For device applications, the TB[n] chromophores would be much more suitable as they can be dispersed in reasonable concentrations. In fact, TB[2] and TB[3] can be prepared in 50% and 75% by weight blends with amorphous polycarbonate, and show surprising stability.

Future studies on TCF-type chromophores should probe the donor group structure to increase solubility. We have looked at dibutylaminophenyl, trimethylindole, and

julolidine derivatives of TCF[1] (results not shown) which show promise in terms of solubility, but have yet to be investigated for their NLO properties.

Moving forward, the primary foresight in the field of nonlinear optics appears to be headed towards the applications of these phenomenon for biological/medical purposes. Using the results presented here, the next step would be to focus on compatibility with host polymers for devices or compatibility with biological systems for microscopy.

4.6. Experimental Methods

4.6.1. Synthesis

General

All materials and reagents were commercially available and used as received except where noted. Tetrahydrofuran was dried using a sodium-benzophenone ketyl pot and freshly distilled for each use. ((1,3-dioxolan-2-yl)methyl)triphenyl phosphonium bromide (*4.1*), while commercially available, was synthesized as described below because it resulted in higher yields. ^{1}H, ^{13}C, and ^{31}P NMR spectra were acquired on one of the following NMR spectrometers: Bruker Avance IIIHD-300 MHz Bruker Avance III-400 MHz, Bruker Avance IIIHD-500 MHz (with Prodigy cryoprobe), Bruker Avance IIIHD-700 MHz, Bruker Avance IIIHD-800 MHz spectrometers. Each NMR will list the field strength used. All chemical shifts are indirectly referenced TMS through the residual solvent peaks as reported in the literature.[36, 47] NMR spectra in CCl_4 are referenced to an insert containing D_2O.

((1,3-dioxylany-2-yl)triphenylphosphonium bromide (*4.1*, Scheme 4.1)

Triphenylphosphine (63.0 g, 240 mmol) and 2-bromomethyl-1,3-dioxolane (40 g, 240 mmol) were heated to 100˚C with stirring overnight. The resulting solid mass was cooled and dissolved in dichloromethane and crashed out by dropping into vigorously stirred diethyl ether. The fine crystalline product is collected by filtration, washed with diethyl ether. After being dried under vacuum (50˚C, 1 torr) overnight, *1* (79 g, 77% yield) was collected as a fine white powder. If resulting product was noticeably brown or orange, it was purified by recrystallization from MeOH or acetonitrile before being dissolved in dichloromethane and crashed out in ether. m.p. 191.2 – 193 ˚C. ^{1}H NMR (500 MHz, CDCl$_3$) δ 7.86 (m, 6H), 7.76 (m, 3H), 7.67 (m, 6H), 5.48 (dt, J = 13.4 Hz, 4.0 Hz, 1H) 4.51 (dd, J = 12.9 Hz, 4.0 Hz, 2H), 3.68 (m, 4H) ppm. ^{13}C NMR (100.58 MHz, CDCl$_3$) δ 134.81, 134.78, 134.17, 134.07, 130.22, 130.09, 119.65, 118.77, 99.31, 99.27, 65.14, 29.86, 28.33. ^{31}P NMR (161.92 MHz, CDCl$_3$, vs H$_3$PO$_4$) δ 20.73 ppm.

General Procedure for polyenal extension (Scheme 4.2)

Polyenals were prepared by stepwise vinylogous extension using Wittig oxyphrenylation and deprotection with acid. Aldehyde (**Al[n]**), ((1,3-dioxolan-2-yl)methyl)triphenyl phosphonium bromide (*4.1)*, and 18-crown-6 were combined in a molar ratio of 1:2:0.02. The resulting mixture was evacuated under high vacuum and backfilled with nitrogen several times before adding dry THF. The mixture was cooled in a salt-ice bath with stirring before NaH (4 equiv.) was added in a single portion. The reaction was removed from cooling and allowed to stir for 2 hours, during which time a noticeable color change occurred. A second portion of NaH (4 equiv.) was added and the reaction was allowed to stir under nitrogen overnight for 16 h. The resulting product mixture was again cooled in

a salt-ice bath and carefully quenched under nitrogen by adding water. The quenched intermediate product mixture was deprotected by adding concentrated HCl (large excess typically 10 equiv) with stirring. After 2 h, the deprotected mixture was again cooled and carefully neutralized with NaOH. The product was extracted with ether and washed with brine before being dried over sodium sulfate and evaporated to dryness. The resulting crude products were purified by recrystallization.

4-(Dimethylamino)cinnamaldehyde (**Al[2]**).

Al[2] prepared according to the general procedure using **Al[1]** (1.01 g, 6.70 mmol), **4.1** (5.76 g, 13.4 mmol), 18-crown-6 (0.04 g, 0.13 mmol), and NaH (0.64 g, 26.8 mmol) in THF (50 mL). **Al[2]** was purified by recrystallization from ethanol to give golden lustrous plates (1.13 g, 96%). Mp 140 – 142 ˚C. ^{1}H NMR (500 MHz, CD_2Cl_2)

5-(4-(Dimethylamino)phenyl)penta-2,4-dienal (**Al[3]**).

Al[3] prepared according to the general procedure using **Al[2]** (4.00 g, 22.8 mmol), **4.1** (19.6 g, 45.7 mmol), 18-crown-6 (0.12 g, 0.46 mmol), and NaH (2.19 g, 91.3 mmol) in THF (250 mL). **Al[3]** was purified by recrystallization from isopropanol to give golden lustrous plates (4.55 g, quantitative yield). Mp 158 – 159 ˚C. ^{1}H NMR (500 MHz, CD_2Cl_2) δ 9.54 (d, J = 8.1 Hz, 1H), 7.40 (d, J = 8.8 Hz, 2H), 7.27 (dd, J = 15.0 Hz, 10.9 Hz, 1H), 6.96 (d, J = 15.4 Hz, 1H), 6.84 (ddd, J = 15.3 Hz, 10.9 Hz, 0.6 Hz, 1H), 6.68 (d, J = 8.9 Hz, 2H), 6.14 (dd, J = 15.0 Hz, 8.1 Hz, 1H), 3.01 (s, 6H) ppm.

7-(4-(dimethylamino)phenyl)hepta-2,4,6-trienal (**Al[4]**).

Al[4] prepared according to the general procedure using **Al[3]** (3.50 g, 17.4 mmol), **4.1** (14.9 g, 34.8 mmol), 18-crown-6 (0.09 g, 0.35 mmol), and NaH (1.67 g, 69.6 mmol) in THF (200 mL). **Al[4]** was purified by recrystallization from ligroin (bp. 90-120 ˚C) to give an intense red crystalline powder (2.69 g, 68%). Mp 185.5 – 187 ˚C. ^{1}H NMR (700 MHz, CD$_2$Cl$_2$) δ 9.50 (d, J = 8.0 Hz, 1H), 7.35 (d, J = 8.9 Hz, 2H), 7.20 (dd, J = 15.1, 11.27 Hz, 1H), 6.86 (AB**M**, J_{MX} = 14.5 Hz, J_{AM} = 0.2 Hz, J_{BM} = 10.5 Hz, 1H), 6.76 (ABq, **A**BMX, $\Delta\delta_{AB}$ = 0 Hz, J_{AB} = 15.3 Hz, J_{AM} = 0.2 Hz, 1H), 6.75 (ABq, A**B**MX, $\Delta\delta_{AB}$ = 0.02 Hz, J_{AB} = 15.3 Hz, J_{BM} = 10.5 Hz, 1H), 6.67 (d, J = 8.9 Hz, 2H), 6.49 (dd, ABM**X**, J = 14.5, 11.4 Hz, 1H), 6.10 (dd, J = 15.1, 8.0 Hz, 1H), 2.99 (s, 6H) ppm.

9-(4-(dimethylamino)phenyl)nona-2,4,6,8-tetraenal (**Al[5]**).

Al[5] prepared according to the general procedure using **Al[4]** (0.76 g, 3.34 mmol), **4.1** (2.83 g, 6.60 mmol), 18-crown-6 (0.02 g, 0.07 mmol), and NaH (0.32 g, 13.2 mmol) in THF (50 mL). **Al[5]** was purified by recrystallization from ligroin (bp. 90 – 120 ˚C) to give deep red crystalline powder (0.76 g, 91%). ^{1}H NMR (500 MHz, CD$_2$Cl$_2$) δ 9.58 (d, J = 8.0 Hz, 1 H), 7.37 (d, J = 8.9 Hz, 2H), 7.22 (dd, J = 15.0, 11.3 Hz, 1H), 6.84 (dd, J = 14.6, 11.2 Hz, 1H), 6.08 – 6.67 (m, 5H), 6.51 (dd, J = 14.6, 11.3 Hz, 1H), 6.44 (dd, J = 14.1, 11.3 Hz, 1H), 6.14 (dd, J = 15.1, 8.0 Hz, 1H).

2-Dicyanomethylene-3-cyano-4,5,5-trimethyl-2,5-dihydrofuran (**TCF**, Scheme 4.3).

A freshly prepared solution of NaOEt in ethanol (0.51 g Na (22.2 mmol) in 20 mL absolute ethanol) was slowly added with stirring to a solution of 3-hydroxy-3-methyl-2-butanone (14.4 g, 141 mmol) and malononitrile (19.1 g, 289 mmol) in 45 ml of absolute

ethanol under inert atmosphere. The reaction was stirred overnight a room temperature. The resulting solid was collected by filtration and twice recrystallized from ethanol to give 18.55 g (66% yield) of light yellow crystals. m.p. 198-200°C ^{1}H NMR (400 MHz, CDCl$_3$) δ 2.36 (s, 3H), 1.63 (s, 6H) ppm. ^{13}C NMR (100.58 MHz, CDCl$_3$) δ 182.24, 175.04, 110.93, 110.27, 108.88, 104.87, 99.61, 24.38, 14.12 ppm.

General Procedure for the synthesis of malononitrile derivatives (**DCV[n]**, Scheme 4.4)

To an equimolar solution of aromatic aldehyde **Al[n]** and malononitrile in ethanol was added a catalytic amount of piperidine (typically around 0.25 molar equiv.), and the reaction was allowed to stir at room temperature until completion (as monitored by TLC typically using 3:1 ethyl acetate / hexane). Once completed, water was added to the resulting product mixture to increase precipitation. The crude product was filtered, washed with cold ethanol and purified by recrystallization.

2-(4-(dimethylamino)benzylidene) malononitrile (**DCV[1]**)

DCV[1] was prepared according to the DCV[n] general procedure using **Al[1]** (1.00 g, 6.70 mmol), malononitrile (0.44 g, 6.70 mmol), and piperidine (0.20 mL, 1.68 mmol) in absolute ethanol (25 mL). Crude **DCV[1]** was filtered and washed with cold ethanol then purified by recrystallization from ethanol and washed with hexane to give shiny orange/pink crystals (1.35 g, 90 %). Mp 182 – 184 °C. ^{1}H NMR (400 MHz, CD$_2$Cl$_2$) δ 7.81 (d, J = 9.2 Hz, 2H), 7.49 (s, 1H), 6.71 (d, J = 9.2 Hz, 2H), 3.14 (s, 6H). ^{13}C NMR (100.62 MHz, CD$_2$Cl$_2$) δ 158.07, 154.35, 133.65, 119.15, 116.04, 115.02, 111.53, 39.88 ppm.

(*E*)-2-(3-(4-(dimethylamino)phenyl)allylidene)malononitrile (**DCV[2]**)

DCV[2] was prepared according to the DCV[n] general procedure using **Al[2]** (1.00 g,

5.71 mmol), malononitrile (0.38 g, 5.71 mmol), and piperidine (0.20 mL, 1.68 mmol) in

absolute ethanol (35 mL). Crude **DCV[2]** was filtered and washed with cold ethanol then

purified by recrystallization from ethanol and washed with hexane to give shiny

red/yellow crystals. Recrystallization from ethyl acetate and hexane gave shiny yellow

and black crystals (1.16 g, 91%). Mp 150 – 152 ˚C. ^{1}H NMR (500 MHz, CD$_2$Cl$_2$) δ 7.53

(d, *J* = 11.8 Hz, 1H), 7.51 (d, *J* = 9.4 Hz, 2H), 7.21 (d, *J* = 14.8 Hz, 1H), 7.03 (dd, *J* =

14.8, 11.8 Hz, 1H), 6.70 (d, *J* = 9.4 Hz, 2H), 3.08 (s, 6H) ppm. ^{13}C NMR (100.62 MHz,

CD$_2$Cl$_2$) δ 160.56, 153.17, 151.54, 131.50, 121.77, 117.12, 115.10, 113.13, 111.87, 39.87

ppm.

2-((2*E*,4*E*)-5-(4-(dimethylamino)phenyl)penta-2,4-dien-1-ylidene)malononitrile

(**DCV[3]**)

DCV[3] was prepared according to the DCV[n] general procedure using **Al[3]** (0.11 g,

0.55 mmol), malononitrile (0.04 g, 0.55 mmol), and piperidine (0.10 mL, 0.84 mmol) in

absolute ethanol (10 mL). Crude **DCV[3]** was filtered and washed with cold ethanol then

purified by recrystallization from ethanol and washed with hexane to give shiny dark

purple crystals (0.11 g, 80%). ^{1}H NMR (400 MHz, CD$_2$Cl$_2$) δ 7.46 (dd, *J* = 12.0, 0.5 Hz,

1H), 7.41 (d, *J* = 8.8 Hz, 2H), 7.10 (dd, *J* = 14.2, 11.2 Hz, 1H), 7.00 (d, *J* = 15.2 Hz, 1H),

6.83 (dd, *J* = 15.1, 11.2 Hz, 1H), 6.69 (dd, *J* = 14.1, 12.0 Hz, 1H), 6.69 (d, *J* = 9.0 Hz,

2H), 3.04 (s, 6H) ppm. ^{13}C NMR (100.62 MHz, CD$_2$Cl$_2$) 160.1, 152.6, 152.5, 146.7, 130.3, 123.8, 123.6, 122.4, 115.3, 113.2, 112.3, 77.8, 40.3 ppm.

2-((2E,4E,6E)-7-(4-(dimethylamino)phenyl)hepta-2,4,6-trien-1-ylidene)malononitrile (DCV[4])

DCV[4] was prepared according to the DCV[n] general procedure using **Al[4]** (0.25 g, 1.1 mmol), malononitrile (0.22 g, 1.1 mmol), and piperidine (0.10 mL, 0.84 mmol) in absolute ethanol (10 mL). Crude **DCV[4]** was filtered and washed with cold ethanol then purified by recrystallization from ethanol and washed with hexane to give shiny dark purple/black crystals (0.25 g, 83%). ^{1}H NMR (500 MHz, CD$_2$Cl$_2$) δ 7.46 (d, J = 11.9 Hz, 1H), 7.38 (d, J = 8.9 Hz, 2H), 7.04 (dd, J = 14.3, 11.6 Hz, 1H), 6.91 (ddd, AB**M**X, J_{MX} = 14.2 Hz, J_{AM} = 1.8 Hz, J_{BM} = 12.3 Hz, 1H), 6.82(ABq, A**B**MX, $\Delta\delta_{AB}$ = 0 Hz, J_{AB} = 15.1 Hz, J_{AM} = 1.8 Hz, 1H), 6.81 (ABq, **A**BMX, $\Delta\delta_{AB}$ = 0.03 Hz, J_{AB} = 15.3 Hz, J_{BM} = 12.3 Hz, 1H), 6.68 (d, J = 8.9 Hz, 2H), 6.48 (dd, J = 14.2, 11.7 Hz, 1H), 3.02 (s, 6H) ppm.

General Procedure for the synthesis of 1,3-indanedione derivatives (ID[n], Scheme 4.4)

Equimolar amounts of aromatic aldehyde (**Al[n]**) and 1,3-indanedione were dissolved in ethanol with stirring and gentle heating. To this solution, was added a catalytic amount of piperidine (typically around 0.25 molar equiv) causing an immediate color change. The reaction mixture was brought to reflux and allowed to stir for about 1 h or until completion (as monitored by TLC typically using 3:1 ethyl acetate / hexane). Once completed, the product mixture was allowed to cool, resulting in precipitation. The crude product was filtered, washed with cold ethanol and purified by recrystallization. An

additional crop of product can be recovered by adding water to the filtrate. The resulting

purified product was dried under vacuum.

 2-(4-(dimethylamino)benzylidene)-indane-1,3-dione (**ID[1]**)

Al[1] (2.00 g, 13.4 mmol) and 1,3-indanedione (2.01 g, 13.4 mmol) were suspended in

100 mL of absolute ethanol. The mixture was gently heated until dissolved. After about

10 minutes of stirring after the dissolution was complete, a red crystalline precipitate

began forming on the walls of the flask. No piperidine was necessary for this reaction.

The reaction mixture was vigorously stirred overnight, and the resulting product was

collected by filtration then washed with cold ethanol and hexanes to give shiny dark red

crystals (3.65 g, 98 %). Other attempts using the ID[n] general procedure were successful

and in good yields, but required recrystallization. Fortunately **ID[1]** can be purified by

recrystallization using a myriad solvent systems (acetone, ethanol, ethyl acetate / hexane,

dichloromethane / hexane, and toluene to name a few) many of which afford single

crystals. Mp 204 – 205 ˚C. ^{1}H NMR (400 MHz, CD_2Cl_2) δ 8.52 (d, J = 9.16 Hz, 2H),

7.91 – 9.73 (m, 4H), 7.71 (s, 1H), 6.77 (d, J = 9.16 HZ, 2H), 3.14 (s, 6H) ppm. ^{13}C NMR

(100 MHz, CD_2Cl_2) δ 191.6, 190.1, 154.5, 147.3, 142.7, 140.3, 138.2, 134.8, 134.5,

123.3, 122.7, 122.6, 122.2, 111.7, 40.3 ppm

(*E*)-2-(3-(4-(dimethylamino)phenyl)allylidene)-indane-1,3-dione (**ID[2]**)

ID[2] was prepared according to the ID[n] general procedure using **Al[2]** (1.00 g, 5.71

mmol), 1,3-indanedione (0.85 g, 5.7 mmol), and piperidine (0.15 mL, 1.4 mmol) in

ethanol (50 mL). Crude **ID[2]** was collected by filtration and washed with cold ethanol

before being recrystallized from ethanol to give incredibly shiny and thin purple actinic

crystals (1.55 g, 90%) which were washed with hexane and dried under vacuum. Mp 252 – 254 °C. ^{1}H NMR (400 MHz, CD$_2$Cl$_2$) δ 8.25 (dd, J = 15.0, 12.2 Hz, 1H), 7.90 – 7.86 (m, 2H), 7.76 – 7.73 (m, 2H), 7.60 (d, J = 12.2 Hz, 1H), 7.60 (d, J = 9.0 Hz, 2H), 7.34 (d, J = 15.0 Hz, 1H), 6.72 (d, J = 9.0 Hz, 2H), 3.08 (s, 6H) ppm.

(2*E*,4*E*)-5-(4-(dimethylamino)phenyl)penta-2,4-dien-1-ylidene)-indane-1,3-dione (**ID[3]**)

ID[3] was prepared according to the ID[n] general procedure using **Al[3]** (0.50 g, 2.5 mmol), 1,3-indanedione (0.36 g, 2.5 mmol), and piperidine (60 µL, 0.62 mmol) in EtOH (15 mL). Crude **ID[3]** was collected by filtration, washed with cold ethanol and recrystallized from DCM/ethanol to give a greenish-grey crystalline powder (0.71 g. 87%)

General Procedure for the synthesis of 1,3-diethyl-2-thiobarbituric acid derivatives (**TB[n], Scheme 4.4**)

Equimolar amounts of aromatic aldehyde **Al[n]** and 1,3-diethyl-2-thiobarbituric acid were separately dissolved in absolute ethanol with heating. Once dissolution was complete, the thiobarbituric acid solution was carefully transferred to the aldehyde solution in small portions by syringe, taking care not to allow the thiobarbituric acid to crystallize. The addition of the thiobarbituric acid solution causes and immediate color change and shortly thereafter (usually before addition is complete) crystalline precipitate began forming on the walls of the flask. Once the addition was complete, the reaction mixture was diluted with ethanol for ease of stirring (if necessary). The reaction mixture was stirred with gentle heat for 1 h or until completion (as monitored by TLC typically

using 3:1 ethyl acetate / hexane) before cooling to room temperature. The resulting

crystalline precipitate was collected by filtration, washed with cold ethanol and

recrystallized. The resulting purified products were dried under vacuum.

1,3-diethyl-5-[4-(dimethylamino)benzylidene]-2-thiobarbituric acid (**TB[1]**)

TB[1] was prepared according to the TB[n] general procedure using **Al[1]** (1.02 g, 6.84

mmol) and 1,3-diethylthiobarbituric acid (1.37 g, 6.84 mmol) dissolved separately in

ethanol (20 mL each) before being combined, causing a color change to bright red. Crude

TB[1] was allowed to cool and collected by vacuum filtration, washed with cold ethanol

and recrystallized from ethanol to give shiny red crystalline powder (2.11 g, 93%). Mp

217 – 218 ˚C. ^{1}H NMR (500 MHz, CD$_2$Cl$_2$) δ 8.44 (d, J = 9.2 Hz, 2H), 8.38 (s, 1H), 6.74

(d, J = 9.2 Hz, 2H), 4.57 (q, J = 7.0 Hz, 2H) 4.54 (q, J = 7.0 Hz, 2H), 3.17 (s, 6H), 1.29

(t, J = 7.0 Hz, 3H), 1.27 (t, J = 7.0 Hz, 3H) ppm. ^{13}C NMR (100 MHz, CD$_2$Cl$_2$) δ 179.4,

162.4, 159.8, 159.6, 155.3, 140.2, 121.8, 111.5, 110.7, 44.2, 43.6, 40.4, 12.7, 12.6 ppm.

(E)-1,3-diethyl-5-(3-[4-(dimethylamino)phenyl]allylidene)-2-thiobarbituric acid (**TB[2]**)

TB[2] was prepared according to the TB[n] general procedure using **Al[2]** (1.00 g, 5.71

mmol) and 1,3-diethylthiobarbituric acid (1.15 g, 5.71 mmol) separately dissolved with

gentile heating in about ethanol (about 15 mL each) before being combined, resulting in

a dramatic color change to pink/purple. Crude **TB[2]** was allowed to cool and collected

by filtration, washed with cold ethanol, and recrystallized from dichloromethane / ethanol

to give silver and purple crystalline powder (1.80 g, 88%). Mp 227.4 (decomposition). ^{1}H

NMR (500 MHz, CD$_2$Cl$_2$) δ 8.45 (dd, J = 14.8, 12.5 Hz, 1H), 8.18 (d, J = 12.5 Hz, 1H)

7.63 (d, $J = 9.1$ Hz, 2H), 7.49 (d, $J = 14.8$ Hz, 1H), 6.72 (d, $J = 9.1$ Hz, 2H), 4.54 (q, $J = 7.0$ Hz, 2H), 4.52 (q, $J = 7.0$ Hz, 2H), 3.11 (s, 6H), 1.28 (t, $J = 7.0$ Hz, 3H), 1.26 (t, $J = 7.0$ Hz, 3H). ^{13}C NMR (100 MHz, CD$_2$Cl$_2$) δ 179.5, 161.4, 160.5, 159.6, 158.5, 154.0, 132.9, 123.8, 121.2, 112.4, 111.2, 43.8, 43.2, 40.4, 12.7, 12.6 ppm.

(*2E, 4E*)-1,3-diethyl-5-(5-[4-(dimethylamino)phenyl]penta-2,4-dienylidene)-2-thiobarbituric acid (**TB[3]**)

TB[3] was prepared according to the TB[n] general procedure using **Al[3]** (0.50 g, 2.5 mmol) and 1,3-diethylthiobarbituric acid (0.51 g, 2.55 mmol) separately dissolved in ethanol (20 mL each) before being combined. The reaction immediately changed to a dark green color that faded to dark blue as the aldehyde was consumed. The product mixture was allowed to cool and crude **TB[3]** was collected by filtration, washed with cold ethanol and recrystallized from dichloromethane and ethanol to give a dark green fibrous powder (0.84 g, 88%). Mp 229 ˚C (decomposition). ^{1}H NMR (500 MHz, CD$_2$Cl$_2$) δ 8.10 (d, $J = 12.6$ Hz, 1H), 8.03 (dd, $J = 13.7, 12.6$ Hz, 1H), 7.46 (d, $J = 9.0$ Hz, 2H), 7.38 (dd, $J = 13.7, 11.0$ Hz, 1H), 7.10 (d, $J = 15.1$ Hz, 1H), 7.02 (dd, $J = 15.1, 11.0$ Hz, 1H), 6.70 (d, $J = 9.0$ Hz, 2H), 4.52 (q, $J = 6.8$ Hz, 2H), 4.51 (q, $J = 6.8$ Hz, 2H), 3.06 (s, 6H), 1.27 (t, $J = 7.01$ Hz, 3H), 1.25 (t, $J = 7.01$ Hz, 3H) ppm. ^{13}C NMR (100 MHz, CD$_2$Cl$_2$) δ 179.5, 161.3, 160.3, 158.8, 158.4, 152.6, 147.5, 130.7, 127.5, 124.2, 124.1, 130.7, 127.5, 124.2, 124.1, 112.4, 112.1, 43.8, 43.3, 40.3, 12.6, 12.5 ppm.

<u>(*2E, 4E, 6E*)-1,3-diethyl-5-(7-[4-(dimethylamino)phenyl]hepta-2,4,6-trienylidene)-2-thiobarbituric acid (**TB[4]**)</u>

TB[4] was prepared according to the TB[n] general procedure using **Al[4]** (0.50 g, 2.2 mmol) and 1,3-diethylthiobarbituric acid (0.44 g, 2.2 mmol) separately dissolved in ethanol (15 mL each) before being combined. The reaction immediately changed to a dark green color that faded to dark blue as the aldehyde was consumed. The product mixture was allowed to cool and crude **TB[4]** was collected by filtration, washed with cold ethanol and recrystallized from dichloromethane and ethanol to give shiny green fibrous powder (0.77 g, 91%). A slower crystallization gave incredibly thin lusterous green actinic crystals, which appeared almost metallic. Mp 205 ˚C (decomposition). ^{1}H NMR (500 MHz, CD_2Cl_2) δ 8.07 (d, J = 12.6 Hz, 1H), 7.99 (dd, J = 14.1, 12.6 Hz, 1H), 7.39 (d, J = 8.9 Hz, 2H), 7.29 (dd, J = 14.1, 11.7 Hz, 1H), 6.99 (apparent dd, AB**M**X J_{MX} = 14.2 Hz, J_{AM} = 3.4 Hz, J_{BM} = 13.4 Hz, 1H), 6.91 (A**B**M, $\Delta\delta_{AB}$ = 0, J_{AB} = 15.0 Hz, J_{AM} = 3.4 Hz, 1H), 6.90 (A**B**M, $\Delta\delta_{AB}$ = 0.03, J_{AB} = 15.0 Hz, J_{BM} = 13.4 Hz, 1H), 6.74 (d, J = 8.9 Hz, 2H), 4.57 (q, J = 6.8 Hz, 2H), 4.53 (q, J = 6.8 Hz, 2H), 3.12 (s, 6H), 1.31 (t, J = 6.8 Hz, 3H), 1.30 (t, J = 6.8 Hz, 3H) ppm.

<u>(*2E, 4E, 6E, 8E*)-1,3-diethyl-5-(9-[4-(dimethylamino)phenyl]nonaa-2,4,6,8-tetraenylidene)-2-thiobarbituric acid (**TB[5]**)</u>

TB[5] was prepared according to the TB[n] general procedure using **Al[5]** (0.25 g, 0.99 mmol) and 1,3-diethylthiobarbituric acid (0.20 g, 1.0 mmol) separately dissolved in ethanol (10 mL each) before being combined. The reaction immediately changed to a dark blue color that faded to nearly to black as the aldehyde was consumed. The product

mixture was allowed to cool and crude **TB[5]** was collected by filtration, washed with cold ethanol and recrystallized from dichloromethane and ethanol to give shiny olive green fibrous powder (0.37 g, 87%). ^{1}H NMR (800 MHz, CD$_2$Cl$_2$) δ 8.06 (d, J = 12.6 Hz, 1H), 8.00 (dd, J = 13.9, 12.6 Hz, 1H), 7.35 (d, J = 8.9 Hz, 2H), 7.26 (dd, J = 13.9, 11.6 Hz, 1H), 6.91 (dd, J = 14.4, 11.5 Hz, 1H), 6.81 – 6.74 (m, 2H), 6.73 (d, J = 14.3 Hz, 1H), 6.67 (d, J = 8.9 Hz, 2H), 6.61 (dd, J = 14.4, 11.6 Hz, 1H), 6.51 – 6.46 (m, 1H), 4.51 (q, J = 6.9 Hz, 2H), 4.50 (q, J = 6.9 Hz, 2H), 3.00 (s, 6H), 1.26 (t, J = 6.9 Hz, 3H), 1.25 (t, J = 6.9 Hz, 3H) ppm. ^{13}C NMR (201 MHz, CD$_2$Cl$_2$) δ 179.5, 161.1, 160.1, 157.7, 156.8, 151.4, 146.8, 143.0, 139.1, 131.5, 130.6, 129.2, 128.9, 125.1, 124.6, 113.3, 112.5, 43.9, 43.3, 40.4, 12.6, 12.5 ppm.

General Procedure for the synthesis of 5,5-dimethyl-tricyanofuran derivatives (**TCF[n]**, **Scheme 4.4**)

Aromatic aldehyde **Al[n]** and **TCF** (1.1 equiv.) were dissolved in dry dichloromethane with stirring. Piperidinium acetate (1.1 equiv.), made by combining equimolar amounts of piperidine and acetic acid in cold diethyl ether and dried under vacuum, was dissolved in a minimal amount of dichloromethane and added to the reaction mixture, causing an immediate color change. The reaction was allowed to stir for about 3 h or until completion (as monitored by TLC typically using 3:1 EtOAc / hexane or 20:1 chloroform / EtOAc) before cooling in an ice bath. The resulting precipitate was collected by filtration and washed extensively with ethanol. A Michael addition side product is possible (especially when using ethanol as the solvent instead of DCM) this Michael addition product can be removed by refluxing isolated **TCF[n]** in ethanol for about an

hour and cooling to room temperature. The product was again collected and checked for purity. The ethanol reflux was repeated if necessary. The crude **TCF[n]** was purified by recrystallization from DCM/ethanol or acetonitrile, collected by filtration and dried under vacuum.

(E)-[4-(dimethylamino)styryl]-5,5-dimethyl-tricyanofuran (**TCF[1]**)

TCF[1] was prepared according to the TCF[n] general procedure using, **Al[1]** (1.00 g, 6.70 mmol), TCF (1.47 g, 7.37 mmol) and piperidinium acetate (1.05 g, 7.35 mmol) in dichloromethane (about 80 mL). Upon the addition of piperidinium acetate, the reaction quickly changed colors to a fluorescent pink. After completion, the product mixture was cooled on an ice bath and ethanol was added to decrease solubility of the product. The resulting precipitate was collected, redissolved in ethanol, refluxed for about one hour and then again cooled and collected. The partially purified product was recrystallized from DCM/EtOH to give a metallic silver and purple crystalline powder (2.04 g, 92%). Mp. >260 ˚C (did not melt). ^{1}H NMR (400 MHz, CD$_2$Cl$_2$) δ 7.65 (d, J = 15.9 Hz, 1H), 7.59 (d, J = 9.1 Hz, 2H), 6.78 (d, J = 15.9 Hz, 1H), 6.74 (d, J = 9.1 Hz, 2H), 3.13 (s, 6H), 1.75 (s, 6H) ppm.

(1E,3E)-(4-[4-(dimethylamino)phenyl]buta-1,3-dienyl-5,5-dimethyl-tricyanofuran (**TCF[2]**)

TCF[2] was prepared according to the TCF[n] general procedure using, **Al[2]** (0.50 g, 2.9 mmol), TCF (0.63 g, 3.1 mmol) and piperidinium acetate (0.46 g, 3.1 mmol) in dichloromethane (about 40 mL). Upon the addition of piperidinium acetate, the reaction

quickly changed colors to a dark blue. After completion, the product mixture was cooled

on an ice bath and ethanol was added to decrease solubility of the product. The resulting

precipitate was collected, redissolved in ethanol, refluxed for about one hour and then

again cooled and collected. The partially purified product was recrystallized from

acetonitrile to give a metallic silver and blue crystalline powder (0.89 g, 86 %). Mp. >260

˚C (did not melt). ^{1}H NMR (700 MHz, CD$_2$Cl$_2$) δ 7.61 (dd, J = 15.2, 11.2 Hz, 1H), 7.47

(d, J = 9.0 Hz, 2H), 7.17 (d, J = 14.9 Hz, 1H), 6.91 (dd, J = 14.9, 11.2 Hz, 1H), 6.71 (d, J

= 9.0 Hz, 2H), 6.42 (d, J = 15.2 Hz, 1H), 3.08 (s, 6H), 1.71 (s, 6H) ppm.

(1E,3E, 5E)-(6-[4-(dimethylamino)phenyl]hexa-1,3,5-trienyl-5,5-dimethyl-tricyanofuran

(TCF[3])

TCF[3] was prepared according to the TCF[n] general procedure using, **Al[3]** (0.50 g,

2.5 mmol), TCF (0.54 g, 2.7 mmol) and piperidinium acetate (0.36 g, 2.5 mmol) in

dichloromethane (about 30 mL). Upon the addition of piperidinium acetate, the reaction

quickly changed colors to a dark blue. After completion, the product mixture was cooled

on an ice bath and ethanol was added to decrease solubility of the product. The resulting

precipitate was collected, redissolved in ethanol, refluxed for about one hour and then

again cooled and collected. The partially purified product was recrystallized from

acetonitrile to give a metallic bronze and green crystalline powder (0.81 g, 85 %). Mp.

258 ˚C (decomposition). ^{1}H NMR (800 MHz, CD$_2$Cl$_2$) δ 7.51 (dd, J = 15.2, 11.4 Hz, 1H),

7.41 (d, J = 8.9 Hz, 2H), 7.08 (dd, J = 14.2, 11.0 Hz, 1H), 6.93 (d, J = 15.1 Hz, 1H), 6.86

(dd, J = 15.1, 11.0 Hz, 1H), 6.69 (d, J = 8.9 Hz, 2H), 6.54 (dd, J = 14.2, 11.4 Hz, 1H),

6.40 (d, J = 15.2 Hz, 1H), 3.04 (s, 6H), 1.70 (s, 6H) ppm.

(1E,3E, 5E, 7E)-(8-[4-(dimethylamino)phenyl]octa-1,3,5,7-tetraenyl-5,5-dimethyl-tricyanofuran (**TCF[4]**)

TCF[4] was prepared according to the TCF[n] general procedure using, **Al[4]** (0.25 g, 1.1 mmol), TCF (0.24 g, 1.2 mmol) and piperidinium acetate (0.16 g, 1.1 mmol) in dichloromethane (about 20 mL). Upon the addition of piperidinium acetate, the reaction quickly changed colors to a dark blue. After completion, the product mixture was cooled on an ice bath and ethanol was added to decrease solubility of the product. The resulting precipitate was collected, redissolved in ethanol, refluxed for about one hour and then again cooled and collected. The partially purified product was recrystallized from acetonitrile to give a metallic blue and green crystalline powder (0.81 g, 85 %). Mp. 221 ˚C (decomposition). ^{1}H NMR (800 MHz, CD$_2$Cl$_2$) δ 7.48 (dd, J = 15.2, 11.5 Hz, 1H), 7.36 (d, J = 8.9 Hz, 2H), 7.00 (dd, J = 14.1, 11.5 Hz, 1H), 6.85 – 6.77 (m, 3H), 6.68 (d, J = 8.9 Hz, 2H), 6.51 (dd, J = 14.1, 11.5, 1H), 6.49 (d, J = 13.2 Hz, 1H), 6.41 (d, J = 15.2 Hz, 1H), 3.01 (s, 6H), 1.70 (s, 6H) ppm.

(1E,3E, 5E, 7E, 9E)-(10-[4-(dimethylamino)phenyl]deca-1,3,5,7,9-pentaenyl-5,5-dimethyl-tricyanofuran (**TCF[5]**)

TCF[5] was prepared according to the TCF[n] general procedure using, **Al[5]** (0.10 g, 0.40 mmol), TCF (86 MG, 0.43 mmol) and piperidinium acetate (60 mg, 0.40 mmol) in dichloromethane (about 20 mL). Upon the addition of piperidinium acetate, the reaction quickly changed colors to a dark blue. After completion, the product mixture was cooled on an ice bath and ethanol was added to decrease solubility of the product. The resulting

precipitate was collected, redissolved in ethanol, refluxed for about one hour and then again cooled and collected. The partially purified product was recrystallized from acetonitrile to give a dark metallic green and purple crystalline powder. ^{1}H NMR (800 MHz, CD$_2$Cl$_2$) δ 7.47 (dd, J = 15.4, 11.4 Hz, 1H), 7.33 (d, J = 9.0 Hz, 2H), 6.97 (dd, J = 14.3, 11.4 Hz, 1H), 6.79- 6.74 (m, 2H), 6.71 – 6.66 (m, 4H), 6.67 (d, J = 9.0 Hz, 2H), 6.52 (dd, J = 14.3, 11.4 Hz, 1H), 6.47 (dd, J – 14.3, 11.6 Hz, 1H), 6.44 (dd, J = 14.2, 11.4 Hz, 1 H), 6.42 (d, J = 15.3 Hz, 1H) ppm.

4.7. References

[1]   Gorman, C. B.; Marder, S. R., An investigation of the interrelationships between linear and nonlinear polarizabilities and bond-length alternation in conjugated organic molecules. *Proceedings of the National Academy of Sciences* **1993,** *90* (23), 11297.

[2]   Goovaerts, E.; Wenseleers, W. E.; Garcia, M. H.; Cross, G. H., Chapter 3 - Design and characterization of organic and organometallic molecules for second order nonlinear optics A2 - Nalwa, Hari Singh. In *Handbook of Advanced Electronic and Photonic Materials and Devices*, Academic Press: Burlington, 2001; pp 127-191.

[3]   Clays, K. J.; Wostyn, K.; Persoons, A. P. In *Enhancing the accuracy and precision in hyper-Rayleigh scattering: frequency- and angle-resolved femtosecond nonlinear scattering*, International Symposium on Optical Science and Technology, SPIE: 2001; p 12.

[4]   Albota, M.; Beljonne, D.; Brédas, J.-L.; Ehrlich, J. E.; Fu, J.-Y.; Heikal, A. A.; Hess, S. E.; Kogej, T.; Levin, M. D.; Marder, S. R.; McCord-Maughon, D.; Perry, J. W.; Röckel, H.; Rumi, M.; Subramaniam, G.; Webb, W. W.; Wu, X.-L.; Xu, C., Design of Organic Molecules with Large Two-Photon Absorption Cross Sections. *Science* **1998,** *281* (5383), 1653.

[5]   Cho, M., Vibrational Characteristics and Vibrational Contributions to the Nonlinear Optical Properties of a Push−Pull Polyene in Solution. *The Journal of Physical Chemistry A* **1998,** *102* (4), 703-707.

[6]   Marder, S. R.; Perry, J. W.; Tiemann, B. G.; Gorman, C. B.; Gilmour, S.; Biddle, S. L.; Bourhill, G., Direct observation of reduced bond-length alternation in

donor/acceptor polyenes. *Journal of the American Chemical Society* **1993,** *115* (6), 2524-2526.

[7]   Rumi, M.; Ehrlich, J. E.; Heikal, A. A.; Perry, J. W.; Barlow, S.; Hu, Z.; McCord-Maughon, D.; Parker, T. C.; Röckel, H.; Thayumanavan, S.; Marder, S. R.; Beljonne, D.; Brédas, J.-L., Structure−Property Relationships for Two-Photon Absorbing Chromophores: Bis-Donor Diphenylpolyene and Bis(styryl)benzene Derivatives. *Journal of the American Chemical Society* **2000,** *122* (39), 9500-9510.

[8]   Lu, D.; Chen, G.; Perry, J. W.; Goddard, W. A., Valence-Bond Charge-Transfer Model for Nonlinear Optical Properties of Charge-Transfer Organic Molecules. *Journal of the American Chemical Society* **1994,** *116* (23), 10679-10685.

[9]   Brooker, L. G. S.; Keyes, G. H.; Williams, W. W., Color and Constitution. V.1 The Absorption of Unsymmetrical Cyanines. Resonance as a Basis for a Classification of Dyes. *Journal of the American Chemical Society* **1942,** *64* (2), 199-210.

[10]   Baughman, R. H.; Kohler, B. E.; Levy, I. J.; Spangler, C., The crystal structure of trans,trans-1,3,5,7-octatetraene as a model for fully-ordered trans-polyacetylene. *Synthetic Metals* **1985,** *11* (1), 37-52.

[11]   Marder, S. R.; Cheng, L.-T.; Tiemann, B. G.; Friedli, A. C.; Blanchard-Desce, M.; Perry, J. W.; Skindhøj, J., Large First Hyperpolarizabilities in Push-Pull Polyenes by Tuning of the Bond Length Alternation and Aromaticity. *Science* **1994,** *263* (5146), 511.

[12]   Capobianco, A.; Esposito, A.; Caruso, T.; Borbone, F.; Carella, A.; Centore, R.; Peluso, A., Tuning Wavefunction Mixing in Push–Pull Molecules: From Neutral to Zwitterionic Compounds. *European Journal of Organic Chemistry* **2012,** *2012* (15), 2980-2989.

[13]   Blanchard-Desce, M.; Alain, V.; Bedworth, P. V.; Marder, S. R.; Fort, A.; Runser, C.; Barzoukas, M.; Lebus, S.; Wortmann, R., Large Quadratic Hyperpolarizabilities with Donor–Acceptor Polyenes Exhibiting Optimum Bond Length Alternation: Correlation Between Structure and Hyperpolarizability. *Chemistry – A European Journal* **1997,** *3* (7), 1091-1104.

[14]   Bourhill, G.; Bredas, J.-L.; Cheng, L.-T.; Marder, S. R.; Meyers, F.; Perry, J. W.; Tiemann, B. G., Experimental Demonstration of the Dependence of the First Hyperpolarizability of Donor-Acceptor-Substituted Polyenes on the Ground-State Polarization and Bond Length Alternation. *Journal of the American Chemical Society* **1994,** *116* (6), 2619-2620.

[15]   Gieseking, R. L.; Risko, C.; Brédas, J.-L., Distinguishing the Effects of Bond-Length Alternation versus Bond-Order Alternation on the Nonlinear Optical

Properties of π-Conjugated Chromophores. *The Journal of Physical Chemistry Letters* **2015,** *6* (12), 2158-2162.

[16]   Meyers, F.; Marder, S. R.; Pierce, B. M.; Bredas, J. L., Electric Field Modulated Nonlinear Optical Properties of Donor-Acceptor Polyenes: Sum-Over-States Investigation of the Relationship between Molecular Polarizabilities (.alpha., .beta., and .gamma.) and Bond Length Alternation. *Journal of the American Chemical Society* **1994,** *116* (23), 10703-10714.

[17]   Buncel, E.; Rajagopal, S., Solvatochromism and solvent polarity scales. *Accounts of Chemical Research* **1990,** *23* (7), 226-231.

[18]   Reichardt, C., Solvatochromic Dyes as Solvent Polarity Indicators. *Chemical Reviews* **1994,** *94* (8), 2319-2358.

[19]   Kamlet, M. J.; Abboud, J. L.; Taft, R. W., The solvatochromic comparison method. 6. The .pi.* scale of solvent polarities. *Journal of the American Chemical Society* **1977,** *99* (18), 6027-6038.

[20]   Dimroth, K.; Reichardt, C.; Siepmann, T.; Bohlmann, F., Über Pyridinium-N-phenol-betaine und ihre Verwendung zur Charakterisierung der Polarität von Lösungsmitteln. *Justus Liebigs Annalen der Chemie* **1963,** *661* (1), 1-37.

[21]   Schuster, P.; Jakubetz, W.; Marius, W. In *Molecular models for the solvation of small ions and polar molecules*, Topics in Current Chemistry, Berlin, Heidelberg, 1975//; Springer Berlin Heidelberg: Berlin, Heidelberg, 1975; pp 1-107.

[22]   Wang, X.; Dao, R.; Yao, J.; Peng, D.; Li, H., Modification of the Onsager Reaction Field and Its Application on Spectral Parameters. *ChemPhysChem* **2017,** *18* (7), 763-771.

[23]   Onsager, L., Electric Moments of Molecules in Liquids. *Journal of the American Chemical Society* **1936,** *58* (8), 1486-1493.

[24]   Bello, K. A.; Cheng, L.; Griffiths, J., Near-infrared absorbing methine dyes based on dicyanovinyl derivatives of indane-1,3-dione. *Journal of the Chemical Society, Perkin Transactions 2* **1987,** (6), 815-818.

[25]   Friedli, A. C.; Yang, E.; Marder, S. R., A convenient synthetic entry into aldehydes with extended conjugation. *Tetrahedron* **1997,** *53* (8), 2717-2730.

[26]   Plażuk, D.; Janowska, I.; Kłys, A.; Hameed, A.; Zakrzewski, J., A Convenient Synthesis of Conjugated ω-Arylpolyenals via Wittig Reaction with (1,3-Dioxan-2-yl-methyl)triphenylphosphonium Bromide/Sodium Hydride. *Synthetic Communications* **2003,** *33* (3), 381-385.

[27]   Gieseking, R. L.; Ravva, M. K.; Coropceanu, V.; Brédas, J.-L., Benchmarking Density Functional Theory Approaches for the Description of Symmetry

Breaking in Long Polymethine Dyes. *The Journal of Physical Chemistry C* **2016,** *120* (18), 9975-9984.

[28]   Antipin, M. Y.; Timofeeva, T. V.; Clark, R. D.; Nesterov, V. N.; Sanghadasa, M.; Barr, T. A.; Penn, B.; Romero, L.; Romero, M., Molecular Crystal Structures and Nonlinear Optical Properties in the Series of Dicyanovinylbenzene and Its Derivatives. *The Journal of Physical Chemistry A* **1998,** *102* (37), 7222-7232.

[29]   Timofeeva, T. V.; N. Nesterov, V.; Dolgushin, F. M.; Zubavichus, Y. V.; T. Goldshtein, J.; Sammeth, D. M.; Clark, R. D.; Penn, B.; Antipin, M. Y., One-pot polymorphism of nonlinear optical materials. First example of organic polytypes. *Crystal Engineering* **2000,** *3* (4), 263-288.

[30]   Chafin, A. P.; Lindsay, G. A., A Pattern for Increasing the First Hyperpolarizability of a Push−Pull Polyene Dye as Indicated from DFT Calculations. *The Journal of Physical Chemistry C* **2008,** *112* (21), 7829-7835.

[31]   Kinnibrugh, T. L.; Timofeeva, T. V.; Clot, O.; Akelaitis, A.; Dalton, L. R., A non-linear optical chromophore: 2-[3-cyano-4-((E)-{5-[4-(diethylamino)styryl]thiophen-2-yl}vinyl)-5,5-dimethylfuran-2-(5H)-ylidene]propanedinitrile. *Acta Crystallographica Section E* **2006,** *62* (11), o4804-o4806.

[32]   Karplus, M., Contact Electron-Spin Coupling of Nuclear Magnetic Moments. *The Journal of Chemical Physics* **1959,** *30* (1), 11-15.

[33]   Karplus, M., Vicinal Proton Coupling in Nuclear Magnetic Resonance. *Journal of the American Chemical Society* **1963,** *85* (18), 2870-2871.

[34]   Reich, H. J. Structure Determination Using Spectroscopic Methods. https://www.chem.wisc.edu/areas/reich/chem605/.

[35]   Parthasarathy, V.; Pandey, R.; Das, P. K.; Castet, F.; Blanchard-Desce, M., Linear and Nonlinear Optical Properties of Tricyanopropylidene-Based Merocyanine Dyes: Synergistic Experimental and Theoretical Investigations. *ChemPhysChem* **2017,** *19* (2), 187-197.

[36]   Fulmer, G. R.; Miller, A. J. M.; Sherden, N. H.; Gottlieb, H. E.; Nudelman, A.; Stoltz, B. M.; Bercaw, J. E.; Goldberg, K. I., NMR Chemical Shifts of Trace Impurities: Common Laboratory Solvents, Organics, and Gases in Deuterated Solvents Relevant to the Organometallic Chemist. *Organometallics* **2010,** *29* (9), 2176-2179.

[37]   Franck, J.; Dymond, E. G., Elementary processes of photochemical reactions. *Transactions of the Faraday Society* **1926,** *21* (February), 536-542.

[38]   Condon, E., A Theory of Intensity Distribution in Band Systems. *Physical Review* **1926,** *28* (6), 1182-1201.

[39]   Skinner, J. G.; Nilsen, W. G., Absolute Raman Scattering Cross-Section Measurement of the 992 cm−1 Line of Benzene*. *J. Opt. Soc. Am.* **1968,** *58* (1), 113-119.

[40]   Grun, J. B.; McQuillan, A. K.; Stoicheff, B. P., Intensity and Gain Measurements on the Stimulated Raman Emission in Liquid O_{2} and N_{2}. *Physical Review* **1969,** *180* (1), 61-68.

[41]   Schaffer, H. E.; Chance, R. R.; Silbey, R. J.; Knoll, K.; Schrock, R. R., Conjugation length dependence of Raman scattering in a series of linear polyenes: Implications for polyacetylene. *The Journal of Chemical Physics* **1991,** *94* (6), 4161-4170.

[42]   Sworakowski, J., How accurate are energies of HOMO and LUMO levels in small-molecule organic semiconductors determined from cyclic voltammetry or optical spectroscopy? *Synthetic Metals* **2018,** *235*, 125-130.

[43]   Ballato, M. C. G.; John, The Handbook of Photonics, Second Edition. **2018**, 1-1020.

[44]   Kajzar, F.; Ledoux, I.; Zyss, J., Electric-field-induced optical second-harmonic generation in polydiacetylene solutions. *Physical Review A* **1987,** *36* (5), 2210-2219.

[45]   Campo, J.; Desmet, F.; Wenseleers, W.; Goovaerts, E., Highly sensitive setup for tunable wavelength hyper-Rayleigh scattering with parallel detection and calibration data for various solvents. *Opt. Express* **2009,** *17* (6), 4587-4604.

[46]   Smith, A. M.; Mancini, M. C.; Nie, S., Second window for in vivo imaging. *Nature Nanotechnology* **2009,** *4*, 710.

[47]   Gottlieb, H. E.; Kotlyar, V.; Nudelman, A., NMR Chemical Shifts of Common Laboratory Solvents as Trace Impurities. *The Journal of Organic Chemistry* **1997,** *62* (21), 7512-7515.

CHAPTER 5

CHROMOPHORES WITH HYPERSENSITIVITY TO ELECTRIC FIELDS FOR THE DETECTION AND IMAGING OF TRANSMEMBRANE POTENTIALS BY SECOND HARMONIC GENERATION

5.1. Introduction

5.1.1. Voltage Sensing

The assessment of the electrical communication between neurons is primarily done by physically inserting microelectrodes and measuring the potential difference[1]. This technique is plagued by numerous issues, first the neuron needs to be large enough to insert the micro electrode, which completely eliminates interrogation of the finest structures of a neuron, dendrites[2]. Secondly, the measurements are labor intensive and invasive, making it nearly impossible to measure a group of neurons while they communicate amongst themselves[3]. A current work arounds involve an electrode array being used to measure numerous neurons at the same time.

Optical methods offer robust solutions to many of the problems that plague physical voltage measurement using electrodes. Firstly, other than the potential toxicity of the voltage probe, optical methods are generally considered non-invasive. Fluorescence and absorbance-based probes offer the distinct advantage of being well adapted to other modern imaging paradigms. Also, by applying newer high resolution
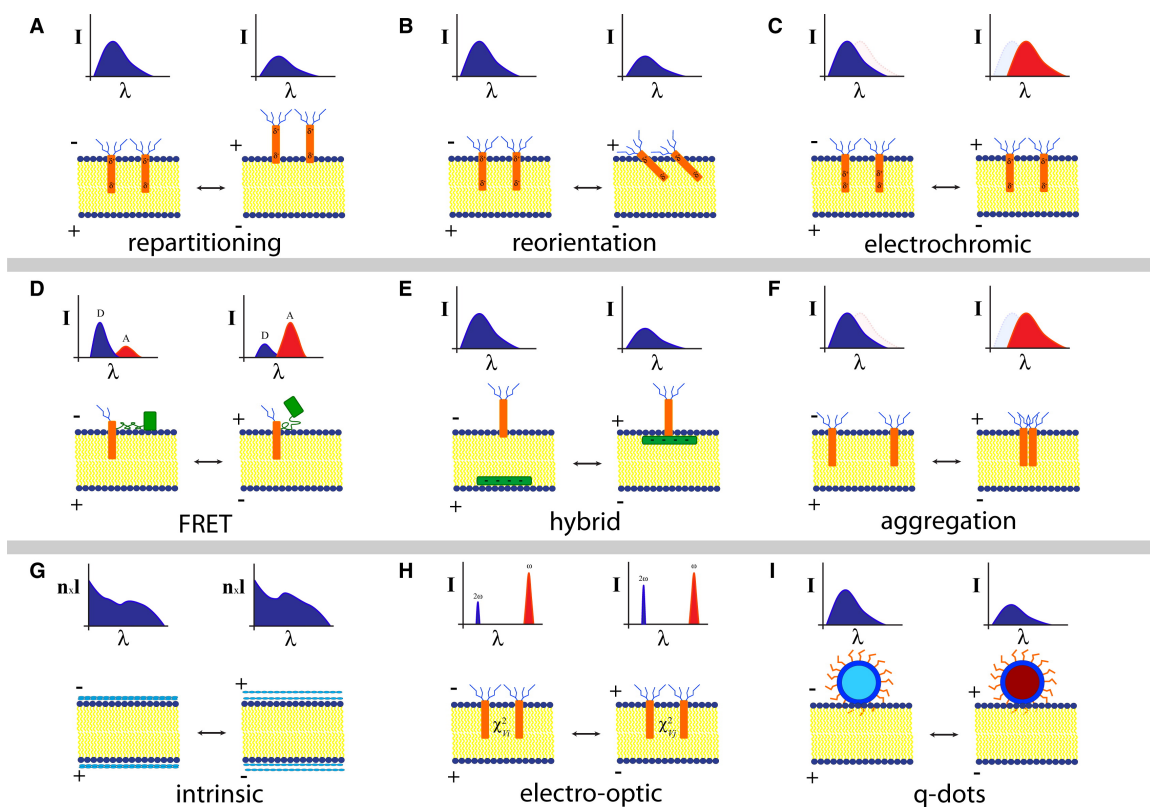
Figure 5.1. Schematic of the mechanisms of voltage sensing in neuronal membranes, along with representative spectral changes. A) repartitioning, where voltage changes cause the dye molecules to move into and out of the membrane, B) reorientation, where the voltage change creates a torque on the dye molecule, C) electrochromism, where the membrane potential changes the relative energies of the ground and excited states, D) FRET, where potential changes induce conformational or electronic changes that alter the efficiency of energy transfer, E) Hybrid, collisional quenching caused by voltage induced motions that affect the fluorescence lifetime and quantum yield, F) aggregation, where voltage changes cause aggregation resulting in spectral shifts, G) intrinsic, voltage induced refractive index changes, H) SHG, where potential changes alter the nonlinear polarizabilities resulting in a change in SHG efficiency, I) nanoparticles, can be used as a novel chromophore or as a sensitivity amplifier. Reprinted from Neuron, Vol. 69, Darcy S. Peterka, Hiroto Takahashi, and Rafael Yuste, Imaging Voltage in Neurons, Pages 9 – 21., Copyright (2011), with permission from Elsevier

(sub-diffraction barrier) imaging techniques, such as multiphoton excitation fluorescence (MPEF) microscopy, can yield high resolution micrographs of voltages in both single cells and networks.[4]

Schematics of the mechanisms associated with nine different voltage sensing paradigms are shown in Figure 5.1. The figure is reproduced with permission from reference [1]. While all of these mechanisms represent an actively pursued subfield in potential sensing, the main paradigm of import for this dissertation is SHG sensing, represented by letter H in Figure 5.1. SHG is particularly useful for the detection and imaging of transmembrane probes for numerous reasons, chief among them is that the SHG effect itself is dependent on the induced polarization generated by the electromagnetic field of the incident light and can be modulated by an external field[1, 3, 5], in our case an action potential. The second major advantage of SHG sensing over other high-resolution techniques such as two-photon excitation fluorescence (TPEF) microscopy is the timeframe on which the probe interacts with the incident light. Since SHG is a scattering process it happens nearly instantaneously, TPEF requires time to absorb two photons relax to the emissive state and emit. The main disadvantage of SHG imaging is that the signal is typically much weaker than fluorescence based microscopy.[6]

5.1.2. Action potential in Neurons

The neuron itself presents some significant challenges for potential imaging. Firstly, in order to better understand the timing, integration and transmission of action potentials within a neural network, the potential sensitive dye must have sufficient temporal resolution in order to respond to a very rapid depolarization of the neuronal membrane.

Typical action potentials in neurons can occur on the 1 – 2 millisecond time scale in neurons.[7] The action potential itself can be broken into two distinct parts, a slower generation of ionic concentration gradients and a fast release of those ions to flow down their respective gradients.[8] It is this rapid flow that presents the largest challenge for potential sensing between neurons.
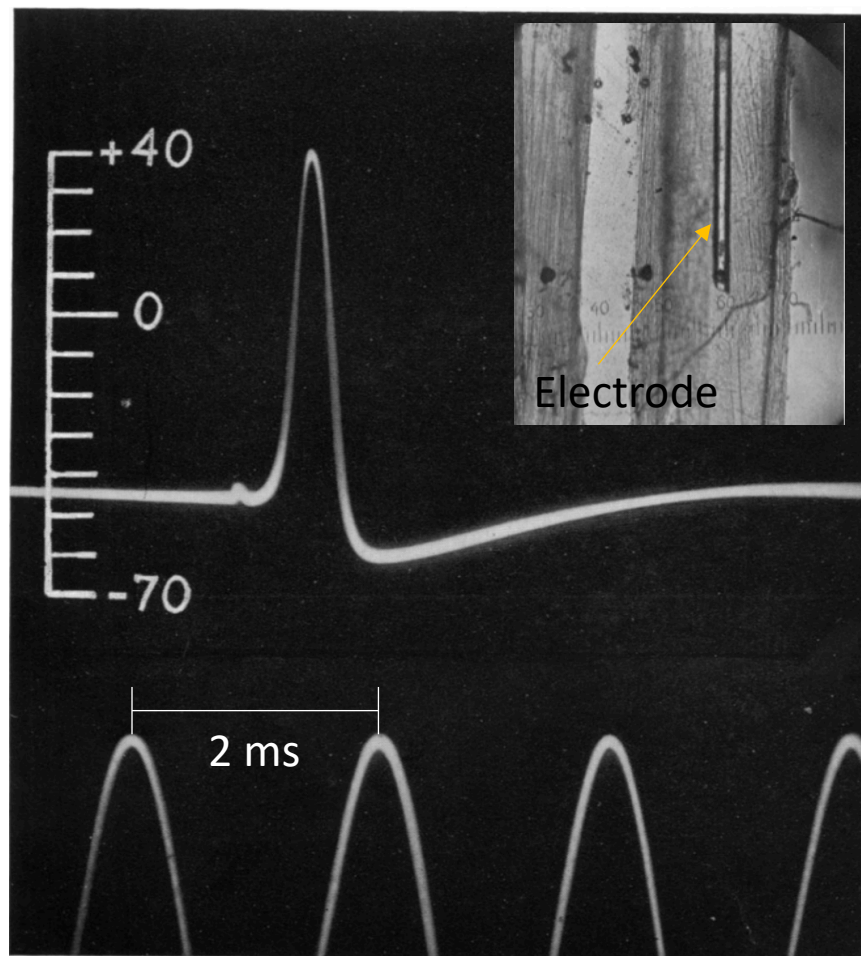
Figure 5.2. First reported action potential measurement by Hodgkin and Huxley in 1939[7, 9-10]. Reprinted with permission from Journal of Physiology, Volume 104, Hodgkin, A. L.; Huxley, A.F., Resting and action potentials in single nerve fibres, Pages 176-195, Copyright 1945 by John Wiley and Sons.

The neuron's membrane potential when not excited rests around -60 to -70 mV. This potential is maintained by actively pumping internal sodium ions out of the cell and potassium ions into the cell.[11] When an impulse of sufficient strength interacts with the neuron, it triggers a very rapid depolarization of the membrane, which allows the membrane potential to climb to around +40 mV before the active ion transport takes over and the membrane is again repolarized. In reestablishing the resting potential, the neuron typically overshoots to -80 to -90 mV. During this hyperpolarization time, it is very hard for another action potential to propagate.[12]

5.2. Background

5.2.1. Electric Field Dependence of NLO Parameters

Previous studies by our group and in collaboration with the Marder and Bredas groups have looked at the nonlinear optical parameters of model donor-acceptors as a function of bond length alternation (or bond order alternation) and as a function of applied field.[13-17] The resulting plot of β vs BLA has even been referred to as the Marder-Perry Plot[18] (Figure 5.3). Numerous versions of the aforementioned Marder-Perry plot are arbitrarily divided into regions based on the change in β.
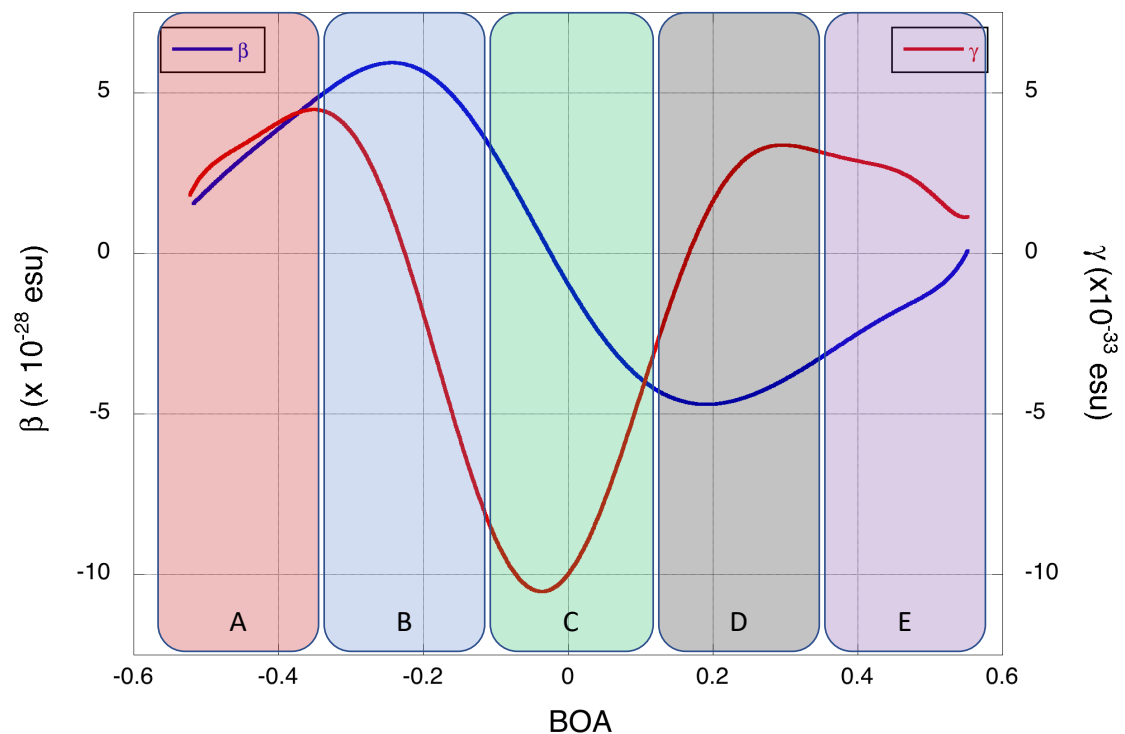
Figure 5.3. Dependence of first hyperpolarizability (β, blue trace) and second hyperpolarizability (γ, red trace) on BOA. The plot is divided into regions arbitrarily.[15]

These arbitrary regions are defined based on the mixing of the neutral and charge transferred forms. Region A is defined approximately 100% neutral form and region E, as nearly 100% charge-separated form. Region C is where the mixing of the two forms is nearly in equal proportions. The remaining two, regions B and D, bridge the divides between regions A and C or C and E respectively.[13, 19] As discussed in the previous chapter, there is a difference in BLA and BOA, however for the most part, they will be used interchangeably.
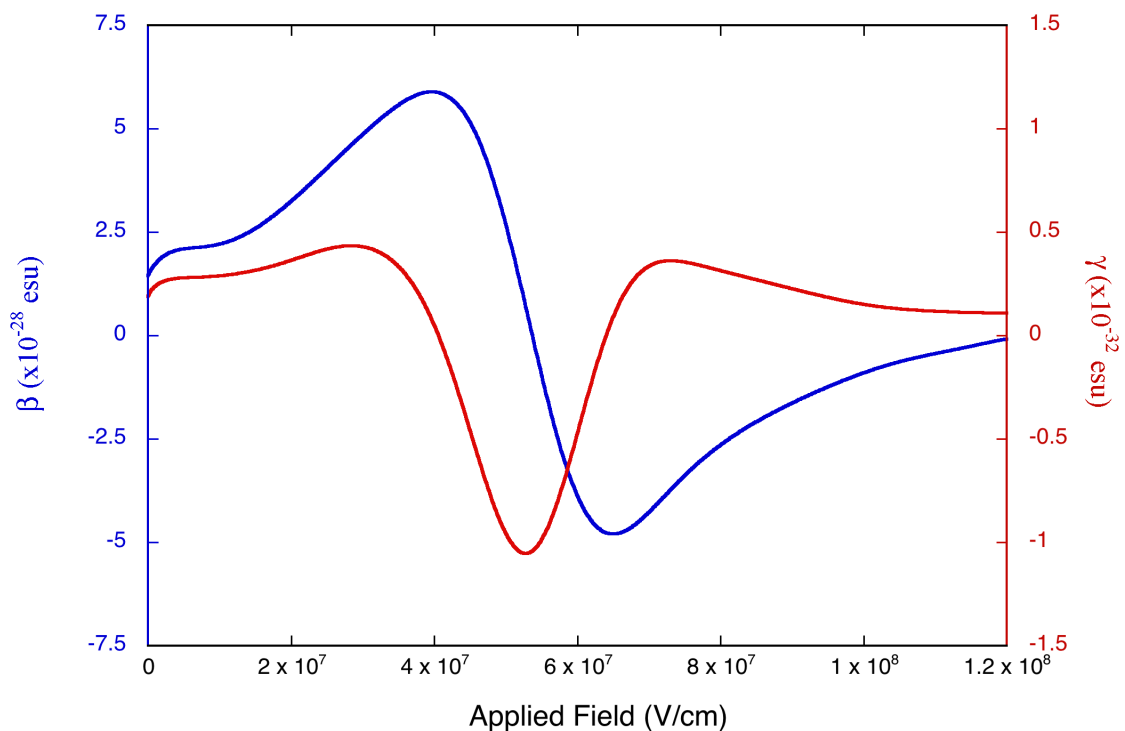
Figure 5.4. Nonlinear optical parameters, β (blue trace) and γ (red trace), as a function of applied electric field.

The SHG response has a quadratic dependence on the hyperpolarizability (β) and number density of the chromophore as well as the laser intensity. In the presence of an electric field, the SHG signal is also dependent on the second hyperpolarizability (γ) and the magnitude of the electric field. Using β and *γ* values measured for all-*trans*-9-dimethylaminonononatetraenal[17] verses bond length alternation, and BLA vs applied field, the SHG sensitivity can be approximated as a function of applied field. As is shown in Figure 5.4 the extreme of γ occurs at the same field that β is equal to zero.

<u>5.2.2. Nonlinear Optical Response and Second Harmonic Generation</u>

Second harmonic generation (SHG) imaging is well suited for investigating neural activity as it can be tailored to the biological window and because the change in electric field will directly impact the response of SHG active chromophores. Second harmonic generation is a hyper scattering phenomenon, in which the electric field of the incident beam of light induces a second order nonlinear polarization in the irradiated media. This results in the emission of a photon at exactly twice the frequency of the incident photons.[1]

5.3. Modeling and Estimation of Second Harmonic Generation Efficiency

As is mentioned above, the incident photons induce a second order nonlinear polarization in the irradiated media which can be described in terms of the number density of chromophores (N), the effective first hyperpolarizability (β_{eff}), and the field from the incident light (E_ω):

$$P_{2\omega}^{ind} = N \beta_{eff} E_\omega^2. \qquad \text{(Eq. 5.1)}$$

The term β_{eff} is equal to the first hyperpolarizability in the static case, but with the application of an external electric field β_{eff} is affected by the magnitude of that applied field and the second hyperpolarizability γ.

The SHG response is proportional to the square of the polarization induced by the incident photons as shown in Eq. 5.2.

$$I_{SHG} \propto \left(P_{2\omega}^{ind} \right)^2 \qquad \text{(Eq. 5.2)}$$

This results in a quadratic dependence on the hyperpolarizability (β) and number density (N) of the chromophore as well as the laser intensity. In the presence of an electric field,

the SHG signal is also dependent on the second hyperpolarizability (γ) and the magnitude of the applied electric field.

$$I_{SHG} = \left(N \left[\beta + \gamma \cdot E_{app} \right] E_{\omega}^2 \right)^2 \qquad \text{(Eq. 5.3)}$$

The SHG sensitivity is the percentage change in SHG signal, or $\Delta I_{SHG}/I_{SHG}$. Sensitivity values are typically scaled to be in units of percent change per 100 mV. Assuming that the same sample is used and the same energy of the incoming laser, the SHG sensitivity can be defined as:

$$\frac{\Delta I_{SHG}(\Delta E)}{I_{SHG}(E_R)} = \frac{\left[\beta + \gamma \left(E_R + \Delta E \right) \right]^2 - \left[\beta + \gamma \left(E_R \right) \right]^2}{\left[\beta + \gamma \left(E_R \right) \right]^2}. \qquad \text{(Eq. 5.4)}$$

If the first and second hyperpolarizabilities are assumed to be static and the resting potential is assumed to be 0 mV, the SHG sensitivity can be estimated as:

$$\frac{\Delta I_{SHG}(\Delta E)}{I_{SHG}(E)} = \frac{\left[\beta + \gamma \left(\Delta E \right) \right]^2 - \left[\beta \right]^2}{\left[\beta \right]^2} \approx 2 \left(\frac{\gamma}{\beta} \right) \cdot \Delta E. \qquad \text{(Eq. 5.5)}$$

Using β and γ values measured for all-*trans*-9-dimethylaminononatetraenal[1] verses bond length alternation, and BLA vs applied field, the SHG sensitivity can be approximated as a function of applied field. As is shown in Figure 1 the greatest change in SHG signal will occur as β approaches zero and γ approaches its extreme. Unfortunately, this is also the region of the continuum which results in the smallest signal.

If the first and second hyperpolarizabilities are not assumed to be static, the SHG signal will depend heavily on the field-dependent β and γ values.

$$\frac{\Delta I_{SHG}(\Delta E)}{I_{SHG}(\Delta E)} = \frac{I_{SHG}\left(E_R + \Delta E \right) - I_{SHG}\left(E_R \right)}{I_{SHG}\left(E_R \right)} \qquad \text{(Eq. 5.6)}$$

$$\frac{\Delta I_{SHG}(\Delta E)}{I_{SHG}(\Delta E)} = \frac{\left[\beta_{\Delta E} + \gamma_{\Delta E}(E_R + \Delta E)\right]^2 - \left[\beta_0 + \gamma_0 \cdot E_R\right]^2}{\left[\beta_0 + \gamma_0 \cdot E_R\right]^2} \qquad \text{(Eq. 5.7)}$$

If the resting membrane potential is approximated as 0 mV, the sensitivity simplifies as follows in Eq. 5.8 and 5.9.

$$\frac{\Delta I_{SHG}(\Delta E)}{I_{SHG}(E)} = \frac{\left[\beta_{\Delta E} + \gamma_{\Delta E} \cdot \Delta E\right]^2 - \left[\beta_0\right]^2}{\left[\beta_0\right]^2} \qquad \text{(Eq. 5.8)}$$

$$\frac{\Delta I_{SHG}(\Delta E)}{I_{SHG}(E)} = \left(\frac{\beta_{\Delta E}^2 - \beta_0^2}{\beta_0^2}\right) + 2\left(\frac{\beta_{\Delta E}}{\beta_0}\right)\left(\frac{\gamma_{\Delta E} \cdot \Delta E}{\beta_0}\right) + \left(\frac{\gamma_{\Delta E} \cdot \Delta E}{\beta_0}\right)^2 \qquad \text{(Eq. 5.9)}$$

With the exception of the region around which β approaches zero, β is roughly four orders of magnitude larger than γ. Therefore, the estimation of the SHG sensitivity can be further simplified to:

$$\frac{\Delta I_{SHG}(\Delta E)}{I_{SHG}(E)} \approx \left(\frac{\beta_{\Delta E}^2 - \beta_0^2}{\beta_0^2}\right). \qquad \text{(Eq. 5.10)}$$

When dissolved, the solvent exerts a reaction field on the chromophore. The reaction field (R) was described by Onsager[20] as:

$$\vec{R} = \left(\frac{1}{4\pi\varepsilon_0}\right)\frac{2(\varepsilon - 1)}{(2\varepsilon + 1)}\frac{\vec{\mu}}{a_0^3}, \qquad \text{(Eq. 5.11)}$$

where μ is the molecular dipole moment of the solute and a_0 is the radius of the cavity of solvent molecules needed to envelope the solute. The reaction field can be modulated by varying the solvent system. Changing the solvent often changes the reaction field by huge amounts on the order of 10^7 V/cm, while the transmembrane electric field is on the order of 10^5 V/cm.
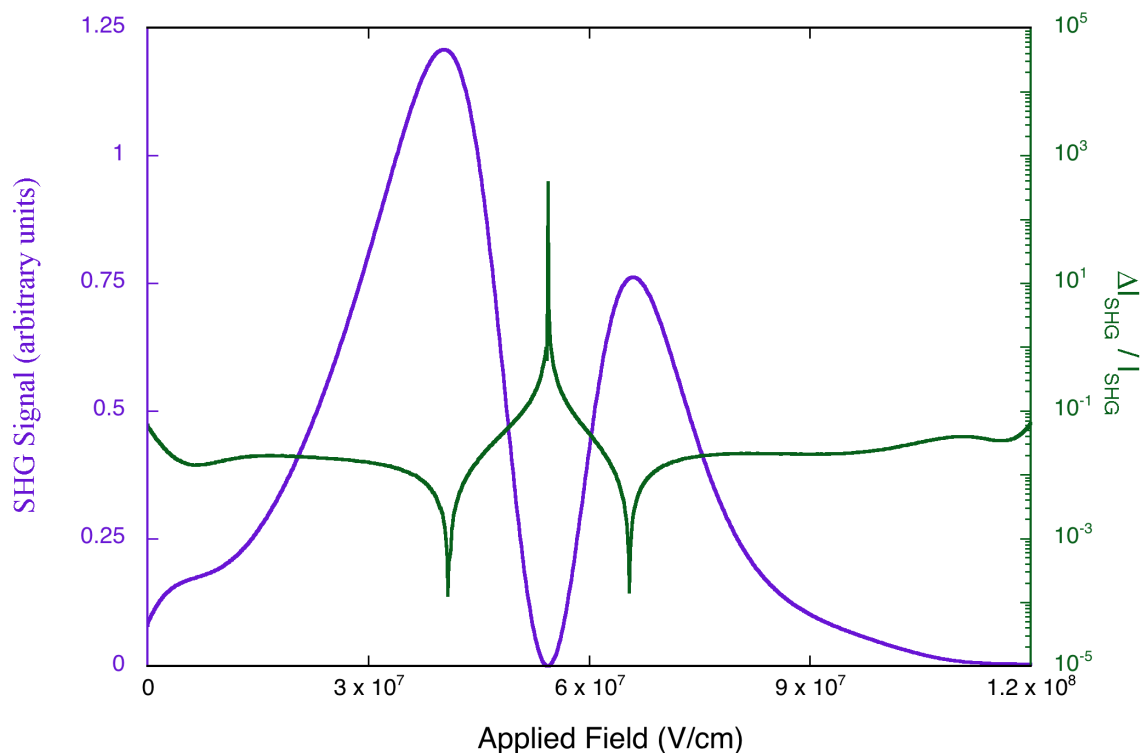
Figure 5.5. Estimated signal (purple trace) and fractional change in SHG intenstity (green trace) as a function of applied field.

5.4. Synthesis

5.4.1. Synthesis of Known SHG Probes

Two of the main SHG standard probes used in this thesis are all-*trans*-retinal, ATR, and FM-4-64 are representative of two of the most common challenges of using commercially available dyes for laser work: ATR is very light and oxygen sensitive and FM-4-64 is very hydroscopic. For these reasons as well as cost, we decided to make these two standard dyes in house. The synthesis of ATR is very straight forward from a significantly less expensive precursor, retinal acetate. The retinal acetate was reduced with sodium metal in methanol and the resulting retinol was oxidized to retinal with manganese

dioxide. The resulting crude product was carefully purified by column chromatography in the dark and stored at -20°C.

FM-4-64 was synthesized by a modification of the Wittig oxophrenylation[21-22], this time using an extended phosphonate and the Horner-Wadsworth-Emmons reaction as shown in Scheme 5.1. The major advantage of this approach is that it is possible to add two double bonds to the back bone in one reaction. In order to make the extended phosphonate, **5.5**, freshly distilled crotonaldehyde (**5.1**) and acetic anhydride are reacted in the presence of base to give 1-acetoxybuta-1,3-diene (**5.2**), which can also be purchased commercially, but is quite expensive. The resulting 1-acetoxybuta-1,3-diene was deprotected, brominated and reprotected with ethylene glycol using molecular bromine and ethylene glycol in DMF. The resulting intermediate, bromocrotonaldehyde (**5.3**), rather unstable, but was isolatable. The (*E*)-2-(3-bromoprop-1-en-1-yl)-1,3-dioxolane (**5.4**), resulting from the one-pot synthesis was isolatable in much higher yield than synthesis by two steps. An Arbuzov reaction with triethylphosphite was used to convert **5.4** in to its corresponding diethyl phosphonate, **5.5**. Extension of diethylaminobenzaldehyde with **5.5** was accomplished in THF using KO^{t}Bu by a HWE reaction in very high yield (about 95%) to give the diethylaminopentadienal (**5.6**).

The synthesis of the pyridyl acceptor group, **5.8**, was accomplished by mono substitution of 1,3-dibromobropane with triethylamine to give **5.7** and subsequent substitution with 4-methylpyridine to give **5.8** as an off-white solid. The synthesis of **FM-4-64** was completed by the knovenagel condensation of **5.7** and **5.8** using piperidine in absolute ethanol. **FM-4-64** is quite hygroscopic and required care in isolation and purification to exclude moisture.
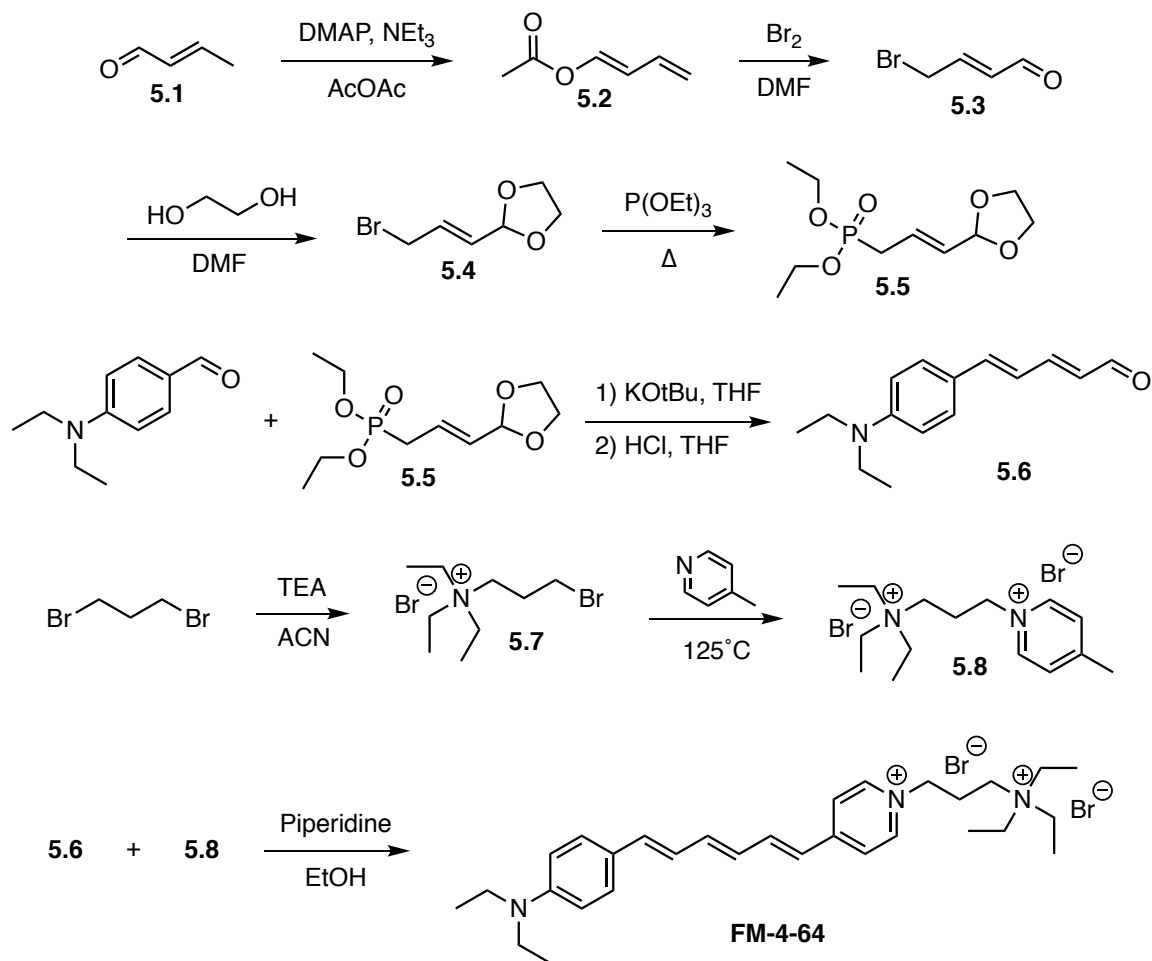
Scheme 5.1. Synthesis of FM-4-64 using a Horner-Wadsworth-Emmons based extension of 4-(diethylamino)benzaldehyde.

5.5. Results

5.5.1. First Hyperpolarizability from Hyper-Rayleigh Scattering in Solution

As is discussed in Chapter 2 (section 2.5.1), hyper-Rayleigh scattering, or HRS, is a useful tool for the direct measurement of first hyperpolarizability, β. It is also very useful because it depends on the instantaneous orientation of molecules and has no requirement for asymmetry. This is particularly well suited to investigating the first hyperpolarizability of cyanines because, unlike SHG, there is no requirement for non-centrosymmetric molecules. Cyanines are particularly interesting as mentioned in the previous sections because they should show to the lowest SHG signal, but the largest SHG sensitivity ($\Delta I_{SHG}/I_{SHG}$) as is depicted in Figure 5.5.

While absolute measurements can be taken using an integrating sphere, hyper-Rayleigh scattering measurements are typically taken relative to a sample of known β, typically the solvent used for the measurement.[23]   The most commonly referenced solvent β is that of chloroform. Unfortunately, there is considerable disagreement on the actual value of β for chloroform. Throughout this dissertation, the first hyperpolarizability of chloroform at 1064 nm is assumed to be 0.49 x 10^{-30} esu.[24] This value was selected in accordance with comparison of first hyperpolarizabilities of solvents as described by Campo *et at*.[25] Using the undamped two-level model and a simple one term Sellmeier equation for the dispersion of the refractive indices, the first hyperpolarizabilities of the relevant solvents were determined at the experimental wavelengths. It is in reference to these β values that the relative β of the chromophores of interest are measured.

The majority of HRS experiments were conducted at 900 nm. This was due to a few factors, most importantly, the absorption spectrum of relevant media. Water makes up

a very large percentage of brain tissue and of neurons, estimated between 68 – 80% by mass. The water has a very small absorption coefficient between 300 – 950 nm, this transparent region of the electromagnetic spectrum is known as the biological window[ref]. The second major consideration is the light source. Our amplified femtosecond system has an average output of 3.7 W at 800 nm. This 800 nm beam is routed into an optical parametric amplifier (TOPAS-C, Light Conversion) which is tunable between 1100 – 2900 nm. Additional regions in the visible and near IR accessible through second harmonic generation (550 – 1120 nm) and sum frequency generation (470 – 630 nm). The power and beam shape of the laser are much better quality below 700 nm, however the chromophores of interest all absorb in the 400 – 800 nm range. Taking the absorption of the chromophores and the biological window into account, 900 nm represents a good compromise as both incident and scattered frequencies are within the biological window, and the TOPAS-C output and beam shape degrade rapidly above 900 nm.

5.5.2. Second Hyperpolarizability from Z-Scan Measurements in Solution

In order to estimate the effect that a change in transmembrane potential will have on SHG efficiency, the second hyperpolarizability, or γ, needs to be determined. As noted in the previous section, all samples were measured at 900 nm or at 1250 nm in the event that the one photon absorption fell too close to 900 nm.

In a typical donor-acceptor polyene type chromophore, the first hyperpolarizability, β, can be around 10 orders of magnitude larger than the second hyperpolarizability. When this is true, the effects that a change in γ will have on the overall SHG intensity will be negligible. For this reason, measurements of γ were only conducted on chromophores with much larger γ/β ratio and commonly used SHG probes. The ratio of

γ/β increases for molecules that are close to the cyanine limit and chromophores with very long conjugated backbones. Second hyperpolarizabilities were measured by closed-aperture Z-scan as is described in Chapter 2.

5.5.3. Estimation of SHG Sensitivities from Static First and Second Hyperpolarizabilities

As shown in equation 4.5 in the discussion of SHG sensitivity earlier in this chapter, the purely electronic fractional change in SHG intensity (SHG sensitivity) is dependent on the fundamental nonlinear optical properties β and $γ$ as well as the change in electric field during an action potential, ΔE. The NLO characterization at 900 nm for two well established SHG probes (all-*trans* retinal (ATR) and a styryl dye, FM4-64) as well as a cyanine dye (JS-II-154) synthesized in-house are shown in Table 4._. Using the experimentally determined values for β and $γ$ from HRS and closed aperture z-scan respectively, the SHG sensitivities have been estimated and are given in Table 5.1 as well. While the signs of the SHG sensitivity for ATR and FM 4-64 are properly predicted, the magnitude of the estimated values are significantly smaller than those measured by taking SHG measurements *in vitro* and in GUV studies, suggesting that mechanisms other than those giving rise to a purely electronic response are responsible for the SHG signals taken in membranes[6, 25]. Nevertheless, the sensitivity of the cyanine dye is estimated to be an order-of-magnitude larger than the established probes. This is due the significantly larger magnitude of $γ$, which suggests that cyanine dyes, as a set of chromophores, should exhibit significantly larger SHG sensitivities due to ultrafast electronic mechanisms than the current state-of-the-art SHG probes.
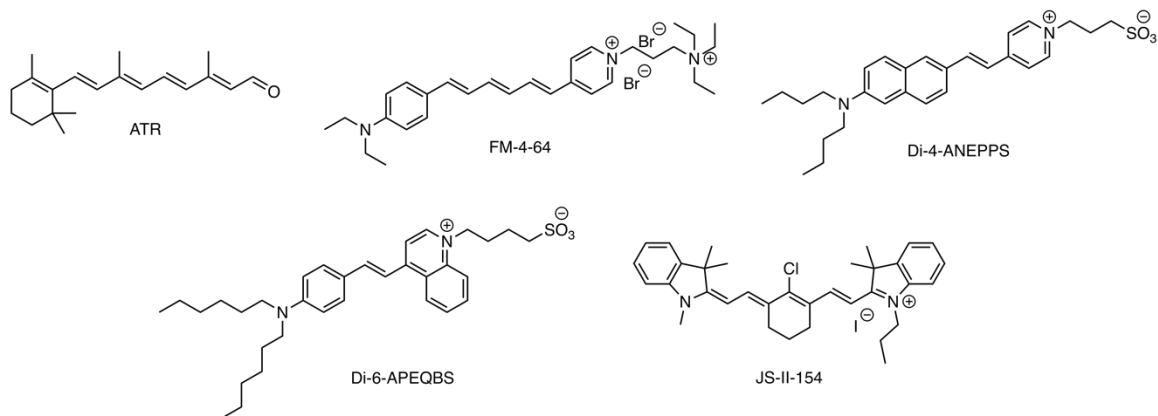
Figure 5.6. Structures of ATR, FM-4-64, Di-4-ANEPPS, Di-6-APEQBS and JS-II-154

Table 5.1. Nonlinear optical parameters and SHG sensitivities at 900 nm for common SHG probes and an indole-terminated cyanine chromophore synthesized in this program

DYE	β X 10^{-48} [C M^3 V^{-2}] [A]	γ X 10^{-58} [C M^4 V^{-3}] [A, B]	2·(γ/β) X 10^{-10} [M V^{-1}]	2·(γ/β)·ΔE_{MEM} [C] SHG SENSITIVITY
ATR	1.8	1.9	2.1	0.3% (estimated) 25% (measured)[3]
FM 4-64	11	-27	-5.0	-0.7% (estimated) -15% (measured)[3]
Di-6-APEQBS	5.1	1.7	6.6	0.9% (estimated) 4% (measured)[5]L
JS-II-154	7.2	-230	-64	-8.6% (estimated)

[a] Measured in acetonitrile; [b] additional factor of five included due to assumed alignment when inside membrane; [c] field size assumed to be 1.3×10^7 V/m based on 100 mV potential and ~8 nm thick membrane.

In order to look for solvent dependent changes in the hyperpolarizabilities of the dyes of interest, it is important to first consider the error associated with the preceding measurements. According to Campo *et al.* [25] the first hyperpolarizabilities determined in reference to chloroform can be as low as 5 %. Unfortunately for our setup this is not the case. The reproducibility of the HRS measurements is noticeably better with increased

signal. In order to estimate our error, standard propagation of errors was employed. The other major source of error is inherent in the accepted value of the hyperpolarizability of chloroform, to which all measurements are directly or indirectly referenced. The most commonly accepted value is 0.49×10^{-30}, recorded by *Zyss et al* by EFISH measurements[24-25], the controversy over this value is discussed in chapter 2. Since there is significant disagreement over this value, we have chosen to neglect the error associated with it because all values are referenced to it, and because if a better value were reported in the future, the results presented in this dissertation can be scaled accordingly. The error in the HRS measurement for chloroform and for ATR solutions in chloroform were about 6% and 10% respectively based on the standard deviation of the integrated signal. This resulted in an estimated 13% error for β values. Second hyperpolarizabilities as determined by solution z-scan have an 8% error. The error of ΔE_{mem} was also neglected as it was arbitrary and based on reports from the literature. The resulting error in $\Delta I_{SHG}/I_{SHG}$ is $\pm 19\%$.

5.5.4. Estimation of Reaction Fields from NLO properties

The chromophores of interest are all sensitive to potential changes in their environment. This potential sensitivity not only includes the application of an external field, changes in field analogous to an action potential, but it also includes an electric field as a result of solvation. The molecular model of solvation[26] describes a solution as consisting of three main components: the solute, the primary solvation shell, and the bulk solvent. The primary solvent shell can be defined as any arrangement of solvent molecules around a solute that differs from the bulk solvent.[26-27] This arrangement of solvent molecules is induced by the polarization of the solvent molecules by the polar solute

molecule. Once polarized, electrostatic interactions between the solvent and solute molecules. The Onsager reaction field theory describes the electric field that results from this polarization and organization of solvent molecules around a polar solute. This resultant electric field, or reaction field, can be described in terms of the dielectric constant of the media (ε), the dipole moment of the solute (μ), and the radius of the spherical cavity created by the solvent around the solute (a)[20]:

$$R = \frac{1}{4\pi\varepsilon_0} \frac{2(\varepsilon-1)}{2\varepsilon+1} \frac{\mu}{a^3}.$$

(Eq. 5.12)

As is shown in the equation above, the reaction field is dependent on the solute's size and dipole moment, this means that two different solutes in the same solvent can have very different reaction fields.

Table 5.3 shows a sizable solvent-dependent changes in β for a set of standard dyes, an indole-terminated cyanine and select donor-acceptors polyenes previously described in chapter 4. In order to translate these observed changes to a projected change in SHG efficiency, it is important to consider the change in reaction field between the given solvents. In order to be useful for sensing changes in transmembrane potentials, the chromophore needs to respond to changes on the order of an action potential. The action potential has a maximal change in potential of about $100 - 110$ mV[1] and it is applied across a membrane that is roughly 4-8 nm wide[1]. The resulting field associated with an action potential is about $1.25 \times 10^5 - 2.75 \times 10^5$ V/cm.
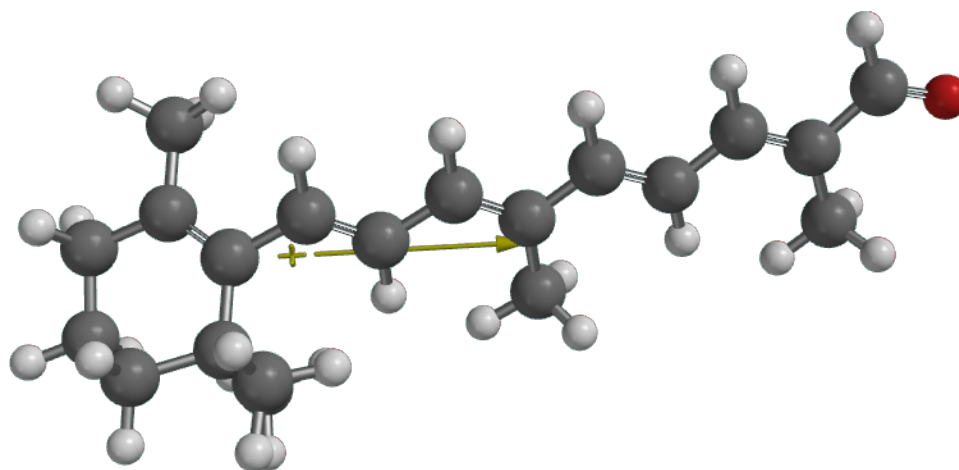
Figure 5.7. All-*trans*-retinal, ATR, geometry optimized using the semi-empirical theory with PM3 basis set from Spartan. The yellow arrow represents the calculated dipole moment of 3.81 Debye.

For ATR, Figure 5.7, the reaction field was calculated using the predicted dipole moment and cavity radius from Spartan. For the cavity radius, the molecular volume predicted by spartan was used to back calculate the radius of a spherical void of the same volume.

Table 5.2. Estimation of Onsager reaction fields for ATR in various solvents. The values for Dipole moment and cavity radius are 3.81 Debye and 4.35 Å respectively, both as calculated by Spartan.

Solvent	ε	Reaction Field (V/m)	ΔReaction Field[a] (V/cm)
CHCl$_3$	4.81	9.98 x 10^8	
ACN	36.64	1.33 x 10^9	3.37 x 10^6
DMF	37.31	1.34 x 10^9	3.38 x 10^6

[a] ΔR calculated by subtracting the smallest reaction field of those estimated from the other reaction fields.

The above estimations predict a change in reaction field that is roughly an order of magnitude larger than an action potential. It seems convenient to take the SHG sensitivity and divide by the change in reaction field, giving a sensitivity change per change in field. In fact, a similar practice is very common in the literature[ref] where the sensitivity, whether predicted, estimated, or measured is scaled to the units of percent change per 100 mV. This approach makes the assumption that there is a linear relationship between the change in potential and the change in SHG efficiency, this assumption introduces significantly more error when the change in field becomes quite large. In order to combat this, solvent systems can be tailored to reduce the change in reaction field.

A more rigorous estimation of the reaction field takes into account the dipole moment of the chromophore when dissolved in different media. The polarity of a solvent has been shown to affect the dipole moment as well as a myriad other molecular properties. Luckily, these changes can be considered using self-consistent reaction field theory or SCRF. The Gaussian software package[28] has a built-in function, SCRF, that calculates the reaction field for a particular molecule in defined solvents. The input arguments for the SCRF calculations are the dye structure, first optimized by Spartan, the solvent and the cavity radius. The cavity radius used is calculated by Gaussian using the Vol keyword. In Gaussian, the volume keyword uses a Monte Carlo integration method to determine the cavity radius, so it is not uniquely determined by the molecular geometry. Carlier *et al* assessed these variations and calculated a cavity radius with a standard deviation of 3.7% over ten separate Gaussian Vol calculations. They use a single value for the cavity radius ± 10% to give a very conservative estimate of the uncertainty.[29] Using the SCRF keyword along with the Opt keyword allows Gaussian to optimize the geometry for the

chromophore in the defined solvent field and calculate the reaction field felt by this optimized geometry.

5.5.5. Estimation of SHG Sensitivity from Field-Dependent First Hyperpolarizabilities

Measuring the first hyperpolarizability of known potentiometric chromophores in various solvents affords a facile screening technique for estimating SHG sensitivity. Various solvents exert a reaction field on the chromophore. By changing the solvent system, the reaction field can be used as an approximation of a field change during an action potential[20, 27].

Although the value of γ is not directly measured through this approach, the effects of the solvent reaction field on the HRS signal will be dependent on both the first and second hyperpolarizabilities by the same γ/β relationship, as above. The main difference in this approach is that the value of the first hyperpolarizability is assumed to both be several (8-10) orders of magnitude larger than the second hyperpolarizability and that it will change with the change in solvent environments. The series of D-A polyenes, TB[1-3] and TCF[1, 3], mostly show the expected trend of increasing SHG sensitivity with increasing length of conjugation[30]. The increased acceptor strength of TCF vs TB also shows the expected increase in SHG sensitivity.

Table 5.3. SHG sensitivity estimation based on reaction field-dependent first hyperpolarizabilities. β values are measured by HRS at 900 nm.

Dye	Solvent	$\beta \times 10^{-48}$ [C m³ V⁻²]	$\dfrac{(\beta_{\Delta E}^2 - \beta_0^2)}{\beta_0^2}$
ATR	ACN	1.8	22.4 %
	DMF	2.0	
FM-4-64	ACN	10.9	-25.3 %
	DMF	9.5	
Di-6-APEQBS	ACN	4.9	6.4%
	DMF	4.7	
JS-III-31	Acetone	15.8	-76%
	ACN	7.8	
JS-II-164	Acetone	15.1	-62%
	ACN	9.8	
TB[1]	ACN	3.9	-74.3%
	DMF	2.0	
TB[2]	ACN	5.8	-40.5%
	DMF	4.5	
TB[3]	ACN	9.6	-45.0%
	DMF	7.2	
TCF[1]	ACN	6.1	-45.0%
	DMF	4.5	
TCF[3]	ACN	11.3	-60%
	DMF	7.2	

Note: Error associated with β values and the resulting sensitivity values are estimated at 13% and 21% respectively

Again, it is important to consider the error in order to compare the estimated sensitivity values. As in the previous discussion, the estimated error for β measurements in chloroform was 13%, β measurements in acetonitrile and DMF had less error and were

estimated around 9%. The error for SHG sensitivity by solvent dependent nonlinearities was taken as the error associated with a β measurement in chloroform and in either ACN or DMF. This represents an "average" error for the sensitivity calculation and was estimated as 21%.
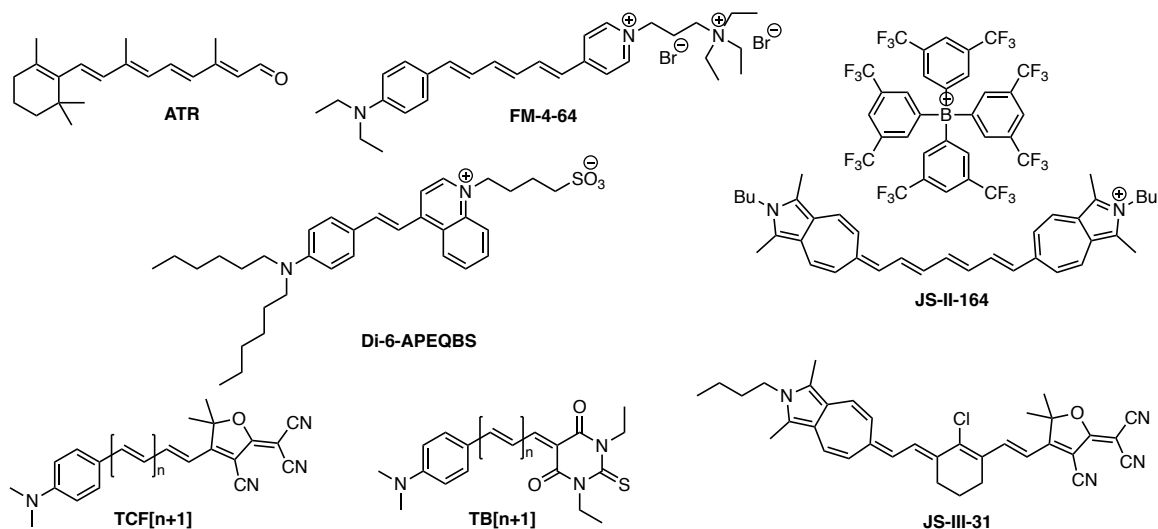
Figure 5.8. Chemical structures for field dependent SHG sensitivity studies

5.5.6. Estimation of SHG Sensitivity from Field-Dependent First Hyperpolarizabilities of Mixed Solvent Systems

As was discussed in sections 4.5.5 and 4.5.7, the resulting change in reaction field between different solvents, for most of the dyes mentioned in the preceding sections, is significantly larger that the change in field due to an action potential. In order to reduce the reaction field change to a more biologically relevant strength, solvent mixtures of acetonitrile (ACN) and chloroform were used. Owing to the necessity that the solvent system stays the same over multiple days and through multiple batches, the refractive indices of the solvent systems were regularly monitored to ensure that they remained the same. All solvent

mixtures and solutions made there from were stored in tightly sealed containers using PTFE
lined caps.
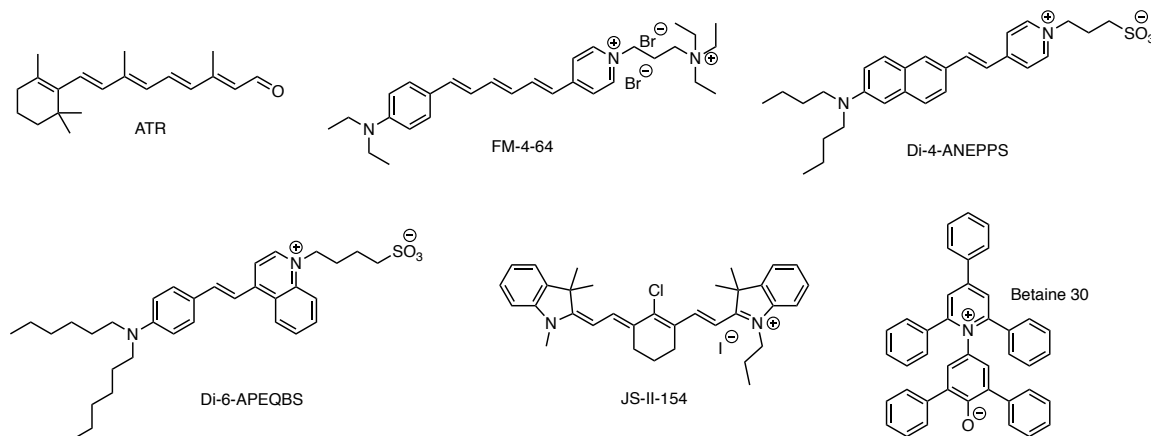
Figure 5.9. Chemical Structures of ATR, FM-4-64, Di-4-ANEPPS, Di-6-APEQBS, JS-II-154 and Betaine 30 (Reichard's Dye) used in mixed solvent studies.
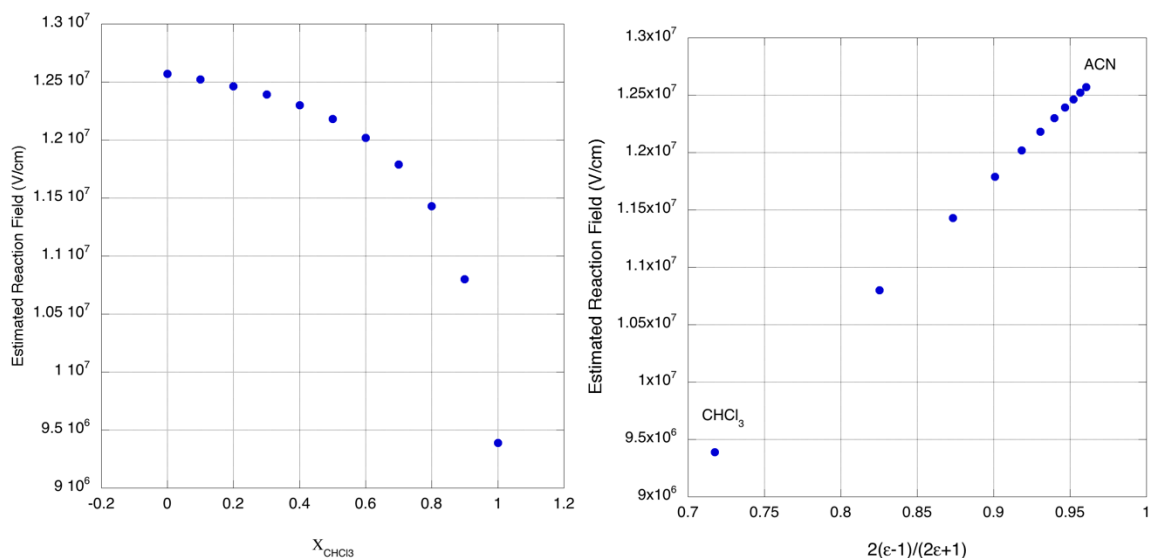
Figure 5.10. Left) Onsager Polarity as a function of the dielectric constant of each solvent mixture. Right) Estimated reaction field as a function of Onsager polarity. Reaction fields are calculated using equation 4.12. The permittivity of the mixtures was calculated by a weighted arithmetic mean of the permittivities of chloroform and acetonitrile based on the mole fraction of each solvent. The Onsager sphere radius and ground state dipole moment for this estimation were 5.53 Å and 7.382 Debye as calculated by Gaussian.

Hyper-Rayleigh scattering, UV-Vis, and Fluorescence measurements of standard dyes (Figure 5.9), such as ATR, FM-4-64, Di-6-APEQBS, and Di-4-ANEPPS, as well as JS-II-154 were measured in the mixtures of acetonitrile and chloroform in Table 5.4 below. As is shown in Figure 5.12 below, In the very narrow range of solvents used in this mixed solvent study, all four standard dyes and JS-II-154 show negative solvatochromism. It is difficult to make any generalizations about their electronic structures, as the solute-solvent interactions between the dyes of interest and these mixed solvent systems may not be indicative of a broader solvatochromic study. That said, a hypsochromic (blue) shift with increasing solvent polarity, or negative solvatochromism, is typically indicative of better stabilization of the ground state molecule by solvation than that of the excited state.[31]

Table 5.4. Chloroform and acetonitrile mixed solvent systems for HRS under Moderate reaction field changes.

Solvent System	χ_{CHCl3}	ε	n	Onsager Polarity	E_T^N
A (ACN)	0	37.50	1.346	0.9605	0.460
B	0.25	29.33	1.371	0.9497	0.473
C	0.50	21.16	1.396	0.9307	0.438
D	0.75	12.98	1.421	0.8887	0.386
E (CHCl$_3$)	1.00	4.81	1.446	0.7175	0.259

Note: E_T^N values are measured using the absorbance of Richardt's Dye in the solvent system

The $E_T(30)$ solvent polarity scale and its normalized counterpart E_T^N were developed by Prof. Christian Reichardt of Phillips University of Marburg is based on the

transition energy of a strongly negative solvatochromic pyridinium phenolate betaine dye (Figure 5.9), which was originally called dye 30.[31-32] The $E_T(30)$ polarity scale is calculated from the molar electronic transition energy of the dye 30 betaine dye dissolved in the solvent under analysis according to the following equation:

$$E_T(30) = \frac{hcN_A}{\lambda_{max}} = \frac{28591 \text{ kcal} \cdot \text{nm} \cdot \text{mol}^{-1}}{\lambda_{max}},$$ (Eq. 5.13)

where h is Planck's constant in kcal, c is the speed of light in nm, N_A is Avagadro's number, and λ_{max} is the wavelength of peak absorbance for the longest wavelength charge-transfer absorption $(\pi - \pi^*)$ of dye 30. The $E_T(30)$ values are put into a more convenient form by normalizing them using TMS and water as nonpolar and polar extremes according to the following equation:

$$E_T^N = \frac{E_T(\text{solvent}) - E_T(\text{TMS})}{E_T(\text{water}) - E_T(\text{TMS})}.$$ (Eq. 5.13)

Instead of assuming that the E_T^N values of the mixed solvent system can be estimated by a weighted average, the absorption of commercially available Betaine 30 was measured in each solvent (Figure 5.11) and the resulting E_T^N values were recorded in Table 5.4. It is worth noting that the peak absorbance of solvent system A and B show unexpected solvatochromism. Solvent A is acetonitrile and should be a more polar environment than solvent B (3:1 acetonitrile/chloroform), however the peak absorbance of betaine 30 in solvent A is red shifted with respect to the peak absorbance in solvent B.
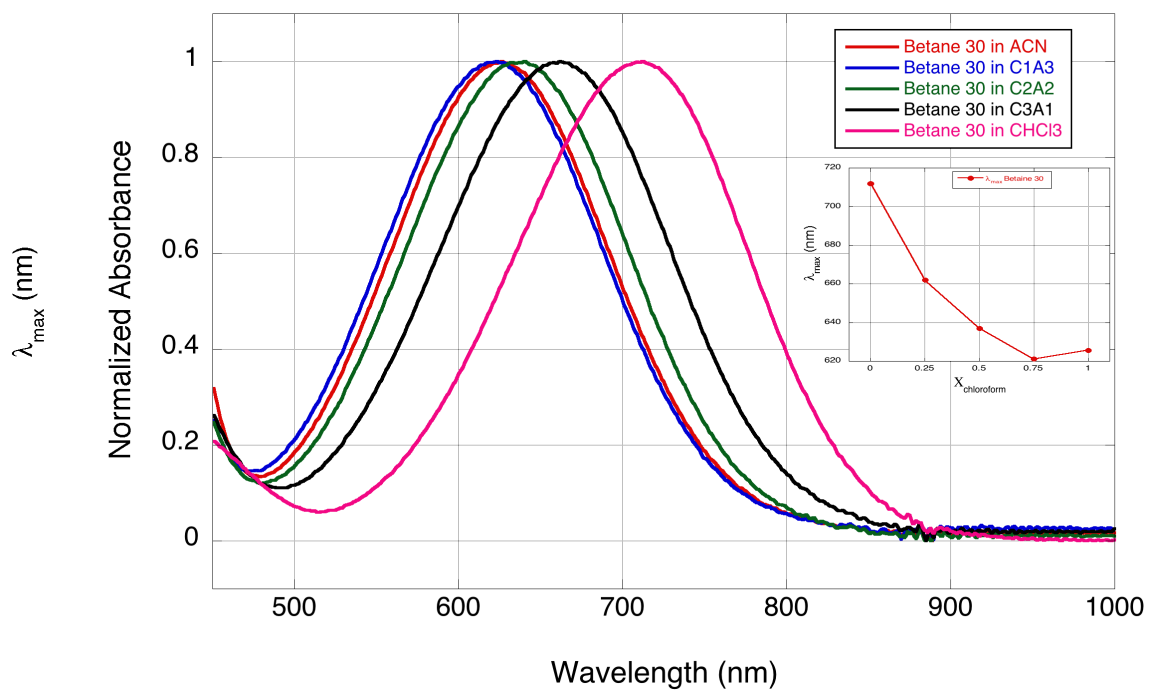
Figure 5.11. Normalized absorbance of Betaine 30 (Reichardt's dye) in acetonitrile/chloroform mixed solvent systems. Inset) peak absorbance as a function of the mole fraction of chloroform.
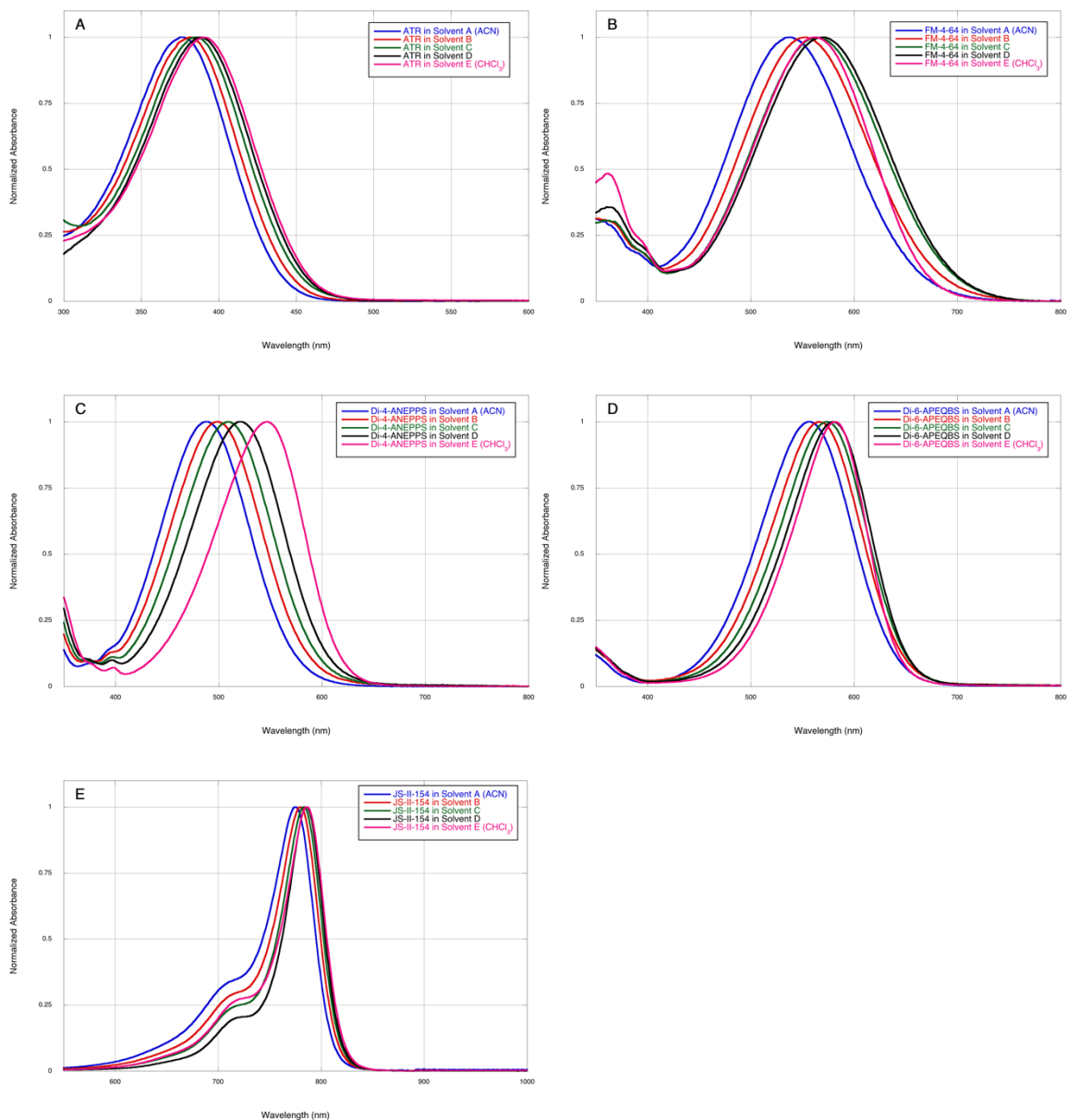
Figure 5.12. Electronic absorption spectra of dyes of interest in acetonitrile/chloroform mixed solvent systems: Solvent A (acetonitrile, blue traces), Solvent B (red traces), Solvent C (green traces), Solvent D (black traces), and solvent E (chloroform, pink traces). The compounds are A) ATR, B) FM-4-64, C) Di-4-ANEPPS, D) Di-6-APEQBS, and E) JS-II-154 (structures shown in Figure 5.9.)

The solvatochromic behavior of the dyes of interest can be related back to the solvent effects on the mixing of the neutral and charge separated wavefunctions according to valence bond – charge transfer theory (VB-CT).

5.5.7. Utilizing Symmetry Breaking as an Approach for Maximal Potential Sensitivity.

Polymethine dyes have been extensively studies for decades for nonlinear optical applications including all-optical switching, optical limiting, telecommunication, and multiphoton imaging. The steady state and nonlinear optical properties of polymethines are extremely dependent on the structural and electronic configuration of the π-electron system.[33-34] A typical symmetric polymethine is characterized by a nearly zero BLA, diminished first excited state energy, and. sharp absorption bands. As the length of the polymethine increases past a certain point, it will undergo a symmetry breaking transition where the BLA increases and charge is localized on the ends of the molecule. Spectroscopically, the sharp absorption band becomes dramatically broadened on the higher energy side, and may even show a hypsochromic shift altogether.[35]

Similarly, to the cyanine dyes, a merocyanine's electronic structure can be controlled by the donor and acceptor strength, and as mentioned earlier by solvation environment. For this reason, it is possible to design merocyanines at varying positions along the polyene-zwitterion continuum. In certain cases, it is also possible to stabilize a merocyanine dye at or near the cyanine limit.[36-38]

Both the symmetry breaking of a cyanine dye and the stabilization of a cyanine-like structure for a merocyanine both represent a large deviation of the bond length alternation from expectation. This large change could effect a sizeable change in SHG

efficiency. In an ideal case, the symmetry breaking, or cyanine-like structure stabilization would happen with a minimal change in field.

Azaazulene- and indole- terminated cyanines have been shown to exhibit this type of symmetry breaking in polar solvents.[36, 38-39] In addition, a recent paper by Pascal *et al.*[40] shows stabilization of merocyanines at or near the cyanine limit in a series of TCF-terminated merocyanines that have chalcogenopyrillium donor groups and a ring locked conjugated backbone. In an attempt to exploit both symmetry breaking and stabilization of a cyanine-like state, we investigated the photophysical properties of a pair of azaazulene dyes as shown in Figure 5.13. JS-II-164 is a symmetric azaazulene terminated heptamethine cyanine with a boron tetraaryl counter ion and JS-III-31 is a ring locked heptamethine merocyanine terminated with an azaazulene donor and a TCF acceptor group. Both azaazulene chromophores were synthesized by Janos Simon formerly of the Marder group.
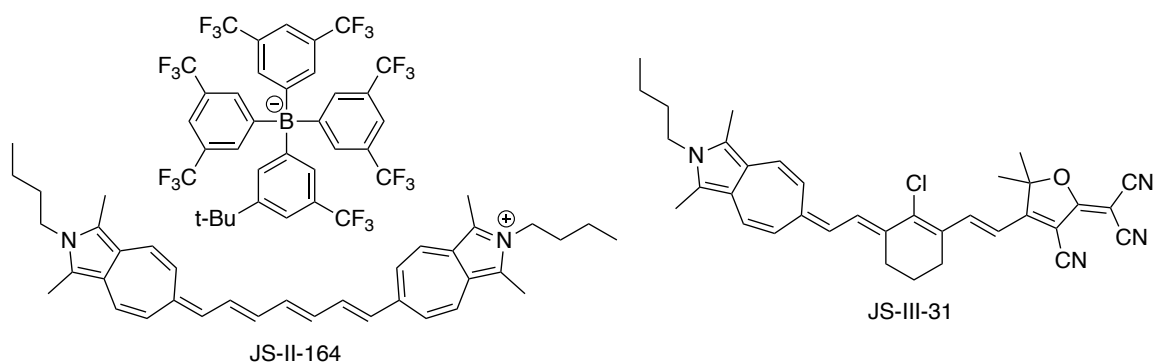
Figure 5.13. Chemical structures of azaazulene terminated nonlinear optical chromophores

The azaazulene cyanine, JS-II-164, shows the development of a high energy shoulder indicative of a charge-transfer (CT) absorbance band, as is shown in Figure 5.14.

The development of this shoulder is indicative of a profound shift in the electronic structure resulting from symmetry breaking.[35]
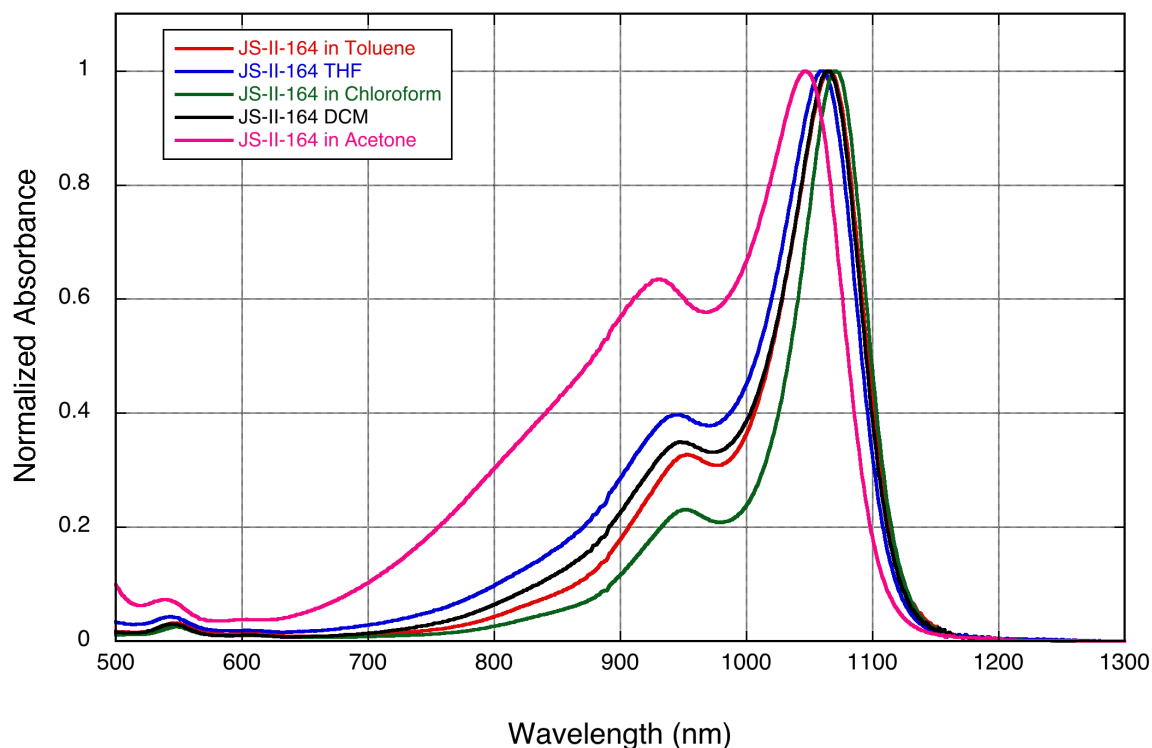
Figure 5.14. Normalized absorbance spectra of JS-II-164 toluene (red trace), tetrahydrofuran (blue trace), chloroform (green trace), dichloromethane (black trace), and acetone (pink trace)

When symmetry breaking occurs it causes a shift from a BLA of approximately zero to a non zero BLA. As is show in in Figure 5.4 this shift in electronic structure should be accompanied by an increase in β. Solvent dependent HRS measurements show a nearly 50% increase in β from THF to acetone (Table 5.5)

Table 5.5. Solvent dependent change in β for JS-II-164

Dye	Solvent	$\beta \times 10^{-48}$ $[C\ m^3\ V^{-2}]$	$\dfrac{(\beta_{\Delta E}^2 - \beta_0^2)}{\beta_0^2}$
JS-II-164	THF	9.4	183 %
	Acetone	15.8	

Note: error on figure of merit is ±21%

As is shown in Table 5.5, there is an enormous jump in β that takes pace as a result of the loss of symmetry in the azaazulene cyanine. While this chromophore is very promising, it will suffer from toxicity and solubility issues when translated into a cell or a membrane mimic. That said, symmetry breaking may be an important step towards SHG voltage sensing.
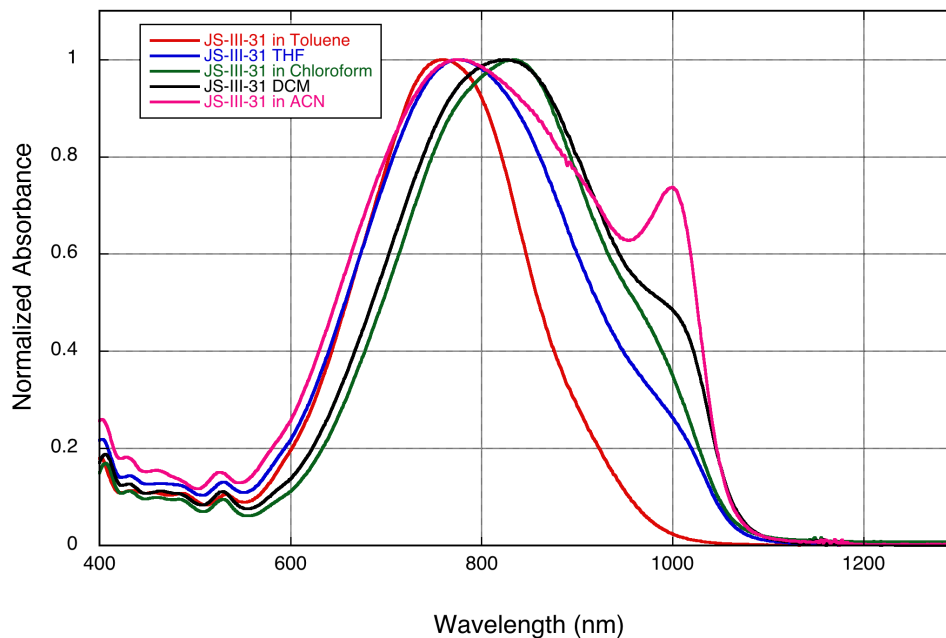
Figure 5.15. Normalized absorbance spectra of azaazulene-TCF merocyanine JS-III-31in toluene (red trace), tetrahydrofuran (blue trace), chloroform (green trace), dichloromethane (black trace), and acetonitrile (pink trace)

The azaazulene-TCF merocyanine, JS-III-31, shows stabilization of a cyanine-like electronic structure in polar solvents. As is shown in Figure 5.15, there is an appearance of a sharp red-shifted shoulder on the side of the charge-transfer absorption band that is indicative of a cyanine-like state. This state should coincide with a decrease in the BLA across the backbone. This decrease in BLA should cause the first hyperpolarizability to decrease as the cyanine – like structure becomes more stabilized.

Table 5.6. Solvent dependent change in hyperpolarizability for an azaazulene – TCF merocyanine, JS-III-31.

Dye	Solvent	β x 10^{-48} [C m^3 V^{-2}]	$\dfrac{(\beta_{\Delta E}^2 - \beta_0^2)}{\beta_0^2}$
JS-III-31	THF	12.1	-59 %
	Acetonitrile	7.8	

Note: error on figure of merit is ±21%

As was expected, the hyperpolarizability of JS-III-31 decreases nearly 36% when the solvent is changed from THF to ACN as is shown in Table 5.6.

5.6. Conclusions

The use of measured first and second hyperpolarizabilities for the estimation of SHG sensitivity is a promising start towards optimization of the SHG response to an action potential. Approaching the problem this way allows for considerations such as toxicity and membrane compatibility be neglected in pursuit of the underlying cause. The estimated static response based on the measured β and γ values is quite different from those reported in the literature. In out estimation of the sensitivity, the only factor considered was a static

electrooptic response. Changing nonlinearities, better estimation of the reaction field, and accounting for reorientation effects should make our estimated values better agree with the literature. Of note is the fact that in its present state, our static approach is able to correctly predict the sign of the sensitivity, which is based on the nonlinear refraction.

In our considerations of a field dependent response, it is apparent that with the exception of a few cyanine limit cases, the β component of the repose dwarfs the γ component. Our estimations based on the changing first hyperpolarizability are quite close to the literature values, especially in comparison to our static estimations. Our field dependent approach represents the only real way to investigate the potential of cyanine-like chromophores for voltage sensing applications, aside from actual cellular studies, or those in membrane mimics as will be presents in the following chapter. The more commonly used method of determining β is by EFISH which excludes symmetric molecules.

Finally, symmetry breaking / cyanine-like structure stabilization as approach seems quite promising. The two azaazulene chromophores, one cyanine and one merocyanine investigated show a nearly 200% increase in signal and a nearly -60% decrease in signal respectively. This approach, while promising presents some significant challenges, most pressing of which is a chromophore whose electronic structure is near the symmetry breaking / cyanine stabilization geometry when in a membrane.

5.7. Experimental Methods

5.7.1. Sample preparation

All samples for HRS and z-scan were prepared by dissolving in spectroscopic grade, or best available, solvents at such a concentration that all of the chromophore can dissolve. All measured samples were serial dilutions of the original solution, so losing dye by insolubility would significantly undermine reproducibility. Solutions were typically made in either 10 or 25 mL volumetric flasks and dilutions by glass volumetric micropipettes. The switch from all other methods, including syringing, measuring by weight and the use of a small graduated pipette, gave the greatest boost to reproducibility. All solutions were filtered through a 0.2 µm PTFE syringe filter (VWR) prior to measurement.

5.7.2. HRS and Z-scan measurements,

HRS measurements were taken on our home built HRS/TPEF setup using 1 cm special optical glass (SOG) cuvettes from Sterna cells and were referenced to neat solvent. The minimum integration time for any of the samples presented in this chapter was 50 s. Each HRS spectrum is recorded relative to a background of equal length to account for electronic noise. The absorbance of each sample was checked after each HRS measurement, and the sample replaced when noticeable degradation was present.

Z-scan measurements were recorded using the same solutions as for the HRS measurements, except in a 1 or 2 mm cuvette. Z-scan measurements were referenced daily to fused silica, ZnS, and ZnSe.

5.7.3. Synthesis

General

All materials and reagents were commercially available and used as received except where noted. Tetrahydrofuran was dried using a sodium-benzophenone ketyl pot and freshly distilled for each use. ^{1}H, ^{13}C, and ^{31}P NMR spectra were acquired on one of the following NMR spectrometers: Bruker Avance IIIHD-300 MHz Bruker Avance III-400 MHz, Bruker Avance IIIHD-500 MHz (with Prodigy cryoprobe), Bruker Avance IIIHD-700 MHz, Bruker Avance IIIHD-800 MHz spectrometers. Each NMR will list the field strength used. All chemical shifts are indirectly referenced TMS through the residual solvent peaks as reported in the literature.[41-42]

(*E*)-1-acetoxy-1,3-butadiene (**5.2**)

Crotonaldehyde (11.8 mL, 143 mmol) was added slowly to a stirred solution of potassium *tert*-butoxide (20.60 g, 183.6 mmol) in dry THF (100 mL) at -78 ˚C. The resulting solution began to turn yellow as the enolate was formed. After about 15 min, a solution of acetyl chloride (11.9 mL, 167 mmol) in THF (25 mL) was added dropwise to the enolate solution, which became dark orange. The reaction mixture was allowed to stir for 20 min before removing the cooling bath and quenching with water. The product was extracted with ether, washed with brine and saturated NaHCO$_3$. The extract was dried over MgSO$_4$, concentrated and purified by distillation to give 1-acetoxy-1,3-butadiene as a clear liquid (11.6 g, 73%) Bp 40 – 41 ˚C / 200 mtorr. R$_f$ (Et$_2$O / hexane, 1:2) = 0.5. ^{1}H NMR (500 MHz, CDCl$_3$) δ 7.39 (dq, *J* = 12.4, 0.7 Hz, 1 H), 6.26 (dddd, *J* = 16.9, 11.0, 10.3, 0.7 Hz, 1 H),

6.03 (ddt, J = 12.4, 11.0, 0.7 Hz, 1 H), 5.21 (ddt, J = 16.9, 1.6, 0.7 Hz, 1 H), 5.08 (ddt, J =

10.3, 1.5, 0.7 Hz, 1H), 2.14 (s, 3 H) ppm.

(E)-2-(3-bromopropenyl)-1,3-dioxolane (**5.4**)

Bromine (0.50 mL, 9.8 mmol) was added slowly to a stirred solution of **5.2** (1.10 g, 9.81

mmol) in dry DMF (8.0 mL) at -30 ˚C. After 15 minutes, a small sample of the reaction

mixture was worked up by extracting with ether and washing with saturated aqueous

$Na_2S_2O_3$. A GCMS showed that the conversion of **5.2** to (E)-4-bromobut-2-enal (**5.3**) was

complete. The crude **5.3** was used without purification. The reaction mixture was removed

from the dry ice bath, and ethylene glycol (5.50 mL 98.1 mmol) was added. The mixture

was stirred at room temperature until completion as monitored by GCMS. Once complete,

the reaction mixture was poured into aqueous $NaHCO_3$ (5%, 100 mL) and the product was

extracted with pentane (3 x 50 mL), dried over anhyd. $MgSO_4$, and concentrated under

vacuum. The crude product was purified by vacuum distillation to give **5.4** as a colorless

oil (1.12 g, 59%). Bp 78 – 80 ˚C / 200 mtorr. ^{1}H NMR (400 MHz, CDCl$_3$) δ 6.11 (dt, J =

15.3, 7.4 Hz, 1H), 5.74 (ddt, J = 15.3, 5.6, 1.1 Hz, 1H), 5.28 (d, J = 5.6 Hz, 1H), 3.94 (m,

6H).

Diethyl (E)-(3-(1,3-dioxolan-2-yl)allyl)phosphonate (**5.5**)

Triethylphosphite (1.30 mL, 7.52 mmol) was combined with dioxolane **5.4** (1.32 g, 6.84

mmol) in toluene (10 mL) and brought to reflux for 12 hours with stirring. Reaction

progress was monitored by GCMS. Once complete, product was purified by distilled under

vacuum to give **5.5** as a colorless oil (1.11 g, 65%). Bp 93 – 96 ˚C / 200 mtorr. ^{1}H NMR

(500 MHz, CDCl$_3$) δ 5.89 (sext, J = 7.4 Hz, 1H), 5.62 (dddt, J = 15.5, 6.1, 4.8, 1.3 Hz, 1H), 5.22 (dd, J = 6.0, 1.1 Hz, 1H), 4.09 (m, 2H), 3.98 – 3.85 (m, 2H), 2.16 (dd, J_{PH} = 22.0, J = 7.5 Hz, 2H), 1.29 (t, J = 7.1 Hz) ppm. . ^{31}P NMR (202.5 MHz, CDCl$_3$) δ 26.76 ppm.

(2E,4E)-5-(4-(diethylamino)phenyl)penta-2,4-dienal (**5.6**)

4-(diethylamino)benzaldehyde (0.14 g, 0.79 mmol) and phosphonate **5.5** (0.20 g, 0.80 mmol) were dissolved in dry THF (5 mL). To this solution, was added a solution of KO^{t}Bu (0.25 g, 2 mmol) in THF (5 mL), which caused an immediate color change. The reaction was allowed to stir at room temperature, and the progress was monitored by TLC (silica gel, diethyl ether). After about an hour the reaction was complete by TLC and was quenched by slowly adding water. The resulting quenched reaction mixture was cooled and deprotected by adding concentrated HCl (2 mL) with stirring. After another hour, the deprotected product was neutralized with NaOH and extracted in ether (3 x 25 mL). The extracts were combined, dried over sodium sulfate and the volatiles driven off on a rotary evaporator. Crude product was purified by recrystallization from isopropanol to give **5.6** as an orange powder (0.17 g, 97%). ^{1}H NMR (500 MHz, CDCl$_3$) δ 9.55 (d, J = 8.1 Hz, 1H), 7.37 (d, J = 8.9 Hz, 2H), 7.25 (dd, J = 15.0, 11.0 Hz, 1H), 6.93 (d, J = 15.3 Hz, 1H), 6.79 (ddd, J = 15.3, 11.0, 0.5 Hz, 1H), 6.64 (d, J = 9.0 Hz, 2H), 6.16 (dd, J = 15.1, 8.2 Hz, 1H), 3.40 (q, J = 7.1 Hz, 4H), 1.19 (t, J = 7.1 Hz, 3H).

(3-bromopropyl)triethylammonium bromide, (**5.7**)

To a solution of triethylamine (6.90 mL, 49.4 mmol) in acetonitrile (70 mL) was added 1,3-dibromopropane (10.0 mL, 98.8 mmol). The mixture was brought to reflux and stirred

for 4 hours. Product mixture allowed to cool and crystallization was initiated with the addition of methanol and ethyl ether. Filtered crystals were recrystallized from ethanol/ether to give **5.7** (14.0 g, 96 %) as a white crystalline solid. Mp 152-154 °C ^{1}H NMR (500 MHz, DMSO-d$_6$) δ 3.62 (t, $J = 6.3$ Hz, 2H), 3.26 (q, $J = 7.2$ Hz, 6H), 6.23 (m, 2H), 2.16 (m, 2H), 1.18 (t, $J = 7.2$ Hz, 9H).

4-Methyl-1-(3-(Triethylammonio)Propyl)Pyridinium Dibromide (**5.8**)

In a nitrogen flushed vial was combined (3-bromopropyl)triethyammonium bromide (5.00 g, 16.5 mmol) and 4-picoline (1.61 mL, 16.5 mmol). The mixture was heated to 125°C in an oil bath. The mixture became homogeneous after a few minutes and began to precipitate shortly thereafter. After 35 minutes of reaction time, the mixture was dissolved in boiling methanol and layered with THF. The crystalline product was filtered and washed with THF then dried under vacuum to give **5.8** (5.20 g, 80%) as an off white solid. ^{1}H NMR (500 MHz, CD$_3$CN) δ 9.01 (d, $J = 6.8$ Hz, 2H), 8.02 (d, $J = 6.4$ Hz, 2H), 4.75 (t, $J = 7.9$ Hz, 2H), 3.42 (q, $J = 7.3$ Hz, 8H), 2.73 (s, 3H), 2.52 (m, 2H), 1.37 (t, $J = 7.3$ Hz, 9H).

FM-4-64

5.6 (75 mg, 0.33 mmol) and **5.8** (130 mg, 0.33 mmol) were dissolved in ethanol (2 mL) with stirring under nitrogen. To this solution was added piperidine (0.2 mL) by syringe. The mixture was stirred overnight under nitrogen then concentrated. The resulting salt was precipitated with dry ether. After solvent removal, the resulting product was again dissolved in ethanol and precipitated with ether before being filtered and dried under nitrogen to give **FM-4-64** (145 mg, 77%) as a dark purple / black solid.

190

5.8. References

[1]   Peterka, D. S.; Takahashi, H.; Yuste, R., Imaging voltage in neurons. *Neuron* **2011,** *69* (1), 9-21.

[2]   Nuriya, M.; Jiang, J.; Nemet, B.; Eisenthal, K. B.; Yuste, R., Imaging membrane potential in dendritic spines. *Proc Natl Acad Sci U S A* **2006,** *103* (3), 786-90.

[3]   Theer, P.; Denk, W.; Sheves, M.; Lewis, A.; Detwiler, P. B., Second-Harmonic Generation Imaging of Membrane Potential with Retinal Analogues. *Biophysical Journal* **2011,** *100* (1), 232-242.

[4]   Nemet, B. A.; Nikolenko, V.; Yuste, R. In *Second harmonic imaging of membrane potential of neurons with retinal*, SPIE: 2004; p 9.

[5]   Pons, T.; Mertz, J., Membrane potential detection with second-harmonic generation and two-photon excited fluorescence: A theoretical comparison. *Optics Communications* **2006,** *258* (2), 203-209.

[6]   Reeve, J. E.; Anderson, H. L.; Clays, K., Dyes for biological second harmonic generation imaging. *Phys Chem Chem Phys* **2010,** *12* (41), 13484-98.

[7]   Hodgkin, A. L.; Huxley, A. F., Action Potentials Recorded from Inside a Nerve Fibre. *Nature* **1939,** *144*, 710.

[8]   Offner, F. F., Kinetics of Excitable Membranes. *The Journal of General Physiology* **1970,** *56* (2), 272.

[9]   Hodgkin, A. L.; Huxley, A. F., Resting and action potentials in single nerve fibres. *The Journal of Physiology* **1945,** *104* (2), 176-195.

[10]   Hodgkin, A. L.; Huxley, A. F., A quantitative description of membrane current and its application to conduction and excitation in nerve. *The Journal of Physiology* **1952,** *117* (4), 500-544.

[11]   Barnett, M. W.; Larkman, P. M., The action potential. *Practical Neurology* **2007,** *7* (3), 192.

[12]   Byrne, J. H.; Roberts, J. L., *From Molecules to Networks : An Introduction to Cellular and Molecular Neuroscience*. Academic Press: Amsterdam, 2004.

[13]   Bourhill, G.; Bredas, J.-L.; Cheng, L.-T.; Marder, S. R.; Meyers, F.; Perry, J. W.; Tiemann, B. G., Experimental Demonstration of the Dependence of the First Hyperpolarizability of Donor-Acceptor-Substituted Polyenes on the Ground-State Polarization and Bond Length Alternation. *Journal of the American Chemical Society* **1994,** *116* (6), 2619-2620.

[14]   Gorman, C. B.; Marder, S. R., An investigation of the interrelationships between linear and nonlinear polarizabilities and bond-length alternation in conjugated organic molecules. *Proceedings of the National Academy of Sciences* **1993,** *90* (23), 11297.

[15]   Marder, S. R.; Cheng, L.-T.; Tiemann, B. G.; Friedli, A. C.; Blanchard-Desce, M.; Perry, J. W.; Skindhøj, J., Large First Hyperpolarizabilities in Push-Pull Polyenes by Tuning of the Bond Length Alternation and Aromaticity. *Science* **1994,** *263* (5146), 511.

[16]   Marder, S. R.; Perry, J. W.; Tiemann, B. G.; Gorman, C. B.; Gilmour, S.; Biddle, S. L.; Bourhill, G., Direct observation of reduced bond-length alternation in donor/acceptor polyenes. *Journal of the American Chemical Society* **1993,** *115* (6), 2524-2526.

[17]   Meyers, F.; Marder, S. R.; Pierce, B. M.; Bredas, J. L., Electric Field Modulated Nonlinear Optical Properties of Donor-Acceptor Polyenes: Sum-Over-States Investigation of the Relationship between Molecular Polarizabilities (.alpha., .beta., and .gamma.) and Bond Length Alternation. *Journal of the American Chemical Society* **1994,** *116* (23), 10703-10714.

[18]   Kay, A. J.; Woolhouse, A. D.; Zhao, Y.; Clays, K., Synthesis and linear/nonlinear optical properties of a new class of 'RHS' NLO chromophore. *Journal of Materials Chemistry* **2004,** *14* (8), 1321-1330.

[19]   Albota, M.; Beljonne, D.; Brédas, J.-L.; Ehrlich, J. E.; Fu, J.-Y.; Heikal, A. A.; Hess, S. E.; Kogej, T.; Levin, M. D.; Marder, S. R.; McCord-Maughon, D.; Perry, J. W.; Röckel, H.; Rumi, M.; Subramaniam, G.; Webb, W. W.; Wu, X.-L.; Xu, C., Design of Organic Molecules with Large Two-Photon Absorption Cross Sections. *Science* **1998,** *281* (5383), 1653.

[20]   Onsager, L., Electric Moments of Molecules in Liquids. *Journal of the American Chemical Society* **1936,** *58* (8), 1486-1493.

[21]   Wadsworth, W. S.; Emmons, W. D., The Utility of Phosphonate Carbanions in Olefin Synthesis. *Journal of the American Chemical Society* **1961,** *83* (7), 1733-1738.

[22]   Maryanoff, B. E.; Reitz, A. B., The Wittig olefination reaction and modifications involving phosphoryl-stabilized carbanions. Stereochemistry, mechanism, and selected synthetic aspects. *Chemical Reviews* **1989,** *89* (4), 863-927.

[23]   Ballato, M. C. G.; John, The Handbook of Photonics, Second Edition. **2018**, 1-1020.

[24]   Kajzar, F.; Ledoux, I.; Zyss, J., Electric-field-induced optical second-harmonic generation in polydiacetylene solutions. *Physical Review A* **1987,** *36* (5), 2210-2219.

[25]   Campo, J.; Desmet, F.; Wenseleers, W.; Goovaerts, E., Highly sensitive setup for tunable wavelength hyper-Rayleigh scattering with parallel detection and calibration data for various solvents. *Opt. Express* **2009,** *17* (6), 4587-4604.

[26]   Schuster, P.; Jakubetz, W.; Marius, W. In *Molecular models for the solvation of small ions and polar molecules*, Topics in Current Chemistry, Berlin, Heidelberg, 1975//; Springer Berlin Heidelberg: Berlin, Heidelberg, 1975; pp 1-107.

[27]   Wang, X.; Dao, R.; Yao, J.; Peng, D.; Li, H., Modification of the Onsager Reaction Field and Its Application on Spectral Parameters. *ChemPhysChem* **2017,** *18* (7), 763-771.

[28]   Frisch, M. J.; Trucks, G. W.; Schlegel, H. B.; Scuseria, G. E.; Robb, M. A.; Cheeseman, J. R.; Scalmani, G.; Barone, V.; Petersson, G. A.; Nakatsuji, H.; Li, X.; Caricato, M.; Marenich, A. V.; Bloino, J.; Janesko, B. G.; Gomperts, R.; Mennucci, B.; Hratchian, H. P.; Ortiz, J. V.; Izmaylov, A. F.; Sonnenberg, J. L.; Williams; Ding, F.; Lipparini, F.; Egidi, F.; Goings, J.; Peng, B.; Petrone, A.; Henderson, T.; Ranasinghe, D.; Zakrzewski, V. G.; Gao, J.; Rega, N.; Zheng, G.; Liang, W.; Hada, M.; Ehara, M.; Toyota, K.; Fukuda, R.; Hasegawa, J.; Ishida, M.; Nakajima, T.; Honda, Y.; Kitao, O.; Nakai, H.; Vreven, T.; Throssell, K.; Montgomery Jr., J. A.; Peralta, J. E.; Ogliaro, F.; Bearpark, M. J.; Heyd, J. J.; Brothers, E. N.; Kudin, K. N.; Staroverov, V. N.; Keith, T. A.; Kobayashi, R.; Normand, J.; Raghavachari, K.; Rendell, A. P.; Burant, J. C.; Iyengar, S. S.; Tomasi, J.; Cossi, M.; Millam, J. M.; Klene, M.; Adamo, C.; Cammi, R.; Ochterski, J. W.; Martin, R. L.; Morokuma, K.; Farkas, O.; Foresman, J. B.; Fox, D. J. *Gaussian 16 Rev. B.01*, Wallingford, CT, 2016.

[29]   Deora, N.; Carlier, P. R., Computational Studies of Ion-Pair Separation of Benzylic Organolithium Compounds in THF: Importance of Explicit and Implicit Solvation. *The Journal of Organic Chemistry* **2010,** *75* (4), 1061-1069.

[30]   Kuzyk, M. G., Physical Limits on Electronic Nonlinear Molecular Susceptibilities. *Physical Review Letters* **2000,** *85* (6), 1218-1221.

[31]   Reichardt, C., Solvatochromic Dyes as Solvent Polarity Indicators. *Chemical Reviews* **1994,** *94* (8), 2319-2358.

[32]   Dimroth, K.; Reichardt, C.; Siepmann, T.; Bohlmann, F., Über Pyridinium-N-phenol-betaine und ihre Verwendung zur Charakterisierung der Polarität von Lösungsmitteln. *Justus Liebigs Annalen der Chemie* **1963,** *661* (1), 1-37.

[33]   Gieseking, R. L.; Ravva, M. K.; Coropceanu, V.; Brédas, J.-L., Benchmarking Density Functional Theory Approaches for the Description of Symmetry Breaking in Long Polymethine Dyes. *The Journal of Physical Chemistry C* **2016,** *120* (18), 9975-9984.

[34]   Gieseking, R. L.; Risko, C.; Brédas, J.-L., Distinguishing the Effects of Bond-Length Alternation versus Bond-Order Alternation on the Nonlinear Optical

Properties of π-Conjugated Chromophores. *The Journal of Physical Chemistry Letters* **2015,** *6* (12), 2158-2162.

[35] Tolbert, L. M.; Zhao, X., Beyond the Cyanine Limit: Peierls Distortion and Symmetry Collapse in a Polymethine Dye. *Journal of the American Chemical Society* **1997,** *119* (14), 3253-3258.

[36] Bouit, P.-A.; Aronica, C.; Toupet, L.; Le Guennic, B.; Andraud, C.; Maury, O., Continuous Symmetry Breaking Induced by Ion Pairing Effect in Heptamethine Cyanine Dyes: Beyond the Cyanine Limit. *Journal of the American Chemical Society* **2010,** *132* (12), 4328-4335.

[37] Würthner, F.; Archetti, G.; Schmidt, R.; Kuball, H.-G., Solvent Effect on Color, Band Shape, and Charge-Density Distribution for Merocyanine Dyes Close to the Cyanine Limit. *Angewandte Chemie International Edition* **2008,** *47* (24), 4529-4532.

[38] Hu, H.; Przhonska, O. V.; Terenziani, F.; Painelli, A.; Fishman, D.; Ensley, T. R.; Reichert, M.; Webster, S.; Bricks, J. L.; Kachkovski, A. D.; Hagan, D. J.; Van Stryland, E. W., Two-photon absorption spectra of a near-infrared 2-azaazulene polymethine dye: solvation and ground-state symmetry breaking. *Physical Chemistry Chemical Physics* **2013,** *15* (20), 7666-7678.

[39] Masunov, A. E.; Anderson, D.; Freidzon, A. Y.; Bagaturyants, A. A., Symmetry-Breaking in Cationic Polymethine Dyes: Part 2. Shape of Electronic Absorption Bands Explained by the Thermal Fluctuations of the Solvent Reaction Field. *The Journal of Physical Chemistry A* **2015,** *119* (26), 6807-6815.

[40] Pascal, S.; Getmanenko, Y. A.; Zhang, Y.; Davydenko, I.; Ngo, M. H.; Pilet, G.; Redon, S.; Bretonnière, Y.; Maury, O.; Ledoux-Rak, I.; Barlow, S.; Marder, S. R.; Andraud, C., Design of Near-Infrared-Absorbing Unsymmetrical Polymethine Dyes with Large Quadratic Hyperpolarizabilities. *Chemistry of Materials* **2018,** *30* (10), 3410-3418.

[41] Fulmer, G. R.; Miller, A. J. M.; Sherden, N. H.; Gottlieb, H. E.; Nudelman, A.; Stoltz, B. M.; Bercaw, J. E.; Goldberg, K. I., NMR Chemical Shifts of Trace Impurities: Common Laboratory Solvents, Organics, and Gases in Deuterated Solvents Relevant to the Organometallic Chemist. *Organometallics* **2010,** *29* (9), 2176-2179.

[42] Gottlieb, H. E.; Kotlyar, V.; Nudelman, A., NMR Chemical Shifts of Common Laboratory Solvents as Trace Impurities. *The Journal of Organic Chemistry* **1997,** *62* (21), 7512-7515.

CHAPTER 6

CHROMOPHORES WITH LARGE HYPERPOLARIZABILITIES FOR THE SENSING AND IMAGING OF TRANSMEMBRANE POTENTIALS IN MEMBRANE ANALOGUES

6.1. Introduction

Investigating the function of neural circuits in the human brain is fundamentally important for understanding brain disease, psychiatric disorders, movement disorders, and addiction. Although the spatial relationships of neurons are important for understanding their function, directly observing electrical communication within and amongst neurons is critical for complete understanding of neural circuitry.[1] The electrical communication between two neurons, called the action potential, is a sub millisecond redistribution of ions across the plasma membrane, caused by the opening/closing of gated ion channels[2]. The transmembrane potential associated with the imbalance of K+ ions across the membrane is described by the Nernst equation (Eq. 6.1).

$$V_{membrane} = \frac{RT}{zF} \ln\left(\frac{\left[K^+ \right]_{outside}}{\left[K^+ \right]_{inside}} \right) \qquad \text{(Eq. 6.1)}$$

In the above Nernst equation, R and F are the universal gas and Faraday constants respectively, T is the temperature in Kelvin, and z is the charge of the mobile ion. For the

[K$^+$] values, inside and outside designate the concentration of potassium ions on the inside and outside the membrane before equilibrium is reached.

Early characterization of the electrical characteristics of biological membranes in the late 1930s showed that biological membranes function more or less as a capacitor, which a capacitance per unit area of 1 μF/cm^2.[3] The capacitance of a cell membrane can be related to the dielectric constant of said membrane by the following equation:

$$\frac{C}{A} = \frac{\kappa \varepsilon_0}{d},$$ (Eq. 6.2)

where C is the capacitance, A is the area, ε_0 is the permittivity of free space, d is the thickness and κ is the dielectric constant of the membrane. The dielectric constant of a cell membrane is a little over three times larger than that of a lipid bilayer by itself. This discrepancy is due to the presence of active proteins which establish ion gradients between the cell and its environment.

Phospholipid vesicles are widely accepted as membrane analogues through-out the literature.[4-6] They offer the advantages of a similar solvation environment to biological membranes as well as being tailorable to applications of interest. For instance giant unilamellar vesicles (GUV) are used routinely as a membrane analogue for microscopy applications because they can actually be created in similar sizes to cells and can be fixed to slides and otherwise processed similarly.[5] Another major benefit of vesicles over actual cells is that there is little effort or equipment required for maintain healthy stock. When the vesicles are no longer behaving correctly the can simply be remade.

Two of the biggest advantages that vesicles offer over living cells that are of particular import to the study at hand are the ability to exclude toxicity from consideration and the ability to mimic an action potential. The exclusion of toxicity may seem like kicking the can down the road if all goes well, but it allows the chromophores to be designed with their electronic structure as the main consideration. In the course of this project, collaborators from the Marder group learned this the hard way when they went to Columbia University to measure actual neurons with Prof. Rafael Yuste. All eleven or so chromophores killed their entire culture of neurons within minutes. Toxicity is crucially important to consider before making *in vitro or in vivo* measurements, but at the early stages of our investigation, neglecting toxicity concerns allowed for a much broader investigation. The other advantage mentioned above is the ability to mimic an action potential. As will be discussed in the following sections, transmembrane potential meant to mimic an action potential can be created by the addition of an ionophore. This action potential is created more or less by the same mechanism as in neurons. This artificial action potential, coupled with the membranes being of roughly equivalent thicknesses, it is possible to create fields that are on the order of the actual fields experienced during an action potential.

6.2. Background

Second harmonic generation (SHG) imaging is well suited for investigating neural activity as it can be tailored to the biological window and because the change in electric field will directly impact the response of SHG active chromophores. The SHG response

is quadratically dependent on the hyperpolarizability (β) and number density of the chromophore as well as the laser intensity. In the presence of an electric field, the SHG signal is also dependent on the second hyperpolarizability (γ) and the magnitude of the electric field.

A common method for the estimation of SHG sensitivity in living cells is the patch-clamp method.[7] This technique involves the using electrodes to vary the voltage across a giant unilamellar vesicle, hemispherical lipid bilayers (Figure 6.1) or actual cells at the focal point of an intense laser beam. This is a complicated experiment that does not lend itself well to screening applications and can be impacted greatly by the toxicity of the dyes of interest. As an alternative to varying the membrane potential with electrodes, the electrochemical gradient can be varied to effect a similar change.
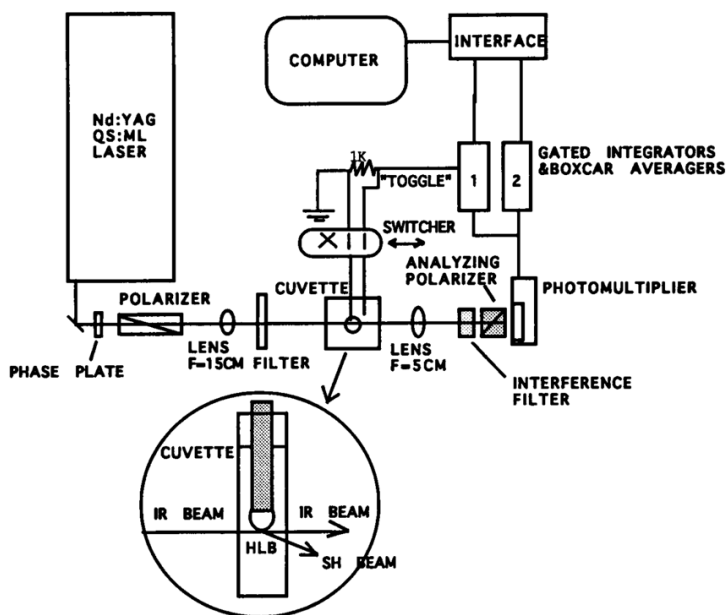
Figure 6.1. Optical set up for potential sensing in hemispherical lipid bilayers. Reprinted from Biophysical Journal, Vol 65, O. Bouevitch,A. Lewis,I. Pinevsky,J.P. Wuskell,L.M. Loew, Probing membrane potential with nonlinear optics, Pages 672-679., Copyright (1993), with permission from Elsevier.

The formation of phospholipid vesicles in buffers of varying K^+ concentration allows for the formation of a K^+ ion gradient. The addition of a K^+ selective ionophore, such as Valinomycin[8], allows the flow of K^+ ions down their concentration gradient, generating a Nernst potential.

6.2.1. Neuronal Transmembrane Potentials During an Action Potential

The action potential is caused by the opening and closing of membrane ion channels which cause a rapid redistribution of charges across a neuronal membrane. These changes occur on a fairly fast time scale, usually sub-millisecond, and result in a transmembrane potential change of about 100 mV. The resulting membrane potential change occurs over a very small distance, only a few nanometers, giving rise to significant electric field changes. These fields are typically on the order of $10^5 - 10^6$ V/cm[2].

Before action potential, a neuron begins at the resting potential of -70 mV, then depolarizes to +40 mV. When reestablishing the resting potential, the neuron will overshoot and the potential will hit a minimum of about -90 mV. With a neuron's phospholipid bilayer about 4 nm thick, this results in a change in electric field on the order of 10^5 V/cm [2].

6.2.2. Formation of Phospholipid Vesicles

Being amphipathic, or possessing both hydrophobic and hydrophilic properties, phospholipids have the ability to spontaneously assemble themselves into orientations which minimize the interaction between the aqueous environment and their hydrophobic

tails. This can be seen at the interface between oil droplets in water or even at the air-water interface[3].

While they form spontaneously, a key aspect of using vesicles as a membrane analog is to form them in such a way that it is possible to control the size, shape, and number of lamellae present. There are countless methods for the formation of lipid vesicles and these methods are typically specific to the size of the desired vesicle. Small unilamellar vesicles (SUV) are commonly produced by sonication, medium unilamellar vesicles (MUV) by extrusion, and giant unilamellar vesicles (GUV) by either extrusion or by electroformation.[6] The electroformation of lipid bilayers typically is accomplished by applying an electric field across two electrodes which are immersed in a mixture of the lipids of interest and aqueous buffer.[5-6, 9]

An alternative method, first described in the early 1970s, involves the injection of an ethanolic solution of phospholipids into the buffer of interest.[4, 10-11] This method offers some significant advantages in terms of a ease of preparation and tunability of the vesicle size based on the concentration.

6.2.3. Creation of Potassium Ion Gradient and Transmembrane Potentials

As has been discussed in previous sections and in chapter 5, a neuron generates an action potential by rapidly changing the concentration of Na^+ and K^+ ions on the inside and outside of the cell. In order to establish a transmembrane potential across phospholipid vesicles, it is necessary to create an imbalance in the charge on either side of the membrane. Simply creating vesicles with varying concentrations of Na^+ and K^+ ions on the inside and the outside of the vesicle will not suffice. Even though there is an

imbalance in the composition, there is still a negative charge for every positive one. In order for an imbalance of charge to be established, there needs to be a way for the monovalent cations to move from the interior of the vesicle to the exterior, or vice versa.

An ion flux across a lipid bilayer can be generated using chemical means by either neutral carriers like valinomycin or by the formation of transmembrane structures, such as gramicidin.[12-13] Both of these two ionophores are relatively specific to a single monovalent cation. Gramicidin is selective for sodium ions and valinomycin for potassium ions. Both ionophores are commonly used for generating transmembrane potentials for Fluorescent membrane potential sensing experiments.[12, 14-16] Valinomycin, in particular, was instrumental in the ground breaking work of Loew towards potential sensitive fluorescent probes.[12, 16-20] It is generally accepted that valinomycin, like most neutral carriers binds to its target ion, in this case K^+ and transports it across the membrane. The kinetics of this ferry service can be described by the basic kinetic model for the carrier mechanism which was developed by Widdas in the early 1950s.[21-22] The basic model asserts that the carrier exists in four states: it can be free or complexed to its ion, and either of these states can be free or bound to the membrane. The basic kinetic model's aim is to quantify the rates of transition between the four states and in so doing describe the kinetics of the total carrier process.[23] The crystal structure of free valinomycin shows a binding pocket for the K^+ ion (Figure 6.2)[24].
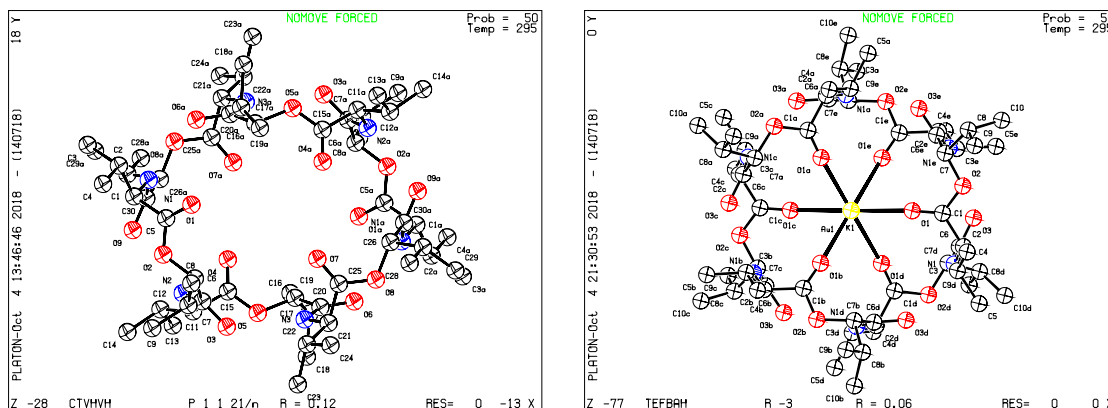
Figure 6.2. Crystal structure of free Valinomycin free and bound to K, reproduced from deposited structure CCDC 1132030 from Vasil'ev, A.D.,Shibanova, T.A., Andrianov, V.I., Simonov, V.I., Sanasaryan, A.A., Ivanov, V.T., Ovchinnikov, Yu.A. *Bioorganicheskaia Khimiia*, 1978, 4, 1157 and CCDC 1268637 from V.Z.Pletnev, I.N.Tsygannik, Yu.D.Fonarev, I.Yu.Mikhaylova, Yu.V.Kulikov, V.T.Ivanov, D.A.Lengs, V.L.Dyueks, *Bioorganicheskaia Khimiia*, 1995, 21, 828.

In the work presented in this chapter, the kinetics and general mechanism of valinomycin play almost no role. For the purposes of this work, valinomycin can be thought of as a simple dodecadepsipeptide ionophore, which is K^+ specific and well established in the literature. The formation of a transmembrane potential is represented schematically in Figure 6.3, where differing concentrations of K_2SO_4 on either side of the membrane lead to an imbalance in charge as potassium ions flow down their concentration gradient, leaving the sulfate, which is too large, behind.
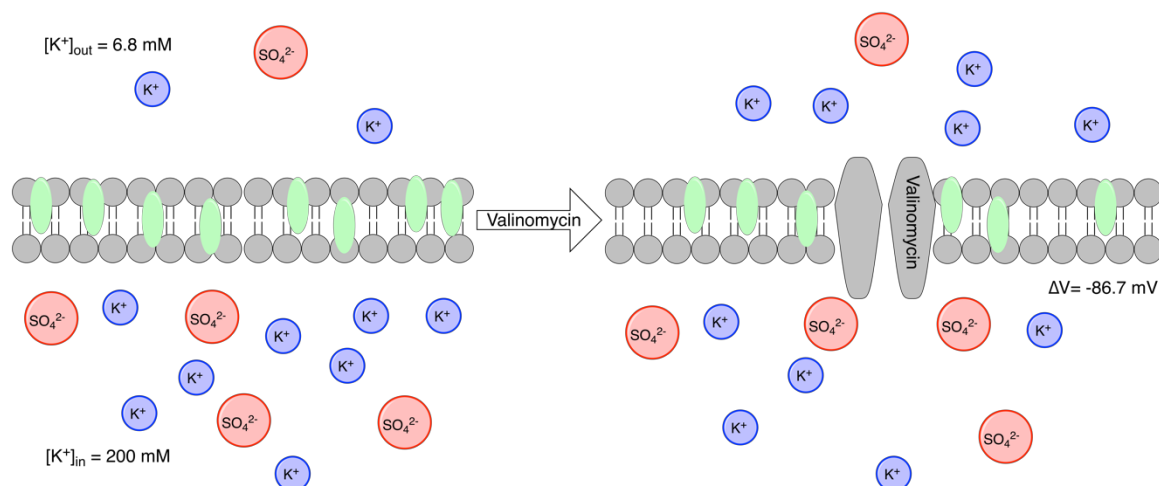
Figure 6.3. Establishment of transmembrane potential by the addition of Valinomycin

The valinomycin/potassium method of transmembrane potential generation is ideal for this study for a number of reasons. Firstly, as is discussed in the previous chapter, it is hard to mimic fields on the order of 10^5 V/cm using reaction fields, and because they are dependent on the dipole moment of the dye of interest, the resulting field will be different for each dye analyzed. Secondly, other methods of modulating membrane potential, such as the patch clamp method and the hemispherical bilayer method do not lend themselves easily to screening type applications and would require huge modifications to our HRS/TPEF setup.

6.3. Results and Discussion

6.3.1. Production and Characterization of Phosphatidyl Choline Vesicles

Phosphatidylcholine vesicles were produced by two methods: electroformation and ethanol injection method. First, GUVs were prepared by the electroformation method on ITO coated glass.[5, 9] In order to create the sandwich cell necessary for the

electroformation method, spacers were cast using polydimethysiloxane (PDMS, Sylgard

184) and were about 1 mm thick. The voltage was applied using a HP function generator

set to a voltage of 2.0 V with a frequency of 10 Hz, applied voltage and frequency were

measured using a Tektronics oscilloscope and monitored periodically throughout the 1 –

3 hour runs.
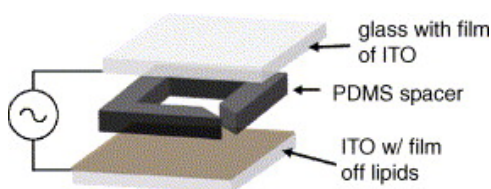
Figure 6.4. Schematic representation of the ITO coated glass sandwich cell used for the electroformation of phopsphatidy choline vesicles. Reprinted from Colloids and Surfaces B: Biointerfaces, Vol 42, Estes, Daniel J., and Mayer, Michael. Electroformation of giant liposomes from spin-coated films of lipids, Pages 115-123., Copyright (2005), with permission from Elsevier.

GUVs prepared in this way were stained with merocyanine 540 and imaged by

confocal and fluorescence microscopy. A composite image of the bright field and

fluorescence micrographs show that the dye is localized in the membrane of the GUVs

and that the electroformation of phosphatidyl choline under our conditions gave rise to

extremely variable vesicle size.
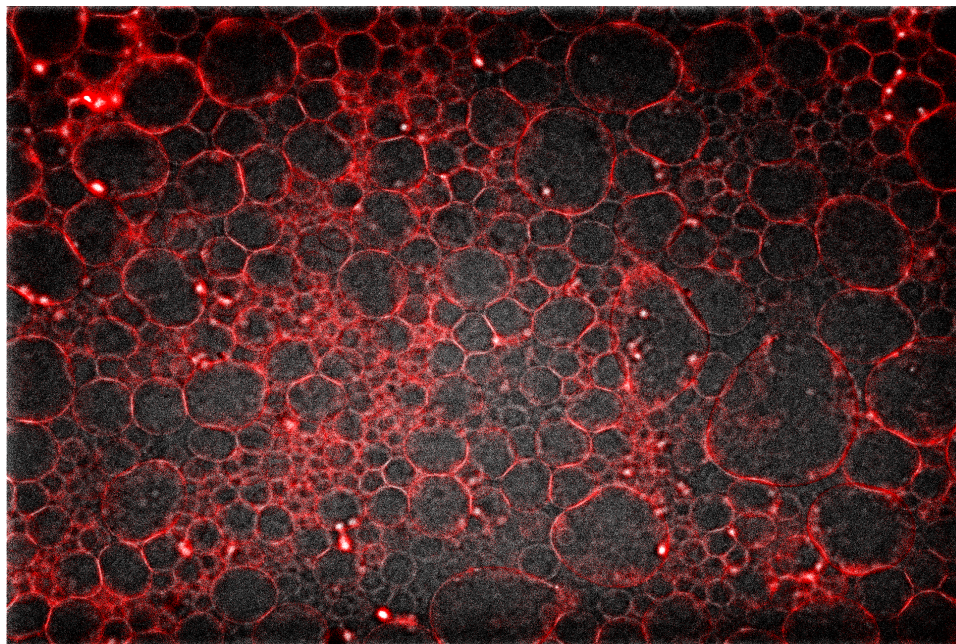
Figure 6.5. Composite image of brighfield (greyscale) and fluorescence (red)confocal micrographs showing the resulting electroformed GUVs.

The electroformed vesicles presented two major issues, first they were extremely variable in size and second they were difficult to remove from the substrate. This method may be ideal for confocal microscopy based studies. All attempts at electroformation of GUVs yielded similar results, so the actual size dispersion was never measured. The electroformed GUVs did serve one fairly important purpose: they gave a visual check for dye crashing out and a qualitative check of dye localization.

For potential sensitivity studies, more uniform vesicles were needed. The ethanol injection method was ideally suited to our purposes as it gave uniform, controllable[4], and buffer suspended vesicles. The ethanol injection method involved dissolving the phospholipids, either dioleylphosphatidylcholine, DOPC, or egg phosphatidylcholine, ePC, in absolute ethanol to make an approximately 30 mM solution. The lipid solution was injected by syringe pump into a ten-fold excess of buffer over the course of 15

minutes. The resulting vesicles were stirred for a minimum of 3 hours before being diluted again for measurement. In order to generate the transmembrane potential, vesicles were prepared in one of two buffers, a high K^+ concentration buffer (200 mM) or a low K^+ concentration buffer (2 mM), which contained an adequate amount of sucrose to maintain the same osmolarity as the high K^+ concentration buffer, these vesicle solutions are referred to as high $[K^+]$ vesicles and low $[K^+]$ vesicles respectively. Both vesicle suspensions were prepared in 20 mM HEPES-Tris buffer at pH 7.0. The buffers had to be made from HEPES free acid and tris base so as to not introduce any additional monovalent cations that would affect the generated Nernst potential.

The high $[K^+]$ and low $[K^+]$ vesicles were diluted 40-fold into a mixture of the high and low potassium buffers that was prepared to give a specific Nernst potential. The extremes of the range of possible transmembrane potentials is -86 mV when high $[K^+]$ vesicles are diluted 40-fold into low potassium concentration buffer and +117 mV when low $[K^+]$ vesicles are diluted 40-fold into high potassium concentration buffer. The sign of the potential indicates the excess charge on the inside of the vesicle as is depicted in Figure 6.3. The size of the vesicles was unaffected by the potential they were set up to have and was in the 50 – 100 nm range as determined by dynamic light scattering.

6.3.2. Characterization of Valinomycin-Mediated Transmembrane potentials with

Common Fluorescent Potential sensor diS-C$_2$(5)
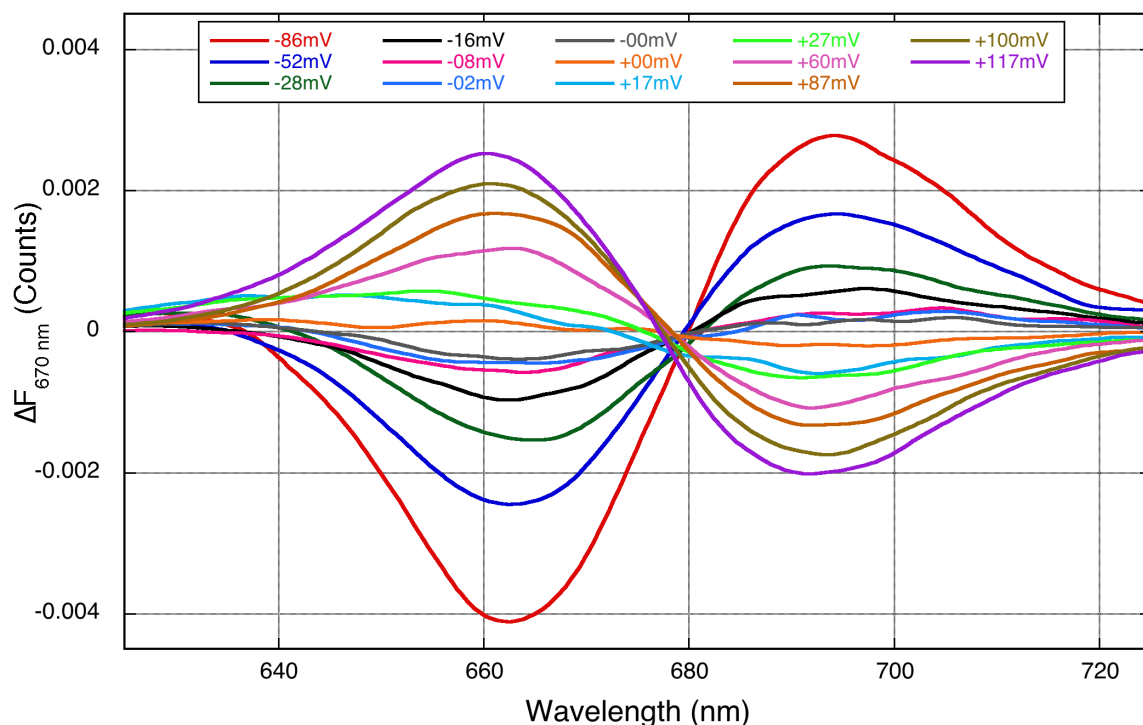
Figure 6.6. Change in DiS-C$_2$(5) fluorescence at 670 nm (normalized by area) with the addition of Valinomycin to dye incorporated into the membranes of DOPC vesicles (80-100 nm diameter) prepared to give a wide range of Nernst potentials.

To demonstrate the efficacy and calibrate the membrane potential generated by varying K$^+$ concentration, the fluorescence of a well-established potentiometric fluorophore, DiSC$_2$(5) [8, 25], was measured in DOPC vesicles of varying K$^+$ gradients before and after the addition of valinomycin. The change in fluorescence intensity, normalized by area, was dependent on the generated Nernst potential.[19] In order to make sure that the addition of valinomycin in ethanol was not the cause of the change in

fluorescence, two "0 mV" samples were prepared by diluting the high and low [K$^+$]

vesicles 40 – fold in more of the same buffer.

6.3.3. Stability of Valinomycin Mediated Nernst Potentials
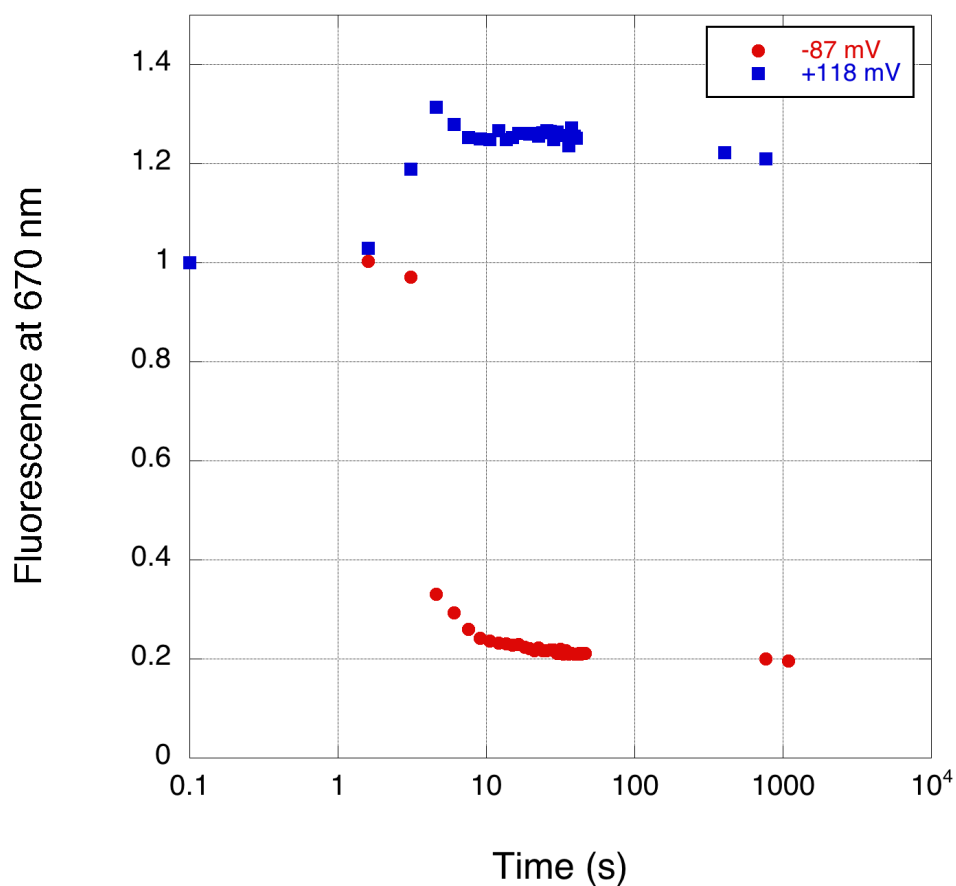
Figure 6.7. Stability of transmembrane potentials generated by the addition of Valinomycin using DiS-C$_2$(5) (6.9 µM) in DOPC vesicles set for +118 mV and -87 mV potential differences.

As was mentioned earlier, the kinetics of the valinomycin mediated

transmembrane potential are not so important to our investigation, though the stability of

the generated field is quite important. HRS requires much longer integration times than most optical and nonlinear optical techniques, and so it is important that the voltange stay reasonably consistent throughout the integration time. In order to check the stability of the potential over time, the fluorescence of DiS-C$_2$(5) was measured over time using the HRS / TPEF setup. In order to better check the stability under measurement conditions, 1200 nm excitation was used to measure the two-photon excited fluorescence spectrum. Using 2PA instead of the 1PA allowed everything in the measurement setup to be consistent with that of the actual sensitivity measurements conducted, most importantly, the focusing geometry and the long pass filter before the sample enclosure (see chapter 2), which have the potential to have profound impacts on the resulting signal.

Interestingly, the potential of the +118 mV phosphatidylcholine vesicles overshoots its equilibrium potential before settling at equilibrium. This is likely due to the +118 mV vesicles being potassium deficient in the interior of the vesicle, and the exterior K$^+$ flooding in once the ionophore is in place. After it overshoots, the K$^+$ ions flow back down their concentration gradient to establish an equilibrium. A second major possibility for the apparent overshoot is that there is reorientation or isomerization causing a change in the fluorescence response of DiS-C$_2$(5) to a potential change. The results of this study indicate that the membrane potential is reasonably consistent after the first 10 s of mixing with valinomycin. All vesicle based SHG sensitivity measurements were conducted such that a minimum of 10 s elapses after the addition of the valinomycin and the opening of the shutter.

6.3.4. Voltage Sensitivity of Common Potentiometric Chromophores in Phospholipid Vesicles

To test out the premise of these experiments, the SHG sensitivity was estimated for a series of common voltage sensitive probes including all-*trans*-retinal (ATR)[26], FM-4-64[1, 26], Di-6-APEQBS, and Di-4-ANEPPS[1, 27-28].
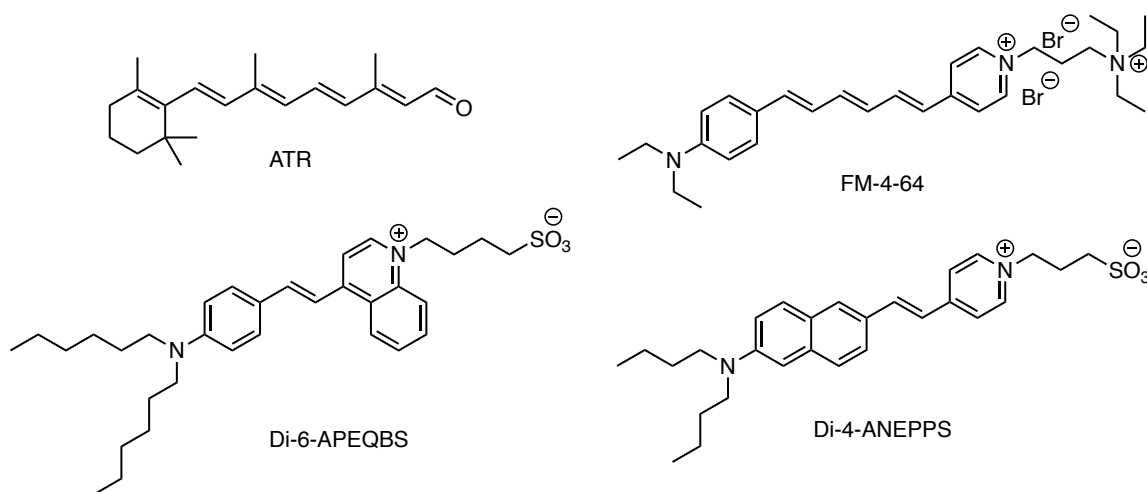
Figure 6.8. Structures of standard chromophores for SHG sensitivity studies

The HRS signal after the addition of valinomycin was subtracted by the signal before the addition to get the difference. This difference was converted into a sensitivity by dividing by the signal before the addition of valinomycin. The spectra in Figure 6.9 are the smoothed HRS data of Di-4-ANEPPS in vesicles leading to -87 mV and +118 mV transmembrane potentials, recorded at 850 nm.
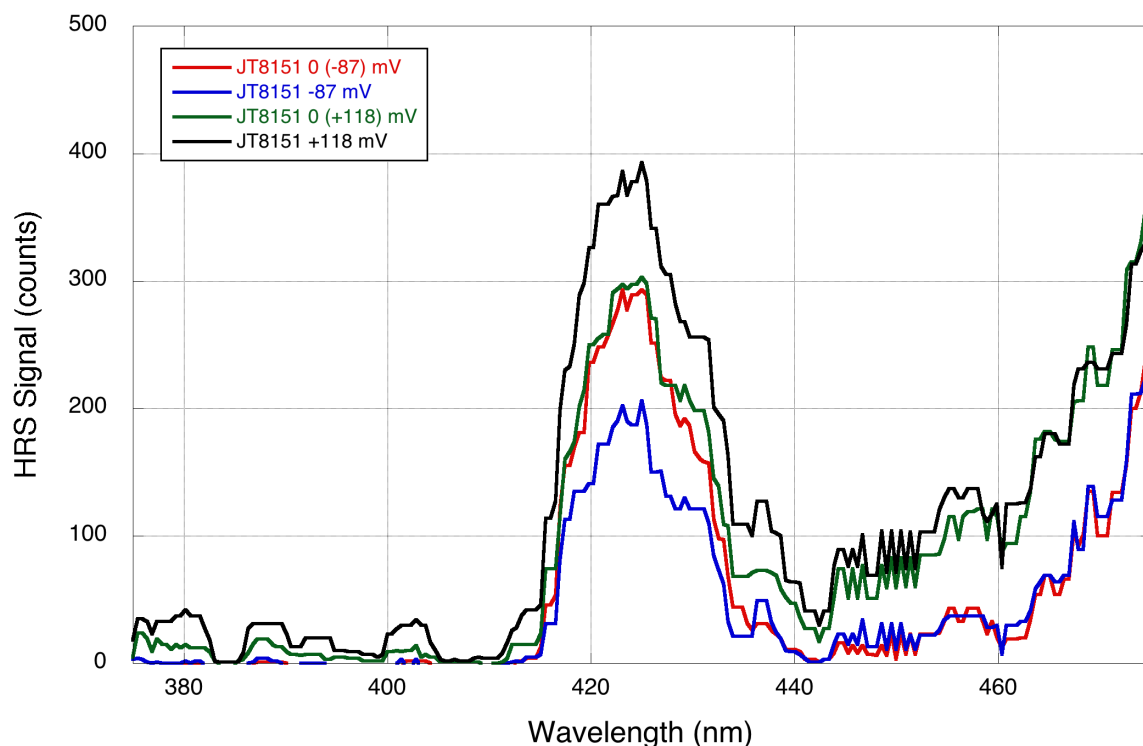
Figure 6.9. HRS signal of Di-4-ANEPPS (JT8151) in soy PC vesicles set up for -87 mV and +118 mV transmembrane potentials before and after the addition of valinomycin. The spectra were recorded at 850 nm.

The wavelength for our most recent measurements was 850 nm, shifted from our typical 900 nm because of laser instability at 900 nm after the high-speed driver was replaced. The spectral bandwidth at 900 nm also suffered greatly, resulting in a band that was more than 100 nm wide at its base.

Also, in the figure above, the signals for the +118 mV and -87 mV samples before the addition of valinomycin are nearly identical. This gives a good baseline for comparison to the samples after valinomycin was added. While this was not always the case, the HRS signal in the vesicles before the addition of valinomycin were always close to one another. Any discrepancy in the HRS signal can be attributed to changing of the ion pairing of the standard chromophores in the buffers of different K^+ concentrations. These

changes in ion pairing can cause a redistribution of electron density along the conjugated

backbones of the standard chromophores.

Table 6.1. Voltage sensitivity of common SHG probes in phosphlipid vesicles. All measurements were done at 850 nm. Error estimated at 18%.

Compound	$\Delta S/S$ (%/100 mV)	$\Delta S/S$ (%/100 mV) (literature Values)
Di-4-ANEPPS	38.7	26.3% [27]
Di-6-APEQBS	6.4	4% [29]
FM-4-64	17.7	-15% [1]

The estimated sensitivities of the common probes matched significantly better than the

estimations in the previous chapter. One potential factor contributing to the better

estimation is that the signal intensity for all measured compounds was significantly

higher, allowing for shorter integration times and lower powers.

6.3.5. Vesicle Based SHG Sensitivity Screening of Target Chromophores

The following table compiles several of the measured dyes that have ties to discussions in

other chapters. TCF[3] is one of the strongest nonlinear chromophores measured in this

work and is described in much more detail in chapter 4. ID[2], also described in chapter 4

has shown numerous favorable properties. At 1200 nm excitation, solid ID[2] undergoes

two-photon fluorescence as well as SHG, a rarity among these samples. Both of these
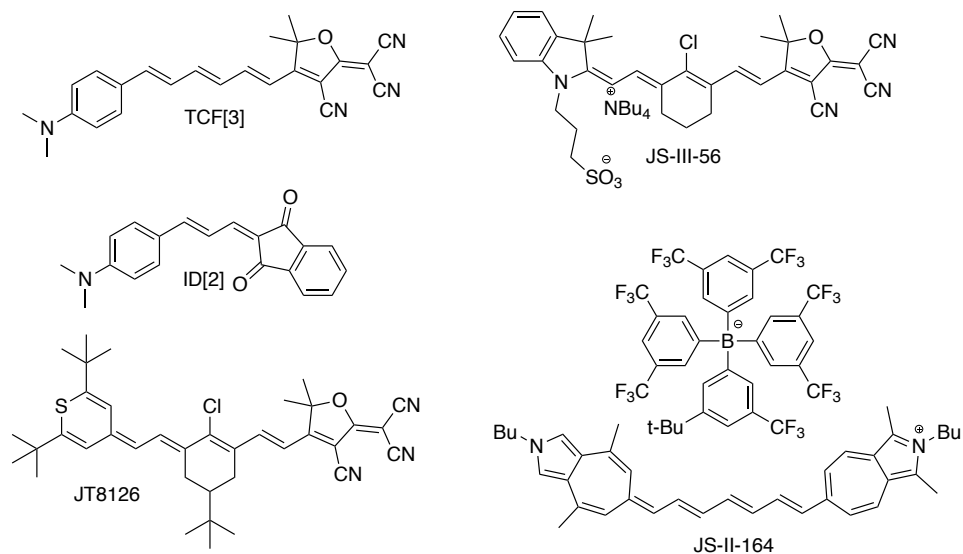
Figure 6.10. Chemical structures of the chromophores of interest measured in phosphaitidylcholine vesicles.

Table 6.2. Potential sensitivity of dyes of interest

Compound	$\Delta S/S$ (%/100 mV)
TCF[3]	25.1
ID[2]	16.4
JS-III-56	-32.5
JS-II-154	-3
JS-II-164	-29
JT8126	-46.4

dyes show sensitivities near state of the art (or at least state of the references) at 15 – 20 %/100 mV. JS-III-56 is another TCF terminated chromophore, but its indole donor group is substituted with a sulfonate terminated alkyl group for better membrane stability.

The incredibly promising symmetry breaking azaazulene chromophore from chapter 5, JS-II-164, showed essentially no sensitivity to the field. JT8126, a chalcogenopyrillium – TCF chromophore, which shows the stabilization of a cyanine like state in solvents of increasing polarity showed a study best -46% /100 mV sensitivity.

6.4. Summary

This method of investigating potential sensitivity in membrane mimics shows promise. It is significantly easier to set up than hemispherical bilayers or patch clamp experiments. Similar to patch clamp experiments, the voltage placed across the membrane can be tuned making it possible to interrogate even small voltage changes. Our results for 3 reference chromophores match quite nicely with the literature, and significantly better than in the previous two attempts to estimate potential sensitivity (chapter 5).

The results presented above also lend credibility to the idea that symmetry breaking / the stabilization of a cyanine-like state is an approach worth pursuing further. It also lends support to the idea of using longer very strong D-A polyenes to exploit the large signal of the polyene and the increased ratio of γ/β with increasing chain length.

This study also brings environmental compatibility in as a consideration. JS-II-164 significantly underperformed expectations, but this may be explained by the reduced stability in the membrane. After approximately 20 minutes the JS-II-164 in soy PC suspension began to noticeably scatter light. Efforts were made to measure its sensitivity as close to adding the chromophore as possible.

6.5. Experimental Details

6.5.1. Preparation of Phosphatidylcholine Vesicles

Dioleoylphospatidylcholine (DOPC, 18:1 cis-Δ^9, Avanti Polar Lipids) vesicles were prepared by the ethanol injection method[4, 11] in either high [K^+] or low [K^+] buffers. Solutions were buffered with 20 mM HEPES/Tris at pH 7.2 (20 ˚C) and contained 100 mM K_2SO_4 or 1 mM K_2SO_4 respectively[19]. An ethanolic solution of DOPC (32 mM, 1 mL) was injected, by syringe, into buffer soltion (10 mL) at 35˚C. The resulting vesicles were diluted 40-fold into a combination of high and low K^+ buffers to achieve the range of concentration gradients across the lipid membrane. The DOPC vesicles were between 80 – 100 nm in diameter by DLS (Wyatt). All dyes were loaded into the vesicle membranes as a solution in DMSO.

The electrochemical gradient was prepared by diluting vesicles in buffer of appropriate potassium ion strength. The transmembrane potential was generated by adding Valinomycin (Sigma Aldrich) as a solution in ethanol (100 mM).

6.5.2. Incorporation of Chromophores into Vesicle Membrane

All dyes were loaded into the vesicles as a solution in DMSO (~1 mM). Dyes were allowed to partition into the membrane over the course of 5 – 10 minutes after being initially agitated by vertexing. All samples were inspected visually to insure the chromophore was not crashing out prior to each measurement.

6.5.3. Linear Absorption and Fluorescence Spectroscopy

Linear absorption measurements were performed using either a UV-Vis-NIR scanning spectrophotometer (UV-3101PC, Shimadzu) or a diode array spectrophotometer (HP). Steady state fluorescence measurements were conducted using a scanning spectrofluorometer (Flurolog-2, SPEX).

In addition to the Fluorolog-2, some fluorescence measurements were recorded using the homebuilt Hyper-Rayleigh Scattering / two-photon induced fluorescence set up with the OPA operating at the one photon absorbance maximum (or at least within the 1PA band). Fluorescence spectra acquired this way are recorded over the whole range of the CCD camera, to protect from saturation, the incident intensity is adjusted to just give sufficient signal and long pass filters were used in place of the normal short pass filters in the setup as described in chapter 2. All spectra before and after the addition of valinomycin were recorded in the same sample cell (1 cm path length, Special Optical Glass, Starna Cells). The cell holder is attached to a movable stage allowing the cuvette to be positioned such that the focus of the beam is just next to the wall of the cell, in order to minimize reabsorption, and the cell was constantly stirred to avoid degradation.

6.5.4. Fluorescence Based Measurement of Transmembrane Potential with diS-C$_2$(5)

Membrane potentials were checked against a well-established electrochromic voltage sensor, DiSC$_2$(5)[25]. A large set of potentials was measured by this method each time new vesicles or buffers were produced as a control. DiSC$_2$(5) was incorporated in to the vesicles by the addition of a DMSO solution (1.0 mM). The mixture was agitated

with a vortex mixer for a few seconds before allowing to equilibrate for 15 minutes. The final concentration of $DISC_2(5)$ was 6.9 µM.

One-photon fluorescence of $DiSC_2(5)$ was measured using the home built Hyper-Rayleigh scattering set up described above. Samples were irradiated at 600 nm for 0.5 s. Afterwards, valinomycin (0.5 µM) was added as a solution in ethanol and the fluorescence was again measured. The resulting fluorescence spectra were normalized by area and subtracted to give differential fluorescence. Due to the ultra brief time frame of the measurement, there was a certain amount of noise to contend with. Correction, smoothing, normalization, and subtraction were all performed in MATLAB. The code used can be found in Appendix A, Section A.4. The smoothing was accomplished using a robust loess fitting with 1% data span.

6.5.5. Stability of Valinomycin induced Potentials

Stability measurements were performed using the same home built HRS/TPIF setup on samples similarly prepared. For simplicity only the extremes, +118 mV and -87 mV were tested. The excitation was at 1200 nm, allowing for strong two-photon absorption. The acquisition setup was controlled by a custom LabView .vi, which can also be found in Appendix A. The .vi allowed for both fast and slow kinetics measured sequentially. The CCD camera signal was integrated over a 0.5 s timeframe, and after the initial fast acquisition, the shutter was closed between each measurement.

The resulting raw spectra were baseline corrected by subtracting the minimum value, and the fluorescence at 670 nm was divided by the average fluorescence at 670 nm

from a sample that received ethanol instead of valinomycin in ethanol, which showed no significant variation over the timeframe of the stability trial.

6.5.6. SHG Sensitivity Measurements

SHG sensitivity measurements were conducted using the same laser set up as the stability measurements, and were largely conducted as normal HRS measurements, as described in chapters 2, 4, and 5. The primary difference was the way that the samples were treated. In order to limit the impact of degradation on these measurements, all samples were prepared in 10 mL batches for each potential measured. In a typical measurement, 2 mL of the 10 mL dye vesicle suspension was placed in a cuvette and 10 µL of 20 proof ethanol was added. The sample was measured in the HRS setup with stirring. Afterwards a fresh 2 mL sample of the dye vesicle suspension was placed in a cuvette and about 10 – 15 s before the shutter opened, a 10 µL aliquot valinomycin in ethanol (100 µM) was added. The HRS was measured again with stirring. This protocol involves fresh dye/vesicle suspension for each measurement. Therefore it is very important to make larger batches of the initial suspension (10 mL for our measurements) and to frequently check the appearance of the unused sample.

6.6. References

[1]   Reeve, J. E.; Anderson, H. L.; Clays, K., Dyes for biological second harmonic generation imaging. *Phys Chem Chem Phys* **2010,** *12* (41), 13484-98.

[2]   Peterka, D. S.; Takahashi, H.; Yuste, R., Imaging voltage in neurons. *Neuron* **2011,** *69* (1), 9-21.

[3]   Ashrafuzzaman, M.; Tuszynski, J., Structure of Membranes. In *Membrane Biophysics*, Ashrafuzzaman, M.; Tuszynski, J., Eds. Springer Berlin Heidelberg: Berlin, Heidelberg, 2013; pp 9-30.

[4]   Kremer, J. M. H.; Van der Esker, M. W.; Pathmamanoharan, C.; Wiersema, P. H., Vesicles of variable diameter prepared by a modified injection method. *Biochemistry* **1977,** *16* (17), 3932-3935.

[5]   Politano, T. J.; Froude, V. E.; Jing, B.; Zhu, Y., AC-electric field dependent electroformation of giant lipid vesicles. *Colloids and Surfaces B: Biointerfaces* **2010,** *79* (1), 75-82.

[6]   Pott, T.; Bouvrais, H.; Méléard, P., Giant unilamellar vesicle formation under physiologically relevant conditions. *Chemistry and Physics of Lipids* **2008,** *154* (2), 115-119.

[7]   Nemet, B. A.; Nikolenko, V.; Yuste, R. In *Second harmonic imaging of membrane potential of neurons with retinal*, SPIE: 2004; p 9.

[8]   Beeler, T. J.; Farmen, R. H.; Martonosi, A. N., The mechanism of voltage-sensitive dye responses on sarcoplasmic reticulum. *The Journal of Membrane Biology* **1981,** *62* (1), 113-137.

[9]   Estes, D. J.; Mayer, M., Electroformation of giant liposomes from spin-coated films of lipids. *Colloids and Surfaces B: Biointerfaces* **2005,** *42* (2), 115-123.

[10]   Batzri, S.; Korn, E. D., Single bilayer liposomes prepared without sonication. *Biochimica et Biophysica Acta (BBA) - Biomembranes* **1973,** *298* (4), 1015-1019.

[11]   Zouni, A.; Clarke, R. J.; Holzwarth, J. F., Kinetics of the Solubilization of Styryl Dye Aggregates by Lipid Vesicles. *The Journal of Physical Chemistry* **1994,** *98* (6), 1732-1738.

[12]   Loew, L. M.; Benson, L.; Lazarovici, P.; Rosenberg, I., Fluorometric analysis of transferable membrane pores. *Biochemistry* **1985,** *24* (9), 2101-2104.

[13]   Urry, D. W., The Gramicidin A Transmembrane Channel: A Proposed π((L,D)) Helix. *Proceedings of the National Academy of Sciences of the United States of America* **1971,** *68* (3), 672-676.

[14]   Bedlack, R. S., Jr.; Wei, M.-d.; Fox, S. H.; Gross, E.; Loew, L. M., Distinct electric potentials in soma and neurite membranes. *Neuron* **1994,** *13* (5), 1187-1193.

[15]   Bedlack, R. S.; Wei, M. d.; Loew, L. M., Localized membrane depolarizations and localized calcium influx during electric field-guided neurite growth. *Neuron* **1992,** *9* (3), 393-403.

[16]   Loew, L. M.; Cohen, L. B.; Dix, J.; Fluhler, E. N.; Montana, V.; Salama, G.; Jian-young, W., A naphthyl analog of the aminostyryl pyridinium class of potentiometric membrane dyes shows consistent sensitivity in a variety of tissue, cell, and model membrane preparations. *The Journal of Membrane Biology* **1992,** *130* (1), 1-10.

[17]   Bouevitch, O.; Lewis, A.; Pinevsky, I.; Wuskell, J. P.; Loew, L. M., Probing membrane potential with nonlinear optics. *Biophysical Journal* **1993,** *65* (2), 672-679.

[18]   Hassner, A.; Birnbaum, D.; Loew, L. M., Charge-shift probes of membrane potential. Synthesis. *The Journal of Organic Chemistry* **1984,** *49* (14), 2546-2551.

[19]   Montana, V.; Farkas, D. L.; Loew, L. M., Dual-wavelength ratiometric fluorescence measurements of membrane potential. *Biochemistry* **1989,** *28* (11), 4536-4539.

[20]   Zhang, J.; Davidson, R. M.; Wei, M.-d.; Loew, L. M., Membrane Electric Properties by Combined Patch Clamp and Fluorescence Ratio Imaging in Single Neurons. *Biophysical Journal* **1998,** *74* (1), 48-53.

[21]   Widdas, W. F., Inability of diffusion to account for placental glucose transfer in the sheep and consideration of the kinetics of a possible carrier transfer. *The Journal of Physiology* **1952,** *118* (1), 23-39.

[22]   Hladky, S. B.; Leung, J. C.; Fitzgerald, W. J., The mechanism of ion conduction by valinomycin: analysis of charge pulse responses. *Biophysical Journal* **1995,** *69* (5), 1758-1772.

[23]   Baughman, R. H.; Kohler, B. E.; Levy, I. J.; Spangler, C., The crystal structure of trans,trans-1,3,5,7-octatetraene as a model for fully-ordered trans-polyacetylene. *Synthetic Metals* **1985,** *11* (1), 37-52.

[24]   A.D. Vasil'ev, T. A. S., V.I. Andrianov, V.I. Simonov, A.A. Sanasaryan, V.T. Ivanov, Yu.A. Ovchinnikov, *Bioorganicheskaia Khimiia* **1978,** *4*, 1157.

[25]   Sims, P. J.; Waggoner, A. S.; Wang, C.-H.; Hoffman, J. F., Mechanism by which cyanine dyes measure membrane potential in red blood cells and phosphatidylcholine vesicles. *Biochemistry* **1974,** *13* (16), 3315-3330.

[26]   Theer, P.; Denk, W.; Sheves, M.; Lewis, A.; Detwiler, P. B., Second-Harmonic Generation Imaging of Membrane Potential with Retinal Analogues. *Biophysical Journal* **2011,** *100* (1), 232-242.

[27]   Millard, A. C.; Jin, L.; Wei, M.-d.; Wuskell, J. P.; Lewis, A.; Loew, L. M., Sensitivity of Second Harmonic Generation from Styryl Dyes to Transmembrane Potential. *Biophysical Journal* **2004,** *86* (2), 1169-1176.

[28]   Millard, A. C.; Jin, L.; Wuskell, J. P.; Boudreau, D. M.; Lewis, A.; Loew, L. M.,
         Wavelength- and Time-Dependence of Potentiometric Non-linear Optical Signals
         from Styryl Dyes. *The Journal of Membrane Biology* **2005,** *208* (2), 103-111.

[29]   Pons, T.; Mertz, J., Membrane potential detection with second-harmonic
         generation and two-photon excited fluorescence: A theoretical comparison. *Optics
         Communications* **2006,** *258* (2), 203-209.

CHAPTER 7

CONCLUSIONS AND FUTURE OUTLOOK

7.1. Conclusions

The majority of this work is focused on the practical translation of photophysical techniques as well as structure-property relationships in conjugated organic chromophores to modern problems in biochemistry and in microscopy. The work presented in this dissertation began as a project to synthesize a set of strong dipolar chromophores to look at potential dyes for all optical signal processing. The project ballooned outward and as mentioned previously, at one point, the D-A polyenes were being used in some capacity in every actively pursued project in our group. Although they have not been great at every application, the versatility of this set of chromophores has been quite impressive. While the compounds themselves may not have set any records, the principles behind their development are applicable to many questions in the nonlinear optical field. Most notably for this work, to the design of potential sensitive probes for SHG imaging[1-2]. The crystallographic studies conducted with the Timofeeva group show significant distortion in BLA in the crystal structure. Nearly every structure indicates that in crystals, the donor group is in its fully charge transferred state with a negative charge residing or delocalized along the conjugated bridge.

222

At the present, multiphoton (or two photon) fluorescence microscopy (MPF or TPF) and MPF based sensing of small molecules remain a very active areas of research. New TPF sensors are targeting everything including metal ions[3], polyatomic ions such as hypochorite[4] and bisultite[5], biological small molecules such as ATP[6], proteins, and even cancer cells. TCF[1] has even been shown to be a highly selective probe for HSO_3^- .[7]

Chapter 3 contained an investigation in to the ability for surface charge to impact the sensing efficacy of a ratiometric Zn(II) sensor. The results presented in chapter 3 clearly show a change in the formation constants in micellular structures with the same and oppostire surface charges as the analyte. Not only was there a very large impact on the sensing ability of SL-35, the Zn(II) sensor, but there was also a modification of the electronic structure as a result of the differing surface change as was evident from the dramatic changes in absorbance and fluorescence spectra upon binding in the micelles of varying charges. From this standpoint, the results of Zn(II) sensing in negatively charged SDS micelles may be the most impactful, as the Zn(II) titration revealed a dramatic increase in sensitivity of the SL-35 probe relative to a neutral micelle (TritonX). In SDS the probe was saturated in a little over greater than an equimolar ratio of Zn(II) to dye. Not only that, but the spectral shift upon binding was increased in both the absorbance spectra and the fluorescence spectra. Results such as this might suggest a future direction of rigid support structures impregnated with fluorescent sensors that have tailored surface properties to maximize sensitivity and response.

On the potential sensitivity side, chapters 5 and 6, the logic behind our figure of merit for the static nonlinearity has been similarly concluded by others[2], however, the

pursuit of cyanine like chromophores for extreme potential sensitivity appears to be the first study of its kind. The investigation of neural circuitry remains one of the biggest challenges of fighting neurodegenerative diseases, and as such the problem is being investigated on numerous fronts, including looking for potential sensitivity in biologically relevant chromophores currently approved for use[8], and investigation of screening methods for potential sensors based on black lipid membranes.[9] Another aspect of the sensing of membrane potentials that will have a large impact on the field is to better characterize the reorientation component of the response. Although this work makes no claim to characterize the reorientation of the target chromophores as a component of the SHG response, the purely electrooptic responses measured and estimated in the first half of chapter 5 suggest that there is more complexity to the mechanism that simply a purely electrooptic response. Other investigators have reported temporal differences in response such as a fast and a slow component reported by Reeve et al.[2] The future directions of the potential sensing and D-A polyene projects should really focus on compatibility with the membrane environment and limiting toxicity.

7.2. References

[1] Pons, T.; Mertz, J., Membrane potential detection with second-harmonic generation and two-photon excited fluorescence: A theoretical comparison. *Optics Communications* **2006,** *258* (2), 203-209.

[2] Reeve, J. E.; Anderson, H. L.; Clays, K., Dyes for biological second harmonic generation imaging. *Phys Chem Chem Phys* **2010,** *12* (41), 13484-98.

[3] Liu, L.; Fan, J.; Ding, L.; Zhu, B.; Huang, X.; Gong, W.; Xin, Y.; Fang, Y., A simple fluorophore/surfactant ensemble as single discriminative sensor platform: Identifying multiple metal ions in aqueous solution. *Journal of Photochemistry and Photobiology A: Chemistry* **2016,** *328*, 1-9.

[4] Wang, K.; Sun, P.; Chao, X.; Cao, D.; Mao, Z.; Liu, Z., A coumarin Schiff's base two-photon fluorescent probe for hypochlorite in living cells and zebrafish. *RSC Advances* **2018,** *8* (13), 6904-6909.

[5] Tamima, U.; Singha, S.; Kim, H. R.; Reo, Y. J.; Jun, Y. W.; Das, A.; Ahn, K. H., A benzocoumarin based two-photon fluorescent probe for ratiometric detection of bisulfite. *Sensors and Actuators B: Chemical* **2018,** *277*, 576-583.

[6] Jun, Y. W.; Wang, T.; Hwang, S.; Kim, D.; Ma, D.; Kim, K. H.; Kim, S.; Jung, J.; Ahn, K. H., A Ratiometric Two-Photon Fluorescent Probe for Tracking Lysosomal ATP: Direct In Cellulo Observation of Lysosomal Membrane Fusion Processes. *Angewandte Chemie International Edition* **2018,** *57* (32), 10142-10147.

[7] Liu, C.; Liu, L.; Li, X.; Shao, C.; Huang, X.; Zhu, B.; Zhang, X., A highly selective colorimetric and far-red fluorescent probe for imaging bisulfite in living cells. *RSC Advances* **2014,** *4* (63), 33507-33513.

[8] Treger, Jeremy S.; Priest, Michael F.; Iezzi, R.; Bezanilla, F., Real-Time Imaging of Electrical Signals with an Infrared FDA-Approved Dye. *Biophysical Journal* **2014,** *107* (6), L09-L12.

[9] Tsemperouli, M.; Sugihara, K., Characterization of di-4-ANEPPS with nano-black lipid membranes. *Nanoscale* **2018,** *10* (3), 1090-1098.

APPENDIX A :
MATLAB CODE

A.1 HRS Processing Gui : HRS_GUI_v6.m

```matlab
function varargout = HRS_GUI(varargin)
% HRS_GUI is a graphical interfacing MATLAB script to process
% Hyper-Rayleigh scattering data. The program allows for the smoothing
of
% data based on a robust Loess (quadratic fit), fitting the spectral
% baseline, and integrating resulting signal. While the name of the
file
% will not affect these functions, the program is set up to take files
of
% the format:
%
% sample_concentration_solvent_wavelength(nm)_energy(µJ)_time(s)_filters
%
% with files named in this format, the program is able to divide up the
% file name and save it along with the data in its output file.
%
% Other inputs that are needed are:
% - a desired smoothing factor (percentage of the data for smoothing)
% - number of pairs of baseline points for fitting
% - a second fitting factor for the baseline corrected spectra
%
% The resulting subtracted and smoothed spectrum can be integrated by
% clicking integrate and then clicking the x-bounds of the desired
% integration range. The save results feature will automatically create
a
% results file for each unique set of sample, solvent, and wavelength
% combinations or it will append the results file if it is already
present.
% The save data feature will save the raw and smoothed spectra, the
% baseline fitting function, and the raw and smoothed baseline
corrected
% spectra in a "processed" folder (which it will create if necessary)
%
%
% Although it was developed for HRS data, it is certainly not limited
to
% only this input. It can take any tab deliminated spectral file,
however
% it will only read the first two columns of data, the first being
assumed
% to be the wavelength.
% (Leave a blank line following the help.)
```

```matlab
% Gui Build

fHRS = figure('Visible','off','Units', 'centimeters','Position',...
[2,5,40,25]);

ha_raw = axes ('Parent',fHRS,'position', [.03, .5, .7, .4]);
ha_fit = axes ('Parent',fHRS,'position', [.03, .05, .7, .4]);
linkaxes([ha_raw, ha_fit], 'off');
label_path = uicontrol(fHRS,'Style','text',...
                'String','File Path',...
                'Units', 'centimeter','Position', [.3,24,1.7,1]);

hpath = uicontrol(fHRS,'Style','edit',...
                'Units','centimeter','Position', [2,24,25.1,1]);
align([label_path,hpath],'None','Middle');

label_fname = uicontrol(fHRS,'Style','text',...
                'String','File Name',...
                'Units', 'centimeter','Position', [.3,22.75,1.7,1]);

hfname = uicontrol(fHRS,'Style','edit',...
                'Units', 'centimeters','Position', [2,22.75,25.1,1]);
align([label_fname,hfname],'None','Middle');

hplot_pb =  uicontrol(fHRS,'Style','pushbutton',...
                'String','Plot','Units', 'centimeters',...
                'Position',[27.1,24,1.5,1],...
                'Callback', @loadplot_call);
hreplot_pb =  uicontrol(fHRS,'Style','pushbutton',...
                'String','Reset','BackgroundColor','c',...
                'Units', 'centimeters','Position',[27.1,22.8,1.5,1],...
                'Callback', @reloadplot_call);
hflip_tb = uicontrol(fHRS,'Style', 'togglebutton', ...
                    'String', 'Flip', ...
                    'Units',
'centimeters','Position',[28.65,22.8,1,2]);

pbkgrnd = uipanel(fHRS,'Title','Background Removal',...
            'Position',[.745 .025 .24 .25]);

hxlim_pb = uicontrol(fHRS,'Style','pushbutton',...
                'String','x limits',...
                'Units', 'normalized','Position',
[.63,0.455,.05,.025],...
                'Callback', @xlimset_call);

hylim_pb = uicontrol(fHRS,'Style','pushbutton',...
                'String','y limits',...
                'Units', 'normalized','Position',
[.68,0.455,.05,.025],...
                'Callback', @ylimset_call);

ppro = uipanel(fHRS,'Title','Process and Integrate',...
            'Position',[.745 .3 .24 .25]);

label_smfac = uicontrol(ppro,'Style','text',...
```

```matlab
                  'String','Raw Smoothing factor',...
                  'Units', 'normalized','Position',
[.0125,0.8,.375,.175]);


hsmfac = uicontrol(ppro,'Style','edit',...
                  'Units', 'normalized','Position', [.4,0.8,.35,.175]);


hsmfac_pb = uicontrol(ppro,'Style','pushbutton',...
                  'String','Smooth',...
                  'Units', 'normalized','Position',
[.75,0.8,.225,.175],...
                  'Callback', @smoothdata_call);


label_basepts= uicontrol(ppro,'Style','text',...
                  'String','# Baseline Points',...
                  'Units', 'normalized','Position',
[.0125,0.58,.375,.175]);
hbasepts = uicontrol(ppro,'Style','edit',...
                  'Units', 'normalized','Position', [.4,0.605,.35,.175]);


hbasepts_pb = uicontrol(ppro,'Style','pushbutton',...
                  'String','Fit',...
                  'Units', 'normalized','Position',
[.75,0.605,.225,.175],...
                  'Callback', @fitbase_call);
label_smfac2 = uicontrol(ppro,'Style','text',...
                  'String','Fit Smoothing factor',...
                  'Units', 'normalized','Position',
[.0125,0.41,.375,.175]);


hsmfac2 = uicontrol(ppro,'Style','edit',...
                  'Units', 'normalized','Position', [.4,0.41,.35,.175]);


hsmfac2_pb = uicontrol(ppro,'Style','pushbutton',...
                  'String','Smooth',...
                  'Units', 'normalized','Position',
[.75,0.41,.225,.175],...
                  'Callback', @smfitdata_call);
hinteg =  uicontrol(ppro,'Style','edit',...
                  'Units', 'normalized','Position',
[.5,0.215,.475,.175]);
hintegrate_pb = uicontrol(ppro,'Style','pushbutton',...
                  'String','Integrate',...
                  'Units', 'normalized','Position',
[.0125,0.215,.475,.175],...
                  'Callback', @integ_call);
hsavedata_pb = uicontrol(ppro, 'Style', 'pushbutton',...
                  'String','Save Data',...
                  'Units', 'normalized','Position',
[.0125,0.02,.475,.175],...
                  'Callback', @save_call);
hsaveres_pb = uicontrol(ppro, 'Style', 'pushbutton',...
                  'String','Save Results',...
                  'Units', 'normalized','Position',
[.5,0.02,.475,.175],...
                  'Callback', @saveres_call);
```

```matlab
pinfo = uipanel(fHRS,'Title','Sample Info',...
            'Position',[.745 .575 .24 .4]);
hsample = uicontrol(pinfo,'Style','edit',...
            'String','Sample',...
            'Units', 'normalized','Position', [.35,.775,.6,.1]);
hsample_label = uicontrol(pinfo,'Style','text',...
            'String','Sample',...
            'Units', 'normalized','Position', [.025,.75,.3,.1]);
hconc = uicontrol(pinfo,'Style','edit',...
            'String','Conc.',...
            'Units', 'normalized','Position', [.35,.65,.6,.1]);
hconc_label = uicontrol(pinfo,'Style','text',...
            'String','Conc.',...
            'Units', 'normalized','Position', [.025,.625,.3,.1]);
hsolvent = uicontrol(pinfo,'Style','edit',...
            'String','Solvent',...
            'Units', 'normalized','Position', [.35,.525,.6,.1]);
hsolvent_label = uicontrol(pinfo,'Style','text',...
            'String','Solvent',...
            'Units', 'normalized','Position', [.025,.5,.3,.1]);

hwav = uicontrol(pinfo,'Style','edit',...
            'String','Wavelength',...
            'Units', 'normalized','Position', [.35,.4,.6,.1]);
hwav_label = uicontrol(pinfo,'Style','text',...
            'String','Wavelength',...
            'Units', 'normalized','Position', [.025,.375,.3,.1]);

henergy = uicontrol(pinfo,'Style','edit',...
            'String','Power',...
            'Units', 'normalized','Position', [.35,.275,.6,.1]);
henergy_label = uicontrol(pinfo,'Style','text',...
            'String','Energy',...
            'Units', 'normalized','Position', [.025,.25,.3,.1]);
htime = uicontrol(pinfo,'Style','edit',...
            'String','Int. Time',...
            'Units', 'normalized','Position', [.35,.15,.6,.1]);
htime_label = uicontrol(pinfo,'Style','text',...
            'String','Int. Time',...
            'Units', 'normalized','Position', [.025,.125,.3,.1]);
hfilter = uicontrol(pinfo,'Style','edit',...
            'String','Filters',...
            'Units', 'normalized','Position', [.35,.025,.6,.1]);
hfilter_label = uicontrol(pinfo,'Style','text',...
            'String','Filters',...
            'Units', 'normalized','Position', [.025,0,.3,.1]);

hsinfo_pb = uicontrol(pinfo,'Style','pushbutton',...
            'String','Split Info','Units', 'normalized',...
            'Position',[.025,.9,.475,.1],...
            'Callback', @split_call);
hsvinfo_pb = uicontrol(pinfo,'Style','pushbutton',...
            'String','Save Info','Units', 'normalized',...
            'Position',[.525,.9,.45,.1],...
            'Callback', @svinfo_call);

 % Make figure visible after adding components
```

```matlab
    fHRS.Visible = 'on';


% Initialization tasks
wav = [];
sig = [];
msig = [];
msig2 = [];
bdat= [];
mbdat = [];
fmbdat = [];
xfit=[];
yfit = [];
lw=1.5;

% label_path = 'normalized';
% hpath = 'normalized';
% label_fname = 'normalized';
% hfname = 'normalized';
% hplot_pb = 'normalized';
% label_smfac = 'normalized';
% hsmfac = 'normalized';
% hsmfac_pb = 'normalized';
% label_basepts = 'normalized';
% hbasepts = 'normalized';
% hbasepts_pb = 'normalized';

% Callbacks for MYUI
    function loadplot_call(hObject,eventdata)
  %Import file
    path=hpath.String;
    filename=hfname.String;
    fullpath=[path,'/',filename];
    dat=dlmread(fullpath,'\t',1,0);
    wav=dat(:,1);
    sig=dat(:,2);

  button_state = get(hflip_tb, 'Value');

  if button_state == 1
   wav = flipud(wav);
   sig = flipud(sig);
  else
  end
  lw;
   hold off;
   rawplot=plot(ha_raw,wav,sig,'LineWidth',lw);

   hold on;

 end

    function reloadplot_call(hObject,eventdata)
  %Import file
    path=hpath.String;
    filename=hfname.String;
```

230

```matlab
        fullpath=[path,'/',filename];
        dat=dlmread(fullpath,'\t',1,0);
        wav=dat(:,1);
        sig=dat(:,2);

    button_state = get(hflip_tb, 'Value');

     if button_state == 1
      wav = flipud(wav);
      sig = flipud(sig);
     else
     end

   lw;

      hold off;
      cla(ha_raw);
      rawplot=plot(ha_raw,wav,sig,'LineWidth', lw);
      cla(ha_fit);
      hold on;

      end

      function xlimset_call(hObject, eventdata)
          laser = str2num(hwav.String);
          center = laser/2;

          xlim(ha_raw, [center-75,center+75]);


      end
      function ylimset_call(hObject, eventdata)
           rawxlim = xlim(ha_raw);

         for k = 1:2
              rawlimpos = abs(wav(:,1)-rawxlim(k));
              rawxlimpos(k) = find(rawlimpos == min(rawlimpos));
         end

%          smoothed = isempty('msig')
%          if smoothed == 0

             ymax = max(msig(rawxlimpos(1):rawxlimpos(2)));
             ymin = min(msig(rawxlimpos(1):rawxlimpos(2)));
%            setymin = ymin- 100;
             setymin = ymin - (0.25*ymax);
             setymax = ymax+(0.5*ymax);
             ylim(ha_raw, [setymin,setymax]);
%          elseif smoothed == 1
%              rawymax = max(sig(rawxlimpos(1):rawxlimpos(2)));
%              rawymin = min(sig(rawxlimpos(1):rawxlimpos(2)));
%          yl = ylim(ha_raw);
%          ylim(ha_raw, [rawymin,rawymax]);
%          end
%
      end
```

231

```matlab
function smoothdata_call(hObject, eventdata)
    lw;
    cla(ha_raw)
     plot(ha_raw,wav,sig, 'LineWidth', lw)
     axes(ha_raw);
    hold(ha_raw, 'on');
    smfactor = str2num (hsmfac.String)

    msig = smooth(sig,smfactor,'rloess');

    smplot = plot(ha_raw,wav,msig,'--','LineWidth', lw);

end

function fitbase_call(hObject, eventdata)
    lw;
    pairs = str2num (hbasepts.String) ;

        pts = 2*pairs;


        [x,~] = ginput(pts);

         for i = 1:pts
        mpos = abs(wav-x(i));
        pos(i) = find(mpos == min(mpos));
         end

            linx = [];
            liny = [];
             for j = 1:pairs
         linx = [linx;wav(pos(2*j-1):pos(2*j))];
         liny = [liny;msig(pos(2*j-1):pos(2*j))];
             end

            [fitp,gofp]= fit(linx,liny,'poly5');

            coeffv = coeffvalues(fitp);
            xfit = wav(pos(1):pos(pts));
            yfit = polyval(coeffv,xfit);

            plot(xfit,yfit,'k')

            bdat = [xfit,sig(pos(1):pos(pts))-yfit];


    plot(ha_fit,bdat(:,1),bdat(:,2), 'LineWidth', lw)
    axes(ha_fit);
    xlim(ha_fit, [min(xfit), max(xfit)]);
%       laser = str2num(hwav.String);
%       center = laser/2;
%       xlim(ha_fit, [center-75,center+75]);
    fymin = min(bdat(:,2)-100);
    fymax = max(bdat(:,2))*1.25;
    ylim(ha_fit, [-100, fymax]);
```

```matlab
        line([bdat(1,1),bdat(size(bdat,1),1)],[0
0],'LineWidth',lw,'Color',[0 0 0])
        hold on
  end

    function smfitdata_call(hObject, eventdata)
   cla(ha_fit)
    plot(ha_fit,bdat(:,1),bdat(:,2),'LineWidth', lw)
        axes(ha_fit);
        line([bdat(1,1),bdat(size(bdat,1),1)],[0
0],'LineWidth',lw,'Color',[0 0 0])
        hold on
     smfactor2 = str2num (hsmfac2.String)
        hold(ha_fit, 'on');
        if smfactor2 ~= 0
            fmbdat = smooth( bdat(:,2),smfactor2,'rloess');
        else
            fmbdat =  bdat(:,2);
        end

%          msig2 = smooth(sig,smfactor2,'rloess');
        size(bdat(:,1));
        size(fmbdat) ;
        smplot2 = plot(ha_fit, bdat(:,1),fmbdat,'--', 'LineWidth',lw);
        fymin = min(fmbdat(:,1)-100);
        fymax = max(fmbdat(:,1))*1.25;
        ylim(ha_fit, [-100, fymax]);
    end

    function split_call(hObject, eventdata)
        splitinfo = strsplit(hfname.String, '_');
        set(hsample, 'String', splitinfo{1});
        set(hconc, 'String', splitinfo{2});
        set(hsolvent, 'String', splitinfo{3});
        set(hwav, 'String', splitinfo{4});
        set(henergy, 'String', splitinfo{5});
        set(htime, 'String', splitinfo{6});
        set(hfilter, 'String', [splitinfo{7:end}]);
    end

    function svinfo_call(hObject, eventdata)
        sampleinfo = {hfname.String, hsample.String, hconc.String,
hsolvent.String, hwav.String, henergy.String, htime.String,
hfilter.String}
        path=hpath.String;
        filename=hfname.String;
        respath=[path,'/',hsample.String, '_', hsolvent.String, '_',
hwav.String,'_sampleinfo.txt'];

        ex2 = cellfun(@ex_func,sampleinfo,'UniformOutput',0);
        size_ex2 = cellfun(@length,ex2,'UniformOutput',0);
        str_length = max(max(cell2mat(size_ex2)));
        ex3 = cellfun(@(x)
ex_func2(x,str_length),ex2,'UniformOutput',0);

        n=str_length;
        ex4 = cell2mat(ex3);
```

```matlab
%            respath=[path,'/',filename,'_sampleinfo.txt'];
         formstr=[];
         for i=1:8
             if i<8
                 formstr=[formstr,strcat('ex4(',int2str((i-
1)*n+1),':',int2str(i*n),'),')];
             else
                 formstr=[formstr,strcat('ex4(',int2str((i-
1)*n+1),':',int2str(i*n),')')];
             end
         end

          if exist(respath, 'file') ~= 2

             h1= 'Filename';
             h2= 'Sample';
             h3= 'Concentration(µM)';
             h4= 'Solvent';
             h5= 'Wavelength(nm)';
             h6= 'Energy(µJ)';
             h7= 'Integration_Time(s)';
             h8= 'Center_and_Filters';

             col_head = {h1, h2, h3, h4, h5, h6, h7, h8};

%            ex2 = cellfun(@ex_func,sampleinfo,'UniformOutput',0);
%          size_ex2 = cellfun(@length,ex2,'UniformOutput',0);
%           str_length = max(max(cell2mat(size_ex2)));
         chex3 = cellfun(@(x)
ex_func2(x,str_length),col_head,'UniformOutput',0);

         n=str_length;
         chex4 = cell2mat(chex3);

         chformstr=[];
%             for i=1:8
%              if i<8
%                  chformstr=[chformstr,strcat('chex4(',int2str((i-
1)*n+1),':',int2str(i*n),'),')];
%              else
%                  chformstr=[chformstr,strcat('chex4(',int2str((i-
1)*n+1),':',int2str(i*n),')')];
%              end
%              chformstr
            chformstr=[];
           for i=1:8
               if i<8
                   chformstr=[chformstr,strcat('chex4(',int2str((i-
1)*n+1),':',int2str(i*n),'),')];
               else
                   chformstr=[chformstr,strcat('chex4(',int2str((i-
1)*n+1),':',int2str(i*n),')')];
               end
           end

%            fprintf(fid, [ h1 '\t' h2 '\t' h3 '\t' h4 '\t' h5 '\t' h6
'\t' h7 '\n']);
```

```matlab
%               fprintf(fid, '%f\t%f\t%f\t%f\t%f\t%f\t%f \n', smdata');
%               fclose(fid);

                fid=fopen(respath,'at');
                str1='''%s %s %s %s %s %s %s %s \n'',';
                eval(['fprintf(fid,',str1,chformstr,');'])

            else
                fid=fopen(respath,'at');
            end
% fid = fopen(respath,'a');
% fprintf(fid,'%s %s %s %s %s %s %s %s %s %s
%s\n',ex4(1:10),ex4(11:20),ex4(21:30),ex4(31:40),ex4(41:50),ex4(51:60),
ex4(61:70),ex4(71:80),ex4(81:90),ex4(91:100),ex4(101:110));
% fprintf(fid,'%s %s %s %s %s %s %s %s %s %s %s\n',formstr);
        str1='''%s %s %s %s %s %s %s %s \n'',';
        eval(['fprintf(fid,',str1,formstr,');'])
        fclose(fid);
    end

    function integ_call(hObject, eventdata)

        data = [bdat(:,1),fmbdat];
        axes(ha_fit);
        [xs,~] = ginput(2);

        for k = 1:2
            ipos = abs(data(:,1)-xs(k));
            xipos(k) = find(ipos == min(ipos));
        end

        filename=hfname.String
        int =
trapz(data((xipos(1):xipos(2)),1),data((xipos(1):xipos(2)),2))
        set(hinteg, 'String', int);

    end

    function save_call(hObject, eventdata)
        path=hpath.String;
        cd(path);
        filename=hfname.String;
        rawlim = xlim;
        rawdata=[wav,sig];
        for k = 1:2
            limpos = abs(wav(:,1)-rawlim(k));
            xlimpos(k) = find(limpos == min(limpos));

        end

        h1= 'Wavelength (nm)';
        h2= [filename,'_raw'];
        h3= [filename,'_sm'];
        h4= 'Wavelength (nm)';
        h5= [filename, '_fit'];
        h6= 'Wavelength (nm)';
```

235

```matlab
        h7= [filename,'_blcor'];
        h8= [filename,'_sm_blcor'];
        col_head = [h1, h2, h3, h4, h5, h6, h7, h8];

raw_export=[rawdata(xlimpos(1):xlimpos(2),1),rawdata(xlimpos(1):xlimpos(2),2),msig(xlimpos(1):xlimpos(2))];
        basefit_export = [xfit, yfit];
        basecor_export = [bdat(:,1),bdat(:,2),mbdat];
%         full_export = {raw_export, basefit_export, basecor_export}
%         full_export = {
        [padded_export, tf] =
padcat(rawdata(xlimpos(1):xlimpos(2),1),rawdata(xlimpos(1):xlimpos(2),2),msig(xlimpos(1):xlimpos(2)),xfit, yfit,bdat(:,1),bdat(:,2),fmbdat);
         padded_export(~tf) = 0;
%           figure
%           plot(bdat(:,1),fmbdat)
%           tpad_export = dataset(padded_export,'VarNames', {h1, h2, h3,
h4, h5, h6, h7, h8});
        path=hpath.String;
    filename=hfname.String;
%     fullpath=[path,'/',filename]

        testpath = [path,'/processed/'];
        % exist (testpath,'dir')
        if exist (testpath,'dir') ~= 7
           mkdir ('processed')
        end

        fullpath2=[path,'/processed/',filename,'_bgd.txt'];
        % eval(['save ',fullpath2,'data -ascii -tabs']);
%          save(fullpath2,'padded_export' , '-ascii', '-tabs');


        fid=fopen(fullpath2,'wt');
        fprintf(fid, [ h1 '\t' h2 '\t' h3 '\t' h4 '\t' h5 '\t' h6 '\t'
h7 '\t' h8 '\n']);
        fprintf(fid, '%f\t%f\t%f\t%f\t%f\t%f\t%f\t%f \n',
padded_export');
        fclose(fid);
    end

    function saveres_call(hObject, eventdata)
        path=hpath.String;
        filename=hfname.String;
        sampleres = {hsample.String, hconc.String, henergy.String,
htime.String, hinteg.String, hsolvent.String, hwav.String,
hfilter.String, hsmfac.String, hsmfac2.String, hfname.String};


        respath=[path,'/',hsample.String, '_', hsolvent.String, '_',
hwav.String,'nm_res.txt'];
%
%          ex2 = cellfun(@ex_func,sampleres,'UniformOutput',0);
%          size_ex2 = cellfun(@length,ex2,'UniformOutput',0);
%          str_length = max(max(cell2mat(size_ex2)));
%          ex3 = cellfun(@(x)
ex_func2(x,str_length),ex2,'UniformOutput',0);
```

```matlab
%
%         n=str_length;
%         ex4 = cell2mat(ex3);
%
%         formstr=[];
%         for i=1:11
%             if i<11
%                 formstr=[formstr,strcat('ex4(',int2str((i-
1)*n+1),':',int2str(i*n),'),')];
%             else
%                 formstr=[formstr,strcat('ex4(',int2str((i-
1)*n+1),':',int2str(i*n),')')];
%             end
%         end
%
        if exist(respath, 'file') ~= 2
%
            h1= 'Filename';
            h2= 'Sample';
            h3= 'Concentration(µM)';
            h4= 'Solvent';
            h5= 'Wavelength(nm)';
            h6= 'Power(µJ)';
            h7= 'Integration_Time(s)';
            h8= 'Center_and_Filters';
            h9= 'Integration';
            h10= 'Raw_Smoothing_Factor';
            h11= 'Fit_Smoothing_Factor';

            col_head = {h2, h3, h6, h7, h9, h4, h5, h8, h10, h11, h1};

            fid=fopen(respath,'at');
            fprintf(fid, [ h2 '\t' h3 '\t' h6 '\t' h7 '\t' h9 '\t' h4
'\t' h5 '\t' h8 '\t' h10 '\t' h11 '\t' h1 '\n']);
%             fprintf(fid, '%f\t%f\t%f\t%f\t%f\t%f\t%f\t%f\t%f\t%f\t%f
\n', sampleres');
            fprintf(fid, [hsample.String '\t' hconc.String '\t'
henergy.String '\t' htime.String '\t' hinteg.String '\t'
hsolvent.String '\t' hwav.String '\t' hfilter.String '\t' hsmfac.String
'\t' hsmfac2.String '\t' hfname.String '\n']);
            fclose(fid);
        else
            fid=fopen(respath,'at');
%             fprintf(fid, '%f\t%f\t%f\t%f\t%f\t%f\t%f\t%f\t%f\t%f\t%f
\n', sampleres');
            fprintf(fid, [hsample.String '\t' hconc.String '\t'
henergy.String '\t' htime.String '\t' hinteg.String '\t'
hsolvent.String '\t' hwav.String '\t' hfilter.String '\t' hsmfac.String
'\t' hsmfac2.String '\t' hfname.String '\n']);
            fclose(fid);
%
        end
%
% %             ex2 = cellfun(@ex_func,sampleinfo,'UniformOutput',0);
% %         size_ex2 = cellfun(@length,ex2,'UniformOutput',0);
% %         str_length = max(max(cell2mat(size_ex2)));
%         chex3 = cellfun(@(x)
ex_func2(x,str_length),col_head,'UniformOutput',0);
```

```matlab
%
%          n=str_length;
%          chex4 = cell2mat(chex3);
%
%
% %
%              chformstr=[];
%            for i=1:11
%                if i<11
%                    chformstr=[chformstr,strcat('chex4(',int2str((i-
1)*n+1),':',int2str(i*n),'),')];
%                else
%                    chformstr=[chformstr,strcat('chex4(',int2str((i-
1)*n+1),':',int2str(i*n),')')];
%                end
%            end
%
% %            fprintf(fid, [ h1 '\t' h2 '\t' h3 '\t' h4 '\t' h5 '\t'
h6 '\t' h7 '\n']);
% %            fprintf(fid, '%f\t%f\t%f\t%f\t%f\t%f\t%f \n', smdata');
% %            fclose(fid);
%            else
%             fid=fopen(respath,'at');
%             str1='''%s %s %s %s %s %s %s %s %s %s %s \n'',';
%             eval(['fprintf(fid,',str1,chformstr,');'])
%        end

% % fid = fopen(respath,'a');
% % fprintf(fid,'%s %s %s %s %s %s %s %s %s %s
%s\n',ex4(1:10),ex4(11:20),ex4(21:30),ex4(31:40),ex4(41:50),ex4(51:60),
ex4(61:70),ex4(71:80),ex4(81:90),ex4(91:100),ex4(101:110));
% % fprintf(fid,'%s %s %s %s %s %s %s %s %s %s %s\n',formstr);
%        str1='''%s %s %s %s %s %s %s %s %s %s %s \n'',';
%        eval(['fprintf(fid,',str1,formstr,');'])
%        fclose(fid);
%         end
    end
% %
% %          ex2 = cellfun(@ex_func,sampleinfo,'UniformOutput',0);
% %          size_ex2 = cellfun(@length,ex2,'UniformOutput',0);
% %          str_length = max(max(cell2mat(size_ex2)));
% %          ex3 = cellfun(@(x)
ex_func2(x,str_length),ex2,'UniformOutput',0);
% %
% %          n=str_length;
% %          ex4 = cell2mat(ex3);
% %          respath=[path,'/',filename,'_results.txt'];
% %          formstr=[];
% %          for i=1:11
% %              if i<11
% %                  formstr=[formstr,strcat('ex4(',int2str((i-
1)*n+1),':',int2str(i*n),'),')];
% %              else
% %                  formstr=[formstr,strcat('ex4(',int2str((i-
1)*n+1),':',int2str(i*n),')')];
% %              end
% %          end
% %
```

238

```
% %
% %         fid = fopen(respath,'a');
% %         % fprintf(fid,'%s %s %s %s %s %s %s %s %s %s
%s\n',ex4(1:10),ex4(11:20),ex4(21:30),ex4(31:40),ex4(41:50),ex4(51:60),
ex4(61:70),ex4(71:80),ex4(81:90),ex4(91:100),ex4(101:110));
% %         % fprintf(fid,'%s %s %s %s %s %s %s %s %s %s
%s\n',formstr);
% %         str1='''s\ s\ s %s %s %s %s %s \n'',';
% %         eval(['fprintf(fid,',str1,formstr,');'])
% %         fclose(fid);
% %
% %
% %         col_head = [h1, h2, h3, h4, h5, h6, h7, h8];
% %
raw_export=[rawdata(xlimpos(1):xlimpos(2),1),rawdata(xlimpos(1):xlimpos
(2),2),msig(xlimpos(1):xlimpos(2))];
% %         basefit_export = [xfit, yfit];
% %         basecor_export = [bdat(:,1),bdat(:,2),mbdat];
% % %       full_export = {raw_export, basefit_export,
basecor_export}
% % %         full_export = {
% %         [padded_export, tf] =
padcat(rawdata(xlimpos(1):xlimpos(2),1),rawdata(xlimpos(1):xlimpos(2),2
),msig(xlimpos(1):xlimpos(2)),xfit, yfit,bdat(:,1),bdat(:,2),mbdat);
% %         padded_export(~tf) = 0;
% % %         tpad_export = dataset(padded_export,'VarNames', {h1, h2,
h3, h4, h5, h6, h7, h8});
% %         path=hpath.String;
% %     filename=hfname.String;
% %     fullpath=[path,'/',filename]
% %         fullpath2=[path,'/processed/',filename,'_bgd.txt'];
% %         % eval(['save ',fullpath2,'data -ascii -tabs']);
% % %         save(fullpath2,'padded_export' , '-ascii', '-tabs');
% %
% %
% %         fid=fopen(fullpath2,'wt');
% %         fprintf(fid, [ h1 '\t' h2 '\t' h3 '\t' h4 '\t' h5 '\t' h6
'\t' h7 '\t' h8 '\n']);
% %         fprintf(fid, '%f\t%f\t%f\t%f\t%f\t%f\t%f\t%f \n',
padded_export');
% %         fclose(fid);
% %     end

    function [ out ] = ex_func( in )

        in_datatype = class(in);

        switch in_datatype
            case 'char'
                out = in;
            case 'double'
                out = num2str(in);
        end
    end

    function [ out ] = ex_func2( in, str_length )
```

239

```
    a = length(in);
    out = [char(32*ones(1,str_length-a)), in];
    end
% Utility functions for MYUI


end
```

A.2 Modeling and Estimation of SHG signal NL_vs_Field.m

```
function [ dat, fit, der] = NL_vs_Field(filepath)
%NL_vs_Field - Function reads NL vs BOA and BOA vs Field data, fits
these
%data, generates NL vs Field curves as well as derivative curves

%   Input parameter is the filepath where data is located. Both Beta
and
%   Gamma vs BOA data are read as well as BOA vs Field data. Polynomial
%   fittings are performed on the data to make smoothed functions.
Using
%   these functions, Beta/Gamma vs Field curves are generated by
%   expressing Beta/Gamma as a function of BOA which has already been
determined
%   as a function of Field. The derivatives of Beta/Gamma vs BOA/Field
are determined
%   using the polynomial derivative function. The outputs are the data
(Beta/BOA,
%   Gamma/BOA, BOA/Field), the polynomial fittings (Beta/BOA,
Gamma/BOA,
%   BOA/Field, Beta/Field, Gamma/Field) and the derivative fittings
(dB/dBOA, dB/dField,
%   dG/dBOA, dG/dField).


% Names of data files to be read in
BetaBOA_name='Beta_vs_BOA';
GammaBOA_name='Gamma_vs_BOA';
BOAField_name='BOA_vs_Field';

% Data are saved in the "dat" cell
dat{1} = dlmread([filepath,'/',BetaBOA_name,'.txt'],'\t',1,0);
% dat{1} = dlmread([filepath,'/',BetaBOA_name],'\t',0,0);
dat{2} = dlmread([filepath,'/',GammaBOA_name,'.txt'],'\t',1,0);
dat{3} = dlmread([filepath,'/',BOAField_name,'.txt'],'\t',1,0);

% Each set of data is fit to a polynomial function and then the fitted
% curves are generated at regularly spaced abscissa points. Fittings
are
% saved in the "fit" cell
for i=1:3

    x = dat{i}(:,1);
    xs = size(x,1);
    y = dat{i}(:,2);
```

```
    p = polyfit(x,y,10);

    poly{i} = p;

    xf = (x(1):abs((x(1)-x(xs))/1000):x(xs));
    f = polyval(p,xf);

    fit{i} = [xf',f'];

end

% Conversion to NL vs Field and generation of derivative curves
for j=1:2

    x1 = fit{j}(:,1);
    y1 = fit{j}(:,2);
    p1 = poly{j};

    x3 = fit{3}(:,1);
    y3 = fit{3}(:,2);

%  NL vs BOA is expressed as a function of the BOA vs Field curve by
using
%  the polynomial evaluation function. Fittings are saved in the "fit"
cell
    nlf = polyval(p1,y3);
    fit{3+j} = [x3,nlf];

%  Derviative of the NL vs BOA curve is generated using the polynomial
%  derivative function and saved in the "der" cell
    h1 = polyder(p1);
    k1 = polyval(h1,x1);
    der{2*j-1} = [x1,k1];

%  Derviative of the NL vs Field curve is generated using the
polynomial
%  derivative function and saved in the "der" cell
    pnlf = polyfit(x3,nlf,20);
    h2 = polyder(pnlf);
    k2 = polyval(h2,x3);
    der{2*j} = [x3,k2];

end


end
```

A.3 SHG_signal_geom2.m

```
% SHG_signal_geom2 takes data on NL vs Field and allows user to choose
a
% two Fields to extract values for estimation of the SHG polarization
and
```

```
% SHG intensity produced during both the resting state potential and
action
% potential. The first Field corresponds to the resting state potential
and
% the second Field to the action potential.

clear all

% Enter filepath where data is located so that NL_vs_Field function can
fit
% generate NL vs Field curves which are listed below
filepath='/Users/jtillotson3/Documents/Research/!PROJECTS/NIH - Voltage
Sensing/SHG signal vs field';
[~,fit,~] = NL_vs_Field(filepath);


Field_s = fit{3}(:,1);   % Fields given in V/cm
Beta_s = fit{4}(:,2);    % Given in cgs units, esu
Gamma_s = fit{5}(:,2);   % Given in cgs units, esu

% Plot of NL vs Field
xs=(0:1e7:12e7);


figure
[AX,H1,H2] = plotyy(Field_s,Beta_s,Field_s,Gamma_s,'plot');
grid on
set(get(AX(1),'Ylabel'),'String','Beta (esu)')
set(AX,'Xlim',[0 12e7],'XTick',[xs],'XMinorTick','On')
set(get(AX(2),'Ylabel'),'String','Gamma (esu)')
xlabel('Field (V/cm)')
set(H1,'LineStyle','--')

% User chooses (either mouse input or direct input) particular Fields
that
% denote geometrical regions that molecule exists during resting state
% potential (first point, red) and action potential (second point,
green).
% Lines are generated on plot.
% [x,~] = ginput(2);
x = [Field_s(436) Field_s(437)];
line([x(1) x(1)],[-3*max(Beta_s)
3*max(Beta_s)],'LineWidth',2,'Color',[0 1 0])
line([x(2) x(2)],[-3*max(Beta_s)
3*max(Beta_s)],'LineWidth',2,'Color',[1 0 0])

% Located array position of Field inputs to extract proper NL for
subsequent
% calculations
mpos1 = abs(Field_s-x(1));
mpos2 = abs(Field_s-x(2));
pos1 = find(mpos1 == min(mpos1))
pos2 = find(mpos2 == min(mpos2))

% Constants
eps = 8.854e-12;    % free-space permittivity
c = 3e8;    % speed of light
n = 1.5;    % index of refraction
```

```matlab
% Conversion from cgs units given by data to MKS units used for SHG
% sensitivity
b_conv = eps*(4*pi*1e-10)/3;
g_conv = eps*(4*pi*1e-14)/9;


% Specifications for generic temporal response which includes resting
state
% potential as well as action potential
res = 0.1;
endtime = 100;
t = 0:res:endtime;
dur = size(t,2);


width = floor(dur/5);
length = floor((dur-width)/2);


% Light field amplitude given along with possibility of including noise
on
% the signal
% I0 = 0.1e12;  % Irradiance given in W/m
% Esq0 = 2*(I0)/eps/c/n;    % Field given in V/m
Esq0 = 5e47;
noise = Esq0/2000;


% Nonlinearities and ground-state dipole moment at resting state
potential
% either denoted explicitly or chosen based on first Field specified on
% data plots above
% Beta1 = 1*7.2e-29*b_conv;  % Input given in cgs units, esu
% mu1 = 0.1*3.34e-30/(5*1.38e-23*300);   % Input given in Debye
% Gamma1 = -1*1.05e-32*g_conv;  % Input given in cgs units, esu

Beta1 = Beta_s(pos1)*b_conv  % Input given in cgs units, esu
mu1 = 0.1*3.34e-30/(5*1.38e-23*300);   % Input given in Debye
Gamma1 = Gamma_s(pos1)*g_conv  % Input given in cgs units, esu


d = 8.1e-9; % Thickness in m
Vr = -0.06; % Resting state potential in V
delV = 0.1; % Action potential in V


% Nonlinearities and ground-state dipole moment at during action
potential
% either denoted explicitly or chosen based on second Field specified
on
% data plots above
% Beta2 = 1*7.2e-29*b_conv;  % Input given in cgs units, esu
% mu2 = 0.1*3.34e-30/(5*1.38e-23*300);   % Input given in Debye
% Gamma2 = -1*1.05e-32*g_conv;  % Input given in cgs units, esu


Beta2 = Beta_s(pos2)*b_conv  % Input given in cgs units, esu
mu2 = 0.1*3.34e-30/(5*1.38e-23*300);   % Input given in Debye
Gamma2 = Gamma_s(pos2)*g_conv  % Input given in cgs units, esu


% Comparing magnitude of response from Beta contribution to Gamma
% contribution both during resting state and action potentials
```

```matlab
ratioB = (Gamma1*delV/d)/Beta1
ratioB_mod = (Beta2-Beta1)/((Beta2+Beta1)/2)

% Comparing magnitude of response from mu*Beta contribution to Gamma
% contribution both during resting state and action potentials
ratioMB = Beta1*mu1/(Gamma1);
ratioMB_mod = Beta2*mu2/(Gamma2);

% Temporal response of potential which includes resting state potential
% as well as action potential.
Vmem_b =
[Beta1*ones(length,1);Beta1*ones(width+1,1);Beta1*ones(length,1)];
Vmem_m =
[Vr*Beta1*mu1*ones(length,1);(Vr+delV)*Beta1*mu1*ones(width+1,1);Vr*Bet
a1*mu1*ones(length,1)];
Vmem_g =
[Vr*Gamma1*ones(length,1);(Vr+delV)*Gamma1*ones(width+1,1);Vr*Gamma1*on
es(length,1)];

% figure
% plot(t',Vmem_g)

% Can choose to average scans to see effect on SNR
avg = 1;

Pol = [];
SHG = [];

for i=1:avg
    % Field with normal distribution of random noise applied
    Esq = random('Normal',Esq0,noise,dur,1);
    % Time-dependent SHG polarization that has Beta, Gamma and mu*Beta
    % contributions multiplied by the temporal response of the
potential
    Polar = (Vmem_b + Vmem_m/d + Vmem_g/d).*Esq;
    % Stored polarization
    Pol = [Pol,Polar.^1];
    % Square of the polarization which is proportional to the SHG
intensity
    SHG = [SHG,Polar.^2];

end

% Average of various signals generated above
Pol_m = mean(Pol,2);
SHG_m = mean(SHG,2);

% Average and standard deviation of signal during resting state
potential
Std_fl = std(SHG_m(1:length));
Mean_fl = mean(SHG_m(1:length));

% Average and standard deviation of signal during action potential
Std_pk = std(SHG_m(length:length+width));
Mean_pk = mean(SHG_m(length:length+width));
```

```matlab
% Determination of a SNR figure as well as the SHG sensitivity which is
% defined by the SHG intensity during the action potential minus the
SHG
% intensity during the resting state potential divided by the SHG
intensity
% during the resting state potential
SNR = (Mean_pk-Mean_fl)/Std_pk
% SNR = (Mean_pk-Mean_fl)/Mean_fl^0.5
Per_ch = (Mean_pk-Mean_fl)/Mean_fl
Prod = Mean_fl

figure
subplot(2,1,1)
plot(t',Pol_m)
xlabel('Time')
ylabel('SHG Polarization')
subplot(2,1,2)
plot(t',SHG_m)
xlabel('Time')
ylabel('SHG Intensity')
```

A.4 dV_check_v2.m

```matlab
% clear all

path='/Users/jtillotson3/Documents/Research/!PROJECTS/NIH - Voltage
Sensing/HRS_ves_4-21-15';
filen='JT8015_20uM_n86mV';

%File name of data file without Valinomycin
% filename_noV='JT8108_12.8uM_DOPC_p40mV_noVal_900nm_100s_500spf_kg5';
filename_noV=[filen,'e_1250nm_8.3uJ_500s_700spf_KG5'];
fullpath_noV=[path,'/',filename_noV];
% dat_noV=dlmread(fullpath_noV,'\t',[551,0,928,1]);
dat_noV=dlmread(fullpath_noV,'\t',1,0);

% File name of data file with Valinomycin
% filename_V='JT8108_12.8uM_DOPC_p40mV_Val_900nm_100s_500spf_kg5';
filename_V=[filen,'_1250nm_8.3uJ_500s_700spf_KG5'];
fullpath_V=[path,'/',filename_V];
% dat_V=dlmread(fullpath_V,'\t',[551,0,928,1]);
dat_V=dlmread(fullpath_V,'\t',1,0);

wav=dat_noV(:,1);
sig_noV=dat_noV(:,2);
sig_V=dat_V(:,2);

% Baseline shift
sigb_noV = sig_noV - min(sig_noV);
sigb_V = sig_V - min(sig_V);

%raw difference
Rdiff = sigb_V-sigb_noV;

% Integrate
area_noV = trapz(wav,sigb_noV);
```

```matlab
area_V = trapz(wav,sigb_V);

% Normalize by area
nrm_noV = sigb_noV/area_noV;
nrm_V = sigb_V/area_V;

% Subtract
diff=nrm_V-nrm_noV;

%Smooth raw
msig_noV = smooth(sig_noV,0.01,'rloess');
msig_V = smooth(sig_V,0.01,'rloess');

%Baseline shift - Smoothed
msigb_noV = msig_noV - min(msig_noV);
msigb_V = msig_V - min(msig_V);

%Smoothed raw Difference
mRdiff = msigb_V - msigb_noV;

% Integrate - smoothed
marea_noV = trapz(wav,msigb_noV);
marea_V = trapz(wav,msigb_V);

% Normalize by area - smoothed
mnrm_noV = msigb_noV/marea_noV;
mnrm_V = msigb_V/marea_V;

% Subtract - smoothed
mdiff=mnrm_V-mnrm_noV;


figure('name', filen,  'Position', [700, 900, 500, 750])
subplot(2,1,1)
plot(wav,nrm_noV,'b',...
     wav,nrm_V,'k',...
     wav,diff,'m-',...
     wav,mnrm_noV,'g',...
     wav,mnrm_V,'r',...
     wav,mdiff,'c-');

 subplot(2,1,2)
plot(wav,sigb_noV,'b',...
     wav,sigb_V,'k',...
     wav,Rdiff,'m-',...
     wav,msigb_noV,'g',...
     wav,msigb_V,'r',...
     wav,mRdiff,'c-');



 % ['Wavelength (nm)', 'No_V_raw', 'No_V_Smooth', 'V_raw', 'V_smooth',
'Diff', 'Diff_smooth'];
h1= 'Wavelength (nm)';
h2= [filen,'_NoV_sm'];
```

```matlab
h3= [filen,'_V_sm'];
h4 = [filen,'_dF_sm'];
h5= [filen, '_NoV_n'];
h6= [filen,'_V_n'];
h7 = [filen,'_dF_n'];


h2b = [filen,'_NoV_smRaw'];
h3b = [filen,'_V_smRaw'];
h4b = [filen,'_dF_smRaw'];
h5b = [filen,'_NoV_Raw'];
h6b = [filen,'_V_Raw'];
h7b = [filen,'_dF_Raw'];


smdata = [wav, mnrm_noV, mnrm_V, mdiff, nrm_noV, nrm_V, diff];


Rdata = [wav, msigb_noV, msigb_V, mRdiff, sigb_noV, sigb_V, Rdiff];


%testing
h8 = [filen, 'adjDiff'];
mnrmB_noV = msigb_noV/marea_noV*marea_V;
adjDiff = msigb_V-mnrmB_noV;


adjdata = [wav, mnrmB_noV, msigb_V, adjDiff ,mdiff];


testpath = [path,'/dV/'];
% exist (testpath,'dir')
if exist (testpath,'dir') ~= 7
    mkdir ('dV')
end


% outpath=[path,'/',filename_noV,'_smooth.txt'];
outpath=[path,'/dV/',filen,'_dV.txt'];
Routpath=[path,'/dV/',filen,'_dV_smRaw.txt'];


% eval(['save ',fullpath2,'data -ascii -tabs']);
% save(outpath, 'smdata', '-ascii', '-tabs');
fid=fopen(outpath,'wt');
fprintf(fid, [ h1 '\t' h2 '\t' h3 '\t' h4 '\t' h5 '\t' h6 '\t' h7
'\n']);
fprintf(fid, '%f\t%f\t%f\t%f\t%f\t%f\t%f \n', smdata');
fclose(fid);

fid=fopen(Routpath,'wt');
fprintf(fid, [ h1 '\t' h2b '\t' h3b '\t' h4b '\t' h5b '\t' h6b '\t' h7b
'\n']);
fprintf(fid, '%f\t%f\t%f\t%f\t%f\t%f\t%f \n', Rdata');
fclose(fid);

Adjoutpath=[path,'/dV/',filen,'_dV_adjusted.txt'];
fid=fopen(Adjoutpath,'wt');
fprintf(fid, [ h1 '\t' h5 '\t' h6 '\t' h8 '\t' h4 '\n']);
fprintf(fid, '%f\t%f\t%f\t%f\t%f \n', adjdata');
fclose(fid);
```